



**SPATIALLY-RESOLVED TEMPERATURE DIAGNOSTIC FOR SUPERSONIC  
FLOW USING CROSS-BEAM DOPPLER-LIMITED LASER SATURATION  
SPECTROSCOPY**

DISSERTATION

Grady T. Phillips, Major, USAF

AFIT/DS/ENP/06-03

**DEPARTMENT OF THE AIR FORCE  
AIR UNIVERSITY**

**AIR FORCE INSTITUTE OF TECHNOLOGY**

**Wright-Patterson Air Force Base, Ohio**

APPROVED FOR PUBLIC RELEASE; DISTRIBUTION UNLIMITED

The views expressed in this dissertation are those of the author and do not reflect the official policy or position of the United States Air Force, Department of Defense, or the United States Government.

AFIT/DS/ENP/06-03

SPATIALLY-RESOLVED TEMPERATURE DIAGNOSTIC FOR SUPERSONIC  
FLOW USING CROSS-BEAM DOPPLER-LIMITED LASER SATURATION  
SPECTROSCOPY

DISSERTATION

Presented to the Faculty

Graduate School of Engineering and Management

Air Force Institute of Technology

Air University

Air Education and Training Command

In Partial Fulfillment of the Requirements for the

Degree of Doctor of Philosophy

Grady T. Phillips, BS, MS

Major, USAF

March 2006

APPROVED FOR PUBLIC RELEASE; DISTRUBUTION UNLIMITED

SPATIALLY-RESOLVED TEMPERATURE DIAGNOSTIC FOR SUPERSONIC  
FLOW USING CROSS-BEAM DOPPLER-LIMITED LASER SATURATION  
SPECTROSCOPY

Grady T. Phillips, BS, MS  
Major, USAF

Approved:

Date

\_\_\_\_\_  
Glen P. Perram (Chairman)

\_\_\_\_\_  
Meir Pachter (Dean's Representative)

\_\_\_\_\_  
Paul J. Wolf (Member)

\_\_\_\_\_  
Paul I. King (Member)

Accepted:

\_\_\_\_\_  
M. U. Thomas

Dean, Graduate School of Engineering and Management

\_\_\_\_\_  
Date



### Abstract

Optical techniques for measuring the temperature in three-dimensional supersonic reactive flows have typically depended on lineshape measurements using single-beam laser absorption spectroscopy. However, absorption over extended path lengths in flows with symmetric, turbulent eddies can lead to systematically high extracted temperatures due to Doppler shifts resulting from flow along the absorption path. To eliminate these problems and provide full three-dimensional spatial resolution, two variants of laser saturation spectroscopy have been developed and demonstrated, for the first time, which utilize two crossed and nearly copropagating laser beams. Individual rotational lines in the visible  $I_2 \ X \ ^1\Sigma(0_g^+) \rightarrow B \ ^3\Pi(0_u^+)$  transition were used to develop the two diagnostics to support research on the Chemical Oxygen-Iodine Laser (COIL), the weapon aboard the USAF Airborne Laser. Cross-Beam Saturation Absorption Spectroscopy (CBSAS) and Cross-Beam Inter-Modulated Fluorescence (CBIMF) were demonstrated as viable methods for recording the spectral signal of an  $I_2$  ro-vibrational line in a small three-dimensional volume using a tunable CW dye laser. Temperature is extracted by fitting the recorded signal with a theoretical signal constructed from the Doppler-broadened hyperfine components of the ro-vibrational line.

The CBIMF technique proved successful for extracting the temperature of an  $I_2$ -seeded, Ar gas flow within a small, Mach 2, Laval nozzle where the overlap volume of the two 1 mm diameter laser beams was  $2.4 \text{ mm}^3$ . At a test point downstream of the nozzle throat, the average temperature of  $146 \text{ K} \pm 1.5 \text{ K}$  extracted from measurements of

the  $I_2$  P(46) 17-1 spectral line compared favorably with the 138 K temperature calculated from isentropic, one-dimensional flow theory. CBIMF provides sufficient accuracy for characterizing the temperature of the gas flow in a COIL device, and could be applied to other areas of flow-field characterization and nozzle design. In contrast, the CBSAS signal was not sufficiently strong for reliable temperature extraction from the  $2.4 \text{ mm}^3$  overlap volume required in the nozzle experiments. Otherwise, the CBSAS technique could have greater success for application in flow field test environments that allow the use of a larger overlap-volume.

CBIMF and CBSAS measurements were also made in a static cell at 293 K. At 50 mTorr of  $I_2$ , the standard error in temperature from CBIMF measurements of the  $I_2$  P(46) 17-1 line was approximately 0.5 K. For CBSAS, the standard error in temperature was approximately 3 K at 50 mTorr of  $I_2$ . Accuracy improved with increasing  $I_2$  pressure. In addition, the spatial-resolution capability of CBIMF and CBSAS was demonstrated in a static cell with an applied temperature gradient ranging from 300 to 365 K. Extracted temperatures were compared to thermocouple measurements at multiple positions in the gradient. Agreement between extracted temperatures and thermocouple measurements was better at the lower temperatures.

Doppler-free measurements of several  $I_2$  hyperfine spectra were also performed to support development of the theoretical model. Saturation Absorption Spectroscopy was used to obtain Ar pressure broadening rates of  $8.29 \pm 0.30 \text{ MHz/Torr}$  for the  $I_2$  P(70) 17-1 hyperfine spectrum, and  $10.70 \pm 0.41 \text{ MHz/Torr}$  for the  $I_2$  P(10) 17-1 hyperfine spectrum.

## **Acknowledgements**

I would like to express my sincere appreciation to Dr. Glen Perram, my faculty advisor, for his guidance, and to the Engineering Physics technicians for their support during the course of this research effort.

Grady T. Phillips

## Table of Contents

	Page
Abstract .....	iv
Acknowledgements .....	vi
List of Figures .....	ix
List of Tables .....	xv
Nomenclature .....	xvii
I. Introduction .....	1
A. Airborne Laser Program.....	1
B. Chemical Oxygen Iodine Laser.....	2
C. Previous Work.....	3
D. Research Objective .....	4
II. Background .....	7
A. Molecular Iodine .....	7
I <sub>2</sub> Electronic Transitions. ....	8
I <sub>2</sub> Hyperfine Transitions.....	17
B. Spectral Line Shape and Line Width.....	25
Natural Line-Broadening. ....	28
Pressure Broadening. ....	31
Doppler Broadening.....	35
C. Laser Saturation Spectroscopy .....	39
Linear and Nonlinear Spectroscopy.....	39
Doppler-Free Saturation Spectroscopy.....	49
D. Supersonic Flow in a Nozzle .....	55
III. Theory .....	58
A. Spatially-Resolved Cross-Beam Doppler-Limited Saturation Spectroscopy .....	58
Cross Beam Saturation Absorption Spectroscopy. ....	58
Cross-Beam Inter-Modulated Fluorescence Spectroscopy.....	61
B. Spectral Profiles for I <sub>2</sub> Ro-vibrational Lines.....	64
III. Experiments and Results .....	69
A. Doppler Free Laser Spectroscopy .....	69

Experiment.....	69
Results.....	72
Discussion.....	84
B. Comparison of Laser Spectroscopy Techniques used for Temperature	
Determination. ....	88
Experiments. ....	88
Results.....	92
Discussion.....	110
C. Spatially-Resolved Temperatures in a Supersonic Nozzle. ....	117
Experiment.....	117
Results.....	123
Discussion.....	135
IV. Conclusion .....	145
Appendix A. Blended Lines.....	149
Bibliography .....	153
Vita.....	160

## List of Figures

Figure	Page
1. COIL supersonic mixing nozzle. The line-integrated temperature measurement obtained with single-beam laser absorption may be biased due to possible symmetric turbulent vortices present at the nozzle exit plane. <sup>9</sup> .....	4
2. Potential energy curves for I <sub>2</sub> . <sup>15</sup> .....	9
3. The I <sub>2</sub> NEQ hyperfine energy levels for large odd $J''$ . The coupling constant is $eQq'' = -2453$ . The small number labeling each level is the $F-J$ value. ....	21
4. The I <sub>2</sub> NEQ hyperfine energy levels for large even $J''$ . The coupling constant is $eQq'' = -2453$ . The small number labeling each level is the $F-J$ value. ....	21
5. Comparison of a Gaussian lineshape to various Voigt lineshapes. The Gaussian width is the same for all lineshapes: 400 MHz FWHM. The dotted line is a Voigt with a 1000 MHz Lorentzian FWHM. The long-dashed line is a Voigt with a 100 MHz Lorentzian FWHM. The short-dashed line is a Voigt with a 10 MHz Lorentzian FWHM. The Gaussian lineshape is the solid line. ....	38
6. Open two-level system.....	41
7. Doppler Free Saturation Absorption Spectroscopy Set-up.....	52
8. Doppler-Free Inter-Modulated Fluorescence experiment.....	54
9. Convergent/divergent nozzle. ....	56
10. Cross-Beam Saturation Absorption Spectroscopy (CBSAS) experiment. ....	59
11. CBSAS experiment showing path lengths along which self-absorption occurs: L <sub>1</sub> , L <sub>2</sub> , L <sub>3</sub> ; and the path length, L', for mutual interaction between the pump and probe beam. ....	60
12. Cross-Beam Inter-Modulated Fluorescence (CBIMF) experiment. ....	62
13. Theoretical spectral profile of P(46) 17-1 for various temperatures. In order of decreasing linewidth, the profile temperatures are 298 K, 250 K, 200 K, 150 K, 100 K, 50 K, 0.01 K. ....	67
14. Theoretical spectral profile of P(53) 19-2 for various temperatures. In order of decreasing linewidth, the profile temperatures are 298 K, 250 K, 200 K, 150 K, 100 K, 50 K, 0.01 K. ....	67

Figure	Page
15. Schematic for Doppler-Free Saturation Absorption Spectroscopy Experiment. ....	71
16. $I_2$ P(12) 17-1 hyperfine spectrum from Doppler-free SAS. ....	73
17. $I_2$ P(12) 17-1 hyperfine spectrum from Doppler-free IMF. ....	74
18. $I_2$ P(130) 17-1 hyperfine spectrum from Doppler-free SAS. ....	74
19. $I_2$ P(130) 17-1 hyperfine spectrum from Doppler-free IMF. ....	75
20. $I_2$ P(53) 19-2 hyperfine spectrum from Doppler-free IMF. ....	75
22. $I_2$ hyperfine spectrum (black) for R(37) 15-0 & R(127) 19-1 blended line from SAS with a 1000 Hz chopping frequency. The Doppler-broadened MPSF profile (gray) is also shown. ....	78
23. $I_2$ hyperfine spectrum (black) for R(37) 15-0 & R(127) 19-1 blended line from SAS with a 3750 Hz chopping frequency. The Doppler-broadened MPSF profile (gray) is also shown. ....	78
25. $I_2$ P(70) 17-1 hyperfine (black) spectrum from SAS, and MPSF (gray) Doppler-broadened profile at an $I_2$ pressure of 200 mTorr. ....	80
26. Absorption parameter as a function of $I_2$ pressure for P(70) 17-1. ....	80
27. SAS (black) and MPSF (gray) spectra of P(70) 17-1 at 0.1635 Torr $I_2$ pressure. ....	82
28. SAS (black) and MPSF (gray) spectra of P(70) 17-1 at 0.1635 Torr $I_2$ pressure and 0.9508 Ar buffer gas pressure. ....	82
29. $I_2$ P(70) 17-1 hyperfine Lorentzian linewidth as a function of Ar buffer gas pressure from Doppler-free SAS measurements. ....	83
30. $I_2$ P(10) 17-1 hyperfine Lorentzian linewidth as a function of Ar buffer gas pressure from Doppler-free SAS measurements. ....	83
31. $I_2$ P(70) 17-1 Lorentzian linewidth from Voigt profile vs. Ar buffer gas pressure from MPSF measurements. ....	85
32. Schematic of the glass cell used for spatially-resolved temperature measurements. ....	89
33. Glass cell used for spatially-resolved temperature measurements. ....	90

Figure	Page
34. I <sub>2</sub> P(70) 17-1 isolated ro-vibrational line Doppler-broadened profile at 17339.8187 cm <sup>-1</sup> obtained from the CBIMF technique. ....	93
35. I <sub>2</sub> P(53) 19-2 isolated ro-vibrational line Doppler-broadened profile at 17340.2214 cm <sup>-1</sup> obtained from the CBIMF technique. ....	93
36. CBIMF profile of I <sub>2</sub> P(46) 17-1 in static cell. The experimental data points are gray. The theoretical fit to the data is represented by the black line. The measurement was taken at room temperature.....	94
37. Residual trend for CBIMF profile of I <sub>2</sub> P(46) 17-1 in static cell. ....	94
38. CBSAS profile of I <sub>2</sub> P(46) 17-1 in static cell. The experimental data points are gray. The theoretical fit to the data is represented by the black line. The measurement was taken at room temperature.....	95
39. Residual trend for CBSAS profile of I <sub>2</sub> P(46) 17-1 in static cell.....	95
40. MPSF profile of I <sub>2</sub> P(46) 17-1 in static cell. The experimental data points are gray. The theoretical fit to the data is represented by the black line. The measurement was taken at room temperature.....	96
41. Residual trend for MPSF profile of I <sub>2</sub> P(46) 17-1 in static cell. ....	96
42. Extracted-temperature error for various chopping frequencies. Static cell measurements at fixed temperature of 297 K. P(70) 17-1 CBSAS (gray circle), P(70) 17-1 CBIMF (white circle), P(70) 17-1 MPSF (black circle), P(53) 19-2 CBSAS (gray square), P(53) 19-2 CBIMF (white square), P(53) 19-2 MPSF (black square).....	97
43. Extracted temperature for various chopping frequencies. Static cell measurements at fixed temperature of 297 K. P(70) 17-1 CBSAS (gray circle), P(70) 17-1 CBIMF (white circle), P(70) 17-1 MPSF (black circle), P(53) 19-2 CBSAS (gray square), P(53) 19-2 CBIMF (white square), P(53) 19-2 MPSF (black square), thermocouple temperature (solid black line).....	98
44. Absorption parameter at various chopping frequencies. Static cell measurements at fixed temperature of 297 K. P(70) 17-1 CBSAS (gray circle), P(70) 17-1 CBIMF (white circle), P(70) 17-1 MPSF (black circle), P(53) 19-2 CBSAS (gray square), P(53) 19-2 CBIMF (white square), P(53) 19-2 MPSF (black square).....	99



Figure	Page
45. Extracted-temperature error as a function of $I_2$ pressure for P(46) 17-1. Static cell measurements at fixed temperature of 295 K. CBSAS (square), CBIMF (circle), MPSF (triangle). .....	100
46. Extracted temperature error as a function of $I_2$ pressure for R(30) 15-0. Static cell measurements at fixed temperature of 295 K. CBSAS (square), CBIMF (circle), MPSF (triangle). .....	101
47. Extracted temperature as a function of $I_2$ pressure for P(46) 17-1. Static cell measurements at fixed temperature of 295 K. CBSAS (square), CBIMF (circle), MPSF (triangle), thermocouple temperature (solid line). .....	101
48. Extracted temperature as a function of $I_2$ pressure for R(30) 15-0. Static cell measurements at fixed temperature of 295 K. CBSAS (square), CBIMF (circle), MPSF (triangle), thermocouple temperature (solid line). .....	102
49. Spatially resolved $T_{ex}$ measurements from $I_2$ P(114) 18-1 in a static cell with thermal gradient. CBSAS (square), CBIMF (black circle), MPSF (triangle), thermocouple temperature (gray circle). Errors bars indicate $\Delta T$ along overlap length centered at $X=1$ as estimated from $T_c$ measurements. ....	103
50. Spatially resolved temperature measurements from $I_2$ P(46) 17-1 in a static cell with thermal gradient. CBSAS (square), CBIMF (black circle), MPSF (triangle), thermocouple temperature (gray circle). Errors bars indicate $\Delta T$ along overlap length centered at $X=1$ as estimated from $T_c$ measurements. ....	103
51. CBIMF P(46) 17-1 spectral profile at three positions/temperature. Position 1/ high temp (black), Position 2 (dark gray), Position 3/low temperature (light gray). .....	106
52. CBSAS P(46) 17-1 spectral profile at three positions/temperatures. Position 1/ high temp (black), Position 2 (dark gray), Position 3/low temperature (light gray). .....	106
53. MPSF P(46) 17-1 spectral profile at three positions/temperatures. Position 1/ high temp (black), Position 2 (dark gray), Position 3/low temperature (light gray). .....	107
54. $I_2$ P(51) 18-2 & P(66) 16-1 blended line in a static cell with thermal gradient. CBSAS (black square), CBIMF (black circle), MPSF (black triangle), thermocouple (gray circle). Errors bars indicate $\Delta T$ along overlap length centered at $X=1$ as estimated from $T_c$ measurements. ....	108

Figure	Page
55. P(46) 17-1 CBIMF profile at $X=1$ in static cell with temperature gradient. Experimental data (gray) is fit with $S_{cb}(\nu)$ (black line).....	115
56. Residual trend from $S_{cb}(\nu)$ fit to P(46) 17-1 CBIMF profile at $X=1$ in static cell with temperature gradient. ....	115
57. P(46) 17-1 CBIMF profile at $X=1$ in static cell with temperature gradient. Experimental data (gray) is fit with $S'_{cb}(\nu)$ (black line).....	116
58. Residual trend from $S'_{cb}(\nu)$ fit to P(46) 17-1 CBIMF profile at $X=1$ in static cell with temperature gradient. ....	116
59. Nozzle side-view (upper schematic) and nozzle assembly (lower schematic). ....	119
60. Supersonic Flow Apparatus (side view). ....	120
61. Six-way cross mounted on pump. ....	121
62. Gas/vapor inlet plumbing (top photo). Supersonic flow experiment (bottom photo). ....	122
63. CBIMF in supersonic nozzle for $I_2$ P(46) 17-1. The experimental data points are gray. The theoretical fit to the data is represented by the black line.....	125
64. Residual trend for CBIMF profile of $I_2$ P(46) 17-1 in supersonic nozzle.....	125
65. CBIMF in supersonic nozzle for $I_2$ P(31) 17-1. The experimental data points are gray. The theoretical fit to the data is represented by the black line.....	127
66. Residual trend for CBIMF profile of $I_2$ P(31) 17-1 in supersonic nozzle.....	127
67. Single Beam Side Fluorescence in supersonic nozzle for P (46) 17-1. The ex- perimental data points are gray. The theoretical fit to the data is represented by the black line. ....	129
68. Residual trend for SBSF profile of $I_2$ P(46) 17-1 in supersonic nozzle.....	129
69. Single Beam Side Fluorescence in supersonic nozzle for P(31) 17-1. The ex- perimental data points are gray. The theoretical fit to the data is represented by the black line. ....	130
70. Residual trend for SBSF profile of $I_2$ P(31) 17-1 in supersonic nozzle.....	131

Figure	Page
71. SBSF in supersonic nozzle for P(10) 19-2 & R(104) 18-1. The y-axis is Relative Intensity (Arbitrary Units). The x-axis is $\Delta\nu$ (GHz). .....	132
72. CBIMF in supersonic nozzle for P(10) 19-2 & R(104) 18-1. The y-axis is Relative Intensity (Arbitrary Units). The x-axis is $\Delta\nu$ (GHz). .....	133
73. CBIMF for P(46) 17-1 in nozzle for various $I_2/Ar$ pressures. ....	134
74. SBSF for P(46) 17-1 in nozzle for various $I_2/Ar$ pressures. ....	136
75. CBIMF in supersonic nozzle for $I_2$ P(46) 17-1. Experimental data (gray) is fit with $S'_{CB}(\nu)$ (black line). ....	139
76. Residual trend from $S'_{CB}(\nu)$ fit to CBIMF in supersonic nozzle for $I_2$ P(46) 17-1. ....	139
77. “Energy-level diagram for the Chemical Oxygen-Iodine Laser illustrating the resonant energy transfer from the metastable reservoir $O_2(a^1\Delta)$ to the upper laser level of atomic Iodine, $I(^2P_{1/2})$ . The energy-levels for several key states involved in the dissociation of molecular Iodine are also provided”. <sup>9</sup> .....	141
78. Schematic diagram of a typical supersonic Chemical Oxygen-Iodine Laser (COIL). <sup>9</sup> .....	141
79. A fit to CBSAS signal of the P(51) 18-2 & P(66) 16-1 blended line recorded in a static cell experiment. The amplitudes of each ro-vibrational line and the common Doppler linewidth are constrained to temperature. The y-axis is Relative Intensity (Arbitrary Units). The x-axis is Relative Frequency (GHz). ....	152

## List of Tables

Table	Page
1. Expansion parameters for the $X^1\Sigma(0_g^+)$ state of $I_2$ . Valid for $v''=0-9$ . ....	12
2. Expansion parameters for the $B^3\Pi(0_u^+)$ state of $I_2$ . Valid for $v'=1-62$ . ....	12
3. Line positions for select $I_2$ $B^3\Pi(0_u^+) \leftrightarrow X^1\Sigma(0_g^+)$ ro-vibrational spectral lines. ...	13
4. Franck-Condon Factors <sup>23</sup> and relative $v''$ -level populations for select $I_2$ $B^3\Pi(0_u^+) \leftrightarrow X^1\Sigma(0_g^+)$ vibrational bands at $T=300$ K. ....	16
5. Relative frequencies and relative intensities for $I_2$ P(46) 17-1 hyperfine tran- sitions. Calculations are shown from the matrix theory and from the high-J approximation theory. ....	26
6. Relative frequencies and relative intensities for $I_2$ P(53) 19-2 hyperfine tran- sitions. Calculations are shown from the matrix theory and from the high-J approximation theory. ....	27
7. Homogeneous lifetimes for $I_2$ B-X transitions. $\tau$ is the lifetime of the transition. $\tau_o$ is the zero-pressure lifetime. $\tau_{rad}$ is the radiative lifetime. $\Delta\nu$ is the FWHM linewidth. ....	30
8. Homogeneous linewidths for $I_2$ B-X transitions. $\Delta\nu$ is the FWHM linewidth. $P_{I_2}$ is the iodine pressure. $\tau$ is the lifetime of the transition. ....	30
9. $I_2$ pressure broadening rates due to buffer gases. ....	34
10. Self-broadening rates for $I_2$ . ....	35
11. $I_2$ saturation intensities from literature. ....	45
12. Ar buffer-gas broadening rates for $I_2$ . ....	85
13. P(46) 17-1 and P(114) 18-1 extracted temperatures from CBIMF, CBSAS, and MPSF in a static cell with a temperature gradient. ....	104
14. Thermocouple measurements and the estimated temperature gradient along the overlap length in static cell for P(46) 17-1 and P(114) 18-1 cross-beam experiments. ....	104

Table	Page
15. P(51) 18-2 & P(66) 16-1 extracted temperatures from CBIMF, CBSAS, and MPSF in a static cell with a temperature gradient. ....	108
16. Thermocouple measurements and the estimated temperature gradient along the overlap length in static cell for P(51) 18-2 & P(66) 16-1 blended line cross-beam experiments. ....	109
17. Extracted temperatures from three positions in the static cell with a temperature gradient for P(46) 17-1 using the CBIMF, CBSAS, MPSF techniques. $T'_{ex}$ values are the results from fits with $S'_{cb}(\nu)$ . $T_{ex}$ values are the results from fits with $S_{cb}(\nu)$ . ....	114
18. Nozzle data and calculations. ....	123
19. CBIMF for $I_2$ P(46) 17-1 in supersonic nozzle with Ar/ $I_2$ . Consecutive measurements for same pressure and location. ....	126
20. CBIMF for $I_2$ P(31) 17-1 in supersonic nozzle with Ar/ $I_2$ . Consecutive measurements for same pressure and location. ....	128
21. Single Beam Side Fluorescence for $I_2$ P(46) 17-1 in supersonic nozzle with Ar/ $I_2$ . Consecutive measurements for same pressure and location. ....	130
22. Single Beam Side Fluorescence for $I_2$ P(31) 17-1 in supersonic nozzle with Ar/ $I_2$ . Consecutive measurements for same pressure and location. ....	131
23. SBSF and CBIMF measurements for P(10) 19-2 & R(104) 18-1 in supersonic nozzle. ....	133
24. CBIMF for P(46) 17-1 in nozzle for various $I_2$ /Ar pressures. ....	134
25. SBSF for P(46) 17-1 in nozzle for various $I_2$ /Ar pressures. ....	136
26. CBIMF for $I_2$ P(46) 17-1 in supersonic nozzle with Ar/ $I_2$ . Consecutive measurements for same pressure and location.. $T'_{ex}$ values are the results from fits with $S'_{CB}(\nu)$ . $T_{ex}$ values are the results from fits with $S_{CB}(\nu)$ . ....	138

## Nomenclature

### Acronyms

ABL	Airborne Laser Program
ATL	Advanced Tactical Laser
BHP	Basic Hydrogen Peroxide
CBIMF	Cross Beam Inter-Modulated Fluorescence Spectroscopy
CBSAS	Cross Beam Saturation Absorption Spectroscopy
COIL	Chemical Oxygen Iodine Laser
FCF	Franck-Condon Factor
FWHM	Full Width at Half Maximum
HFS	Hyperfine Spectrum
IMF	Inter-Modulated Fluorescence Spectroscopy
LIF	Laser Induced Fluorescence
MPSF	Modulated-Pump Side-Fluorescence
ND	Neutral Density
NEQ	Nuclear Electric Quadrupole
PMT	Photo-Multiplier Tube
SAS	Saturation Absorption Spectroscopy
SBSF	Single-Beam Side-Fluorescence
SNR	Signal to Noise Ratio
SR	Spin-Rotation
STP	Standard Temperature and Pressure

### Molecular Spectroscopy

$A_{ji}$	Einstein A-coefficient, also expressed as $A(v' J', v'' J'')$
$B_{ij}$	Einstein B-coefficient for absorption
$\alpha_{zZ}$	direction cosine
$B_{ji}$	Einstein B-coefficient for stimulated emission
$B$	rotational constant
$^1\Pi(1_u)$	excited electronic state of $I_2$ with an unbound potential
$B\ ^3\Pi(0_u^+)$	second excited electronic state of $I_2$ with a bound potential
$\tilde{B}$	eigenvector matrices from calculations of $B\ ^3\Pi(0_u^+)$ state energy levels
$c$	speed of light in vacuum
$C_{SR}$	Spin-Rotation coupling constant
$e$	electronic charge
$eQq_I$	NEQ coupling constant
$E$	energy
$\vec{F}$	total angular momentum vector

$F_v(J)$	rotational term value
$g_i$	degeneracy of $i^{\text{th}}$ energy level
$g_n$	nuclear spin degeneracy of a rotational level energy
$G(v)$	vibrational term value
$H$	Hamiltonian operator
$I_{abs}$	intensity of an absorption line
$I_{em}$	intensity of emission for spectral line
$\vec{I}$	total nuclear spin vector for molecule
$I_i$	nuclear spin quantum number for $i^{\text{th}}$ atom
$I_2$	molecular iodine
$J$	rotational energy-level quantum number
$\lambda$	wavelength
$M_{el}$	electronic dipole moment
$M_F$	component of $\vec{F}$ along a fixed space-axis
$N_{hyp}$	number of degenerate hyperfine levels
$\mu_e$	electronic transition moment
$\mu_z$	electronic transition moment in the molecule-fixed coordinate z-direction
$\tilde{\mu}$	electronic transition moment matrix
$P_{ij}$	relative transition probability between an $i$ - and $j$ -state
$\Psi$	wavefunction
$q_{v'v''}$	Franck-Condon Factor
$q_J$	average electric-field gradient along the $J$ direction
$Q$	electric quadrupole moment
$Q_i$	partition function
$R$	internuclear separation distance
$\bar{R}$	R-centroid
$\sigma$	wavenumber
$\sigma_o$	vibrational band origin
$\sigma_P$	P-branch term value for ro-vibrational line
$\sigma_R$	R-branch term value for ro-vibrational line
$\nu$	vibrational energy-level quantum number
$S_{J',J''}$	Hönl-London factor
$T_e$	energy difference between upper- and lower-level electronic state potential minima
$X^1\Sigma(0_g^+)$	ground electronic state of $I_2$ with a bound potential
$\tilde{X}$	eigenvector matrices from calculations of $X^1\Sigma(0_g^+)$ state energy levels
$Z_{ij}$	electronic transition moment matrix elements dependent on $M_F$

## Laser Spectroscopy and Lineshape Theory

$A$	amplitude parameter for Doppler-broadened theoretical profile of an I <sub>2</sub> ro-vibrational line
$A_i^{rad}$	radiative transition probability per unit time for energy level $E_i$
$\alpha$	absorption coefficient (in general)
$\alpha_o$	unsaturated absorption coefficient
$\alpha_s$	saturated absorption coefficient due to single monochromatic light beam
$C_i$	rate for the repopulation of level $i$ from other levels
$D_i$	diffusion rate of $i$ -level molecules into the excitation volume $dV$
$dV$	excitation volume element
$\Delta N$	saturated population difference
$\Delta N^o$	unsaturated population difference
$\Delta N^o(v_z)$	unsaturated population difference with a Maxwellian velocity distribution
$\Delta \nu$	relative frequency; $\nu - \nu_{minimum}$ or $\nu - \nu_o$ according to graphical scale
$\Delta \nu_{coll}$	collision-induced linewidth (FWHM) due to elastic and inelastic collisions
$\Delta \nu_e$	elastic collision-induced linewidth (FWHM)
$\Delta \nu_D$	spectral linewidth due to Doppler-broadening (FWHM)
$\Delta \nu_{in}$	inelastic collision-induced linewidth (FWHM)
$\Delta \nu_h$	homogeneous linewidth (FWHM)
$\Delta \nu_L$	Lorentzian linewidth (FWHM)
$\Delta \nu_n$	natural linewidth (FWHM)
$\Delta \nu_s$	saturation-broadened linewidth (FWHM)
$\Delta v_z$	z-component-velocity interval
$\delta(\Delta \nu_D)$	standard error in Doppler-broadened linewidth (FWHM)
$\delta T$	standard error in temperature
$\vec{E}$	electric field vector
$f$	linear frequency of an optical chopper
$f_i^{hyp}$	relative intensity of the $i^{th}$ I <sub>2</sub> hyperfine spectral line
$g(\nu)$	spectral profile (in general)
$\bar{g}(\nu)$	lineshape normalized to unity at line center, i.e. $\bar{g}(\nu_o) = 1$
$g_D(\nu)$	Doppler-broadened theoretical profile of an I <sub>2</sub> ro-vibrational line
$g_h(\nu)$	homogeneous lineshape
$g_n(\nu)$	natural lineshape
$G(\nu)$	Gaussian lineshape as a function of linear frequency
$h$	Planck's constant
$I$	intensity



$I_o$	incident intensity
$I_{IMF}$	intensity due to Inter-Modulated Fluorescence
$I_\nu$	intensity of incident radiation at frequency $\nu$
$I_{pump}$	intensity of a “pump” laser beam
$I_{probe}$	intensity of a “probe” laser beam
$I_s$	saturation intensity
$I_t$	transmitted intensity
$I_{probe}^{trans}$	transmitted intensity of a “probe” laser beam
$k_B$	Boltzmann’s constant
$k$	absorption parameter
$\vec{k}$	propagation vector
$k_z$	propagation vector component in z-direction
$K$	pressure broadening coefficient
$K_{buffer}$	pressure broadening coefficient of $I_2$ due to a buffer gas
$L(\nu)$	Lorentzian lineshape, area normalized to 1
$L$	length
$m$	mass of a chemical species in kg
$m_{I_2}$	mass of $I_2$ molecule in kg
$\mathcal{M}_{I_2}$	molecular mass of $I_2$ molecule in amu
$m_p$	mass of proton in kg
$\mu$	reduced mass
$N$	number of molecules per unit volume; number density
$N_B$	number density of collision partner $B$
$\nu$	linear frequency
$\nu_o$	resonant frequency
$\Omega$	angular frequency of an optical chopper
$P_{laser}(\nu)$	output power of a laser as a function of frequency
$\rho_\nu$	energy density at frequency $\nu$ (units of J/m <sup>3</sup> )
$\rho(\nu)$	spectral energy density (units of J s/m <sup>3</sup> )
$R_i$	total relaxation probability per unit time for energy level $E_i$
$R^*$	relaxation probability per unit time due to upper- and lower-level total relaxation probabilities
$S_{CB}(\nu)$	signal for a cross-beam (CBIMF or CBSAS) experiment
$S_{CBIMF}$	signal for Cross-Beam Inter-Modulated Fluorescence experiment
$S_{CBSAS}$	signal for Cross-Beam Saturation Absorption Spectroscopy experiment
$S_{IMF}$	signal for an Inter-Modulated Fluorescence experiment
$S_{MPSF}$	signal for Modulated Pump Side-Fluorescence experiment

$S_{SAS}$	signal for a Saturation Absorption Spectroscopy experiment
$S(\nu)$	frequency-dependent saturation parameter
$S(\nu_o)$	saturation parameter at line-center
$S_o$	$S(\nu_o)$
$\sigma_e$	elastic collision cross-section
$\sigma_{in}$	inelastic collision cross-section
$\sigma_{12}$	absorption cross-section between energy-levels 1 and 2
$\sigma_{12}(\nu)$	frequency-dependent absorption cross-section
$\sigma(\nu_o)$	absorption cross-section at line-center
$\sigma_o$	$\sigma(\nu_o)$
$\sigma_s$	cross-section for line-shift
$s$	shift in line center
$T$	temperature, absolute
$T_{coll}$	mean time between molecular collisions
$\tau_o$	zero-pressure lifetime
$\tau_{nr}$	non-radiative lifetime due to spontaneous predissociation
$\tau_{rad}$	radiative lifetime
$\vec{v}$	velocity vector
$v_p$	most probable velocity for a Maxwellian velocity distribution
$v_z$	velocity component in z-direction
$\bar{v}$	mean relative velocity
$V(\nu)$	Voigt lineshape as function of linear frequency
$dW_{12} / dt$	rate at which the energy per unit volume is absorbed on the transition from energy level 1 to energy level 2

#### Flow dynamics

$A$	cross-sectional area of the nozzle at a measurement-point downstream from the throat
$A^*$	cross-sectional area of the nozzle throat
$C_p$	specific heat at constant pressure
$C_v$	specific heat at constant volume
$\gamma$	specific heat ratio, $C_p/C_v$
$M$	Mach number
$\mathcal{M}$	atomic mass in amu
$P$	pressure
$P_o$	stagnation pressure
$R_o$	universal gas constant
$R$	gas constant with mass dependence
$\rho$	mass density

$S$	speed of vacuum pump
$S_{max}$	maximum speed of a vacuum pump
$T$	temperature, absolute
$T_o$	stagnation temperature
$VR$	volume rate
$VR_{max}$	maximum volume rate
$w_{max}$	maximum mass flow rate at throat

#### Units

amu	atomic mass units
$\text{cm}^{-1}$	wavenumber
cfm	cubic feet per minute (fluid flow rate)
GHz	GigaHertz (frequency)
K	Kelvin (temperature)
m	meters
MHz	MegaHertz (frequency)
ns	nanosecond
Pa	Pascal (pressure)
Torr	(pressure)
W	Watts (power)

#### Notation in experimental results

$A_{test}$	cross-sectional area of nozzle at point where the cross-beam laser measurements were made
$\Delta\nu$	relative frequency; $\nu - \nu_{minimum}$ or $\nu - \nu_o$ according to graphical scale
$\Delta T_{ol}^{high}$	the difference between $T_c$ at the center-point of the beam overlap volume and the temperature at 0.25" towards the hot end of the static cell
$\Delta T_{ol}^{low}$	the difference between $T_c$ , at the center-point of the beam overlap volume and the temperature at 0.25" towards the cold end of the static cell
$\delta T_{ex}$	standard error in extracted temperature
$\varepsilon$	small correction term
$k$	absorption parameter
$M^*$	Mach number at nozzle throat
$M_{test}$	calculated Mach number at point where the cross-beam laser measurements were made in nozzle
$M_{exit}$	calculated Mach number at the exit plane of the nozzle
$P_{Ar}$	Argon pressure
$P_{exit}$	calculated pressure at nozzle exit plane
$P_{I_2}$	$I_2$ pressure
$P_{inlet}$	pressure of gas measured at entrance to the six-way cross chamber
$P_{nozzle}$	pressure of gas measured at point where the cross-beam laser measurements were made in nozzle

$P_{standard}$	standard pressure (760 Torr)
$P_{throat}$	calculated pressure of gas at nozzle throat
$\rho_{throat}$	calculated density of gas at nozzle throat
$\theta$	crossing angle of laser beams
$T_c$	temperature measured by thermocouple
$T_{ex}$	temperature extracted from Doppler linewidth of the measured signal
$T_{standard}$	standard temperature, 273.15 K
$T_{test}$	calculated temperature at point where the cross-beam laser measurements were made in nozzle
$T_{throat}$	calculated temperature at nozzle throat
$X$	position along the long-axis of the cylindrical static cell

# SPATIALLY-RESOLVED TEMPERATURE DIAGNOSTIC FOR SUPERSONIC FLOW USING CROSS-BEAM DOPPLER-LIMITED LASER SATURATION SPECTROSCOPY

## **I. Introduction**

### **A. Airborne Laser Program**

The Air Force began development of the Airborne Laser (ABL) in 1996 as part of a Department of Defense strategy to defend American armed forces from the growing threat of Theater Ballistic Missiles (TBMs) such as the Scuds used by Iraq in Desert Storm.<sup>1</sup> The Airborne Laser (ABL), the world's first laser-armed combat aircraft, is a modified Boeing 747-400F freighter equipped with a megawatt-class chemical laser.<sup>2</sup> At distances in excess of several hundred kilometers, the ABL will be used to attack Theater Ballistic Missiles during their boost phase and destroy them before their warheads separate from the boost vehicle. In this scenario, warheads and destroyed missile components fall on enemy territory, rendering the aggressor vulnerable to the effects of the warheads.

In May of 2002, a turret was installed in the aircraft's nose and modifications were made to incorporate the laser, optics and computer hardware. After a series of flight tests in July 2002, the aircraft received airworthiness certification. Following installation

of the beam control/fire control system, the aircraft was tested again in December 2004 for airworthiness and passed certification. In November 2004, all six modules of the laser weapon were fired for the first time.<sup>3</sup> Installation of the laser weapon is expected in late 2005. The first ABL prototype is scheduled for delivery in 2006.

## **B. Chemical Oxygen Iodine Laser**

The ABL laser weapon is the Chemical Oxygen Iodine Laser (COIL): a megawatt class laser that emits light with a wavelength of 1.315  $\mu\text{m}$ . It was invented in 1977 by scientists at the Air Force Research Laboratory at Kirtland Air Force Base.<sup>4</sup> To generate the laser light, a liquid reservoir of Basic Hydrogen Peroxide (BHP) is combined with chlorine gas to produce oxygen in the  $\text{O}_2(a^1\Delta)$  excited state. The gaseous mixture is then injected with molecular iodine as it passes through a set of nozzles to reach supersonic speeds. As the gases exit the nozzles, the energy in the excited oxygen separates the iodine molecule and produces atomic iodine in an excited state. The 1.315  $\mu\text{m}$  light is extracted from the atomic iodine with a laser cavity positioned transverse to the gas flow.<sup>5</sup> The expended gases are scrubbed to remove residual chlorine and iodine and then exhausted from the system. Several excellent reviews of laser hardware, chemistry, laser physics, and fluid dynamics of these devices are available.<sup>6-8</sup>

Since the COIL requires the consumption of chemicals to operate, these substances must be carried onboard the ABL aircraft. There is a weight limit on the amount of chemical laser “fuel” that can be carried onboard the aircraft as determined by ABL’s maximum allowable payload. As a result, there is a practical requirement for the

COIL laser to operate as efficiently as possible for a given chemical payload. The efficiency of the laser is strongly dependent on the gas temperature in the laser gain region. The amount of  $O_2(a^1\Delta)$  necessary to achieve lasing on the atomic iodine transition decreases with a decrease in the temperature of the mixed gases in the gain region. In addition, a measured temperature that is higher than expected could indicate the presence of waste heat release due to undesired chemical reactions. An accurate measure of the gas temperature in the laser gain region is an essential diagnostic in assessing COIL performance.

### C. Previous Work

Two-dimensional spatial distributions of the small signal gain and the gas temperature in the gain region of a supersonic COIL device have been measured previously by diode laser spectroscopy on the  $5p^5\ ^2P_{1/2}(F'=3) \rightarrow ^2P_{3/2}(F=4)$  transition of atomic iodine.<sup>9</sup> The resulting experimental gas temperatures were between 220 K and 240 K. The computational model predicted a gas temperature of 180 K, disagreeing with the experimental results. The technique is limited to measuring an average temperature along the path length in which the diode laser interacts with the medium and may be biased due to directed flow resulting from symmetrical turbulent vortices, as illustrated in Figure 1.





species. The laser is frequency-tuned across a spectral line of the gas. Through the use of modulation techniques, a detector records the signal due only to interaction of the laser radiation with the collection of gas molecules that are present in the volume defined by the intersection of the two laser beams. Since the two beams propagate in the same direction, they always interact with the same molecular velocity group. Simultaneously tuning the two laser beams across a spectral line produces a signal with a Doppler-limited profile. The temperature of the absorbing molecules within the beam-overlap volume can then be determined from the Doppler linewidth of the spectral signal.

In this work, the non-intrusive, optical temperature diagnostics of Cross-Beam Saturation Absorption Spectroscopy (CBSAS) and Cross-Beam Inter-Modulated Fluorescence (CBIMF) will be developed and demonstrated in a static environment and in a small supersonic nozzle. The techniques will be applied to individual rotational lines in the visible  $I_2 \ X \ ^1\Sigma(0_g^+) \rightarrow B \ ^3\Pi(0_u^+)$  transition. Experiments performed in a static cell containing  $I_2$  vapor will include varying modulation frequency and varying  $I_2$  pressure to assess the effects on the accuracy of the temperature extracted from a spectral signal in addition to performing measurements at different locations within a temperature gradient to demonstrate the spatial resolution of the techniques. A comparison of extracted temperatures will be made to thermocouple measurements. In the nozzle experiments, CBSAS and CBIMF measurements will be performed in a supersonic  $I_2$ -seeded Ar gas flow. The extracted temperatures will be compared to temperature calculations from isentropic, one-dimensional flow theory.

The extraction of a temperature from the spectral signal recorded with CBSAS or CBIMF will be accomplished by fitting the data with a theoretical signal based on the

hyperfine structure of an  $I_2$  ro-vibrational spectral line. Using well-known Doppler-free laser spectroscopy techniques, experimental investigations of the  $I_2$  hyperfine structure will be undertaken to assess phenomena that influence the  $I_2$  hyperfine structure and must, consequently, be accounted for in the theoretical model. In particular, Saturation Absorption Spectroscopy will be used to determine Ar-pressure broadening rates of  $I_2$  hyperfine components.

## II. Background

The temperature of a molecular gas (or vapor) can be extracted from spectral data recorded in a laser spectroscopy experiment. This is accomplished by fitting a theoretical signal, consisting of a small set of parameters, to the experimental intensity vs. frequency data of a Doppler-broadened spectral line. The molecular structure of the chemical species partly determines the shape of the profile. In this work, molecular iodine was selected for use in the diagnostic. Diatomic molecular spectroscopy and lineshape theory are presented in this chapter to the extent that the subjects are needed for construction of the theoretical profiles.

In addition, some of the well-known laser saturation spectroscopy methods are reviewed for the techniques that were utilized during the course of this work. The review also provides a framework for presenting the simple theory for the spatially-resolved, Doppler-limited, cross-beam techniques discussed in the next chapter.

Finally, the theory of one-dimensional flow is discussed as it pertains to the supersonic expansion of a gas through a nozzle. Temperatures calculated from the flow theory are compared to the temperatures extracted from spectral measurements performed in a small supersonic nozzle.

### A. Molecular Iodine

Molecule iodine,  $I_2$ , was selected for the temperature diagnostic because it is present in the COIL gain region where a spatially-resolved Doppler-limited technique is

intended for application.  $I_2$  is also a suitable candidate for exploitation due to its low saturation intensity and the abundance of spectral lines at visible wavelengths.

Several aspects of the  $I_2$  diatomic molecular spectroscopy are discussed in regards to utilization for the temperature diagnostic. Knowledge of the  $I_2$  electronic and ro-vibrational structure is necessary to identify and select suitable spectral lines for the temperature diagnostic. The transition intensity and the population distribution of ro-vibrational lines are discussed since a temperature can be obtained from this information in addition to the method of extracting temperature from the profile linewidth. The hyperfine intensities and resonant frequencies of a specific  $I_2$  ro-vibrational line are discussed since these quantities are essential for constructing the theoretical profile for a ro-vibrational line.

### $I_2$ Electronic Transitions.

#### *Energy Levels.*

Absorption of radiation at visible wavelengths induces transitions between the  $X^1\Sigma(0_g^+)$  and  $B^3\Pi(0_u^+)$  electronic states of  $I_2$  where  $X$  is the ground electronic state and  $B$  is the second excited electronic state.<sup>11</sup> The first few potential energy curves for  $I_2$  electronic states are shown in Figure 2. Each electronic energy level is composed of several vibrational energies. Each of these vibrational levels consists of several rotational energy levels. With narrow-band laser radiation, it is possible to excite molecules from a specific rotational-vibrational level in the  $X^1\Sigma(0_g^+)$  state to a specific rotational-vibrational level in the  $B^3\Pi(0_u^+)$  state. Using various techniques, researchers have produced spectral atlases for several wavelength bands in molecular iodine.<sup>12-15</sup>

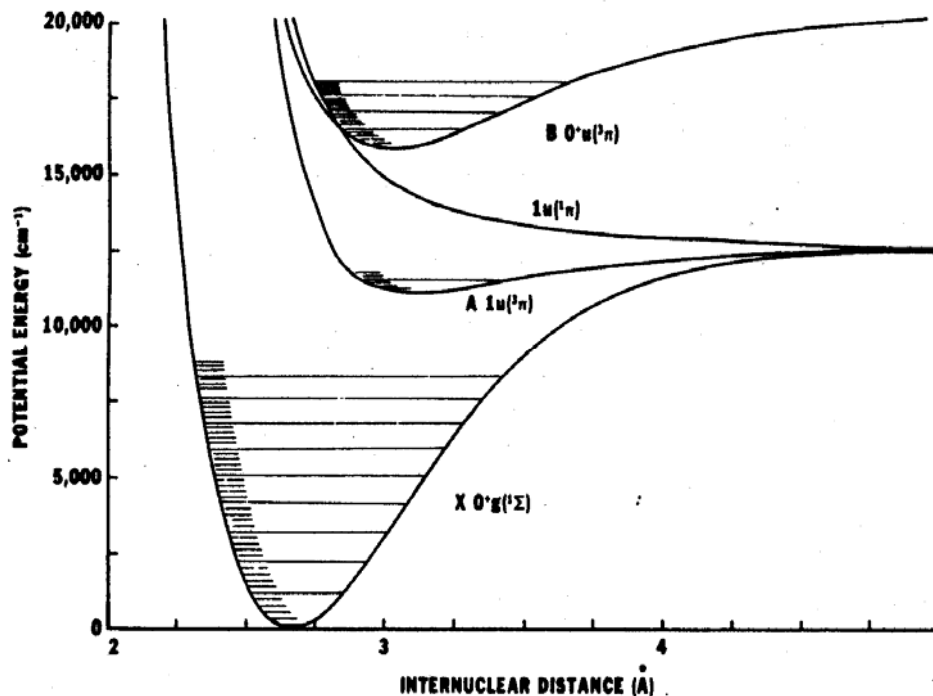


Figure 2. Potential energy curves for  $I_2$ .<sup>16</sup>

The bound  $B \ ^3\Pi(0_u^+)$  potential curve overlaps the unbound  $^1\Pi(1_u)$  potential curve. It is possible for a molecule in the excited, bound  $B \ ^3\Pi(0_u^+)$  state to cross over to the overlapping, unbound  $^1\Pi(1_u)$  state and dissociate into two iodine atoms. This natural predissociation has been observed experimentally through measurement of fluorescence-decay lifetimes. Results show the predissociation rate depends on the excited-state vibrational-level quantum number,  $v'$ .<sup>17</sup> It is also proportional to  $J'(J' + 1)$ , where  $J'$  is the excited-state rotational-level quantum number.<sup>18</sup>

To predict the allowed ro-vibrational energies of an electronic transition, the diatomic molecule can be modeled as a vibrating rotor.<sup>19</sup> The rotational term values are given by

$$F_v(J) = B_v J(J+1) - D_v [J(J+1)]^2 + H_v [J(J+1)]^3 + \dots \quad (1)$$

where  $J$  is the rotational quantum number. The rotational constants:  $B_v, D_v, H_v$ , each have a vibrational dependence, and are represented by the following polynomial expansions:<sup>20</sup>

$$B_v = \sum_{p=0}^{p_{\max}} Y_{p1} \left(v + \frac{1}{2}\right)^p \cong B_e - \alpha_e \left(v + \frac{1}{2}\right) + \gamma_e \left(v + \frac{1}{2}\right)^2 + \dots \quad (2)$$

$$D_v = \sum_{p=0}^{p_{\max}} Y_{p2} \left(v + \frac{1}{2}\right)^p \cong D_e + \beta_e \left(v + \frac{1}{2}\right) + \dots \quad (3)$$

$$H_v = \sum_{p=0}^{p_{\max}} Y_{p3} \left(v + \frac{1}{2}\right)^p \quad (4)$$

where  $v$  is the vibrational energy quantum number and the  $Y_{pq}$  are the Dunham expansion parameters which can be related to the familiar spectral constants<sup>21</sup> ( $B_e, D_e$ , etc.) for small values of the ratio of  $B_e$  to  $\omega_e$ , the first-order vibrational molecular constant - an acceptable assumption for  $I_2$ . The vibrational term values are given by<sup>21</sup>

$$G(v) = \sum_{p=1}^{p_{\max}} Y_{p0} \left(v + \frac{1}{2}\right)^p \cong \omega_e \left(v + \frac{1}{2}\right) - \omega_e x_e \left(v + \frac{1}{2}\right)^2 + \omega_e y_e \left(v + \frac{1}{2}\right)^3 + \dots \quad (5)$$

where the first expression represents energy levels due to a harmonic oscillator potential and the others expressions account for the anharmonicity of the real diatomic potential.

The visible absorption lines in  $I_2$  occur for transitions from an  $X^1\Sigma(0_g^+)$ -state rotational-vibrational level,  $(v'', J'')$ , to a  $B^3\Pi(0_u^+)$ -state rotational-vibrational level,  $(v', J')$ . Within a given  $v' - v''$  vibrational band, the allowable rotational transitions are

divided into two branches according to the selection rule:  $\Delta J = J' - J'' = \pm 1$ .<sup>21</sup> The P branch consists of all  $\Delta J = -1$  rotational transitions, and the R branch consists of all  $\Delta J = +1$  rotational transitions. For a specific vibrational band, the term values, in wavenumbers, for the R and P branches are given by<sup>21</sup>

$$\sigma_R(J) = +B'_{v'} (J+1)(J+2) - D'_{v'} (J+1)^2 (J+2)^2 + H'_{v'} (J+1)^3 (J+2)^3 - B''_{v''} J (J+1) + D''_{v''} J^2 (J+1)^2 + \sigma_o(v', v'') \quad (6)$$

$$\sigma_P(J) = +B'_{v'} J (J-1) - D'_{v'} J^2 (J-1)^2 + H'_{v'} J^3 (J-1)^3 - B''_{v''} J (J+1) + D''_{v''} J^2 (J+1)^2 + \sigma_o(v', v'') \quad (7)$$

where  $J$  is the lower-level rotational quantum number, and  $H''_{v''}$  is assumed negligible and set equal to zero. The expression

$$\sigma_o(v', v'') = T'_e - T''_e + G(v') - G(v'') \quad (8)$$

is the band origin in which  $T_e$  is the term value corresponding to the minimum electronic energy of a given stable electronic state.  $T_e$  is related to  $Y_{00}$ . For the  $X^1\Sigma(0_g^+)$  state,  $T''_e = 0$ .

The expansion parameters in Equations (2-4) for the rotational constants and the expansion parameters for the vibrational term values in Equation (5) have been previously determined for  $I_2$ .<sup>22</sup> The values for the expansion parameters are listed in Table 1 for the  $X^1\Sigma(0_g^+)$  state and in Table 2 for the  $B^3\Pi(0_u^+)$  state. Line positions for the set of  $I_2 B^3\Pi(0_u^+) \leftrightarrow X^1\Sigma(0_g^+)$  ro-vibrational lines used in this work were calculated using molecular constants from Reference (22). These ro-vibrational line positions are listed in Table 3 along with the corresponding spectroscopic assignments in

which the notation indicates the branch (P or R),  $J''$  in parentheses, and the vibrational band,  $v' - v''$ .

**Table 1. Expansion parameters for the  $X^1\Sigma(\theta_g^+)$  state of  $I_2$ . Valid for  $v''=0-9$ .**

$Y_{pq}$	$G(v'') \text{ (cm}^{-1}\text{)}$ $q = 0$	$B_{v''} \text{ (cm}^{-1}\text{)}$ $q = 1$	$D_{v''} \text{ (cm}^{-1}\text{)}$ $q = 2$
$p = 1$	2.145186E+02	3.736870E-02	4.568123E-09
$p = 2$	-6.072284E-01	-1.139897E-04	2.120439E-11
$p = 3$	-1.38611E-03	-2.720291E-07	6.737406E-13
$p = 4$		-5.447708E-09	

**Table 2. Expansion parameters for the  $B^3\Pi(\theta_u^+)$  state of  $I_2$ . Valid for  $v'=1-62$ .**

$Y_{pq}$	$G(v') \text{ (cm}^{-1}\text{)}$ $q = 0$	$B_{v'} \text{ (cm}^{-1}\text{)}$ $q = 1$	$D_{v'} \text{ (cm}^{-1}\text{)}$ $q = 2$	$H_{v'} \text{ (cm}^{-1}\text{)}$ $q = 3$
$p = 0$	15769.0485 ( $T_e'$ )	2.8993694599E-02	6.125767E-09	-2.15004734E-15
$p = 1$	125.6724	-1.406799398E-04	1.418420E-10	7.915679522E-15
$p = 2$	-7.526770E-01	-5.088972976E-06	-2.825041E-12	-1.02396618E-14
$p = 3$	-3.246282E-03	8.7511454030E-07	5.544495E-13	4.852619270E-15
$p = 4$	1.875736E-05	-1.171736403E-07	-2.644252E-14	-1.19975156E-15
$p = 5$	-3.414124E-06	9.7025967839E-09	9.539521E-16	1.792143124E-16
$p = 6$	2.004998E-07	-5.304859892E-10	-1.864100E-17	-1.75575349E-17
$p = 7$	-6.950414E-09	1.9571123281E-11	1.813907E-19	1.185081818E-18
$p = 8$	1.517899E-10	-4.894864050E-13	-6.053203E-22	-5.67595443E-20
$p = 9$	-1.899790E-12	8.1736417235E-15		1.958960707E-21
$p = 10$	1.226941E-14	-8.715621632E-17		-4.88849274E-23
$p = 11$	-3.137312E-17	5.3609973831E-19		8.739722535E-25
$p = 12$		-1.445945450E-21		-1.09126306E-26
$p = 13$				9.034911061E-29
$p = 14$				-4.45560254E-31
$p = 15$				9.904029815E-34



**Table 3. Line positions for select  $I_2 B^3\Pi(0_u^+) \leftrightarrow X^1\Sigma(0_g^+)$  ro-vibrational spectral lines.**

<b>Spectral Assignment</b>	<b><math>\sigma</math> (<math>\text{cm}^{-1}</math>)</b>
P(130) 17-1	17199.7205
P(51) 18-2	17249.9632
P(66) 16-1	17249.9632
P(114) 18-1	17337.7606
P(70) 17-1	17339.8188
P(53) 19-2	17340.2200
P(46) 17-1	17372.7581
P(10) 19-2	17374.2727
R(104) 18-1	17374.3107
P(31) 17-1	17386.7211
P(12) 17-1	17397.1205
R(37) 15-0	17403.2498
R(127) 19-1	17403.2772
R(30) 15-0	17408.1066

*Transition Intensity.*

The fluorescence intensity of a spectral line in emission due to an electronic transition in a diatomic molecule follows the expression

$$I_{em}(v' J', v'' J'') = N_{v' J'} h c \frac{1}{\lambda} A(v' J', v'' J'') \quad (9)$$

where  $N_{v' J'}$  is the  $v' J'$  -level population,  $h$  is Planck's constant,  $c$  is the speed of light,

$\lambda$  is the wavelength of the emission, and  $A(v' J', v'' J'')$  is the Einstein coefficient for

spontaneous emission given by<sup>21</sup>

$$A(v' J', v'' J'') = \frac{64 \pi^4}{3 h} c \frac{1}{\lambda^3} \left( \frac{S_{J', J''}}{2 J' + 1} \right) \left| \langle \Psi_{v'} | \mu_e(R) | \Psi_{v''} \rangle \right|^2 \quad (10)$$

where  $S_{J',J''}$  is the Hönl-London rotational line strength. For a given  $J'$ , the  $S_{J',J''}$  values for the allowed transitions sum to  $(2J' + 1)$ .<sup>21</sup> Thus, the expression in parentheses on the right hand side of Equation (10) is the relative rotational line strength. In  $I_2$   $B \leftrightarrow X$  transitions, the relative rotational line strength is approximately  $1/2$  for large  $J'$  in the P or R branch.<sup>23</sup> The last expression on the right hand side of Equation (10), the transition moment, is the absolute square of the integral of the product of the upper- and lower-level vibrational wavefunctions, and the electronic transition moment:

$$\mu_e(R) = \langle \Psi'_e | M_{el} | \Psi''_e \rangle \quad (11)$$

where  $\Psi_e$  is the electronic wavefunction,  $M_{el}$  is the portion of the dipole moment operator dependent on *electronic* coordinates only, and  $R$  is the internuclear separation distance. A typical approach for describing the transition moment in Equation (10) is to use the R-centroid approximation in which

$$|\langle \Psi_{v'} | \mu_e(R) | \Psi_{v''} \rangle|^2 = |\mu_e(\bar{R})|^2 |\langle \Psi_{v'} | \Psi_{v''} \rangle|^2 \quad (12)$$

where  $\bar{R}$  is the R-centroid:

$$\bar{R} = \frac{|\langle \Psi_{v'} | R | \Psi_{v''} \rangle|}{\langle \Psi_{v'} | \Psi_{v''} \rangle}, \quad (13)$$

and

$$q_{v'v''} = |\langle \Psi_{v'} | \Psi_{v''} \rangle|^2 \quad (14)$$

is the Franck-Condon Factor (FCF) which determines the vibrational dependence of intensities in molecular electronic transitions.<sup>23</sup> Some calculated FCFs for select  $I_2$

$B \ ^3\Pi(0_u^+) \leftrightarrow X \ ^1\Sigma(0_g^+)$  vibrational bands are shown in Table 4.

Assuming equilibrium conditions, the population of molecules in a specific rotational state belonging to a particular vibrational state of a given electronic state has the form of a Boltzmann distribution so that

$$N_{evJ} = N_e N_v N_J = N g^{elec} \frac{\exp\left(-\frac{E^{elec}}{k_B T}\right)}{Q_e} \frac{\exp\left(-\frac{G(v)}{k_B T}\right)}{Q_v} g_n(2J+1) \frac{\exp\left(-\frac{F_v(J)}{k_B T}\right)}{Q_r} \quad (15)$$

where  $N$  is the total number of molecules,  $g^{elec}$  is the electronic state degeneracy,  $G(v)$  is given by Equation (5),  $(2J+1)$  accounts for the rotational state degeneracies, and  $F_v(J)$  is given by Equation (1). The nuclear spin degeneracy is given by  $g_n$ .  $Q_i$  is the partition function for the particular type of transition where

$$Q_e = \sum_{i=0}^{\infty} g_i^{elec} \exp\left(-\frac{E_i^{elec}}{k_B T}\right) \quad (16)$$

is the electronic partition function where  $g_i^{elec}$  is the degeneracy of the  $i^{\text{th}}$  electronic energy state,

$$Q_v = \sum_{v=1}^{\infty} g_v \exp\left(-\frac{G(v)}{k_B T}\right) \quad (17)$$

is the vibrational partition function where  $g_v$  is the degeneracy of the  $i^{\text{th}}$  vibrational energy state, and

$$Q_r = \sum_{J=0}^{\infty} g_n(2J+1) \exp\left(-\frac{F_v(J)}{k_B T}\right) \quad (18)$$

is the rotational partition function which is dependent on  $v$ , the vibrational quantum number. The electronic-state population is not explicitly included in Equation (9). For this work, temperatures in the range of 140-400 K were encountered in experiment. The

fraction of molecules in an excited electronic state in this temperature range is negligibly small; for the  $I_2 B$  state,  $\exp(-E_B^{elec}/(k_B T))/Q_e \approx 1$ .

For comparison to  $I_{em}$ , the intensity of an absorption line, for thin absorbing layers, follows the expression

$$I_{abs} = \frac{8 c \pi^3}{3 h} \frac{I_o N_{v''J''} \Delta x}{\lambda} \frac{S_{J',J''}}{(2 J' + 1)} \left| \mu_e(\bar{R}) \right|^2 q_{v'v''} \quad (19)$$

where  $I_o$  is the incident intensity of the radiation, and  $N_{v''J''}$  is the  $v''J''$ -level population density,  $\Delta x$  is the thickness of the absorbing layer, and  $\lambda$  is in cm. The Franck-Condon factor and the lower vibrational-level population  $N_{v''}$  can be used as discriminators when selecting an absorption line for the temperature diagnostic where the most intense lines are preferred in order to achieve a satisfactory signal-to-noise ratio. Both the FCFs<sup>23</sup> and relative  $v''$ -level population values are listed in Table 4 for the  $I_2 B \leftrightarrow X$  transitions presented in Table 3.

**Table 4. Franck-Condon Factors<sup>23</sup> and relative  $v''$ -level populations for select  $I_2 B \rightarrow X$   ${}^3\Pi(0_u^+) \leftrightarrow X \rightarrow {}^1\Sigma(0_g^+)$  vibrational bands at  $T=300 K$ .**

$v' - v''$	$100 \cdot q_{v'v''}$	$\frac{N_{v''}(T = 300K)}{N_{v''=0}(T = 300K)}$	$100 \cdot q_{v'v''} \cdot \frac{N_{v''}(T = 300K)}{N_{v''=0}(T = 300K)}$
15-0	0.5321	1.00	0.532
16-1	2.960	0.360	1.064
17-1	3.318	“	1.193
18-1	3.582	“	1.288
19-1	3.730	“	1.341
18-2	2.838	0.130	0.369
19-2	2.165	“	0.282

## I<sub>2</sub> Hyperfine Transitions.

It has been shown, for a given I<sub>2</sub>  $B^3\Pi(0_u^+) \leftrightarrow X^1\Sigma(0_g^+)$  vibrational band, that the spectral linewidth is greater for odd  $J''$  than for even  $J''$  ro-vibrational lines.<sup>24</sup> The source of the non-Doppler contribution to the linewidth is the *hyperfine* structure of the transition, which is observable with high resolution Doppler-free laser techniques.<sup>25</sup>

The hyperfine structure is a manifestation of interactions between the nuclei of the molecule and the magnetic and electric fields generated by the molecule's electrons. The energy levels due to these interactions can be predicted from the following Hamiltonian

$$H_{hfs} = H_{NEQ} + H_{SR} \quad (20)$$

which is composed of a Nuclear Electric Quadrupole (NEQ) term and a magnetic Spin-Rotation (SR) term.<sup>26</sup> Higher-order terms can be included in  $H_{hfs}$  to improve the accuracy of the predicted hyperfine energy levels.<sup>27</sup>

For large rotational quantum number values,  $J \geq 20$ ,  $H_{NEQ}$  for a homonuclear diatomic molecule can be approximated as the sum of two single-nucleus NEQ energies so that

$$H_{NEQ} = e Q q_J \left( \frac{3(\vec{I}_1 \cdot \vec{J})^2 + \frac{3}{2}(\vec{I}_1 \cdot \vec{J})^2 - |\vec{I}_1|^2 |\vec{J}|^2}{2 I_1 (2 I_1 - 1) J (2 J - 1)} + \frac{3(\vec{I}_2 \cdot \vec{J})^2 + \frac{3}{2}(\vec{I}_2 \cdot \vec{J})^2 - |\vec{I}_2|^2 |\vec{J}|^2}{2 I_2 (2 I_2 - 1) J (2 J - 1)} \right) \quad (21)$$

where  $e$  is the electron charge, and the constant  $Q$  is the electric quadrupole moment,

$I_1 = I_2 = 5/2$  is the nuclear spin angular momentum for the iodine atom, and  $\vec{J}$  is the

molecule's rotational angular momentum vector.<sup>24, 26</sup> The average electric-field gradient along the  $\vec{J}$  direction is given by

$$q_J = \left\langle \frac{\partial^2 V}{\partial^2 z} \right\rangle_J = - \left\langle \frac{\partial^2 V}{\partial^2 z} \right\rangle_M \frac{J}{2J+3} = -q \frac{J}{2J+3} \quad (22)$$

where the relationship to the average electric-field gradient along the molecule's symmetry axis (indicated by the subscript  $M$ ) is shown in the second expression.<sup>20</sup>

The NEQ energy levels are derived by diagonalizing the NEQ energy matrix using the  $I_1 I_2 I J F M_F$  representation where the total nuclear spin vector is given by

$$\vec{I} = \vec{I}_1 + \vec{I}_2, \quad (23)$$

the total angular momentum vector is given by

$$\vec{F} = \vec{J} + \vec{I}, \quad (24)$$

and  $M_F$  is the component of  $\vec{F}$  along a fixed space-axis. The resulting eigenvalues are labeled with the following quantum numbers:  $J$  for the rotational angular momentum,  $F$  for the total angular momentum, and  $\varepsilon$  for the pseudo-spin angular momentum which represents the value of the molecule's total nuclear spin  $|\vec{I}| = |\vec{I}_1 + \vec{I}_2|$  that makes the largest contribution to the eigenstate.<sup>28</sup>

In the assumption of large  $J$ , where  $J \gg I_1$ , the rotational angular momentum vector is almost parallel to  $\vec{F}$ , and may be treated as having a fixed direction in space. The nuclear angular momenta may then be independently quantized along this direction. Defining quantum numbers  $M_1$ , and  $M_2$  where  $-I_{1,2} \leq M_{1,2} \leq I_{1,2}$  so that  $F_1 = J + M_1$ ,

with  $\vec{F}_1 = \vec{J} + \vec{I}_1$ , and  $F_2 = J + M_2$ , with  $\vec{F}_2 = \vec{J} + \vec{I}_2$ , the coupling terms in Equation (21) can be written approximately as

$$(\vec{I}_1 \cdot \vec{J}) = M_1 J + \frac{1}{2} (M_1 (M_1 + 1)) - I_1 (I_1 + 1) \quad (25)$$

$$(\vec{I}_1 \cdot \vec{J})^2 = M_1^2 J^2 + M_1 J [M_1 (M_1 + 1) - I_1 (I_1 + 1)] + O(I_1^4) \quad (26)$$

$$(\vec{I}_2 \cdot \vec{J}) = M_2 J + \frac{1}{2} [M_2 (M_2 + 1) - I_1 (I_1 + 1)] \quad (27)$$

$$(\vec{I}_2 \cdot \vec{J})^2 = M_2^2 J^2 + M_2 J [M_2 (M_2 + 1) - I_1 (I_1 + 1)] + O(I_2^4) \quad (28)$$

where the  $O(I_i^4)$  indicate higher-order terms. Substituting Equations (25) through (28) into Equation (21) gives the approximate NEQ energy levels:

$$E_{NEQ} \approx \frac{e Q q}{8 I_1 (2 I_1 - 1)} \left( 3 (M_1^2 + M_2^2) + \frac{3}{J} M_1 \left[ M_1 (M_1 + 1) - I_1 (I_1 + 1) + \frac{1}{2} \right] + \frac{3}{J} M_2 \left[ M_2 (M_2 + 1) - I_1 (I_1 + 1) + \frac{1}{2} \right] - 2 I_1 (I_1 + 1) \right). \quad (29)$$

Equation (29) predicts 36 possible NEQ energy levels. However, only a subset of the 36 levels is allowable for a given quantum state. The iodine isotope,  $^{127}\text{I}_2$ , is a homonuclear diatomic molecule in which each nucleus has a nuclear spin of  $5/2$ . The total wavefunction representing the molecule must change sign when the nuclei are interchanged by a permutation operation acting on the total wavefunction.<sup>21</sup> This symmetrization requirement limits the possible combinations of  $I$  and  $J$ ; and, therefore, the values of  $F$  that are associated with  $J$ . For the  $\text{I}_2 X^1\Sigma(0_g^+)$  state, the  $I$  values of 5, 3, and 1 can only combine with odd  $J''$  values, and the  $I$  values of 4, 2, and 0 can only combine with even  $J''$  values. For the  $\text{I}_2 B^3\Pi(0_u^+)$  state, the  $I$  and  $J$  combinations are

reversed due to the ungerade symmetry of the electronic wave function so that  $I$  values of 5, 3, and 1 can only combine with even  $J'$  values, and the  $I$  values of 4, 2, and 0 can only combine with odd  $J'$  values.<sup>24</sup> The number of hyperfine energy levels for a particular  $I$  is  $2I + 1$ . For odd  $J''$ , the total number of hyperfine states is 21. For an even  $J''$ , the total number of hyperfine states is 15. In contrast, the total number of hyperfine states is 15 for odd  $J'$ , and 21 for even  $J'$ . Therefore, the NEQ energy levels predicted by Equation (29) consist of either a set 15 or 21 hyperfine energy splittings as determined by  $J$ . The hyperfine energy levels from Equation (29) for odd  $J'' \geq 20$  are shown in Figure 3, and for even  $J'' \geq 20$  in Figure 4. The frequency spacing between adjacent levels in a multiplet decreases with increasing  $J''$ .

In early saturation absorption experiments, it was found that the high- $J$  NEQ energy approximation alone was not sufficient to accurately describe experimental hyperfine splittings.<sup>29</sup> It was necessary to include an additional term describing the interaction between the nuclear magnetic moment and the molecular magnetic field. The Hamiltonian for the magnetic Spin-Rotation (SR) energy is given by

$$H_{SR} = C_{SR} (\vec{I}_1 + \vec{I}_2) \cdot \vec{J}, \quad (30)$$

where  $C_{SR}$  is the Spin-Rotation coupling constant. Inserting the coupling terms from Equations (25) and (27) into Equation (30) yields

$$E_{SR} \approx C_{SR} (M_1 + M_2) J \quad (31)$$



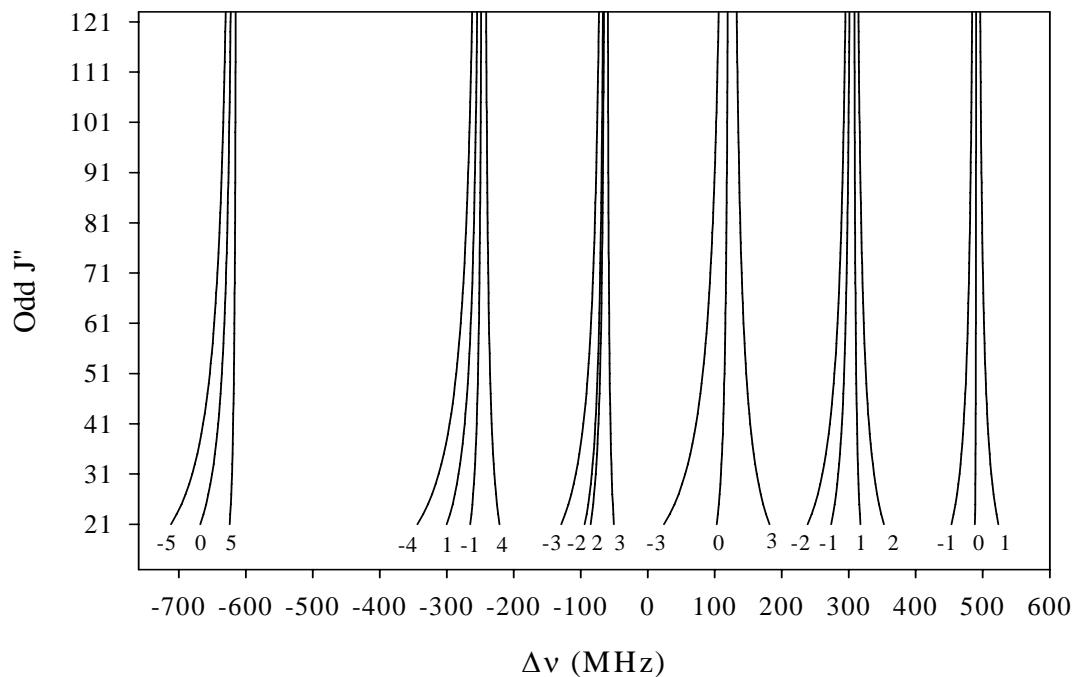


**Figure 3.** The  $I_2$  NEQ hyperfine energy levels for large odd  $J''$ . The coupling constant is  $eQq'' = -2453$ . The small number labeling each level is the  $F-J$  value.

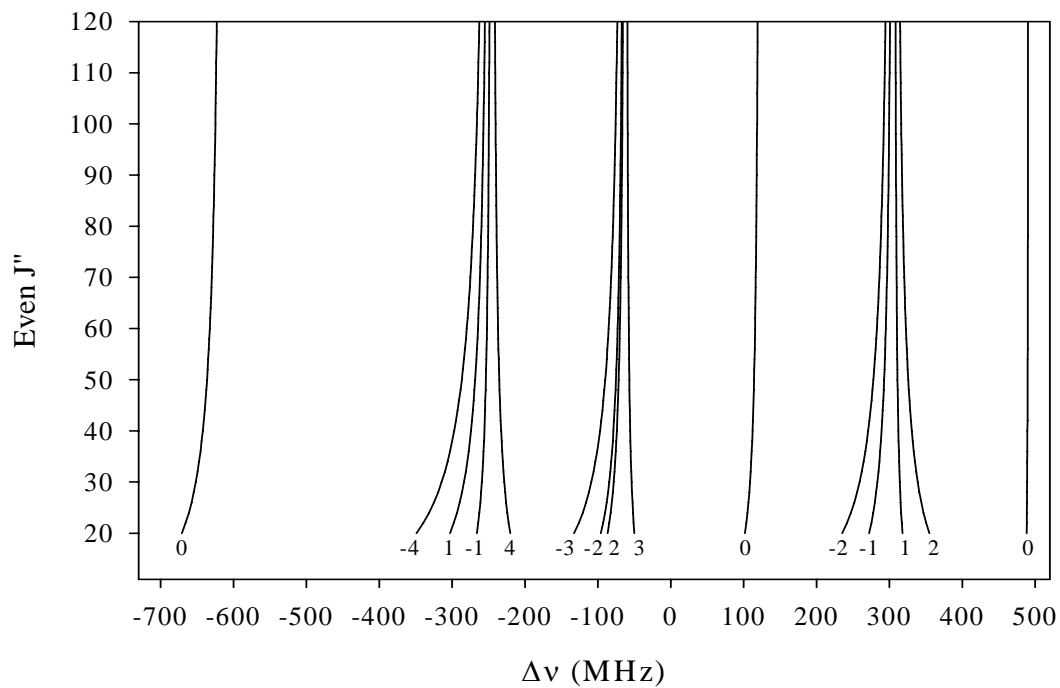


**Figure 4.** The  $I_2$  NEQ hyperfine energy levels for large even  $J''$ . The coupling constant is  $eQq'' = -2453$ . The small number labeling each level is the  $F-J$  value.

for the approximate magnetic Spin-Rotation energy levels.<sup>26</sup> The approximate energy for a hyperfine state is sum of Equation (29) and Equation (31):

$$E_{hfs} \approx E_{NEQ} + E_{SR} . \quad (32)$$

The hyperfine structures of single  $I_2$   $B \ ^3\Pi(0_u^+) \leftrightarrow X \ ^1\Sigma(0_g^+)$  ro-vibrational transitions closely approximate the NEQ energy-level structures in Figure 3 and Figure 4. For high  $J$ , the strongest hyperfine transitions in  $I_2$   $B \ ^3\Pi(0_u^+) \leftrightarrow X \ ^1\Sigma(0_g^+)$  follow the selection rule:  $\Delta F = \Delta J = \pm 1$ .<sup>20, 24</sup> The  $J''$ -level will have the same number of hyperfine states as the  $J'$ -level so a single ro-vibrational transition will consist of either 15 or 21 hyperfine transitions. At high  $J$ , the relative intensities of these hyperfine lines are proportional to  $2F + 1$ , the degeneracy of the total quantum number; and, thus, are very nearly the same in magnitude.<sup>20</sup>

While the high- $J$  approximation theory is useful for understanding the structure of the hyperfine levels and the variation in energy-level splittings with  $J$ , a more accurate method of predicting hyperfine energy levels was pursued for use in this temperature diagnostic by solving the hyperfine Hamiltonian through a matrix approach. Using a Visual FORTRAN computer program<sup>30</sup>, the hyperfine energy levels were calculated using the two-term Hamiltonian:

$$H_{hfs} = H_{NEQ} + H_{SR} . \quad (33)$$

The matrix elements were defined by a case (b)<sub>BJ</sub> coupling scheme in which the nuclear spins are coupled to give the resultant spin,  $\vec{I}$ , which is then coupled to the rotational angular momentum,  $\vec{J}$ , to give the total angular momentum:  $\vec{F} = \vec{J} + \vec{I}$ .<sup>31</sup> From the

coupling scheme, a set of basis functions:  $|I, J, F, M_F\rangle$  were defined so that  $H_{SR}$  would contribute only diagonal matrix elements of the form

$$\langle I, J, F, M_F | H_{SR} | I, J, F, M_F \rangle = \frac{C_{SR}}{2} (F(F+1) - I(I+1) - J(J+1)) \quad (34)$$

where  $C_{SR}$  is the spin-rotation coupling constant.<sup>32</sup> The matrix elements for  $H_{NEQ}$  are given by

$$\begin{aligned} \langle I', J', F, M_F | H_{NEQ} | I, J, F, M_F \rangle = & -e Q q \frac{J}{2(2J+3)} (-1)^{F+J+1} \sqrt{(2I'+1)(2I+1)} \\ & \times \begin{Bmatrix} I_1 & I_1 & I \\ 2 & I' & I_1 \end{Bmatrix} \begin{Bmatrix} F & J & I \\ 2 & I' & J' \end{Bmatrix} \left[ \begin{pmatrix} I_1 & I_1 & 2 \\ I_1 & -I_1 & 0 \end{pmatrix} \begin{pmatrix} J' & J & 2 \\ J & -J & 0 \end{pmatrix} \right]^{-1} \end{aligned} \quad (35)$$

in which non-vanishing matrix elements occur for  $\Delta I = 0, \pm 2$ , and  $\Delta J = 0, \pm 2$ . The matrix is diagonal in  $F$  and  $M_F$ . For highly accurate calculations with given values of  $F$  and  $M_F$ , the matrix for  $H_{hfs}$  of the  $I_2 X$  electronic state has an order of 63 X 63 for odd  $J$ , and an order of 45 X 45 for even  $J$ .<sup>32</sup> The order is reversed for the  $I_2 B$  electronic state. It is found that omitting the  $\Delta J = 2$  terms produces only small errors in the results.<sup>32</sup>. This approximation was used for the computer calculations to reduce the order of the  $I_2(X)$  matrix down to 21 X 21 for odd  $J$  and 15 X 15 for even  $J$ .

The hyperfine coupling constants are used as inputs to the energy-level computations. For the  $I_2 X^1 \Sigma(0_g^+)$ -state coupling constants, the values of  $e Q q'' = -2452.5837$  MHz, and  $C_{SR}'' = 3.162$  kHz for  $v'' = 0$ ,  $J'' = 13$  were obtained from experimental data in the literature.<sup>33</sup> To determine the  $I_2 B^3 \Pi(0_u^+)$ -state coupling constants, the following empirical formulas were used:

$$\Delta e Q q(v') = 1964.8 - 0.0130 \cdot G(v') - 1.51 \cdot 10^{-6} \cdot G(v')^2 \quad (36)$$

where  $\Delta e Q q$  is given in units of MHz and  $G(v')$ , the vibrational term-value expression from Equation (5), is given in units of  $\text{cm}^{-1}$ , and

$$\Delta C_{SR}(v', J') = 23 + 418 \cdot \exp\left(\frac{-4381.249 + G(v')}{653}\right) + 0.012 \cdot F_{v'}(J') \quad (37)$$

where  $\Delta C_{SR}$  is given in units of kHz, and  $F_{v'}(J')$ , the rotational term-value expression from Equation (1), is given in  $\text{cm}^{-1}$ .<sup>27</sup> The upper state hyperfine coupling constants for P(46) 17-1 are  $e Q q' = -518.89$  MHz, and  $C'_{SR} = 36.92$  kHz. For P(53) 19-2, the hyperfine coupling constants are  $e Q q' = -522.51$  MHz, and  $C'_{SR} = 40.52$  kHz.

The hyperfine line intensities were also calculated by computer program. The transition probabilities were calculated by considering the effect of radiation polarized in the space-fixed coordinate Z-direction. The  $B-X$  transition moment is oriented along the  $\text{I}_2$  bond-axis which is taken to be in the molecule-fixed coordinate z-direction. The matrix elements of the transition moment for the *case (b)* <sub>$\beta J$</sub>  basis are derived by first transforming to a *case (a)* basis. The matrix elements are then

$$\begin{aligned} \langle J', I, F', M_F | \mu_z | J, I, F, M_F \rangle = & \sum_{M_J, M_I} -\sqrt{(2F'+1)(2F+1)} \begin{pmatrix} J' & I & F' \\ M_J & M_I & -M_F \end{pmatrix} \\ & \times \begin{pmatrix} J & I & F \\ M_J & M_I & -M_F \end{pmatrix} \times \langle J', M_J | \alpha_{zZ} | J, M_J \rangle \langle B | \mu_z | X \rangle \end{aligned} \quad (38)$$

where  $\alpha_{zZ}$  is the direction cosine and  $\langle B | \mu_z | X \rangle$  is the electronic transition moment.

The direction cosine terms for the P and R branch rotational lines of  $\text{I}_2$  are<sup>34</sup>

$$\langle J-1, M_J | \alpha_{zZ} | J, M_J \rangle = \sqrt{\frac{(J+M_J)(J-M_J)}{(2J+1)(2J-1)}} \quad (39)$$

and

$$\langle J+1, M_J | \alpha_{zZ} | J, M_J \rangle = \sqrt{\frac{(J+M_J+1)(J-M_J+1)}{(2J+1)(2J+3)}}. \quad (40)$$

To obtain the transition probabilities, the transition moment matrix,  $\tilde{\mu}$ , is transformed using the eigenvector matrices from calculations of the *B*- and *X*-state energy levels so that

$$\tilde{Z} = \tilde{B}^T \tilde{\mu} \tilde{X} \quad (41)$$

in which the individual matrix elements  $Z_{ij}$  are dependent on  $M_F$ . The relative transition probability between an *i* and *j* state,  $P_{ij}$ , is calculated by squaring the  $Z_{ij}$  values and summing over  $M_F$  to give

$$P_{ij} = 3 \sum_{M_F} |Z_{ij}(M_F)|^2. \quad (42)$$

Relative frequencies and relative intensities calculated using the matrix theory are shown in Table 5 for the I<sub>2</sub> P(46) 17-1 hyperfine transitions. Calculations from the high-*J* approximation theory using Equation (32) are also shown for comparison. In Table 6, relative frequencies and relative intensities for the I<sub>2</sub> P(53) 19-2 hyperfine transitions are shown for the matrix theory and the high-*J* approximation theory.

## B. Spectral Line Shape and Line Width

The spectral lines in absorption or emission spectra are not absolutely monochromatic. Each spectral line has, in fact, an intensity distribution of absorbed or emitted radiation in a frequency interval about the resonant frequency  $\nu_o = (E_2 - E_1)/h$

of the molecular transition where  $E_2$  is the upper energy level,  $E_1$  is the lower energy level, and  $h$  is Planck's constant.

The spectral "line" can vary in shape or width according to the influence of physical processes. In general, lineshapes fall into two categories: homogeneous and inhomogeneous. The homogenous lineshape results when all the molecules in the system have the same lineshape function as in pressure broadening. In contrast, inhomogeneous broadening results where the probability of absorption or emission of monochromatic radiation is not equal for all the molecules in the sample, as in Doppler broadening.

**Table 5. Relative frequencies and relative intensities for I<sub>2</sub> P(46) 17-1 hyperfine transitions. Calculations are shown from the matrix theory and from the high-J approximation theory.**

<b>F-J</b>	<b>Matrix Theory, <math>\Delta\nu</math> (GHz)</b>	<b>High J-Approx. Theory, <math>\Delta\nu</math> (GHz)</b>	<b>Matrix Theory, Relative Intensity (arbitrary units)</b>	<b>High J-Approx. Theory, Relative Intensity (arbitrary units)</b>	<b>Hyperfine Component</b>
0	0	0	1	1	t
-4	0.27752	0.26832	0.9132	0.9140	r
1	0.28522	0.29157	1.0202	1.0215	q
-1	0.29453	0.30107	0.9772	0.9785	p
4	0.30219	0.32432	1.0868	1.0860	o
-3	0.41604	0.42583	0.9328	0.9355	n
-2	0.4296	0.43988	0.9543	0.9570	m
2	0.43892	0.44908	1.0418	1.0430	l
3	0.45315	0.46313	1.0633	1.0645	k
0	0.5794	0.59264	0.9980	1	i
-2	0.7144	0.71740	0.9556	0.9570	g
-1	0.715	0.73145	0.9758	0.9785	f
1	0.73355	0.75016	1.0189	1.0215	e
2	0.73596	0.76421	1.0424	1.0430	d
0	0.86976	0.88897	0.9987	1.0000	b

**Table 6. Relative frequencies and relative intensities for I<sub>2</sub> P(53) 19-2 hyperfine transitions. Calculations are shown from the matrix theory and from the high-J approximation theory.**

<b>F-J</b>	<b>Matrix Theory, <math>\Delta\nu</math> (GHz)</b>	<b>High J-Approx. Theory, <math>\Delta\nu</math> (GHz)</b>	<b>Matrix Theory, Relative Intensity (arbitrary units)</b>	<b>High J-Approx. Theory, Relative Intensity (arbitrary units)</b>	<b>Hyperfine Component</b>
-5	0	0	1	1	u
0	0.02357	0.02328	1.1045	1.1031	t
5	0.04651	0.04657	1.2090	1.2062	s
-4	0.2721	0.29145	1.0194	1.0206	r
1	0.30951	0.31473	1.1245	1.1237	q
-1	0.31635	0.32172	1.1245	1.0825	p
4	0.3524	0.34501	1.1865	1.1856	o
-3	0.43657	0.44766	1.0401	1.0412	n
-2	0.45184	0.46046	1.0613	1.0619	m
2	0.46251	0.47094	1.1452	1.1443	l
3	0.47329	0.48375	1.1665	1.1649	k
-3	0.57419	0.58290	1.0407	1.0412	j
0	0.60201	0.61317	1.1033	1.1031	i
3	0.63368	0.64345	1.1652	1.1649	h
-2	0.71356	0.73911	1.0594	1.0619	g
-1	0.73689	0.7519	1.0814	1.0825	f
1	0.75457	0.76938	1.1239	1.1237	e
2	0.7778	0.78219	1.1427	1.1443	d
-1	0.87856	0.89531	1.0814	1.0825	c
0	0.88965	0.90812	1.1008	1.1031	b
1	0.9037	0.92093	1.1227	1.1237	a

The lineshape for a homogeneously-broadened spectral line can be represented by the area-normalized Lorentzian function defined as

$$L(\nu) = \frac{1}{2\pi} \frac{\Delta\nu_L}{(\nu - \nu_o)^2 + \left(\frac{\Delta\nu_L}{2}\right)^2} \quad (43)$$

where  $\nu_o$  is the resonant frequency, and  $\Delta\nu_L$  is the Full Width at Half Maximum (FWHM) Lorentzian linewidth in units of frequency.

Two cases of homogeneous broadening are discussed in the next two sections: natural line-broadening and collision broadening. This is followed by a discussion of Doppler broadening (the phenomenon essential to the temperature diagnostic).

#### Natural Line-Broadening.

An excited molecule can spontaneously emit radiation to produce a spectral line shape with a fundamental width called the natural linewidth. The probability per unit time that a molecule in an excited-state energy level  $E_2$  makes a transition to a lower energy level  $E_1$  by spontaneous emission is represented by  $A_{21}$ , the Einstein coefficient for spontaneous emission. The inverse of  $A_{21}$  is the mean time the molecule remains in  $E_2$  before it spontaneously radiates a photon and transitions to  $E_1$  and is referred to as the radiative lifetime,

$$\tau_{rad} = \frac{1}{A_{21}}. \quad (44)$$

The lineshape for natural broadening is Lorentzian. Following the form of Equation (43), the natural lineshape can be written as

$$g_n(\nu) = \frac{1}{2\pi} \frac{\Delta\nu_n}{(\nu - \nu_o)^2 + \left(\frac{\Delta\nu_n}{2}\right)^2} \quad (45)$$

where the FWHM natural linewidth  $\Delta\nu_n$  is related to the radiative lifetime by



$$\Delta \nu_n = \frac{1}{2 \pi \tau_{rad}} . \quad (46)$$

Lifetime measurements for I<sub>2</sub> *B-X* transitions from the literature are shown in Table 7.<sup>17, 18, 35, 36</sup> The zero-I<sub>2</sub>-pressure lifetime  $\tau_o$  is related to the radiative lifetime  $\tau_{rad}$  by

$$\frac{1}{\tau_o} = \frac{1}{\tau_{rad}} + \frac{1}{\tau_{nr}} , \quad (47)$$

where  $\tau_{nr}$  is the non-radiative de-excitation lifetime due to spontaneous predissociation.<sup>17</sup> It has been shown experimentally that the radiative decay rate ( $1/\tau_{rad}$ ) decreases with increasing excited-state vibrational quantum number,  $\nu'$ .<sup>37</sup> Homogeneous linewidth measurements for I<sub>2</sub> *B-X* transitions are shown in Table 8 as FWHM values.<sup>25, 32, 38-41</sup> The generic symbols of  $\Delta \nu$  for linewidth and  $\tau$  for lifetime are used for column headings in Table 8 to encompass the variety of specific linewidths and lifetimes presented in each of the corresponding columns. In general,  $\Delta \nu$  is computed from  $\Delta \nu = 1/(2 \pi \tau)$ .

There is an order of magnitude discrepancy between experimentally measured lifetimes and the lifetimes computed from linewidth measurements that has been noted previously.<sup>32, 35, 42-44</sup> While the linewidth/lifetime discrepancy has been present in many experiments, an I<sub>2</sub> hyperfine component linewidth of 1.7 MHz @ 31 mTorr was measured recently using a third-harmonic demodulation technique and shows the best correspondence with measured lifetime values.<sup>41</sup>

**Table 7. Homogeneous lifetimes for I<sub>2</sub> B-X transitions.  $\tau$  is the lifetime of the transition.  $\tau_0$  is the zero-pressure lifetime.  $\tau_{rad}$  is the radiative lifetime.  $\Delta\nu$  is the FWHM linewidth.**

Measured $\tau$ (ns)	I <sub>2</sub> Spectral Assignment	Experimental Method	Reference	Computed $\Delta\nu$ (MHz)
$\tau_0 = 310 \pm 10$	$v'=6, J'=32$	fluor. decay, pulse method	35	$0.513 \pm 0.017$
$\tau_0 = 410 \pm 15$	$v'=11, J'=128$	“	35	$0.388 \pm 0.014$
$\tau_0 = 1.18 \pm 0.76$	$v'=17$	“	17	$0.135 \pm 0.087$
$\tau_0 = 1146 \pm 40$	$v'=17, J'=27$	“	18	$0.139 \pm 0.004$
$\tau_{rad} = 183$	$v'=17$	“	18	$0.87 \pm 0.05$
$\tau_0 = 286 \pm 20$	R(93) 16-2	fluorescence demodulation	36	$0.556 \pm 0.039$
$\tau_0 = 279 \pm 20$	P(95) 14-1	“	36	$0.57 \pm 0.041$

**Table 8. Homogeneous linewidths for I<sub>2</sub> B-X transitions.  $\Delta\nu$  is the FWHM linewidth.  $P_{I_2}$  is the iodine pressure.  $\tau$  is the lifetime of the transition.**

Measured $\Delta\nu$ (MHz)	$P_{I_2}$ (mTorr)	I <sub>2</sub> Spectral Assignment	Experimental Method	Ref.	Computed $\tau$ (ns)
9	~10	HFS P(33) 6-3	SAS	32	17.7
$10 \pm 1.6$	250	HFS P(117) 21-1	SAS	25	$15.9 \pm 2.5$
$7 \pm 2$	zero pressure, low intensity	HFS P(13) 43-0, HFS R(15) 43-0	IMF	38	$22.7 \pm 6.5$
7	21	HFS R(47) 9-2	Intracavity SAS	39	22.7
8	not stated	HFS P(62) 17-1	beam-overlap modulation	40	19.9
$1.7 \pm 0.1$	31	b10 hyperfine component of R(106) 28-0	3 <sup>rd</sup> harmonic demodulation	41	$93 \pm 5.5$

### Pressure Broadening.

In a real source, forces of neighboring molecules, ions, or electrons perturb the state of the radiating molecule leading to a broadening of the spectral line which is often greater than the natural width. The increase in linewidth is a function of the density of the perturbing species and is referred to as pressure broadening. In addition, the perturbations can produce a shift in the center-frequency of the spectral line.

In general, the excited molecule may interact with several perturbers making it necessary to average over the various orientations and paths of these perturbers. For line broadening at pressures from 0-100 Torr (as was encountered in this work), this averaging is performed with reasonable success in the limiting case of the impact (or phase shift) approximation in which the mean time between collisions is assumed to be much greater than the duration of a single collision.<sup>45</sup>

To account for the phenomenon of line shift along with line broadening, Lindholm and Foley developed a theory which included the effects of weak, distant collisions as well as strong collisions.<sup>46</sup> This theory assumes the perturbation causes no change in the internal state of the system; the so-called adiabatic approximation. The resulting spectral profile due only to elastic collisions is given by

$$g(\nu) = \frac{1}{2\pi} \frac{\Delta\nu_e}{(\nu - \nu_o - s)^2 + \left(\frac{\Delta\nu_e}{2}\right)^2} \quad (48)$$

which is a Lorentzian lineshape with a FWHM linewidth of

$$\Delta\nu_e = \frac{N \bar{\nu} \sigma_e}{\pi} \quad (49)$$

where  $N$  is the number density of the perturbing species,  $\bar{v}$  is the mean relative velocity, and  $\sigma_e$  is the elastic collision cross-section. The shift in line center is given by

$$s = \frac{N \bar{v} \sigma_s}{2 \pi} \quad (50)$$

where  $\sigma_s$  is the cross-section associated with the line shift. It is the weak, distant collisions that are responsible for the shift  $s$  in the spectral line's center frequency. In foreign-gas broadening of atoms, most of the perturbing gases produce a shift of line center towards the red end of the spectrum. Of the noble gases, He and sometimes Ne produce shifts towards the violet end of the spectrum.<sup>45</sup> In  $I_2$ , the pressure shift of a hyperfine component of R(56) 32-0 due to perturbing  $I_2$  molecules has been reported as 0.17 MHz/Torr.<sup>47</sup>

Since it is known that inelastic collisions of atoms and molecules can cause transitions between degenerate or nearly degenerate levels, modern developments in the theory have attempted to include these non-adiabatic effects.<sup>46</sup> On the plausible assumption that inelastic (quenching) collisions and elastic (phase-changing collisions) occur independently, the two effects can be superimposed so that the spectral lineshape can be written as

$$g(\nu) = \frac{1}{2\pi} \frac{(\Delta \nu_n + \Delta \nu_{coll})}{(\nu - \nu_o - s)^2 + \left( \frac{\Delta \nu_n + \Delta \nu_{coll}}{2} \right)^2} \quad (51)$$

where  $\Delta \nu_n$  is the FWHM natural linewidth and the FWHM collision linewidth due to both inelastic and elastic collisions is given by

$$\Delta \nu_{coll} = \Delta \nu_{in} + \Delta \nu_e. \quad (52)$$

The inelastic collision linewidth can be expressed as

$$\Delta \nu_{in} = \frac{1}{\pi T_{coll}} = \frac{N \bar{v} \sigma_{in}}{\pi} \quad (53)$$

where  $T_{coll}$  is the mean time between collisions and  $\sigma_{in}$  is the inelastic collision cross-section. Using Equations (49) and (53), the total collision-induced linewidth can be expressed as

$$\Delta \nu_{coll} = \frac{\sigma_{in} + \sigma_e}{\pi} N \bar{v} . \quad (54)$$

Substituting into Equation (54) the relations

$$\bar{v} = \sqrt{\frac{8 k_B T}{\pi \mu}} , \quad (55)$$

and

$$P = N k_B T , \quad (56)$$

where  $k_B = 1.380658 \cdot 10^{-23}$  J/K is the Boltzmann constant,  $T$  is the gas temperature,  $\mu$  is the reduced mass of the excited species and the perturber, and  $P$  is gas pressure due to the perturbing species, yields

$$\Delta \nu_{coll} = K P \quad (57)$$

where  $K$  is the pressure broadening rate due to the perturbing species given by

$$K = \frac{\sigma_{in} + \sigma_e}{\pi} \sqrt{\frac{8}{\pi \mu k_B T}} . \quad (58)$$

Buffer-gas pressure-broadening rates for  $I_2$  from the literature are shown in Table 9.<sup>48-51</sup> In a search of the literature over the past 35 years, only one study addressed the broadening of  $I_2$  hyperfine lines due to a buffer gas. Most of the broadening rates were obtained from fluorescence-type experiments. Self-broadening rates for  $I_2$  are displayed

in Table 10.<sup>38, 47, 52-56</sup> Most of these results are related to efforts concerning the frequency-stabilization of a laser to an I<sub>2</sub> hyperfine component.

**Table 9. I<sub>2</sub> pressure broadening rates due to buffer gases.**

<b>Buffer Gas</b>	<b>K<sub>buffer</sub> (MHz/Torr)</b>	<b>I<sub>2</sub> Spectral Assignment</b>	<b>Spectral Description</b>	<b>Experimental Method</b>	<b>Reference</b>
He	7.12	P(46) 17-1	hyperfine component	polarization spectroscopy	48
Xe	6.2	“	“	“	“
He	6.2	P(33) 6-3	ro-vibrational line	laser induced fluorescence	49
Ne	6.4	“	“	“	“
Ar	6.6	“	“	“	“
Kr	7.6	“	“	“	“
Xe	9.4	“	“	“	“
Air	10.4	“	“	“	“
CO <sub>2</sub>	11.9	“	“	“	“
He	8.28	v'=62 @ 501.7 nm	upper vibrational level	fluorescence depolarization	50
Ne	4.22	“	“	“	“
Ar	5.92	“	“	“	“
Kr	5.28	“	“	“	“
Xe	5.84	“	“	“	“
He	0.474	v'=43 @ 514.5 nm	upper vibrational level	fluorescence depolarization	50
Ne	0.868	“	“	“	“
Ar	0.632	“	“	“	“
Kr	0.671	“	“	“	“
Xe	0.829	“	“	“	“
Air	9.93	P(60) 27-0 &R(97) 28-0 @ 543 nm	overlapped ro-vibrational lines	laser induced fluorescence	51

**Table 10. Self-broadening rates for I<sub>2</sub>.**

<b>K<sub>I2</sub></b> <b>(MHz/Torr)</b>	<b>I<sub>2</sub> Spectral</b> <b>Assignment</b>	<b>Spectral</b> <b>Description</b>	<b>Experimental</b> <b>Method</b>	<b>Reference</b>
19.7	R(56) 32-0 @ λ=532 nm	hyperfine component	modulation transfer spectroscopy	47
11.6	λ=633 nm	hyperfine components	beat frequency / 1st derivative measurement	52
8.75	R(127) 11-5 @ λ=633 nm	hyperfine component	intracavity absorption/ 2nd derivative technique	53
16.9	633 nm	hyperfine component	beat frequency	54
14.13	P(48) 11-3 @ λ=612 nm	hyperfine component	third harmonic detection	55
9.5	λ=633 nm	hyperfine component	intracavity absorption/ 3rd derivative technique	56
16	P(13) 43-0, R(15) 43-0 @ λ=514.5 nm	hyperfine components	inter-modulated fluorescence	38

**Doppler Broadening.**

For a gas at low pressure, the primary contribution to spectral linewidth is Doppler broadening due to the thermal motion of the absorbing or emitting molecules. In this case, a Doppler-broadened spectral line can be represented by the Gaussian lineshape function defined as

$$G(\nu) = \frac{1}{\nu_o} \left( \frac{m c^2}{2 \pi k_B T} \right)^{\frac{1}{2}} \cdot \exp \left( - \frac{m c^2 (\nu - \nu_o)^2}{2 k_B T \nu_o^2} \right) \quad (59)$$

where  $\nu_o$  is the resonant frequency in Hz,  $c = 2.99792458 \cdot 10^8$  m/s is the speed of light (in vacuum),  $m$  is the mass of the molecule in kg, and  $T$  is temperature of the gas in Kelvin. For the  $I_2$  molecule,  $m_{I_2} = 4.2453 \cdot 10^{-25}$  kg is calculated from  $\mathcal{M}_{I_2} = 126.9045$  amu and the proton mass  $m_p = 1.6726231 \cdot 10^{-25}$  kg.

The Doppler linewidth at FWHM is given by

$$\Delta \nu_D = \frac{\nu_o}{c} \cdot \sqrt{\frac{8 k_B T \ln(2)}{m}}. \quad (60)$$

Once the Doppler width of a spectral line in a gas is determined, the temperature of the gas can be obtained by solving Equation (60) for  $T$  to yield

$$T = \frac{m}{8 k_B \ln(2)} \frac{c^2}{\nu_o^2} \Delta \nu_D^2. \quad (61)$$

The standard error in the temperature is<sup>57</sup>

$$\delta T = \frac{2m c^2}{8 k_B \nu_o^2 \ln(2)} \Delta \nu_D \delta(\Delta \nu_D) \quad (62)$$

where  $\delta(\Delta \nu_D)$  is the standard error in the Doppler linewidth. For a single hyperfine component of an  $I_2$  ro-vibrational line, the Doppler width varies from approximately 285 MHz at 150 K to 400 MHz at 300 K.

Except for the case of very low gas pressure and a large Doppler width, a Gaussian lineshape is not sufficient to completely describe a Doppler-broadened spectral line. In the rest frame of a select group of gas molecules, the intensity of the emitted radiation follows a Lorentzian lineshape that is centered about a resonant frequency  $\nu_o$ . If each molecule in the select group moves with a definite velocity component  $\nu_z$



towards an observer in the laboratory frame, then the observer measures emitted radiation that is homogenously broadened about a resonant frequency  $\nu'_o$  that is Doppler-shifted with respect to  $\nu_o$  so that

$$\nu'_o = \nu_o \left( 1 + \frac{v_z}{c} \right) \quad (63)$$

where  $v_z$  is the velocity component in the z direction. The emitted radiation for a specific molecular velocity group follows a Lorentzian lineshape given by

$$L(\nu, v_z) = \frac{1}{2\pi} \frac{\Delta \nu_L}{(\nu - \nu_o - \nu_o v_z / c)^2 + \left( \frac{\Delta \nu_L}{2} \right)^2} \quad (64)$$

The emitted radiation from each of the molecular velocity groups combines to produce the total intensity distribution of the spectral line observed in the laboratory frame. Each  $L(\nu, v_z)$  contributing to the total intensity of the spectral line is weighted by the number of molecules that have velocity  $v_z$ . Since the number of molecules with velocity  $v_z$  follows the Maxwellian velocity distribution, the spectral line is represented by a convolution of the Gaussian and Lorentzian lineshapes called a Voigt lineshape given by

$$V(\nu) = \left( \frac{m}{2\pi k_B T} \right)^{\frac{1}{2}} \int_{-\infty}^{\infty} \left( \frac{\Delta \nu_L}{2\pi \left( (\nu - \nu_o - \nu_o v_z / c)^2 + (\Delta \nu_L / 2)^2 \right)} \right) \cdot \exp \left( -\frac{m}{2k_B T} v_z^2 \right) dv_z \quad (65)$$

Several Voigt lineshapes, each with a different Lorentzian width, are shown in Figure 5. These lineshapes were calculated using the TableCurve<sup>®</sup> computer program.<sup>58</sup> The Gaussian component of each Voigt has the same FWHM Doppler linewidth of 400 MHz as does the pure Gaussian lineshape included in Figure 5 for comparison. The Voigt

lineshape with a Lorentzian FWHM linewidth of 10 MHz shows only a slight difference from the pure Gaussian lineshape in the wings. At very low pressures, a Voigt lineshape is approximately Gaussian. At high pressures, the Lorentzian contribution to the Voigt lineshape causes the Voigt to deviate significantly from a pure Gaussian lineshape.

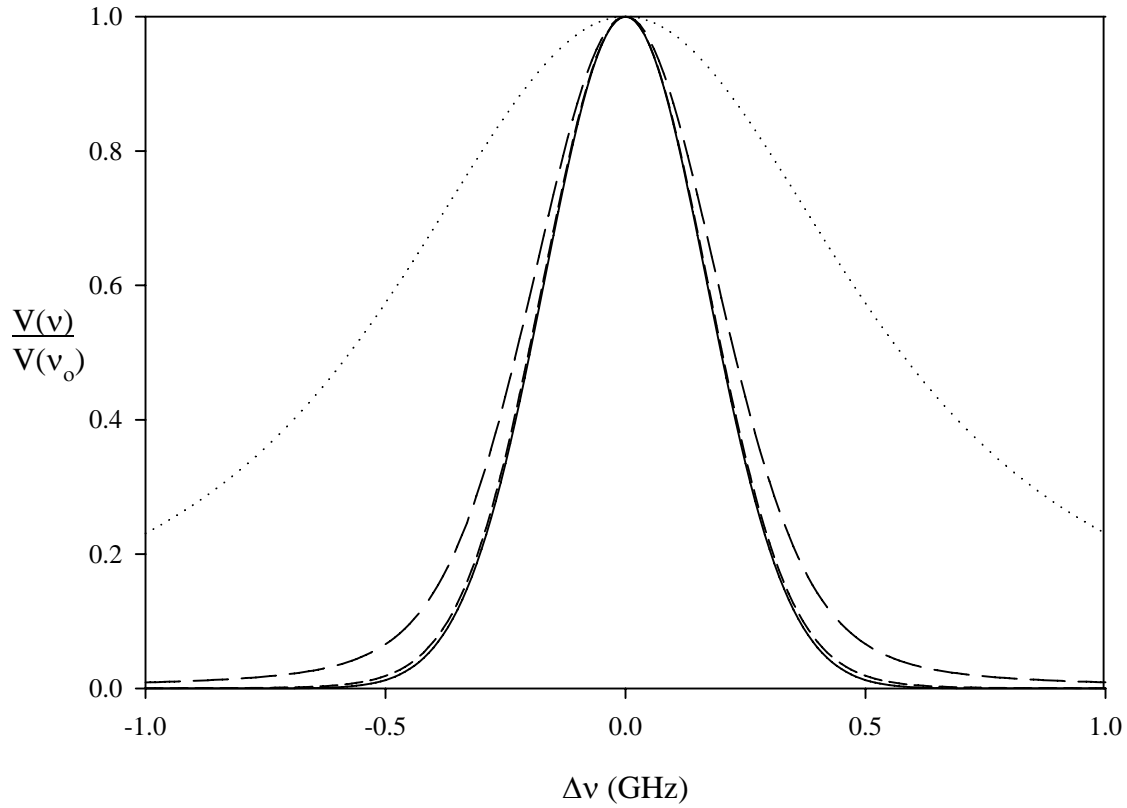


**Figure 5. Comparison of a Gaussian lineshape to various Voigt lineshapes. The Gaussian width is the same for all lineshapes: 400 MHz FWHM. The dotted line is a Voigt with a 1000 MHz Lorentzian FWHM. The long-dashed line is a Voigt with a 100 MHz Lorentzian FWHM. The short-dashed line is a Voigt with a 10 MHz Lorentzian FWHM. The Gaussian lineshape is the solid line. The y-axis is the relative intensity of the lineshape, and the x-axis is the relative frequency.**

### C. Laser Saturation Spectroscopy

Numerous spectroscopic techniques have been developed which utilize a laser to saturate a molecular transition. Several monographs provide comprehensive surveys of the experimental and theoretical aspects of these techniques.<sup>59-61</sup> In this section, some of the basic concepts of linear and nonlinear absorption are briefly reviewed to provide a framework for the theory of the cross-beam laser techniques presented in the next chapter. In addition, the two well-known, Doppler-free techniques of Saturation Absorption Spectroscopy (SAS), and Inter-Modulated Fluorescence (IMF) spectroscopy are discussed since these methods were utilized experimentally to investigate phenomena that influence the  $I_2$  hyperfine structure and consequently the temperature diagnostic. In fact, the two new cross-beam techniques developed in this work are variants on the Doppler-free techniques.

#### Linear and Nonlinear Spectroscopy.

A rate-equation approach serves to describe the interaction of an incident, parallel beam of monochromatic light with an open two-level system representing a sample of gas molecules. An energy-level diagram for the system is shown in Figure 6. For the population densities  $N_1, N_2$  of the non-degenerate energy-levels  $E_1$  and  $E_2$ , the rate equations are

$$\frac{dN_1}{dt} = B_{12} \rho_\nu g(\nu)(N_2 - N_1) - R_1 N_1 + C_1 \quad (66)$$

and

$$\frac{dN_2}{dt} = B_{12} \rho_\nu g(\nu)(N_1 - N_2) - R_2 N_2 + C_2 \quad (67)$$

where  $R_i N_i$  is the total relaxation rate including spontaneous emission that depopulates level  $i$ , and

$$C_i = \sum_{k \neq 1,2} R_{ki} N_k + D_i \quad (68)$$

accounts for relaxation paths from other  $k$  levels that populate level  $i$  in addition to the diffusion rate,  $D_i$ , of  $i$ -level molecules into the excitation volume  $dV$ . The Einstein coefficient for absorption is  $B_{12}$  in units of  $\text{m}^3/(\text{J} \cdot \text{s}^2)$ ,  $\rho_\nu$  is the energy density (in units of  $\text{J}/\text{m}^3$ ) at frequency  $\nu$  of the incident radiation. The lineshape is represented by  $g(\nu)$  which has units of  $1/\text{Hz}$  (or seconds). The integral of  $g(\nu)$  over all frequencies is

$\int_0^\infty g(\nu) d\nu = 1$ . The product  $g(\nu) d\nu$  can be interpreted as the relative probability that

radiation in the frequency interval  $\nu$  to  $\nu + d\nu$  will be absorbed by the molecules in energy-level 1. In the rate equations, the spectral width of the *spectral* energy density  $\rho(\nu)$  (in units of  $\text{J s}/\text{m}^3$ ) is assumed to be very small compared to  $g(\nu)$  so  $\rho(\nu)$  can be

approximated by a  $\delta$  function and  $\int_0^\infty \rho(\nu') g(\nu') d\nu' \cong \int_0^\infty \rho_\nu \delta(\nu' - \nu) g(\nu') d\nu' \cong \rho_\nu g(\nu)$ .

For steady state conditions ( $dN_i / dt = 0$ ), and  $C_i$  that are not significantly affected by the incident radiation, the unsaturated population difference for energy density  $\rho_\nu = 0$  is

$$\Delta N^o = \Delta N(\rho_\nu = 0) = N_1^o - N_2^o = \frac{C_1 R_2 - C_2 R_1}{R_1 R_2}. \quad (69)$$

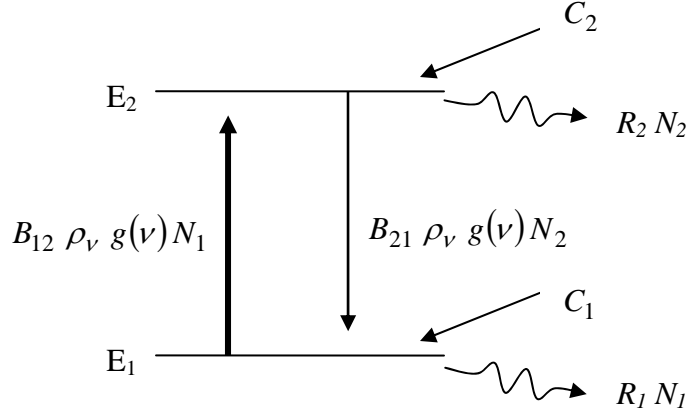


**Figure 6. Open two-level system.**

For the saturated population difference ( $\rho_\nu \neq 0$ ),

$$\Delta N = \frac{\Delta N^o}{1 + B_{12} \rho_\nu g(\nu) \left( \frac{1}{R_1} + \frac{1}{R_2} \right)} = \frac{\Delta N^o}{1 + S(\nu)} \quad (70)$$

where

$$S(\nu) = \frac{B_{12} \rho_\nu}{R^*} g(\nu) \quad (71)$$

is the frequency-dependent saturation parameter, and

$$R^* = \frac{R_1 R_2}{R_1 + R_2}. \quad (72)$$

For a homogeneously-broadened spectral line,  $S(\nu)$  has a Lorentzian lineshape so that

$$S(\nu) = S_o \frac{(\Delta \nu_h / 2)^2}{(\nu - \nu_o)^2 + (\Delta \nu_h / 2)^2} \quad (73)$$

where

$$S_o = S(\nu_o) = \frac{B_{12} \rho_\nu}{R^*} \frac{2}{\pi \Delta \nu_h} . \quad (74)$$

The rate at which the energy per unit volume,  $W_{12}$ , is absorbed on the transition from level 1 to level 2 by molecules with population densities  $N_1, N_2$  irradiated with a monochromatic optical wave is given by

$$\frac{dW_{12}}{dt} = h \nu B_{12} \rho_\nu g(\nu) \Delta N = h \nu B_{12} \rho_\nu g(\nu) \frac{\Delta N^o}{1 + S(\nu)} . \quad (75)$$

Substituting Equation (73) into Equation (75) yields

$$\frac{dW_{12}}{dt} = h \nu R^* S_o \Delta N^o \frac{(\Delta \nu_h/2)^2}{(\nu - \nu_o)^2 + (\Delta \nu_s/2)^2} . \quad (76)$$

The lineshape in Equation (76) is Lorentzian with a FWHM linewidth of

$$\Delta \nu_s = \Delta \nu_h \sqrt{1 + S_o} . \quad (77)$$

The molecular transition is saturation-broadened. Its linewidth increases as  $S_o$  increases.

Usually, the frequency-dependent saturation parameter is expressed in terms of the intensity of the incident radiation and a collection of constants. The Einstein absorption coefficient is related to the spontaneous emission coefficient by

$$B_{12} = \frac{g_2}{g_1} c \frac{\lambda^2}{8 \pi} \frac{A_{21}}{h \nu} \quad (78)$$

where  $h$  is Planck's constant,  $A_{21}$  is the Einstein coefficient for spontaneous emission,  $\lambda$  is the wavelength. The energy-level degeneracies are given by  $g_1$  and  $g_2$ . For this discussion,  $g_1 = g_2 = 1$ . Substituting Equation (78) into Equation (71), and recognizing that the intensity of the incident radiation at frequency  $\nu$  is  $I_\nu = c \rho_\nu$ , provides a means

of expressing the frequency-dependent saturation parameter in terms of the intensity of the incident radiation so that

$$S(\nu) = A_{21} \frac{c \lambda^2}{8 \pi} \frac{1}{h \nu R^*} \frac{I_\nu}{c} g(\nu) = \left( \frac{\sigma_{12}(\nu)}{h \nu R^*} \right) I_\nu \quad (79)$$

where

$$\sigma_{12}(\nu) = \sigma_o \frac{(\Delta \nu_h / 2)^2}{(\nu - \nu_o)^2 + (\Delta \nu_h / 2)^2}, \quad (80)$$

is the frequency-dependent absorption cross-section with dimensions of area and

$$\sigma_o = \sigma_{12}(\nu_o) = \left( A_{21} \frac{\lambda^2}{8 \pi} \right) \frac{2}{\pi \Delta \nu_h} = A_{21} \frac{\lambda^2}{4 \pi^2 \Delta \nu_h} \quad (81)$$

is the absorption cross-section at line-center of the transition. The reciprocal of the expression in parentheses in Equation (79) has dimensions of power per unit area so that the frequency-dependent saturation parameter can be interpreted as

$$S(\nu) = \bar{g}(\nu) \frac{I_\nu}{I_s}, \quad (82)$$

where

$$\bar{g}(\nu) = \frac{g(\nu)}{g(\nu_o)} \quad (83)$$

and

$$I_s = \frac{4 \pi^2 \Delta \nu_h}{A_{21} \lambda^2} h \nu R^* \quad (84)$$

is the saturation intensity. For  $\nu = \nu_o$  and  $I_\nu = I_s$ , the population-density difference

$\Delta N$  is reduced to one-half its unsaturated value  $\Delta N^o$ , and the linewidth of the absorption

transition is increased by a factor of  $\sqrt{2}$ . Some experimental values for  $I_s$  of transitions in the  $I_2$   $B$ - $X$  system are listed Table 11.<sup>25, 26, 38, 41, 42, 62, 63</sup> Two results express  $I_s$  in terms of a pressure dependence.

Since the absorbed power per unit volume equals the intensity decrease per unit length of the incident radiation having intensity  $I_\nu$ :

$$dW_{12} / dt = -dI_\nu / dz, \quad (85)$$

Equation (75) can be written as

$$dI_\nu = -I_\nu \sigma_{12}(\nu) \frac{\Delta N^o}{1 + \bar{g}(\nu) \frac{I_\nu}{I_s}} dz \quad (86)$$

For weak light sources, such as spectral lamps, where  $I_\nu \ll I_s$ , Equation (86) can be approximated to yield

$$dI_\nu = -I_\nu \sigma_{12}(\nu) \Delta N^o dz = -\alpha_o(\nu) I_\nu dz \quad (87)$$

where  $\alpha_o(\nu)$  is the unsaturated absorption coefficient. In Equation (87), the absorbed intensity increases linearly with incident intensity. Integration of Equation (87) over a length  $L$  yields the *Lambert-Beer* law of linear absorption for the transmitted intensity:

$$I_t = I_o \exp(-\alpha_o(\nu) L). \quad (88)$$

In contrast to saturation broadening of homogeneous lines, saturation effects in Doppler-broadened transitions give rise to the phenomenon of *hole burning*. In the rest frame of an observer, consider a monochromatic optical wave of frequency  $\nu$  moving in the + $z$ -direction with a wave vector  $\vec{k} = k_z \hat{z}$  through a gaseous sample of molecules with a Maxwellian velocity distribution. The optical wave frequency observed in the reference



**Table 11. I<sub>2</sub> saturation intensities from literature.**

<b>I<sub>s</sub> (mW/mm<sup>2</sup>)</b>	<b>I<sub>2</sub> Spectral Assignment</b>	<b>Beam Power</b>	<b>Experimental Method</b>	<b>Reference</b>
60 ± 20	P(117) 21-1	10 mW beams	SAS	25
150	P(117) 21-1 & lines @ 514.5 nm	6 mW beams	SAS	26
80 - 200	P(13) 43-0 & R(15) 43-0 blended line	30 to 1000 mW/mm <sup>2</sup>	IMF	38
0.425(1+0.214P) <sup>2</sup> pressure in Pa	R(47) 9-2	-	intracavity absorption	62
120(1+0.039P) <sup>2</sup> pressure in Pa	R(127) 11-5	-	4th harmonic detection SA	42
3.1 ± 0.6	R(77) 15-2 hyperfine component	1.8 mW max	1st harmonic from SAS	63
2.4 ± 0.24	P(38) 14-2 hyperfine component	1.35 mW average	double modulation technique (freq. & amp.)	63
0.385 ± 0.142	R(106) 28-0 hyperfine component at 543 nm	< 120 μW	3rd harmonic demodulation technique	41

frame of molecules moving in the +z-direction with velocity  $v_z$  is

$$\nu' = \nu - \frac{\nu}{c} v_z. \quad (89)$$

The incident wave is absorbed when  $\nu'$  equals the resonance frequency  $\nu_o$  of the molecule at rest. Under this condition,

$$\nu = \nu_o / \left(1 - \frac{v_z}{c}\right) \cong \nu_o \left(1 + \frac{v_z}{c}\right) \quad (90)$$

for  $v_z \ll c$ . The incident optical wave of frequency  $\nu$  is absorbed by the select group of molecules moving in the +z-direction with velocity component  $v_z = (\nu - \nu_o) \cdot c / \nu_o$ . Furthermore, the frequency response of molecules belonging to a specific velocity group follows a Lorentzian lineshape due to the homogeneous broadening of the absorption transition. Thus, the absorption cross-section for a transition between energy levels  $E_1$  and  $E_2$  of a molecule moving with velocity  $v_z$  is

$$\sigma_{12}(\nu, v_z) = \sigma_o \frac{(\Delta \nu_h / 2)^2}{(\nu - \nu_o - \nu_o \cdot v_z / c)^2 + (\Delta \nu_h / 2)^2} \quad (91)$$

where  $\sigma_o$  is the absorption cross-section maximum at line center. The saturation of the molecular transition by the incident optical wave *burns a hole* in the population density  $N_1(v_z)dv_z$  of energy-level  $E_1$  in the velocity interval  $\Delta v_z \cong \Delta \nu_h \cdot c / \nu_o$ , and simultaneously produces a peak in  $N_2(v_z)dv_z$  of  $E_2$  within the same velocity interval according to

$$N_1(\nu, v_z) = N_1^o(v_z) - \frac{[N_1(v_z) - N_2(v_z)] R^*}{R_1} \frac{S_o (\Delta \nu_h / 2)^2}{(\nu - \nu_o - \nu_o \cdot v_z / c)^2 + (\Delta \nu_h / 2)^2}, \quad (92)$$

and

$$N_2(\nu, v_z) = N_2^o(v_z) + \frac{[N_1(v_z) - N_2(v_z)] R^*}{R_2} \frac{S_o (\Delta \nu_h / 2)^2}{(\nu - \nu_o - \nu_o \cdot v_z / c)^2 + (\Delta \nu_h / 2)^2}, \quad (93)$$

where  $R_1$  and  $R_2$  are the relaxation rates for  $E_1$  and  $E_2$ , respectively.<sup>61, 64</sup> The homogeneous FWHM linewidth is related to the relaxation rates by the relation  $\Delta \nu_h = (R_1 + R_2) / (2\pi)$ , and  $R^*$  is given by Equation (72). From Equations (92) and (93), the difference in the saturated population density is then

$$\Delta N(\nu, \nu_z) d\nu_z = \Delta N^o(\nu_z) \frac{1}{1 + \frac{S_o (\Delta \nu_h/2)^2}{(\nu - \nu_o - \nu_o \cdot \nu_z / c)^2 + (\Delta \nu_h/2)^2}} d\nu_z \quad (94)$$

where  $\Delta N^o(\nu_z)$  follows a Maxwellian velocity distribution. The velocity-selective minimum occurring at  $\nu_z = (\nu - \nu_o) \cdot c / \nu_o$  in the velocity distribution of Equation (94) is referred to as a Bennet hole.<sup>65</sup>

The saturated absorption coefficient  $\alpha_s(\nu)$  can be obtained by recognizing that molecules having velocity components in the  $\nu_z$  to  $\nu_z + d\nu_z$  interval contribute

$$\frac{d\alpha_s(\nu, \nu_z)}{d\nu_z} d\nu_z = \Delta N(\nu, \nu_z) \sigma(\nu, \nu_z) d\nu_z \quad (95)$$

to the total absorption coefficient due to all molecular velocity groups so that

$$\alpha_s(\nu) = \int_{-\infty}^{\infty} \Delta N(\nu, \nu_z) \sigma_{12}(\nu, \nu_z) d\nu_z. \quad (96)$$

Substituting Equation (94) for the saturated population-density difference, and Equation (91) for the absorption cross-section into Equation (96) yields, with  $\Delta N^o(\nu_z)$  expressed explicitly in terms of a Maxwellian velocity distribution,

$$\alpha_s(\nu) = \frac{\Delta N^o \sigma_o}{\nu_p \sqrt{\pi}} \left( \frac{\Delta \nu_h}{2} \right)^2 \int_{-\infty}^{\infty} \frac{\exp\left(-(\nu_z/\nu_p)^2\right)}{(\nu - \nu_o - \nu_o \cdot \nu_z/c)^2 + \left(\frac{\Delta \nu_s}{2}\right)^2} d\nu_z \quad (97)$$

where  $\Delta N^o = \int_{-\infty}^{\infty} \Delta N^o(\nu_z) d\nu_z$ , and  $\nu_p = (2 k_B T / m)^{1/2}$  is the most probable velocity

for a Maxwellian velocity distribution. As shown in Equation (97), the absorption coefficient due to saturation of an absorption transition by a monochromatic light source has a Voigt profile with a homogeneous FWHM of  $\Delta \nu_s$  given by Equation (77).

The exponential term in Equation (97) has little variation over the velocity interval  $\Delta v_z = \Delta v_s \cdot c / v_o$  in the limit  $S_o \ll 1$  where the Doppler width is typically much larger than  $\Delta v_s$  for a low-pressure gas. In this circumstance, factoring the exponential term out of the integral is a reasonable approximation. Solving the remaining integral with  $dv_z = d[(v - v_o) \cdot c / v_o] = c / v_o dv$ , the saturated absorption coefficient then becomes

$$\alpha_s(\nu) \cong \frac{\alpha_o(\nu_o)}{\sqrt{1+S_o}} \exp \left\{ - \left( \frac{c(\nu - \nu_o)}{\nu_o v_p} \right)^2 \right\} = \frac{\alpha_o(\nu)}{\sqrt{1+S_o}} \quad (98)$$

where

$$\alpha_o(\nu_o) = \sqrt{\pi} \sigma_o \Delta N_o \frac{c}{\nu_o v_p} \frac{\Delta \nu_h}{2}, \quad (99)$$

and the FWHM Doppler width is

$$\Delta \nu_D = 2 \sqrt{\ln 2} \frac{\nu_o v_p}{c} = \frac{\nu_o}{c} \sqrt{\frac{8 k_B T \ln 2}{m}}. \quad (100)$$

If a single laser-beam incident on a low-pressure gas of molecules is frequency-tuned across a molecular transition, the Bennett hole burned into  $\Delta N(\nu, v_z)$  of Equation (94) due to absorption would not be directly observable in the recorded signal. Equation (98) shows that the effect of saturation by the laser merely reduces the unsaturated absorption coefficient  $\alpha_o(\nu)$  by a constant factor of  $\sqrt{1+S_o}$ . It is possible, however, to observe the hole by using two laser beams simultaneously.<sup>59, 61</sup> A two-beam experiment is discussed in the next section.

### Doppler-Free Saturation Spectroscopy.

The Doppler-free techniques of SAS and IMF are discussed because they are used to investigate the  $I_2$  hyperfine spectrum and because the theory contains concepts which apply to the theory for new cross-beam techniques. The key concepts for Doppler-free techniques are (1) the selection of a single molecular velocity group, namely the zero velocity group, for laser excitation which removes the Doppler-broadening in the recorded spectral profiles, (2) modulation of one or both laser beams to periodically alter the population densities of the upper- and lower-levels of a particular molecular transition through laser saturation, (3) to detect the effects of the modulation by recording the transmitted laser intensity or laser excitation through a phase sensitive detection scheme to eliminate Doppler-broadened background and parasitic noise sources.

### *Saturation Absorption Spectroscopy.*

In a Doppler-free Saturation Absorption Spectroscopy (SAS) experiment, the output beam of a narrow-linewidth, tunable laser is split into a pump beam of intensity  $I_{pump}$  and a probe beam of intensity  $I_{probe}$ . The beams are directed counter-propagating to each other and overlapped in a sample cell containing a low pressure gas (or vapor) of molecules. When the laser frequency  $\nu$  is tuned to a resonant frequency  $\nu_o$  of the gas molecules, both the pump and probe beams will interact with the  $v_z = 0$  velocity group of molecules. The detected signal  $S_{SAS} \propto I_{probe} - I_{probe}^{trans}$  as function of frequency for a series of closely spaced Doppler-broadened absorption transitions reveals a broad absorption background with small dips (called Lamb dips) in the background at each of the resonant frequencies.<sup>66</sup> Doppler-free experiments have been performed with a sample

cell of  $I_2$  placed inside a laser cavity. When the output power of the laser  $P_{laser}(\nu)$  is recorded as a function of frequency for a single  $I_2$  ro-vibrational absorption transition, the resulting profile shows a broad absorption background with small peaks (inverted Lamb dips) centered at the resonant frequencies of the hyperfine transitions.<sup>39, 62, 67, 68</sup>

Numerous Doppler-free measurements have been performed with a sample cell placed external to the laser. This arrangement eliminates the influence of the absorber on the frequency and amplitude of the laser. For two counter-propagating waves of equal intensity,  $I_1 = I_2 = I$ , interacting in a sample cell external to the laser, the saturated population-density difference is

$$\Delta N(\nu, v_z) dv_z = \frac{\Delta N^o(v_z)}{1 + \frac{S_o (\Delta \nu_h / 2)^2}{\left( \nu - \nu_o - \nu_o \frac{v_z}{c} \right)^2 + \left( \frac{\Delta \nu_h}{2} \right)^2} + \frac{S_o (\Delta \nu_h / 2)^2}{\left( \nu - \nu_o + \nu_o \frac{v_z}{c} \right)^2 + \left( \frac{\Delta \nu_h}{2} \right)^2}} dv_z \quad (101)$$

where  $\Delta N^o(v_z)$  is the unsaturated population-density difference having a Maxwellian velocity distribution, and  $S_o$  is the saturation parameter due to one of the running waves.<sup>59</sup>

Using Equation (101), the saturated absorption coefficient, in the weak-field approximation ( $S_o \ll 1$ ), for two counter-propagating beams of *equal* intensity is given by

$$\alpha(\nu) = \alpha_o(\nu) \left[ 1 - \frac{S_o}{2} \left( 1 + \frac{(\Delta \nu_h / 2)^2}{(\nu - \nu_o)^2 + (\Delta \nu_h / 2)^2} \right) \right] \quad (102)$$

which is an unsaturated, Doppler-broadened absorption coefficient,  $\alpha_o(\nu)$ , with a Lamb dip at line-center,  $\nu = \nu_o$ .<sup>59</sup>

The absorption coefficient of a weak probe-beam counter-propagating against a strong pump-beam (with  $S_o \ll 1$ ) is given by

$$\alpha(\nu) = \alpha_o(\nu) \left[ 1 - \frac{S_o}{2} \frac{(\Delta \nu_s^* / 2)^2}{(\nu - \nu_o)^2 + (\Delta \nu_s^* / 2)^2} \right] \quad (103)$$

where  $\Delta \nu_s^* = (\Delta \nu_h + \Delta \nu_s) / 2$ .<sup>60</sup>

If the pump beam is modulated by a mechanical chopper, and the transmitted intensity of the probe beam is monitored with a lock-in amplifier referenced to the chopping frequency as illustrated in Figure 7, the Doppler background can be removed from the absorption profile of a group of closely-spaced, Doppler-broadened absorption transitions. The resulting signal consists of the same group of transitions having only homogeneously broadened lineshapes. The crossing angle for the beams is exaggerated in the schematic. Experimentally, the counter-propagating beams should be overlapped as closely as possible within the sample cell to minimize residual Doppler broadening. For a strong, chopped pump-beam and a weak probe-beam, the recorded signal for the configuration in Figure 7 is proportional to the relative saturated absorption, obtained from Equation (103), yielding

$$S_{SAS} \propto \frac{\alpha_o(\nu) - \alpha(\nu)}{\alpha_o(\nu)} = \frac{S_o}{2} \frac{(\Delta \nu_s^* / 2)^2}{(\nu - \nu_o)^2 + (\Delta \nu_s^* / 2)^2}. \quad (104)$$

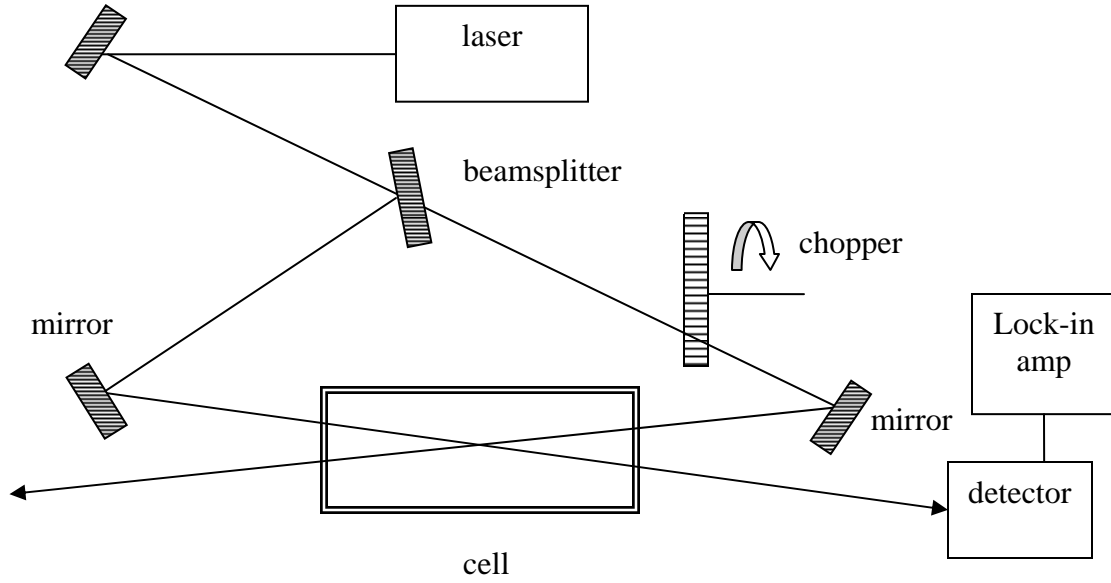


**Figure 7. Doppler Free Saturation Absorption Spectroscopy Set-up.**

#### *Inter-Modulated Fluorescence Spectroscopy.*

Experiments employing the Doppler-free technique of Inter-Modulated Fluorescence Spectroscopy (IMF) were also pursued in this research effort. This technique, shown in Figure 8, involves chopping one of the counter-propagating beams at frequency  $f_1$ , chopping the other beam at frequency  $f_2$ , and subsequently detecting the fluorescence signal at the sum frequency  $f_{sum} = f_1 + f_2$ .<sup>38</sup> This technique can provide greater sensitivity than SAS especially in low density samples, or when the path length is small. The IMF technique overcomes the difficulty in SAS of detecting a very small change in the transmitted probe intensity.

The fluorescence intensity in an IMF experiment can be written as

$$I_{IMF} = C \Delta N_s (I_1 + I_2) \quad (105)$$



where the constant  $C$  accounts for transition probability and detector efficiency,  $I_1$  and  $I_2$  are the incident intensities due to the two counter-propagating beams, and  $\Delta N_s$  is the change in the saturated population density given by<sup>61</sup>

$$\Delta N_s(\nu, \nu_z) = \Delta N^o(\nu_z) \cdot \left[ 1 - \frac{2}{\pi \Delta \nu_h I_s} \left( \frac{I_1 (\Delta \nu_h / 2)^2}{\left( \nu - \nu_o - \nu_o \frac{\nu_z}{c} \right)^2 + \left( \frac{\Delta \nu_s}{2} \right)^2} + \frac{I_2 (\Delta \nu_h / 2)^2}{\left( \nu - \nu_o + \nu_o \frac{\nu_z}{c} \right)^2 + \left( \frac{\Delta \nu_s}{2} \right)^2} \right) \right]. \quad (106)$$

Evaluating Equation (106) at the center of the absorption line ( $\nu_z = 0$ ), yields

$$\Delta N_s(\nu) = \Delta N^o \left[ 1 - a^* \frac{(\Delta \nu_h / 2)}{(\nu - \nu_o)^2 + \left( \frac{\Delta \nu_s}{2} \right)^2} (I_1 + I_2) \right] \quad (107)$$

where

$$a^* = \frac{1}{\pi I_s}. \quad (108)$$

Substituting Equation (106) into Equation (105) yields

$$I_{IMF} = C \left( \Delta N^o (I_1 + I_2) - a^* \frac{(\Delta \nu_h / 2)}{(\nu - \nu_o)^2 + \left( \frac{\Delta \nu_s}{2} \right)^2} \Delta N^o (I_1 + I_2)^2 \right). \quad (109)$$

The intensities of the two chopped beams are  $I_1 = I_1^o (1 + \cos(\Omega_1 t))$  and

$I_2 = I_2^o (1 + \cos(\Omega_2 t))$  where  $\Omega_i = 2\pi f_i$ . The quadratic expression in Equation (109)

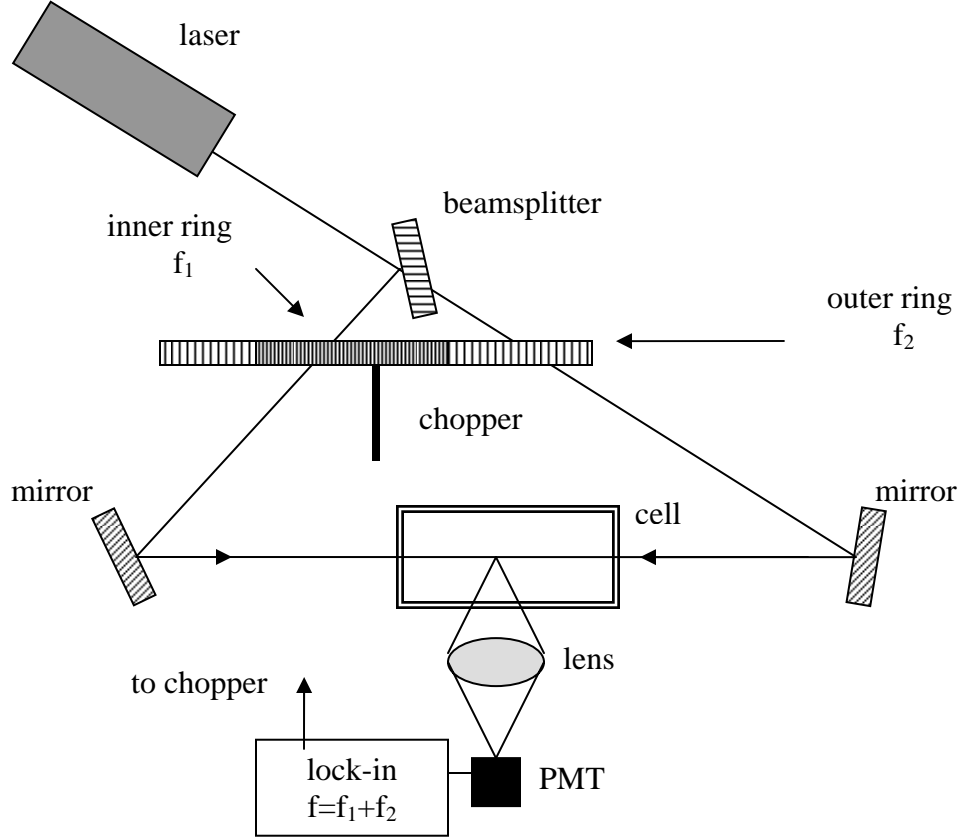


**Figure 8. Doppler-Free Inter-Modulated Fluorescence experiment.**

has a term

$$2 I_1^o I_2^o \cos(\Omega_1 t) \cos(\Omega_2 t) \quad (110)$$

which can be restated, using a trigonometric identity, as

$$2 I_1^o I_2^o \left[ \frac{1}{2} \cos((\Omega_1 + \Omega_2) t) + \frac{1}{2} \cos((\Omega_1 - \Omega_2) t) \right]. \quad (111)$$

When the fluorescence is monitored through a lock-in amplifier at the sum frequency

where  $f_{sum} = f_1 + f_2$ , only the first term in Equation (111) contributes to the detected

signal yielding

$$S_{IMF} = C a^* I_1^o I_2^o \Delta N^o \frac{(\Delta v_h / 2)}{(v - v_o)^2 + \left(\frac{\Delta v_s}{2}\right)^2} . \quad (112)$$

#### D. Supersonic Flow in a Nozzle

To employ the spatially-resolved temperature diagnostic in a supersonic flow, a small convergent/divergent nozzle like the one depicted in Figure 9 is used to simulate the conditions in a COIL supersonic nozzle. The one dimensional approximation of an isentropic flow provides formulas useful for characterizing the nozzle. Following this approach, the Mach number at any point along the direction of flow in the nozzle downstream of the throat can be obtained from the expression for the area ratio:<sup>69</sup>

$$\frac{A}{A^*} = \frac{1}{M} \left[ \left( \frac{2}{\gamma + 1} \right) \left( 1 + \frac{\gamma - 1}{2} M^2 \right) \right]^{\frac{\gamma + 1}{2(\gamma - 1)}} \quad (113)$$

where  $A$  is the cross-sectional of the nozzle at measurement point downstream of the throat,  $A^*$  is the cross-sectional area of the throat,  $\gamma = C_p / C_v$  is the ratio of the heat capacity at constant pressure to the heat capacity at constant volume, and  $M$  is the Mach number. For supersonic flow, the Mach number is 1 at the throat. Assuming the flow is accelerated to a uniform Mach number, the drop in temperature  $T$  and pressure  $P$  for a given Mach number can be computed from<sup>69</sup>:

$$\frac{T_o}{T} = 1 + \frac{\gamma - 1}{2} M^2, \quad (114)$$

and

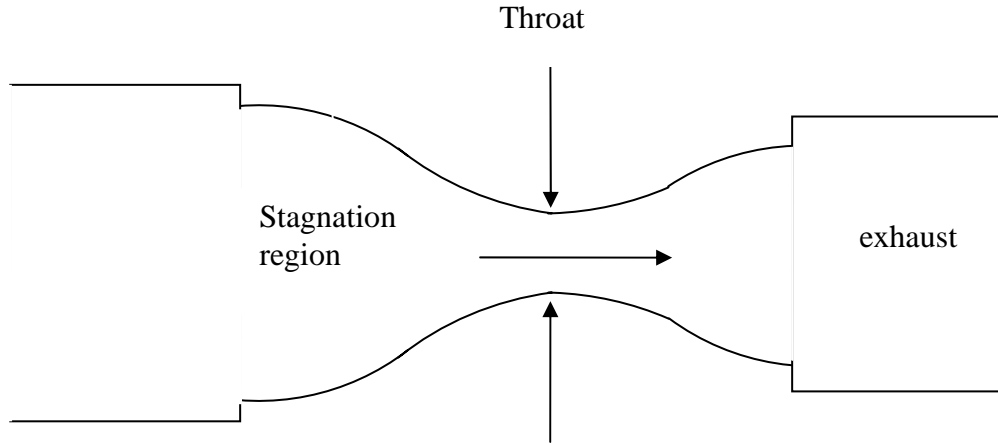


**Figure 9. Convergent/divergent nozzle.**

$$\frac{P_o}{P} = \left(1 + \frac{\gamma - 1}{2} M^2\right)^{\left(\frac{\gamma}{\gamma - 1}\right)} \quad (115)$$

where  $T_o$  is the stagnation temperature, and  $P_o$  is the stagnation pressure in the pre-expansion, stagnation region. The maximum mass flow rate occurs at the throat and is given by the expression

$$w_{\max} = A^* \sqrt{\left[ \frac{\gamma}{R} \left( \frac{2}{\gamma + 1} \right)^{\frac{\gamma + 1}{\gamma - 1}} \right] \frac{P_o}{\sqrt{T_o}}} \quad (116)$$

where  $R$  is the mass-dependent gas constant.

A laser-based temperature measurement is not expected to have exact agreement with the temperature calculated from Equation (114). Factors such as (1) flaws in the nozzle design, (2) complex phenomena such as boundary layer effects, and (3) the

introduction of heat into the flow due to the laser-excitation of  $I_2$  molecules are not assumed in the derivations of the above flow equations. Despite the simplicity of the flow model, the temperature calculated from Equation (114) does serve to assess whether or not the laser diagnostic temperature is realistic. The other formulas for  $A$ ,  $P$ , and  $w_{\max}$  were used to estimate the vacuum system requirements necessary to achieve supersonic flow in the nozzle.

### III. Theory

#### A. Spatially-Resolved Cross-Beam Doppler-Limited Saturation Spectroscopy

The idea of a saturation absorption experiment with two laser beams crossed to achieve a small interaction volume has been pursued in the past. The applications have been saturation absorption measurements in flames for determining species concentration.<sup>70-72</sup> In one experiment, the beams were crossed at right angles; and, in the other two experiments, beams were crossed at an acute angle and oriented with *counter-propagating* directional components.

##### Cross Beam Saturation Absorption Spectroscopy.

This research effort demonstrates the feasibility of extracting temperature information from a spectral profile due to two laser beams crossed at an angle and oriented with *co-propagating* directional components. A schematic for a Cross Beam Saturation Absorption Spectroscopy (CBSAS) experiment is shown in Figure 10. The probe and modulated pump beams are oriented to interact with the *non-zero* molecular velocity groups within the small volume defined by intersection of pump and probe. The beams can be reoriented to overlap at various points within the cell to provide spatial resolution not achievable in a single beam experiment where the beam must interact with the gas molecules in its path along the entire length of the cell. Thus, the CBSAS technique provides a means of correlating a Doppler-broadened spectrum with a spatial location within a gas medium.

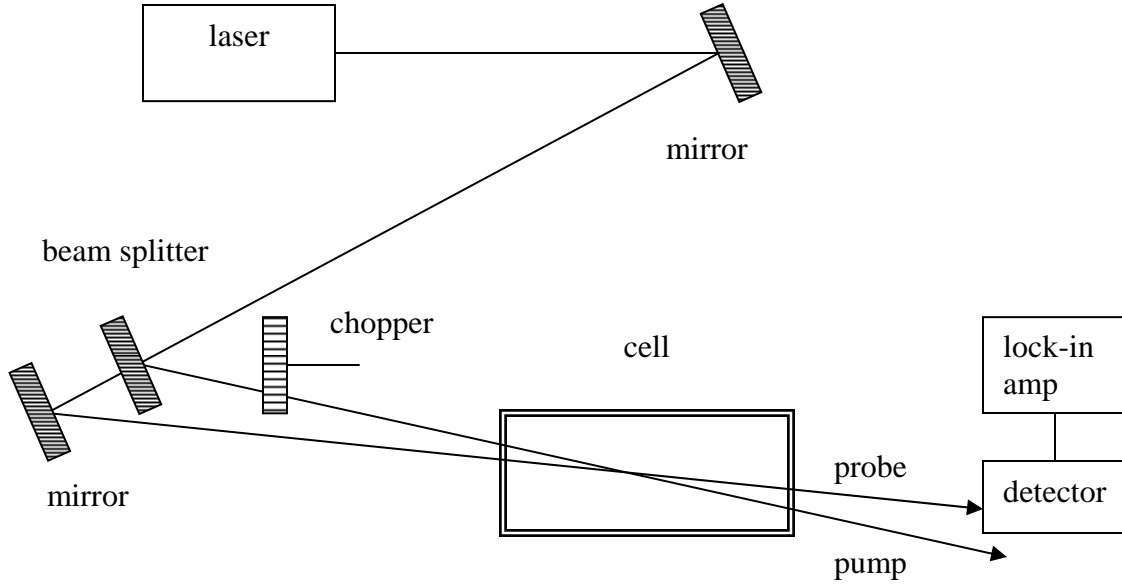


**Figure 10. Cross-Beam Saturation Absorption Spectroscopy (CBSAS) experiment.**

The signal observed at the photodiode detector can be obtained by considering Figure 11. If the direction of propagation for the probe beam is chosen to be the +z direction, then the probe interacts with molecules having a velocity components  $v_z$ . Since the pump beam crosses the probe beam at an angle, the directional component of the pump beam that lies in the +z-direction also interacts with molecules with velocity components  $v_z$ . Along the length  $L'$ , the absorption coefficient for a weak probe-beam due to the strong pump-beam component overlapping the probe beam unidirectionally is given by

$$\alpha(\nu) = \alpha_o \left( \frac{1}{\sqrt{1 + S_o}} - \frac{S_o}{2(1 + S_o)^{3/2}} \right) g(\nu) \quad (117)$$

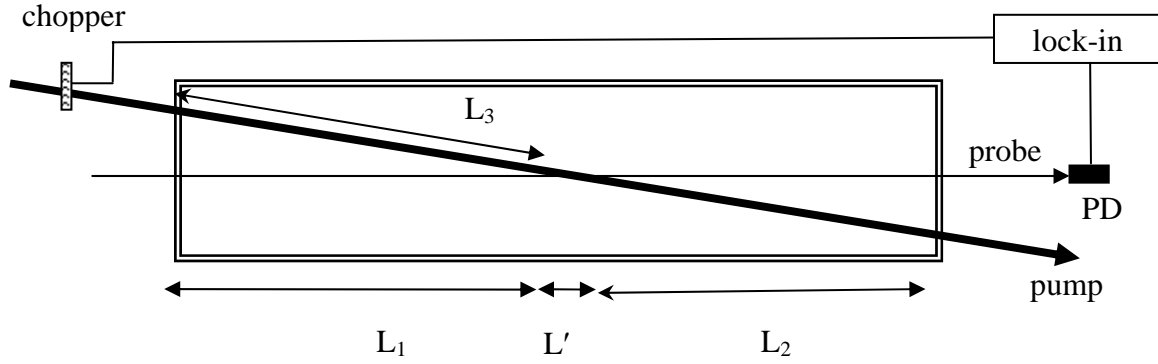


**Figure 11. CBSAS experiment showing path lengths along which self-absorption occurs:  $L_1$ ,  $L_2$ ,  $L_3$ ; and the path length,  $L'$ , for mutual interaction between the pump and probe beam.**

where  $\alpha_o$  is the unsaturated absorption coefficient with dimensions of length per unit time, and  $g(\nu)$  is the Doppler-broadened spectral profile with dimensions of time.<sup>73</sup> For  $S_o \ll 1$ , Equation (117) can be approximated by

$$\alpha(\nu) \approx \alpha_o (1 - S_o) g(\nu) \quad (118)$$

so that the change in the absorption coefficient of the probe beam due to the pump beam along length  $L'$  is

$$\Delta\alpha(\nu) = \alpha_o(\nu) - \alpha(\nu) = \alpha_o \frac{I_{pump}}{I_s} g(\nu) = \alpha' I_{pump} g(\nu). \quad (119).$$

The transmitted intensity, for a weak probe, is given by

$$I_{probe}^{trans} = I_{probe}^o \exp(-\alpha_o L_1 g(\nu) - \alpha_o L' g(\nu) + \alpha' I_{pump} L' g(\nu) - \alpha_o L_2 g(\nu)). \quad (120)$$



where  $I_{probe}^o$  is the incident intensity of the probe beam. The linear absorption of the probe beam occurs along paths  $L_1$  and  $L_2$ . Since the contribution to  $I_{probe}^{trans}$  due to  $(\alpha' I_{pump} L' g(\nu))$  is relatively small,

$$I_{probe}^{trans} \approx I_{probe}^o (1 + \alpha' I_{pump} L' g(\nu)) \exp(-(\alpha_o L_1 + \alpha_o L' + \alpha_o L_2) g(\nu)). \quad (121)$$

The pump beam intensity, chopped at frequency  $f$ , is

$$I_{pump} = I_{pump}^o (1 + \cos(\Omega t)) \exp(-\alpha_o L_3 g(\nu)) \quad (122)$$

where  $I_{pump}^o$  is the incident intensity of the pump beam, and  $\Omega = 2\pi f$ . Equation (122) is substituted into Equation (121). From  $I_{probe}^{trans}$ , the signal at the detector monitored through a lock-in amplifier at frequency  $f$  is given by

$$S_{CBSAS} = C \alpha' g(\nu) L' I_{probe}^o I_{pump}^o \exp(-k g(\nu)) = C' g(\nu) \exp(-k g(\nu)) \quad (123)$$

where  $C$  is a collection of constants related to detector efficiency,  $g(\nu)$  is the Doppler-broadened spectral profile, and  $k = \alpha_o (L_1 + L' + L_2 + L_3)$  is the absorption parameter which has units of (seconds)<sup>-1</sup>.

### Cross-Beam Inter-Modulated Fluorescence Spectroscopy.

When poor SNR was encountered with CBSAS in the supersonic nozzle measurements, a Cross-Beam Inter-Modulated Fluorescence (CBIMF) technique was used to overcome this difficulty. A schematic of the experiment is shown in Figure 12 with the two beams intersecting in a small volume within the gas cell. The laser excitation is monitored as side-fluorescence at the sum of the two chopping frequencies. The observed signal can be derived by a method similarly used for the Doppler-free IMF

signal. By analogy to Equation (106), the saturated population-density difference for two nearly co-propagating beams with different intensities can be expressed as

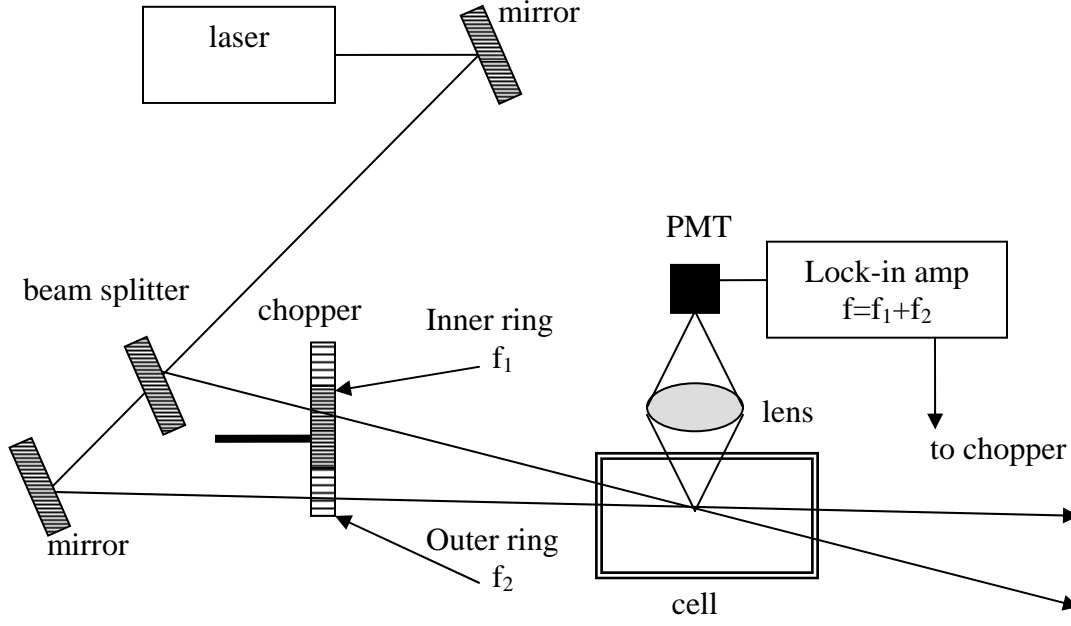


**Figure 12. Cross-Beam Inter-Modulated Fluorescence (CBIMF) experiment.**

$$\Delta N(v_z) dv_z \approx \Delta N^o(v_z) \cdot \left[ 1 - \frac{S_o^1 (\Delta v_h / 2)^2}{\left( v - v_o - v_o \frac{v_z}{c} \right)^2 + \left( \frac{\Delta v_s}{2} \right)^2} - \frac{S_o^2 (\Delta v_h / 2)^2}{\left( v - v_o - v_o \frac{v_z}{c} \right)^2 + \left( \frac{\Delta v_s}{2} \right)^2} \right] dv_z \quad (124)$$

where  $S_o^1$  and  $S_o^2$  are the saturation parameters for each of the respective beams, and

$\Delta N^o(v_z) dv_z$  is the unsaturated population-density difference containing a Maxwellian distribution. The contribution to the fluorescence intensity, analogous to Equation (109), due to molecules in the interval  $v_z$  to  $v_z + dv_z$  is

$$dI_{CBIMF}(v_z) = C \Delta N^o(v_z) \cdot \left( (I_1 + I_2) - a^* \frac{\Delta v_h / 2}{\left( v - v_o - v_o \frac{v_z}{c} \right)^2 + \left( \frac{\Delta v_s}{2} \right)^2} (I_1 + I_2)^2 \right) dv_z \quad (125)$$

where  $a^*$  is given by Equation (108). The intensities for the two chopped beams are

$$I_1 = I_1^o \exp(-\alpha_1 L_1 g(v)) (1 + \cos(\Omega_1 t)) \quad (126)$$

and

$$I_2 = I_2^o \exp(-\alpha_2 L_3 g(v)) (1 + \cos(\Omega_2 t)) \quad (127)$$

where the  $L_i$  path-lengths refer to Figure 11, the  $\alpha_i$  are absorption coefficients, and  $g(v)$  is a Doppler-broadened profile. Substituting Equations (126) and (127) into Equation (125), the signal, due to all contributing molecules, observed at the sum frequency of the two chopping frequencies is

$$S_{CBIMF}(v) = C' a^* \Delta N^o I_1^o I_2^o \exp(-\alpha_1 g(v) L_1 - \alpha_2 g(v) L_3) \cdot \int_{-\infty}^{\infty} \exp\left(-\left(\frac{v_z}{v_p}\right)^2\right) \cdot \frac{\Delta v_h / 2}{\left( v - v_o - v_o \frac{v_z}{c} \right)^2 + \left( \frac{\Delta v_s}{2} \right)^2} dv_z \cdot \quad (128)$$

For conditions where the Doppler width is much larger than the homogeneous width and  $S_o \ll 1$ , the Lorentzian lineshape can be approximated as a delta function so that Equation (128) can then be expressed as

$$S_{CBIMF}(v) = C' a^* \Delta N^o I_1^o I_2^o \exp(-\alpha_1 g(v) L_1 - \alpha_2 g(v) L_3) \cdot \int_{-\infty}^{\infty} \exp\left(-\left(\frac{v_z}{v_p}\right)^2\right) \cdot \delta\left(v - v_o - v_o \frac{v_z}{c}\right) dv_z \cdot \quad (129)$$

The remaining integral can be solved so that the CBIMF signal is

$$S_{CBIMF}(\nu) = C'' a^* \Delta N^o I_1^o I_2^o g(\nu) \exp(-k g(\nu)) = C''' g(\nu) \exp(-k g(\nu)) \quad (130)$$

where  $k = (\alpha_1 L_1 + \alpha_2 L_3)$ . Equation (130) for the CBIMF signal has the same form as Equation (123) for the CBSAS signal.

Finally, while making CBSAS measurements, it is possible to simultaneously observe the side fluorescence due only to the modulated pump-beam (Modulated Pump Side Fluorescence (MPSF)). For  $S_o \ll 1$ , and small  $\alpha_s L$ , the signal is

$$S_{MPSF}(\nu) = C I^{pump} [1 - \exp(-\alpha_s(\nu) L)] \cong C I^{pump} \alpha_s(\nu) L \quad (131)$$

where  $\alpha_s(\nu)$ , for a low pressure gas, is given by Equation (98) so that

$$S_{MPSF}(\nu) = C L I^{pump} \alpha_s(\nu) = C L I^{pump} \frac{\alpha_o(\nu_o)}{\sqrt{1 + S_o}} \exp \left\{ - \left( \frac{c(\nu - \nu_o)}{\nu_o \nu_p} \right)^2 \right\} \quad (132)$$

for a single Doppler-broadened transition.

## B. Spectral Profiles for I<sub>2</sub> Ro-vibrational Lines

To represent the spectral profile for a single, isolated I<sub>2</sub> ro-vibrational line obtained from a cross-beam experiment, it is necessary to use a theoretical profile composed of a sum of Gaussian lineshapes with resonant frequencies and intensities determined by the hyperfine structure of the I<sub>2</sub> ro-vibrational line.

For a low-pressure I<sub>2</sub> vapor, the theoretical profile  $g_D(\nu)$  consists of a sum of 15 or 21 Gaussian lineshapes corresponding to the number of hyperfine lines composing the ro-vibrational line yielding

$$g_D(\nu) = A \sum_{i=1}^{15 \text{ or } 21} G(\nu; f_i^{hyp}, \nu_{oi}, \Delta \nu_D). \quad (133)$$

where  $A$  is amplitude parameter for the profile,  $G$  indicates a Gaussian lineshape as defined in Equation (59),  $\nu$  is the frequency,  $f_i^{hyp}$  is the relative intensity of the  $i^{\text{th}}$  hyperfine line, the  $\nu_{oi}$  are the hyperfine resonant frequencies constrained to the relative hyperfine energy-splittings, and the Doppler width  $\Delta \nu_D$  is chosen to be the same for all hyperfine lines.

Using Equation (133), the  $\text{I}_2$  spectral data from a cross-beam experiment (either CBSAS or CBIMF) was fit with the theoretical signal

$$S_{CB}(\nu) = g_D(\nu) \cdot \exp(-k \cdot g_D(\nu)) + a \cdot \nu + b. \quad (134)$$

The parameter  $k$  in Equation (134) is required to model the self-absorption of the laser beam(s) by the  $\text{I}_2$  vapor. A linear baseline is represented by the parameters  $a$  and  $b$ . The commercial curve-fitting software programs, PeakFit<sup>®</sup> and Tablecurve<sup>®</sup>, were used to calculate the nonlinear least-squares fit of Equation (134) to the data. The value for the Doppler width obtained from the fit was used in Equation (61) to compute the corresponding temperature of the  $\text{I}_2$  vapor within the small volume defined by the crossed laser beams.

The theoretical signal predicted by Equation (134) for a single, isolated  $\text{I}_2$  ro-vibrational line with a 15-line hyperfine spectrum is shown in Figure 13 for different temperatures (i.e., Doppler widths). As the temperature decreases, the ro-vibrational spectral profile resolves into the individual Doppler-broadened hyperfine spectral lines. Statistically, the nonlinear least-squares fit of  $S_{CB}(\nu)$  to cross-beam spectral data is

expected to improve with decreasing temperature. At room temperature and higher, the spectral profile is a broad and relatively featureless. More than one set of parameters could produce a reasonable fit. At temperatures well below 300 K, there are more features present in the spectral profile which increases the likelihood that only one set of parameters could result in a fit to such a unique profile. The theoretical signal predicted by Equation (134) for a single, isolated I<sub>2</sub> ro-vibrational line with a 21-line hyperfine spectrum is shown for several temperatures in Figure 14.

To analyze “blended” ro-vibrational line spectra consisting of two, overlapped ro-vibrational lines, it was necessary to create a program in Mathematica<sup>®</sup>. The commercial curve-fitting software programs, PeakFit<sup>®</sup> and Tablecurve<sup>®</sup>, used to fit the isolated ro-vibrational line profiles lacked the capability to accommodate a sum of 30 or more Gaussian lineshapes. Therefore, a Mathematica<sup>®</sup> program was developed to fit a theoretical signal to the blended-line spectral data and provide fit parameters with standard errors. As with the isolated lines, the temperature was extracted from the common Doppler width of the hyperfine lines. For two overlapped ro-vibrational lines, labeled line *A* and line *B*, the blended-line theoretical signal has the form

$$S_{CB}(\nu) = (g^A(\nu) + g^B(\nu)) \cdot \exp(-k \cdot (g^A(\nu) + g^B(\nu))) + a \cdot \nu + b \quad (135)$$

where

$$g^A(\nu) = A^A \sum_{i=1}^{15 \text{ or } 21} G\left(\nu; (f_i^{hyp})^A, \nu_{oi}^A, \Delta \nu_D\right), \quad (136)$$

and

$$g^B(\nu) = A^B \sum_{i=1}^{15 \text{ or } 21} G\left(\nu; (f_i^{hyp})^B, \nu_{oi}^B, \Delta \nu_D\right) \quad (137)$$

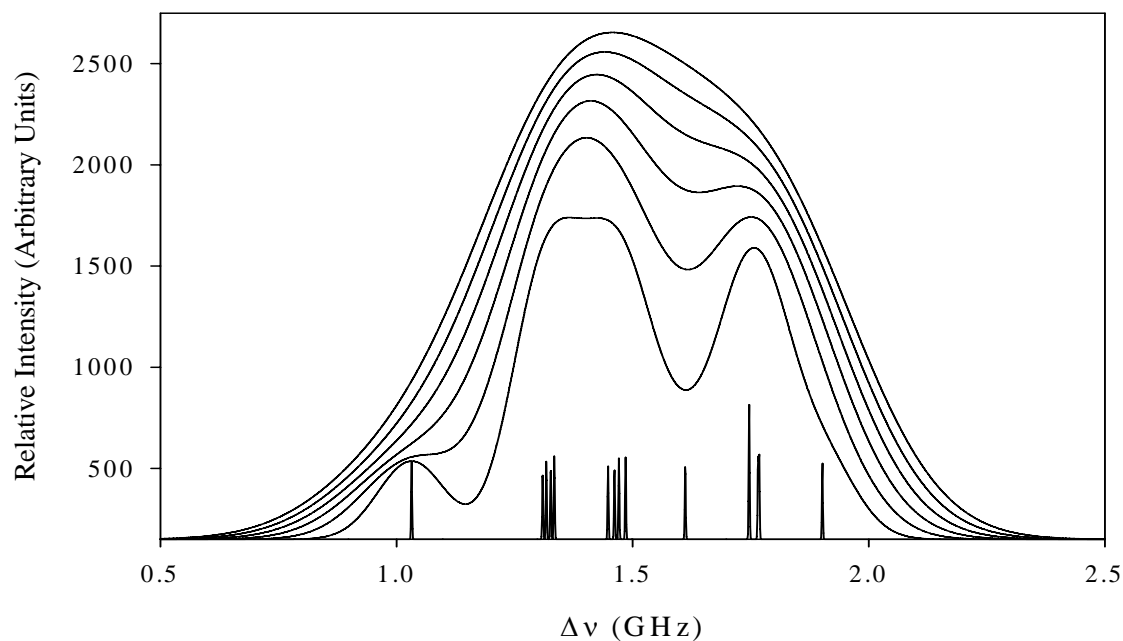


**Figure 13. Theoretical spectral profile of P(46) 17-1 for various temperatures. In order of decreasing linewidth, the profile temperatures are 298 K, 250 K, 200 K, 150 K, 100 K, 50 K, 0.01 K.**

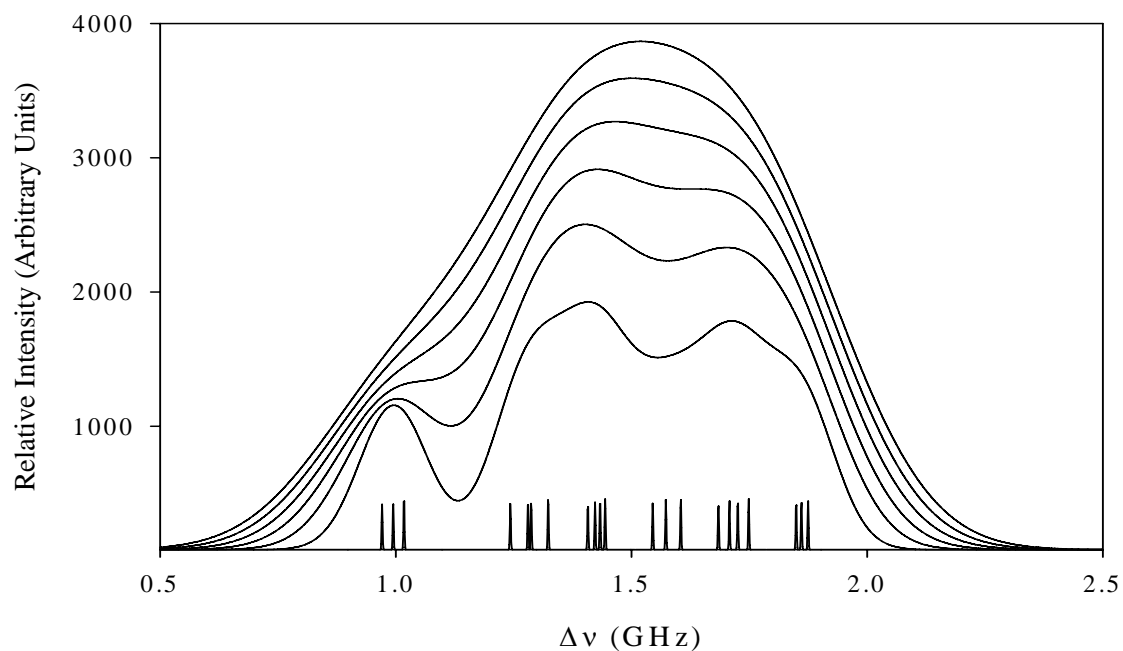


**Figure 14. Theoretical spectral profile of P(53) 19-2 for various temperatures. In order of decreasing linewidth, the profile temperatures are 298 K, 250 K, 200 K, 150 K, 100 K, 50 K, 0.01 K.**

in which  $A^{A,B}$  is the amplitude parameter and  $f_i^{A,B}$  are the relative hyperfine intensities;  $k$  is the absorption parameter, and  $a \cdot \nu + b$  is a linear baseline. The sum of the two theoretical profiles,  $g^A(\nu) + g^B(\nu)$ , is needed in the exponential term of Equation (135) to account for the absorption of the laser beams along the distances in the vapor cell leading to (or from) the crossing volume due to both ro-vibrational lines in the frequency range where the two ro-vibrational lines overlap.

The temperature information contained in the amplitudes of two overlapped spectral lines can be explicitly incorporated into the theoretical signal. The amplitude parameter has a direct dependence on the Boltzmann factor. This allows the possibility of simultaneously constraining the theoretical signal to the temperature dependence in the Boltzmann factor for each of the two overlapped ro-vibrational lines and to the temperature dependence in the Doppler linewidth. The amplitude parameter is also proportional to the Franck Condon factor which can be used to constrain the amplitudes of the two overlapped ro-vibrational lines relative to one another.



### III. Experiments and Results

#### A. Doppler Free Laser Spectroscopy

As discussed in the theory section, the theoretical signal used to fit an  $I_2$  ro-vibrational spectral profile is constructed from the hyperfine spectrum of the ro-vibrational line. To better understand the physical phenomena that affect the hyperfine spectrum and to ascertain the impact of these influences on the temperature diagnostic, several experiments were performed using Doppler-free spectroscopy techniques. The results presented consist of (1) a comparison of Doppler free spectra obtained from two different spectroscopic techniques, (2) the influence of velocity-changing collisions, (3) self-absorption of the interrogating laser beams in the  $I_2$  vapor, and (4) the pressure broadening of  $I_2$  due to a buffer gas of Ar.

##### Experiment.

The Doppler-free Saturation Absorption Spectroscopy (SAS) experiment utilized a Coherent 899-21 ring laser configured for dye operation. The pump source for the dye laser was a Spectra Physics Beam-Lok model 2080-15 Ar-Ion Laser operating at 514.5 nm. The dye laser utilized Rhodamine 590 laser dye, from Exciton, Inc., to provide wavelength coverage from 553 to 615 nm with maximum output power at 590 nm. A typical Ar-Ion laser power was 6 W. The dye laser power varied from 300-500 mW.

The experiment was performed by splitting the output beam from the Coherent 899-21 laser into two beams: a high-power pump beam and a low-power probe beam. The two beams were then directed counter-propagating through a glass cell containing  $I_2$

vapor so that the beams overlapped along the axial length of the cell. A set-up schematic for the Doppler-free saturation absorption experiment in a pressure-variable cell is shown in Figure 15. The transmitted probe beam intensity was detected with a Hamamatsu S2281, BNC-connector type, Silicon photodiode. Simultaneously, the side fluorescence, from the Doppler-limited laser excitation due to the modulated pump beam was collected with a Burle C31034A02 Photomultiplier Tube (PMT) via a fiber optic with a shuttered lens positioned above the midpoint of the cell. The signal from each detector was filtered through a Stanford Research Systems Model SR850 lock-in amplifier referenced to the frequency of a Stanford Research Systems SR540 optical chopper.

The dye laser is frequency-tuned by computer through Coherent's Autoscan software package. The filtered signals from the lock-in amplifiers were routed to the Autoscan system to display the real-time signals during a frequency scan, and to record the spectral profile data on computer disk. Autoscan allows the user to set the scan start wavelength and adjust the following three parameters: (1) the data interval, in MHz, between each recorded data point, (2) the segment scan time in seconds/10 GHz, (3) the scan distance in GHz. A typical set of parameters for a Doppler free 15-line hyperfine spectrum of a single ro-vibrational line scan is: (1) .04 MHz data interval, (2) 1000 s/10 GHz segment scan time, (3) a scan distance of 1.1 GHz. For these particular settings, 30,000 data points were generated for a scan time of 1.83 minutes.

The Pyrex<sup>®</sup> glass cell was equipped with quartz windows; each cut at the 590 nm Brewster's angle for optimal optical transmission. The cell length along the beam path was 41.5 cm. The maximum cell width was 4 inches. All connections of periphery

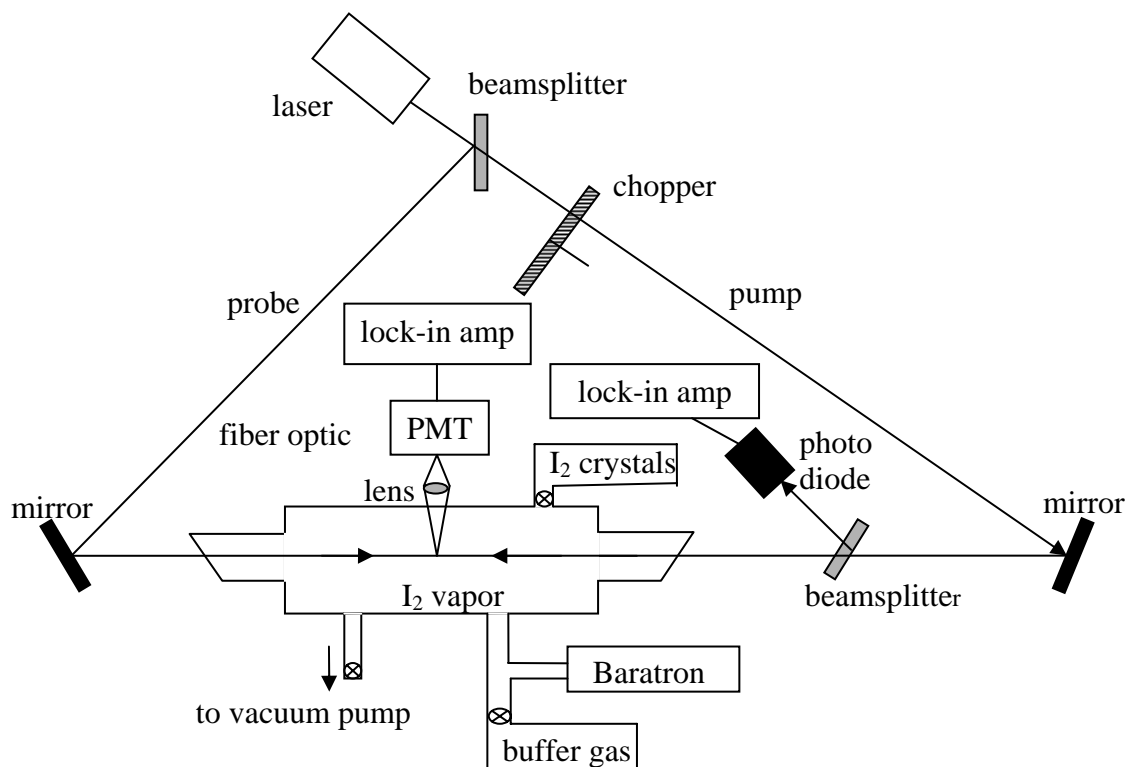


**Figure 15. Schematic for Doppler-Free Saturation Absorption Spectroscopy Experiment.**

equipment to the cell ports were made with Cajon<sup>®</sup> fittings incorporating Viton<sup>®</sup> O-rings. The total cell pressure was measured with a MKS 390HA (1 Torr) pressure transducer, or when necessary with a MKS 690A (1000 Torr) pressure transducer. The transducer signal was processed and readout provided by a MKS Type 270 Signal Conditioner. The cell was evacuated with an Alcatel 2015 C2 rotary vane pump having a maximum speed of 10.6 cubic feet per minute (cfm), and ultimate pressure of  $10^{-3}$  Torr. I<sub>2</sub> vapor was leaked into the cell from a side-arm tube containing 5-10 g of I<sub>2</sub> crystals (Alfa Aesar, 99.5% purity).<sup>74</sup>

Inter-Modulated Fluorescence Spectroscopy (IMF) was performed with the same set-up except the chopper was repositioned so that the outer ring of slots in the chopper

wheel intersected one beam, and the inner ring, with a different number of the slots, intersected the other beam. The fluorescence signal was detected with the PMT which was then filtered through the lock-in amplifier referenced to the sum of the inner- and outer-ring chopping frequencies.

## Results.

### *Doppler-Free Spectra of $I_2$ Ro-vibrational Lines.*

Doppler-Free spectra collected with SAS and IMF for  $I_2$  P(12) 17-1, and  $I_2$  P(130) 17-1 are shown in Figure 16 - Figure 19. For these measurements, there are a few differences in the set-up as shown in Figure 15. All of these spectra were collected from the vapor of a few  $I_2$  crystals *sealed* in a glass cell six inches long and one inch in diameter as opposed to the pressure variable cell in Figure 15. Also, the fiber optic leading to the PMT was not used. The PMT, with a shuttered lens, was mounted directly above the glass cell for maximum SNR. For both the SAS and IMF experiments,  $I_{pump}$  was 40 mW, and  $I_{probe}$  was 10 mW.

Each of the four graphs shows 15-line hyperfine spectra of a single ro-vibrational line. The hyperfine lines are labeled according to an established convention.<sup>75</sup> Some of the hyperfine lines were not resolved due to the limit imposed by the dye laser linewidth which was  $\geq 500$  kHz. Even so, a comparison of the low  $J$  spectra to the high  $J$  spectra reveals the variation in the hyperfine resonant frequencies with  $J$ , the rotational quantum number, as expected from the theory. Also, a comparison of the SAS spectra to the IMF spectra shows the improvement of IMF over SAS in terms of the signal-to-noise ratio. The 21-line hyperfine spectrum for P(53) 19-2 is shown in Figure 20 in which all but two

of the hyperfine lines are completely resolved. Finally, the overlapping hyperfine spectra of P(51) 18-2 and P(66) 16-1 are shown Figure 21 as recorded in an IMF experiment. The high-frequency hyperfine components of the 21-line P(51) 18-2 spectrum overlap the low-frequency hyperfine component of the 15-line P(66) 16-1 spectrum. The overlapped spectra serve to illustrate a phenomenon discussed in the next section.

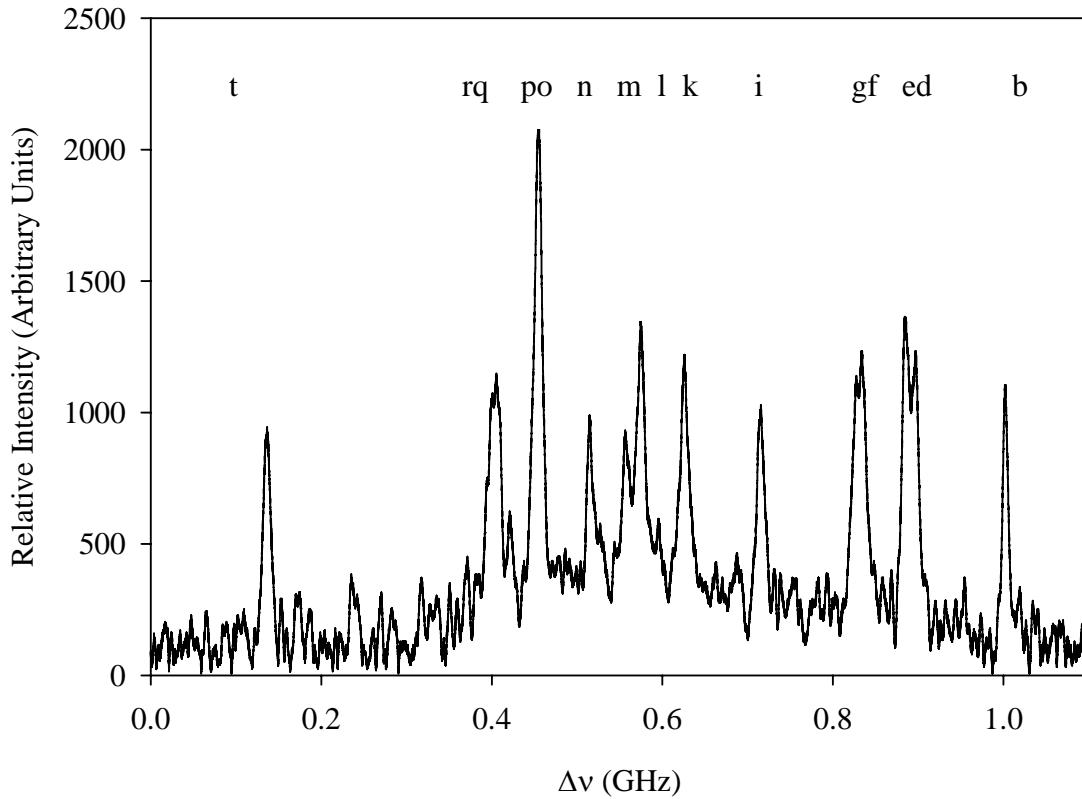


**Figure 16.  $I_2$  P(12) 17-1 hyperfine spectrum from Doppler-free SAS.**

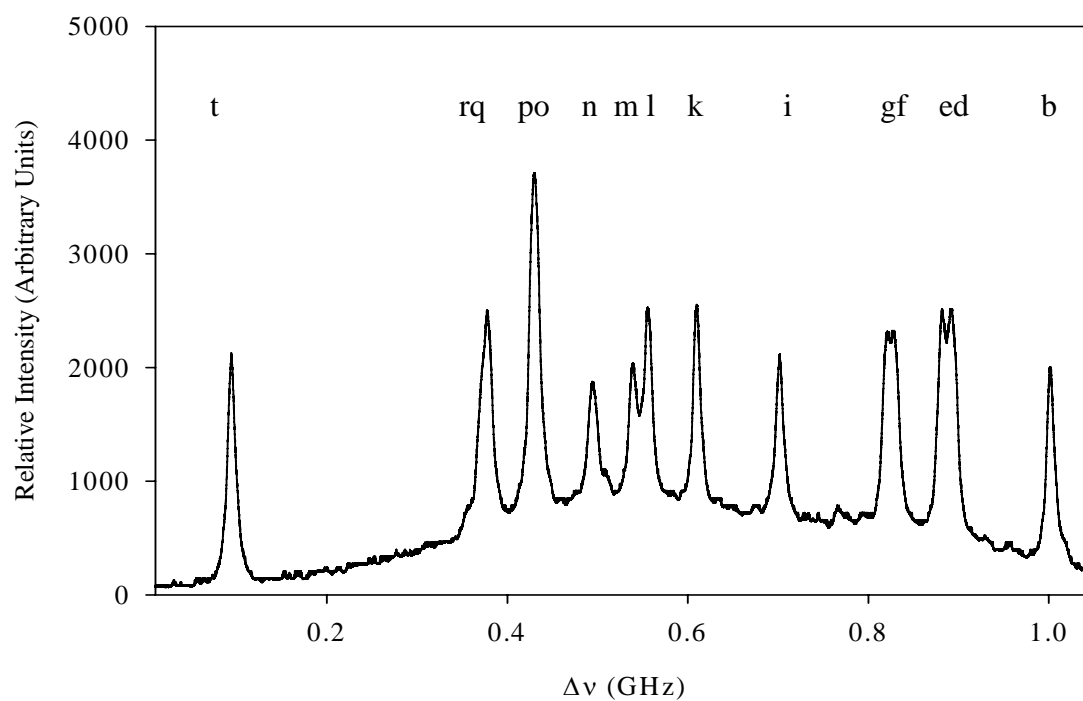


**Figure 17.  $I_2$  P(12) 17-1 hyperfine spectrum from Doppler-free IMF.**

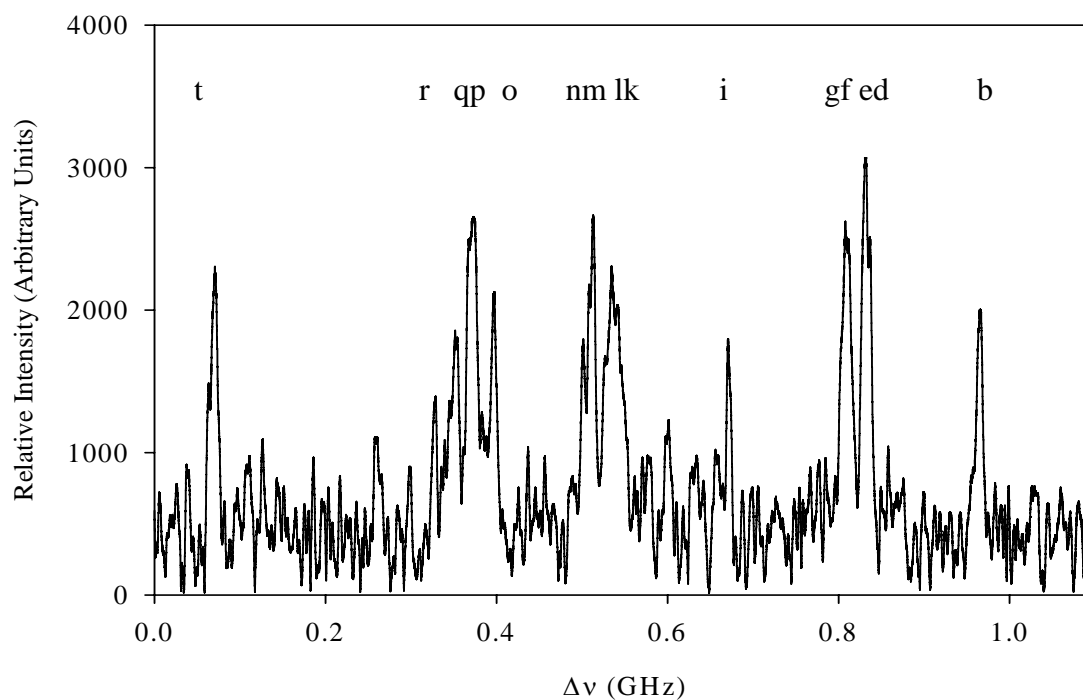


**Figure 18.  $I_2$  P(130) 17-1 hyperfine spectrum from Doppler-free SAS.**

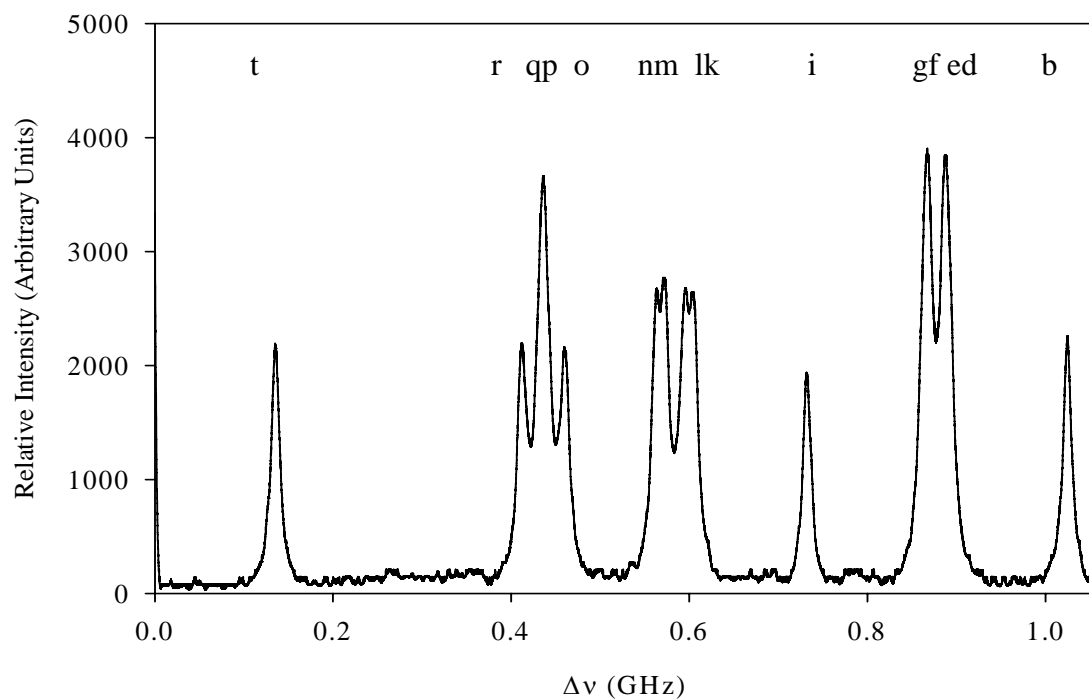


**Figure 19.  $I_2$  P(130) 17-1 hyperfine spectrum from Doppler-free IMF.**

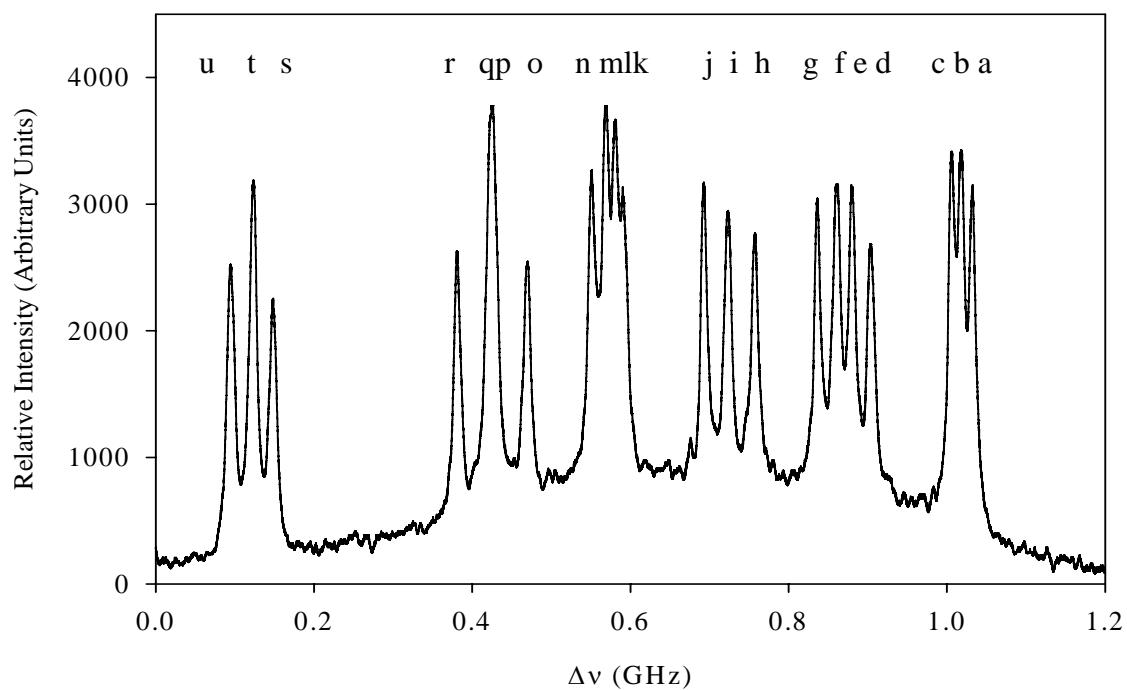


**Figure 20.  $I_2$  P(53) 19-2 hyperfine spectrum from Doppler-free IMF.**

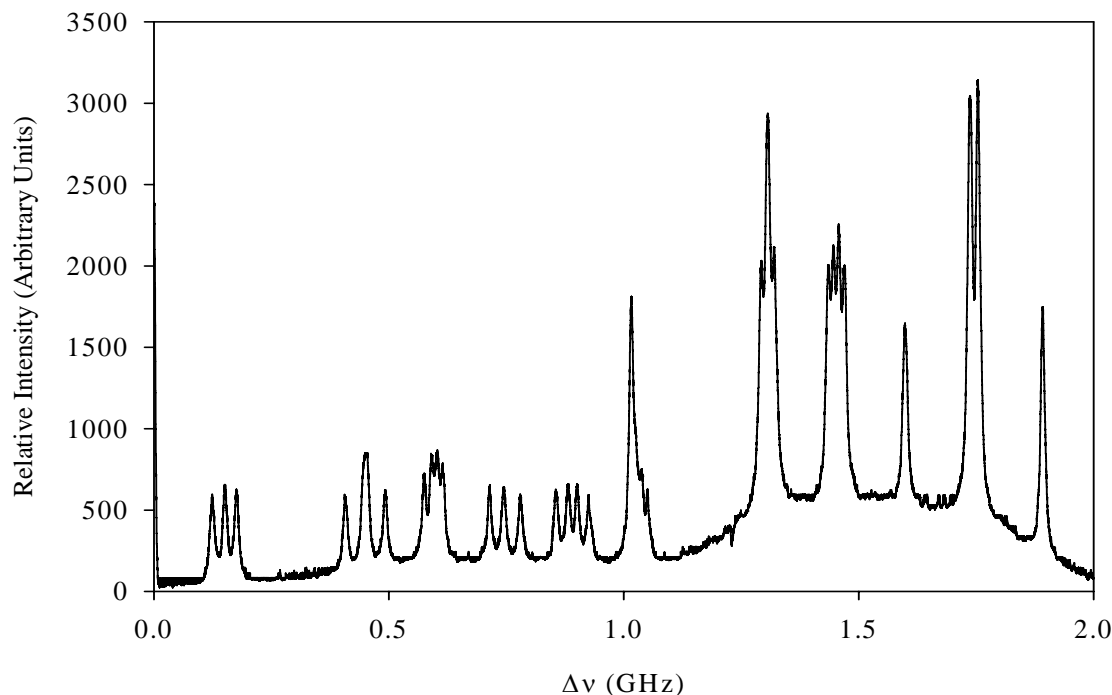


**Figure 21.**  $\text{I}_2$  P(51) 18-2 & P(66) 16-1 blended line from Doppler-free IMF. The 21-line P(51) 18-2 spectrum is on the left and the 15-line P(66) 16-1 spectrum is on the right. The hyperfine spectra overlap at approximately 1.0 GHz.

#### *Velocity Cross Relaxation.*

Doppler-free experiments reveal a pronounced baseline pedestal in the hyperfine spectra of some ro-vibrational lines. For example, this pedestal is noticeable in the P(12) 17-1 spectrum of Figure 17, but is negligible in the P(130) 17-1 spectrum of Figure 19. In Figure 22, the low  $J$  hyperfine spectrum of R(37) 15-0 (on the left) is shown overlapping the high  $J$  spectrum of R(127) 19-1 (on the right). This data was collected using the SAS set-up and cell of Figure 15 (a buffer gas was not used) at a chopping frequency of 1000 Hz. It is easily observed that the low- $J$  hyperfine spectrum has a pronounced pedestal and the high  $J$  hyperfine spectrum is essentially devoid of one. The R(37) 15-0 & R(127) 19-1



blended line is shown again in Figure 23 where the SAS data was collected at a chopping frequency of 3750 Hz. The increase in chopping frequency reduced the magnitude of the pedestal in the low  $J$  hyperfine spectrum. The Modulated Pump-Beam Side-Fluorescence (MPSF) data in Figure 22 is a portion of the Doppler-limited spectrum of the two overlapping ro-vibrational lines. It is the fluorescence signal from the chopped pump beam as detected with the PMT shown in Figure 15.

### *Self Absorption.*

The intensities of the hyperfine lines are important for the temperature diagnostic. In the model used to fit to the spatially-resolved spectral data, the 15 or 21 hyperfine lines are constrained to their statistically-weighted relative intensities. Experimental evidence shows deviation from these expected intensities in some instances. Compare the P(70) 17-1 hyperfine and MPSF profiles in Figure 24 at an  $I_2$  pressure of 80 mTorr to those in Figure 25 collected at an  $I_2$  pressure of 200 mTorr. At the higher pressure, the hyperfine spectrum shows an increase in the spectral line intensities in the wings. There is also a noticeable flattening of the MPSF profile at 200 mTorr. The effect is attributed to the linear absorption of the beams as they pass through the  $I_2$  vapor. This self-absorption increases as the laser is tuned to the center of the ro-vibrational line resonance.

From these observations, it was apparent that an absorption term needed to be included in the theoretical signal. Using the set-up of Figure 15, MPSF profiles were collected at various  $I_2$  pressures. Each of these profiles was fitted with the theoretical profiles shown in Equation (134) in which the Doppler width was held constant since all the measurements were performed at room temperature. The common profile for the

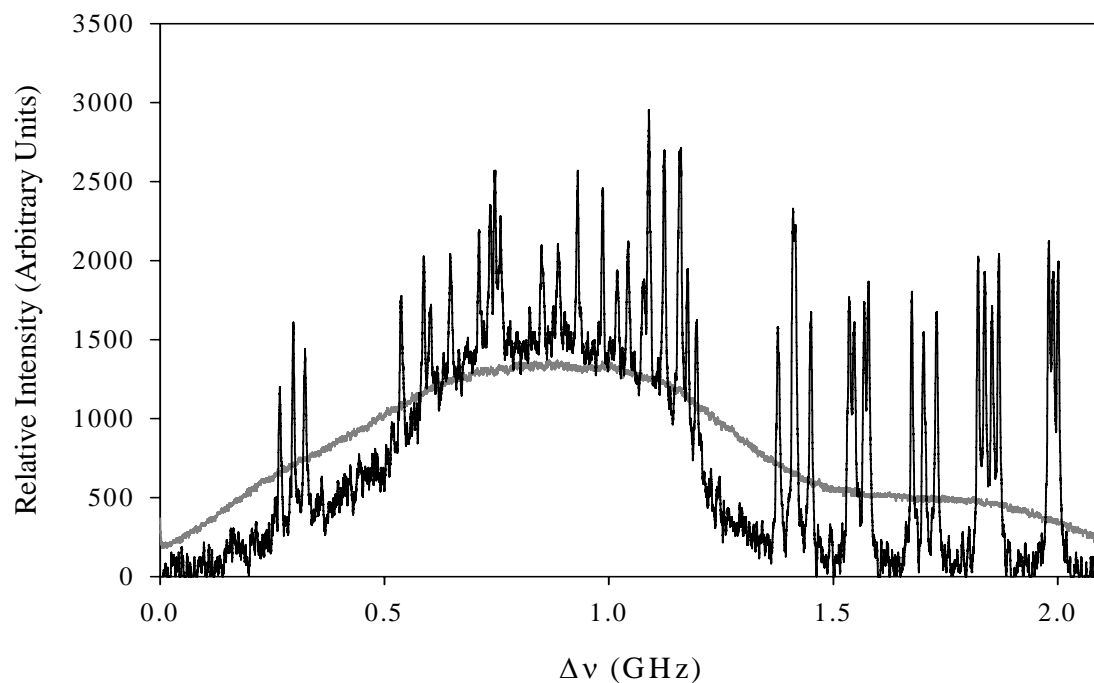


**Figure 22.** I<sub>2</sub> hyperfine spectrum (black) for R(37) 15-0 & R(127) 19-1 blended line from SAS with 1000 Hz chopping frequency. The Doppler-broadened MPSF profile (gray) is also shown.

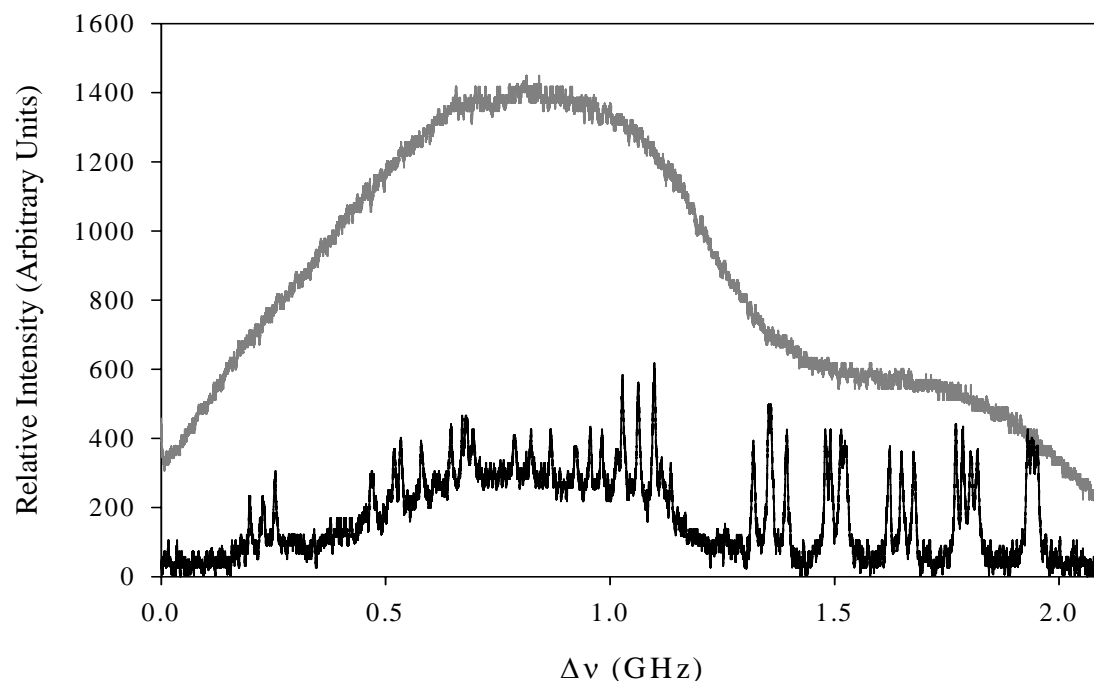


**Figure 23.** I<sub>2</sub> hyperfine spectrum (black) for R(37) 15-0 & R(127) 19-1 blended line from SAS with a 3750 Hz chopping frequency. The Doppler-broadened MPSF profile (gray) is also shown.

hyperfine lines was Gaussian because  $P_{I_2}$  was sufficiently low,  $< 0.31$  Torr, that Voigt profiles could not provide a better fit. A plot of the absorption parameter,  $k$  from Equation (134), versus  $P_{I_2}$  is shown in Figure 26 for the  $I_2$  P(70) 17-1 ro-vibrational line. A linear regression with the y intercept forced to zero gives a slope of  $(2.66 \pm 0.03) \times 10^{-4} \text{ (s Torr)}^{-1}$ . For the regression analysis, each data point was weighted according its standard error. The deviation from linearity at low pressure is due primarily to the poor SNR in the data and the difficulty fitting to it.

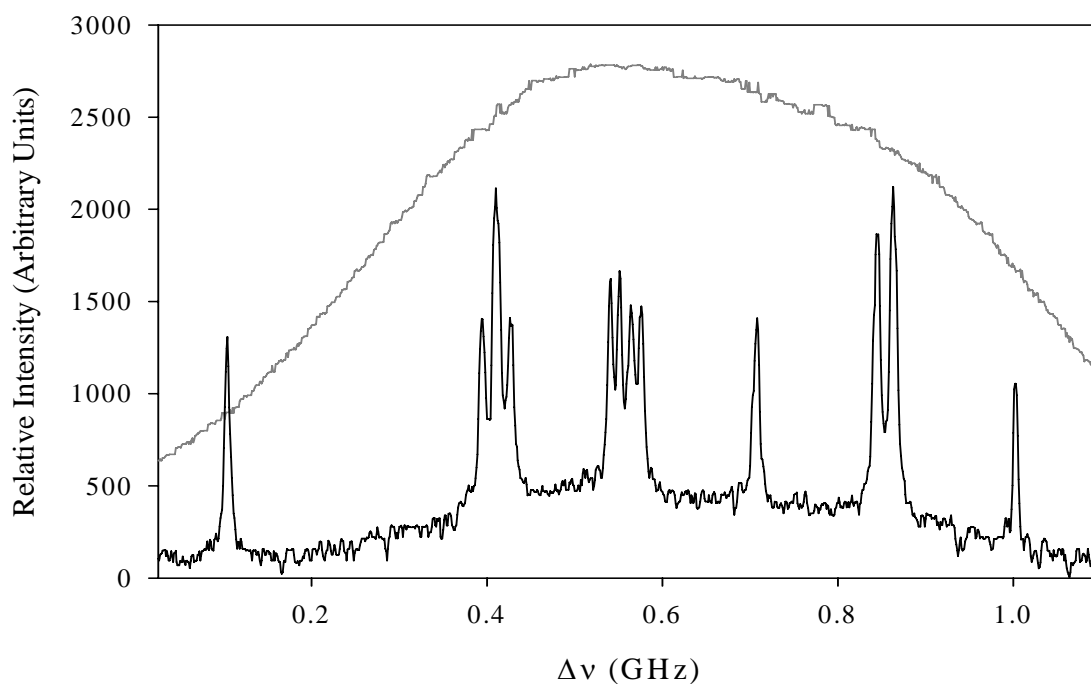


**Figure 24.  $I_2$  P(70) 17-1 hyperfine (black) spectrum from SAS, and MPSF (gray) Doppler-broadened profile at an  $I_2$  pressure of 80 mTorr.**

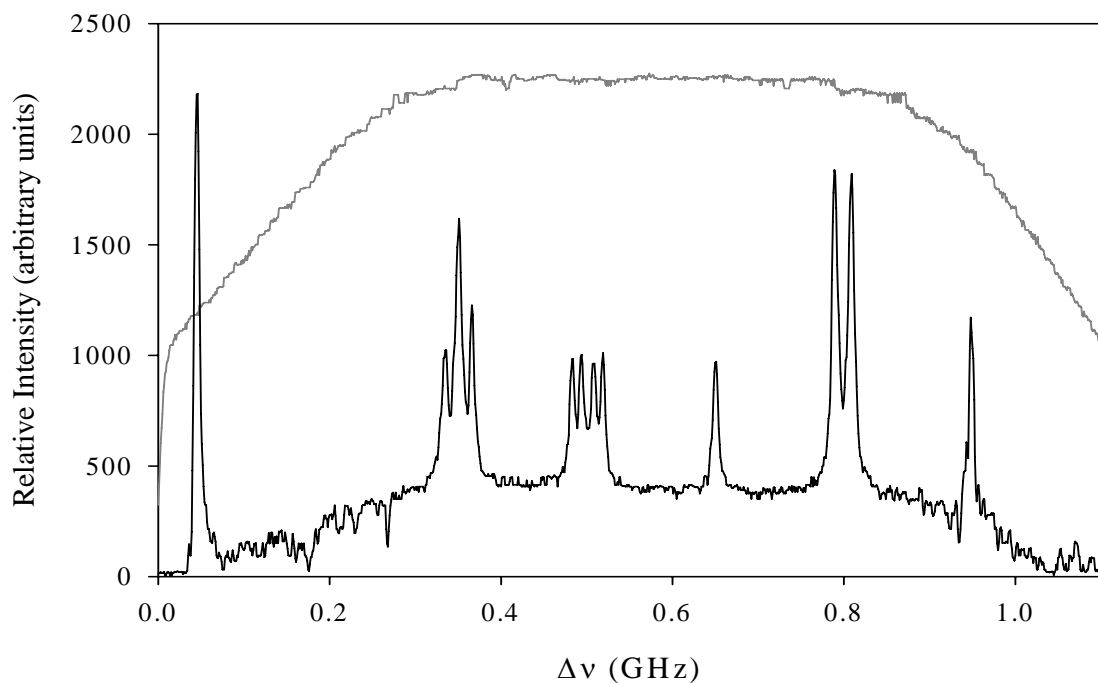


**Figure 25.**  $I_2$  P(70) 17-1 hyperfine (black) spectrum from SAS, and MPSF (gray) Doppler-broadened profile at an  $I_2$  pressure of 200 mTorr.

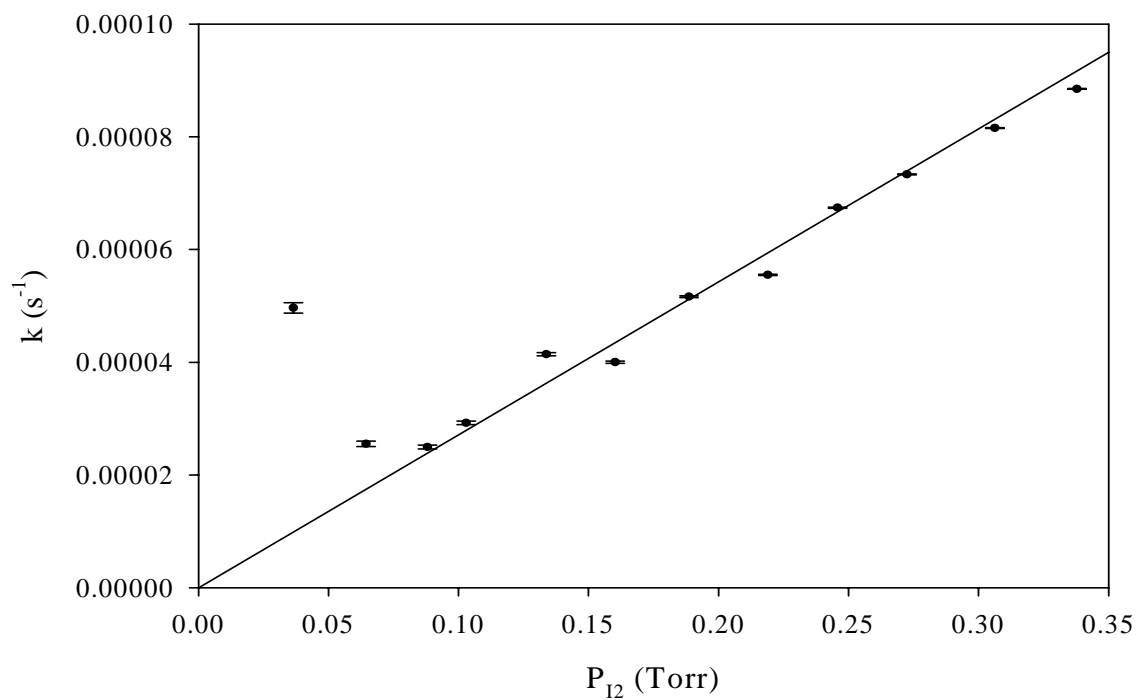


**Figure 26.** Absorption parameter as a function of  $I_2$  pressure for P(70) 17-1.

### *Ar Pressure Broadening of $I_2$ .*

For the purposes of the temperature diagnostic, pressure broadening of the hyperfine linewidth may need to be accounted for in the construction of the theoretical profile. The profile of Figure 27 shows the  $I_2$  P(70) 17-1 hyperfine spectrum obtained from SAS and a portion of the side fluorescence profile from MPSF for an  $I_2$  pressure of 0.1635 Torr. The hyperfine spectrum in Figure 28 was collected at the same  $I_2$  pressure with 0.9508 Torr of added Ar buffer gas. The effects of broadening by the buffer gas are evident in the hyperfine spectrum of Figure 28 where the individual components are less resolved and reduced in intensity. There is no discernable change in the shape of the MPSF profile. A series of Doppler-free profiles for  $I_2$  P(70) 17-1 were collected at various Ar buffer gas pressures for a fixed  $I_2$  pressure of 0.1635 Torr. Each hyperfine spectrum was fitted with 15 Lorentzian lineshapes constrained to share the same width. A broad Gaussian lineshape was also included in the fit to account for the baseline pedestal. The variation in hyperfine linewidth as a function Ar buffer gas pressure is shown in Figure 29. Linear regression resulted in a pressure broadening rate of  $8.29 \pm 0.30$  MHz/Torr. The y-intercept gave a zero-Ar-pressure linewidth of  $8.70 \pm 0.17$  MHz. The pressure broadening effects were also obtained for the  $I_2$  P(10) 17-1 line. The variation in hyperfine linewidth as a function Ar buffer gas pressure is shown in Figure 30. Linear regression gave a pressure broadening rate of  $10.70 \pm 0.41$  MHz/Torr. The y-intercept gave a zero-Ar-pressure linewidth of  $7.74 \pm 0.10$  MHz.

Measurements of the hyperfine spectral width at Ar pressures higher than 1 Torr were not possible due to the low SNR. For Ar pressures greater than 1 Torr,

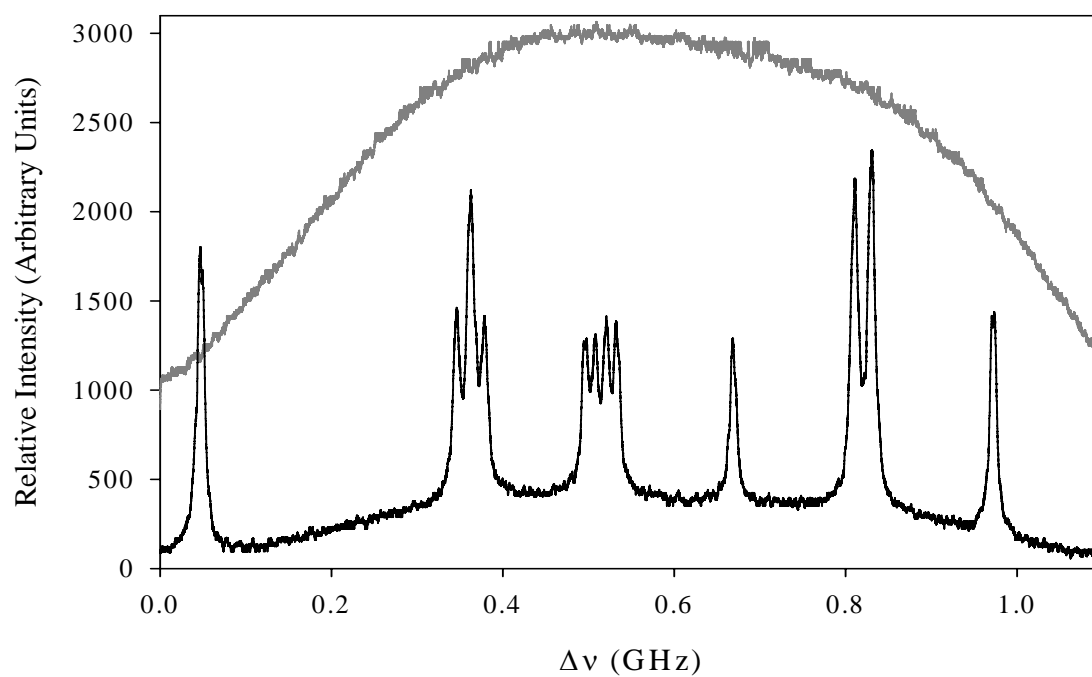


**Figure 27. SAS (black) and MPSF (gray) spectra of P(70) 17-1 at 0.1635 Torr I<sub>2</sub> pressure.**

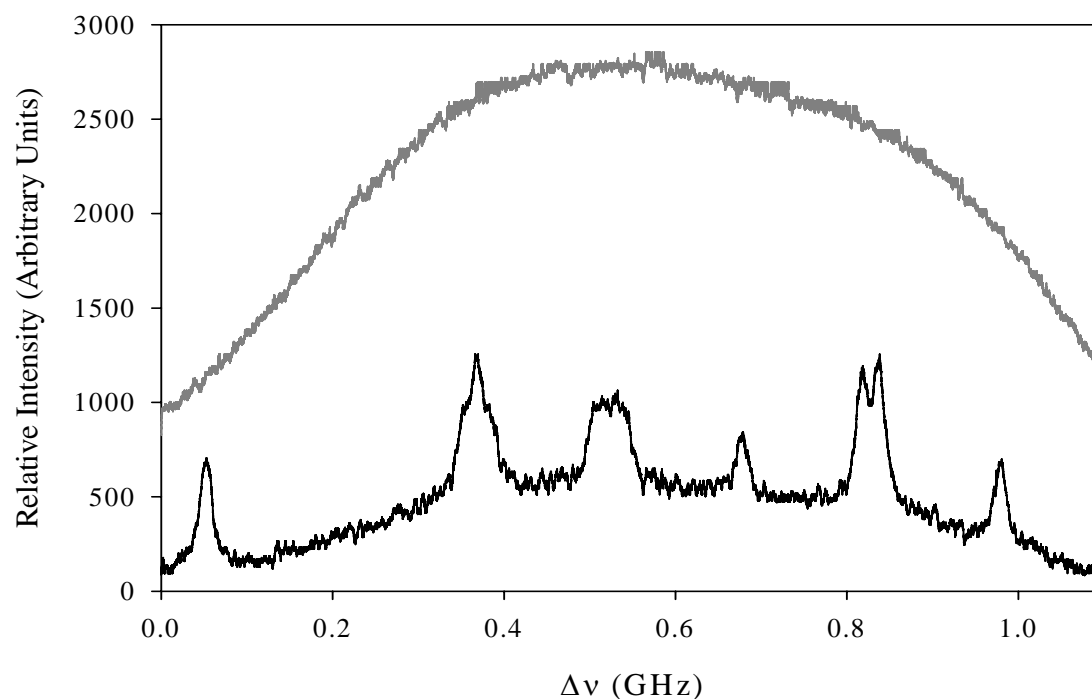


**Figure 28. SAS (black) and MPSF (gray) spectra of P(70) 17-1 at 0.1635 Torr I<sub>2</sub> pressure and 0.9508 Ar buffer gas pressure.**

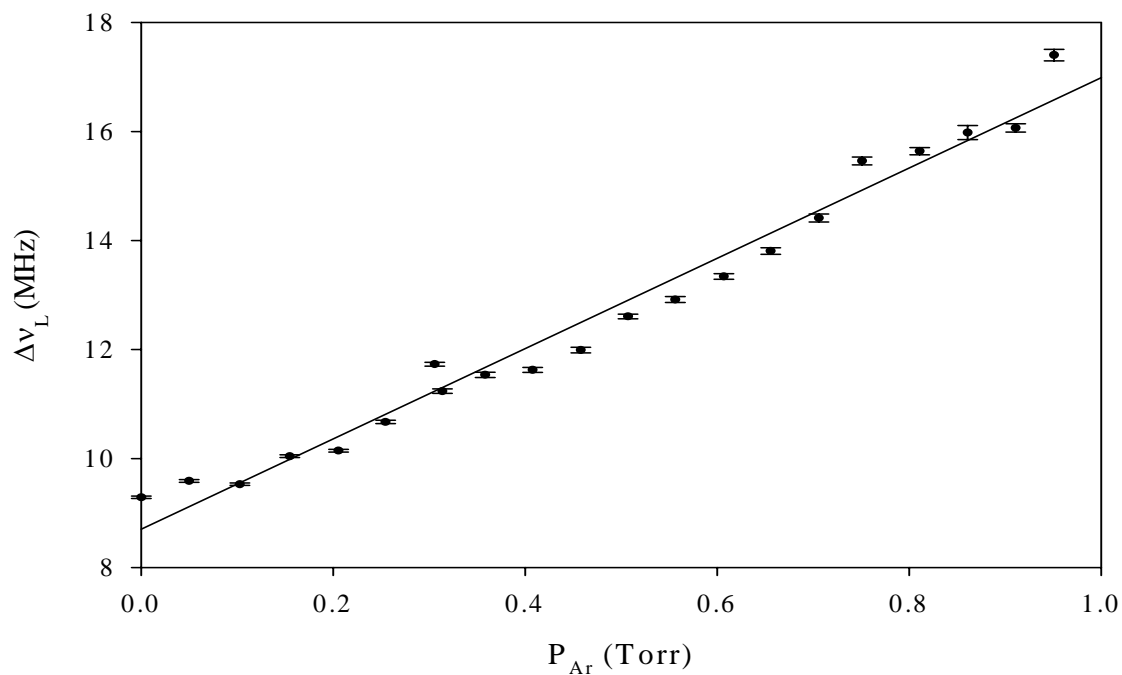


**Figure 29.  $I_2$  P(70) 17-1 hyperfine Lorentzian linewidth as a function of Ar buffer gas pressure from Doppler-free SAS measurements.**

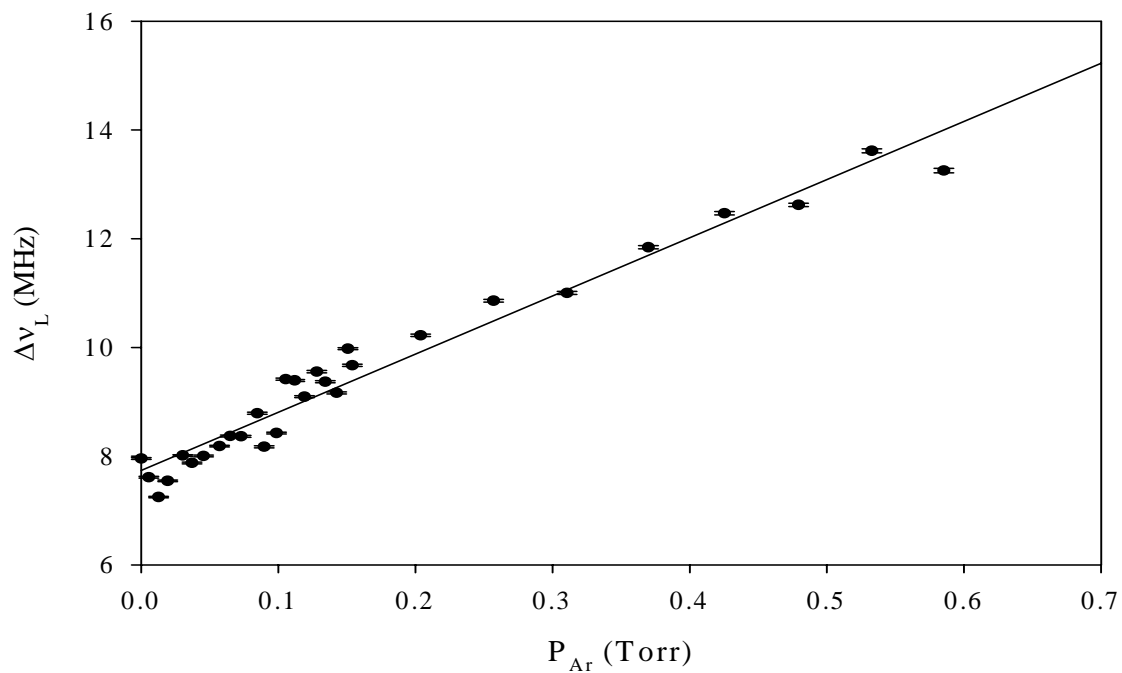


**Figure 30.  $I_2$  P(10) 17-1 hyperfine Lorentzian linewidth as a function of Ar buffer gas pressure from Doppler-free SAS measurements.**

measurements were made using the MPSF signal obtained from a Doppler-free SAS set-up. Fits were then made to the MPSF signals using a theoretical signal composed of Voigt lineshapes. The Gaussian linewidth of the Voigt lineshape was fixed to room temperature. A plot of the  $I_2$  P(70) 17-1 Lorentzian linewidth as a function Ar buffer gas pressure is shown in Figure 31. Linear regression gave a pressure broadening rate of  $8.50 \pm 0.5$  MHz/Torr and a zero-Ar-pressure width of  $16.8 \pm 8.6$  MHz. All of the Ar broadening rates discussed here are listed in Table 12.

### Discussion.

Hyperfine spectra collected with the IMF Doppler-free technique provided better SNR than those collected with SAS. The SAS technique is based on the difficult task of detecting a very small change in the comparatively large transmitted intensity of the probe beam. The IMF technique circumvents this difficulty by monitoring the laser-induced fluorescence which is proportional to the absorbed laser power. Furthermore, IMF suppresses the normal Doppler-broadened laser induced fluorescence due to each of the beams, and retains only the fluorescence signal due to the mutual interaction of the two beams, eliminating the substantial background contribution due to the linear terms in Equation (109).

Investigations of the baseline pedestal in SAS hyperfine spectra were pursued to understand: (1) what conditions influence the pedestal shape and magnitude, and (2) the effect the pedestal might have on the spatially-resolved temperature measurements. The pedestal magnitude depends on  $J$ , the rotational quantum number, and the chopping frequency.<sup>76</sup> The pedestal is more pronounced for lower  $J$ . It was also shown that the choice of a higher chopping frequency suppressed the pedestal. The pedestal phenome-



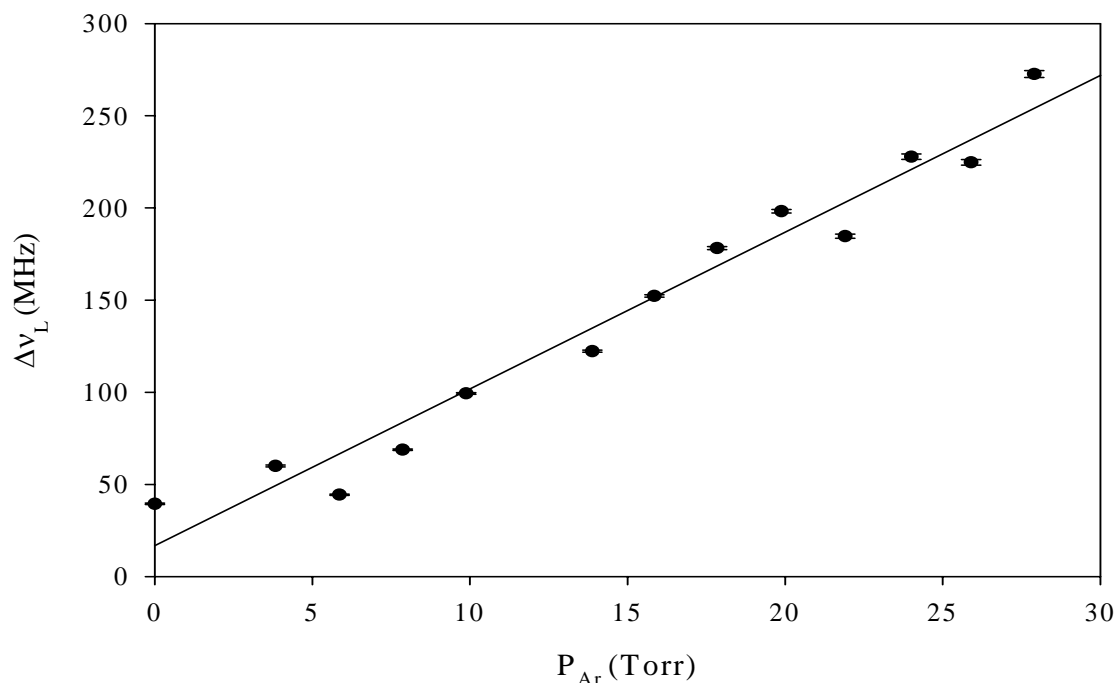


**Figure 31.  $I_2$  P(70) 17-1 Lorentzian linewidth from Voigt profile vs. Ar buffer gas pressure from MPSF measurements.**

**Table 12. Ar buffer-gas broadening rates for  $I_2$ .**

$K_{Ar}$ (MHz/Torr)	$I_2 \Delta\nu_h$ for $P_{Ar} \rightarrow 0$ (MHz)	$I_2$ Spectral Assignment	Method	Spectral Description	$P_{Ar}$ Range
$8.29 \pm 0.30$	$8.7 \pm 0.17$	P(70) 17-1	SAS	hyperfine components, shared Lorentzian width	< 1 Torr
$10.7 \pm 0.41$	$7.74 \pm 0.10$	P(10) 17-1	SAS	hyperfine components, shared Lorentzian width	< 1 Torr
$8.5 \pm 0.5$	$16.8 \pm 8.6$	P(70) 17-1	MPSF	Lorentzian width from Voigt profile, Gaussian fixed to room temp.	1-30 Torr

non is attributed to cross-relaxation, a velocity-changing collision effect, which can be illustrated by considering the following example: a non-zero velocity group  $v_g$  of  $I_2$  molecules interacts with the pump beam and then suffers a collision that converts the velocity group to  $-v_g$ . The probe beam is then in resonance with the new velocity group. As long as the collision occurs during a single modulation cycle, the probe laser intensity is correlated with chopping frequency. Since such collisions can occur for any velocity group,  $v_g$ , a broad feature with Gaussian shape is obtained. At higher pressures and lower modulation frequencies, more collisions occur and contribute to a more intense feature. Apparently, the dynamics are dominated by rotationally inelastic collisions, yielding a strong dependence on rotational state. The effects of cross-relaxation are not expected to influence the Doppler-limited profiles (i.e. the extracted temperature) obtained with the cross-beam spatially-resolved techniques.

The inclusion of a self-absorption parameter in the theoretical cross-beam signal is necessary. Without this term, the temperature extracted from the linewidth tends to be consistently higher than expected. From fitting numerous cross-beam signals, it was found that a strong, low noise signal was critical to achieve a small standard error in the absorption parameter.

In a literature search over the past 35 years, scarce information was readily found on foreign gas pressure-broadening rates of  $I_2$  derived from the SAS or IMF technique. The only available rates from the literature, as shown in Table 9, for Ar pressure broadening were 6.6 MHz/Torr obtained from a single-beam, Doppler-limited experiment<sup>49</sup> and values of 0.31-2.96 MHz/Torr from fluorescence depolarization studies.<sup>50</sup> There is not good agreement between these values and the results of this work

shown in Table 12. This can be attributed in part to the differences in the techniques and the extent of the systematic errors associated with them. As for the two hyperfine broadening rates shown in Table 12, both spectral assignments lie in the same vibrational band, but differ substantially in rotational quantum number. There is a difference in the two Ar-broadening rates that exceeds the standard errors. The P(10) line is located near the 17-1 vibrational band head where the ro-vibrational lines are closely spaced. It was observed that the hyperfine spectrum for P(10) collected with SAS tended to be noisier than the hyperfine spectrum for P(70) resulting in comparatively lower quality fits which could contribute to the difference in the two broadening rates. The two hyperfine linewidths from SAS extrapolated to zero Ar pressure are comparable to the literature values for low pressure I<sub>2</sub> linewidths obtained from SAS and IMF experiments listed in Table 7. The zero-Ar-pressure linewidth from MPSF is at least twice as large as the linewidths from SAS and very poorly determined. This is attributed to the difficulty of fitting at pressures where the Lorentzian width in the Voigt lineshape is very small, a few MHz, compared to the Gaussian linewidth which is approximately 400 MHz at room temperature. The fit parameters tended to have greater statistical errors as the pressure approached zero. The MPSF broadening rate for P(70) 17-1, however, does agree within the statistical error with the P(70) 17-1 SAS broadening rate. Collecting MPSF data was convenient since it could be accomplished simultaneously with the SAS data collection. It was found that the hyperfine spectra from SAS were severely broadened and reduced in intensity at  $P_{Ar} \geq 1$  Torr. Fits to the individual components were not achievable so the MPSF signals were used for analysis at these higher Ar pressures.

## **B. Comparison of Laser Spectroscopy Techniques used for Temperature Determination.**

Although the ultimate application for a temperature diagnostic is in the low-temperature ( $\approx 150$  K) expansion region of a supersonic nozzle, all of the experiments discussed in this section were performed in a static cell environment at temperatures from 293 K to 400 K. This was done primarily because the available supersonic nozzle apparatus posed size, operation, and accessibility limitations that prohibited these types of experiments.

The purpose of the static cell experiments was to make comparisons between the CBSAS, and the CBIMF techniques to assess their suitability as a temperature diagnostics. The MPSF signal was also included in the comparison. The experiments involved (1) varying chopping frequency, (2) varying  $I_2$  pressure (3) and performing measurements at different locations within a temperature gradient. The statistical error in the temperature extraction obtained from nonlinear least squares fitting was correlated to each of the experimentally varied parameters. The temperatures extracted from spectroscopic data were compared to thermocouple measurements.

### Experiments.

Each technique was performed in the static pressure cell illustrated in Figure 32. The cell was constructed of glass Pyrex<sup>®</sup> tubing with 1" outside diameter (OD). The cell measured 15" in length. Ports of 1/2" OD allowed for connection to a pump and the  $I_2$  crystal source as well as for insertion of the thermocouples. Quartz glass windows were mounted at Brewster's angle to each end of the cell for maximum optical transmission as shown in Figure 33. Vacuum connections were made with Cajon<sup>®</sup> O-ring fittings. The

overlap length of the two beams in the cell's axial direction was  $\approx 1.3$  cm. The crossing angle was  $\theta \approx 3.4^\circ$ . Each beam had a 1 mm diameter. The overlapping volume was  $12 \text{ mm}^3$ . A Burle C31034A02 PMT with a long-pass filter was positioned directly above the measurement point for the MPSF and CBIMF measurements as shown in Figure 33. For CBSAS, the exiting probe beam was directed through a series of irises and ND filters onto a Hamamatsu S2281, BNC-connector type, silicon photodiode detector.

In the first experiment, measurements of the variation in extracted temperature,  $T_{ex}$ , with chopping frequency,  $f$ , were performed in  $\text{I}_2$  vapor only; no buffer gas. A series of measurements was performed at different frequencies at a fixed  $P_{\text{I}_2}$  for a specific ro-vibrational line. The cell was then pumped out with an Alcatel 2015 rotary

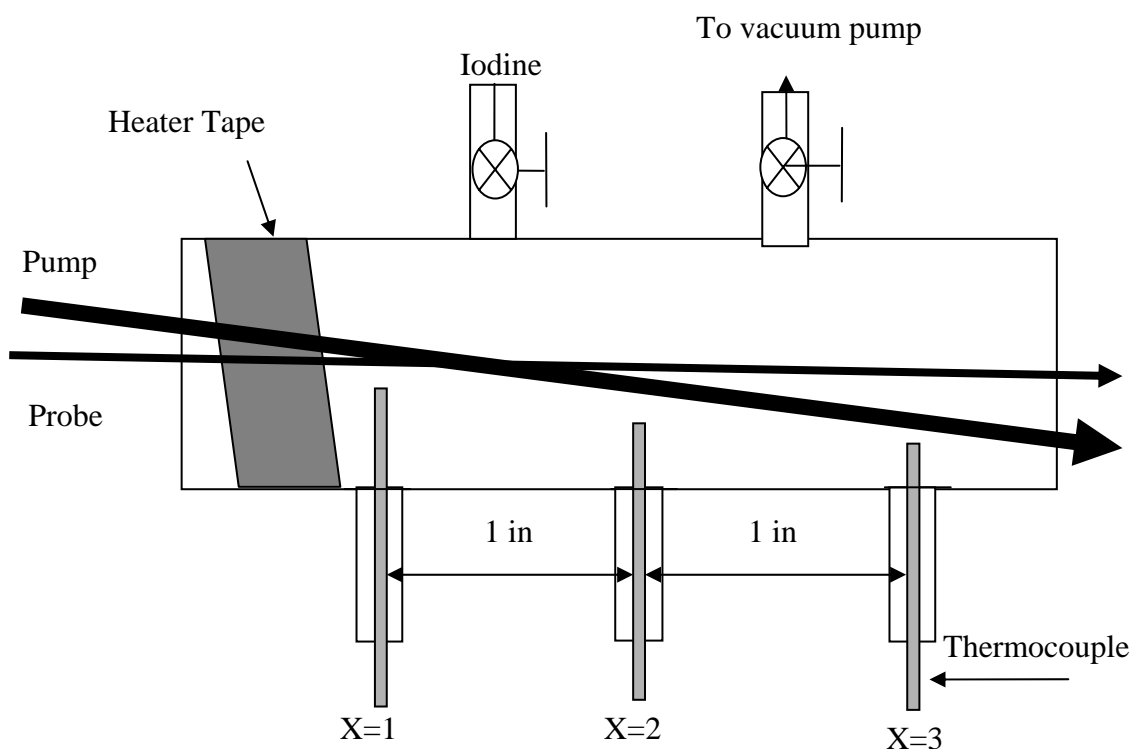


**Figure 32. Schematic of the glass cell used for spatially-resolved temperature measurements.**

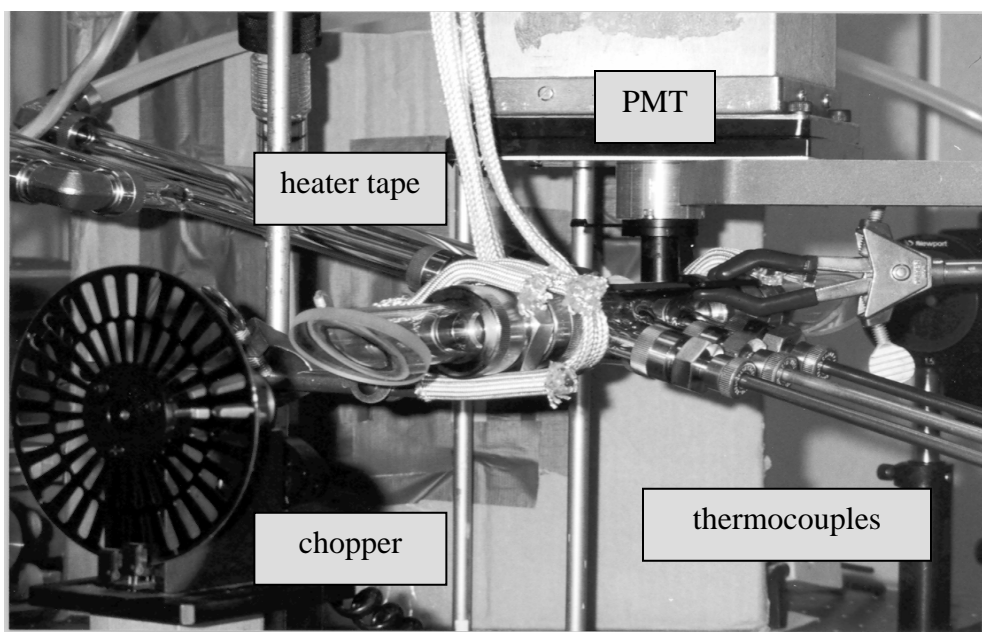


**Figure 33. Glass cell used for spatially-resolved temperature measurements.**

vane pump to an ultimate pressure of 20-30 mTorr. The cell was then sealed off from the pump by closing a valve.  $I_2$  vapor was leaked back into the cell from a glass side-arm containing  $\approx 10$  g of  $I_2$  crystals. A different ro-vibrational line was selected and the series of chopping frequency measurements was repeated at the same  $I_2$  pressure. This procedure was performed for each laser spectroscopic technique.

For the second experiment, measurements were made at a fixed chopping frequency  $f$  while varying the  $I_2$  pressure. A series of pressure measurements were made for a specific ro-vibrational line. The purpose was to determine how the statistical temperature error,  $\delta T_{ex}$ , varied with  $P_{I_2}$  for each of the three laser techniques. All measurements were performed at position  $X = 3$  in the cell (see Figure 32). A temperature gradient was not established. The entire cell was maintained at room temperature.

In the third experiment, a temperature gradient was established along the length of the glass tube by wrapping heater tape around the end of the tube nearest where the laser beams entered the cell. Three thermocouples were oriented in the cell perpendicular to the beam direction and positioned one inch apart. The overlap region of the two crossed laser beams was positioned radially in the center of the tube at a position  $X$  and a spectral profile recorded. To avoid clipping the beam(s), the thermocouples had to be positioned sufficiently far from the overlap region resulting in a discernable difference in the location from which optical and thermocouple measurements were made. The overlap length of the two beams was  $\approx 1.3$  cm as measured along the beam direction. The distance from the tip of the thermocouple to the center point of the beam overlap region was  $\approx 0.25$  cm at position  $X = 1$  (the highest temperature), 1 cm at  $X = 2$ , and 2 cm at  $X = 3$ . This spatial discrepancy allowed for a difference in thermocouple and optically measured temperatures especially in the steep thermal gradient at the high temperature end of the cell. The purpose of the thermocouple was to verify that the optical temperatures were within reasonable expectations. Measurements were performed in  $I_2$  vapor (no buffer gas) for several ro-vibrational lines using each of the following three techniques: CBIMF, CBSAS, and MPSF. For a specific position  $X$  along the cell length, CBIMF was performed, then the chopper re-positioned and beam powers adjusted to make CBSAS measurements along with the simultaneous MPSF measurements. The beams were then crossed at the next position and the procedure repeated. For the fluorescence measurements, the tip of an optical fiber fitted with an Oriel lens was positioned directly above the beam-overlap volume so the signal was directed through the 3 ft fiber optic to the PMT. In the CBSAS set-up,  $I_{pump}$  was  $127 \text{ mW/mm}^2$  and  $I_{probe}$

was 13mW/mm<sup>2</sup>. For the CBIMF set-up, each of the two beam intensities was 64 mW/mm<sup>2</sup>.

### Results.

In all of the experiments, the data consisted of Doppler-limited spectral profiles which were analyzed by fitting them to the appropriate theoretical signal consisting of 15 or 21 Gaussian lineshapes. A Doppler-broadened spectrum of an even  $J''$  isolated ro-vibrational line is shown in Figure 34 and that of an odd  $J''$  line is shown in Figure 35. Both profiles are from a CBIMF experiment performed at room temperature. As expected, the shape of each profile has a noticeable asymmetry due to the hyperfine structure and a FWHM linewidth larger than that predicted by the Doppler broadening alone to be 400 MHz @ 21.3 °C. The data indicates the significant contribution the hyperfine structure makes to the overall width of the spectral profile. A difference in shape is discernable between the P(70) 17-1 spectrum consisting of 15 hyperfine lines and the P(53) 19-2 spectrum having a 21-line hyperfine spectrum.

A fit to an I<sub>2</sub> P(46) 17-1 CBIMF profile is shown in Figure 36. The corresponding residual trend is shown in Figure 37. The data was collected in the static cell with an applied temperature gradient. The measurement was taken at the point where  $T_c = 300$  K and  $T_{ex} = 316$  K  $\pm$  1 K. Likewise, a fit to an I<sub>2</sub> P(46) 17-1 CBSAS profile is shown in Figure 38 from which  $T_{ex} = 302$  K  $\pm$  4.3 K. The residuals are shown in Figure 39. The measurement point was the same for the CBIMF collection. Finally, a fit to a MPSF profile shown in Figure 40 was collected under the same conditions as the previous two signals giving  $T_{ex} = 312 \pm 1$  K. Its residuals are shown in Figure 41.



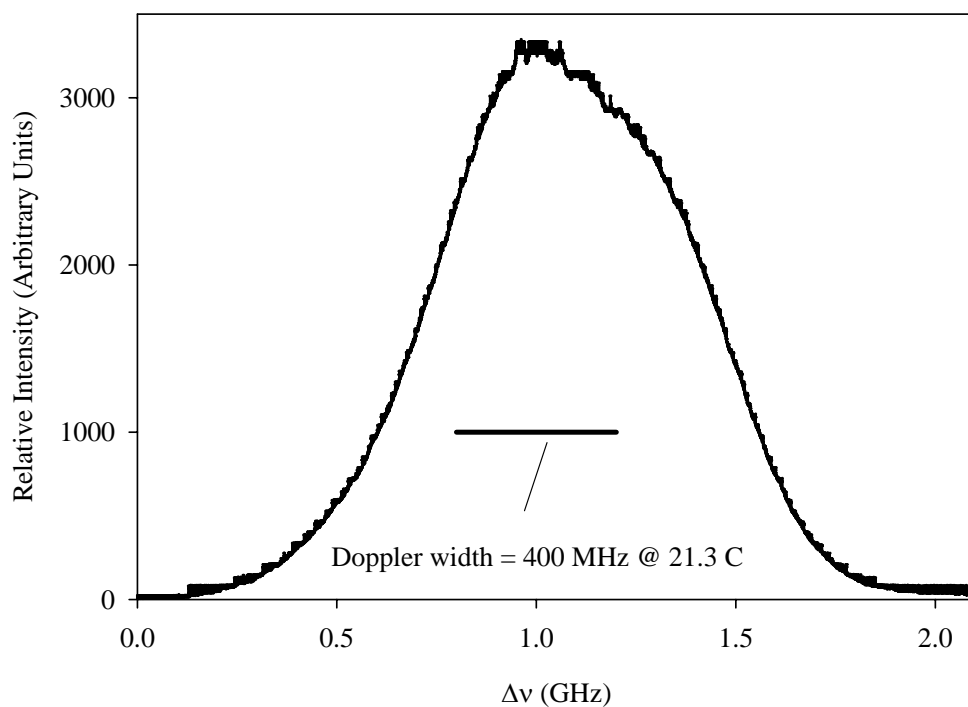


**Figure 34.  $I_2$  P(70) 17-1 isolated ro-vibrational line Doppler-broadened profile at  $17339.8187\text{ cm}^{-1}$  obtained from the CBIMF technique.**

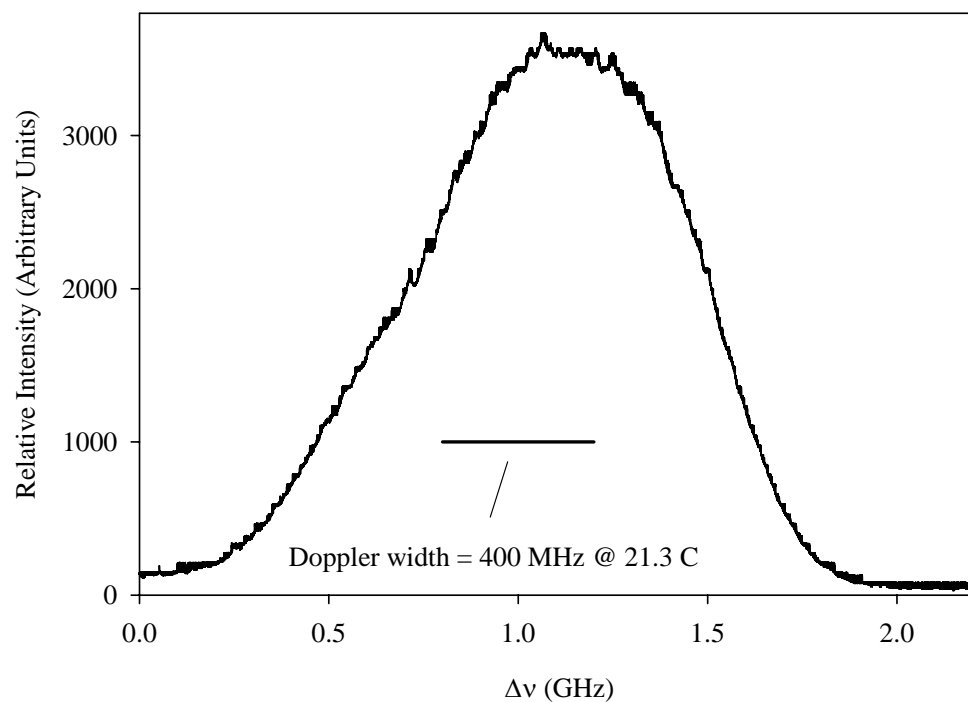


**Figure 35.  $I_2$  P(53) 19-2 isolated ro-vibrational line Doppler-broadened profile at  $17340.2214\text{ cm}^{-1}$  obtained from the CBIMF technique.**

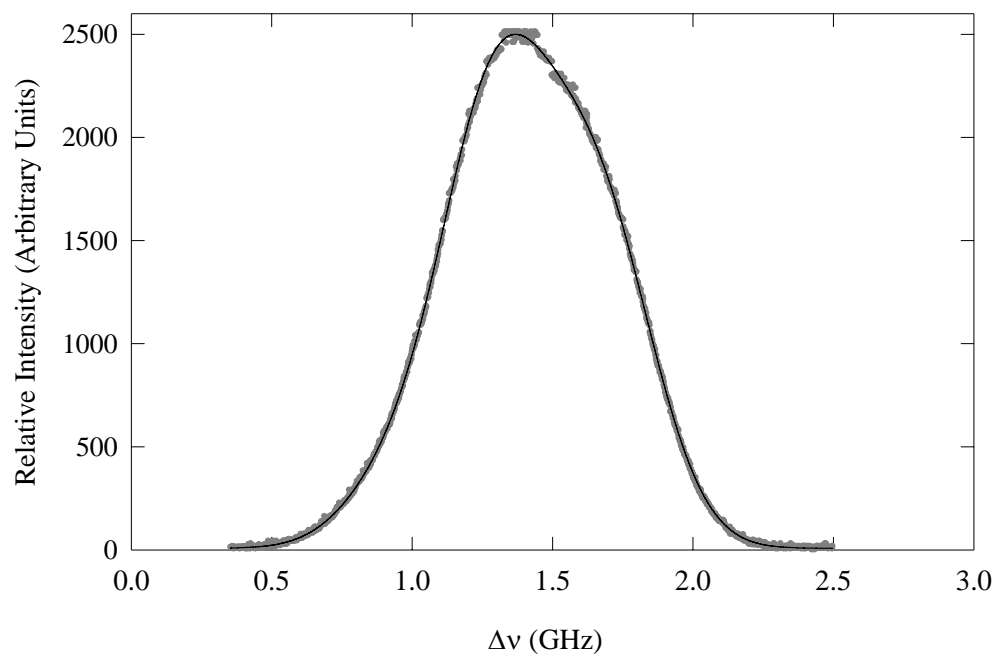


**Figure 36. CBIMF profile of  $I_2$  P(46) 17-1 in static cell. The experimental data points are gray. The theoretical fit to the data is represented by the black line. The measurement was taken at room temperature.**

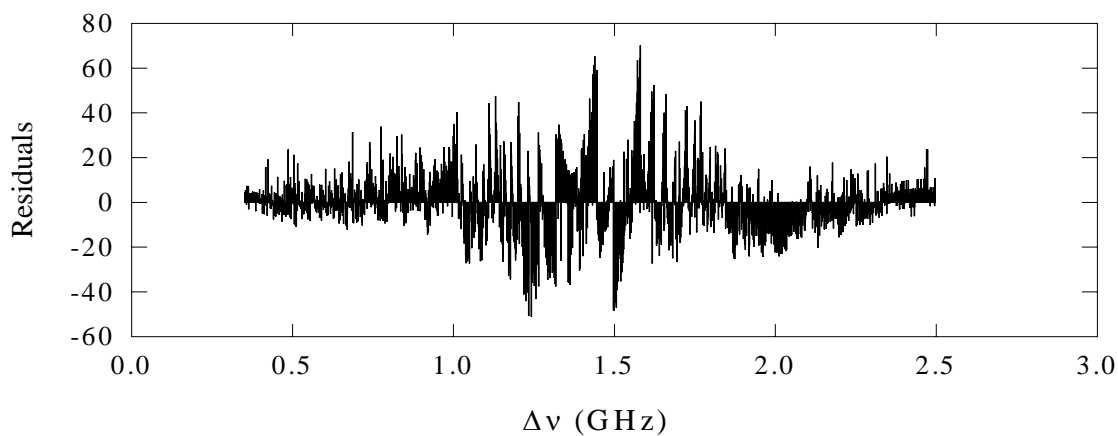


**Figure 37. Residual trend for CBIMF profile of  $I_2$  P(46) 17-1 in static cell.**

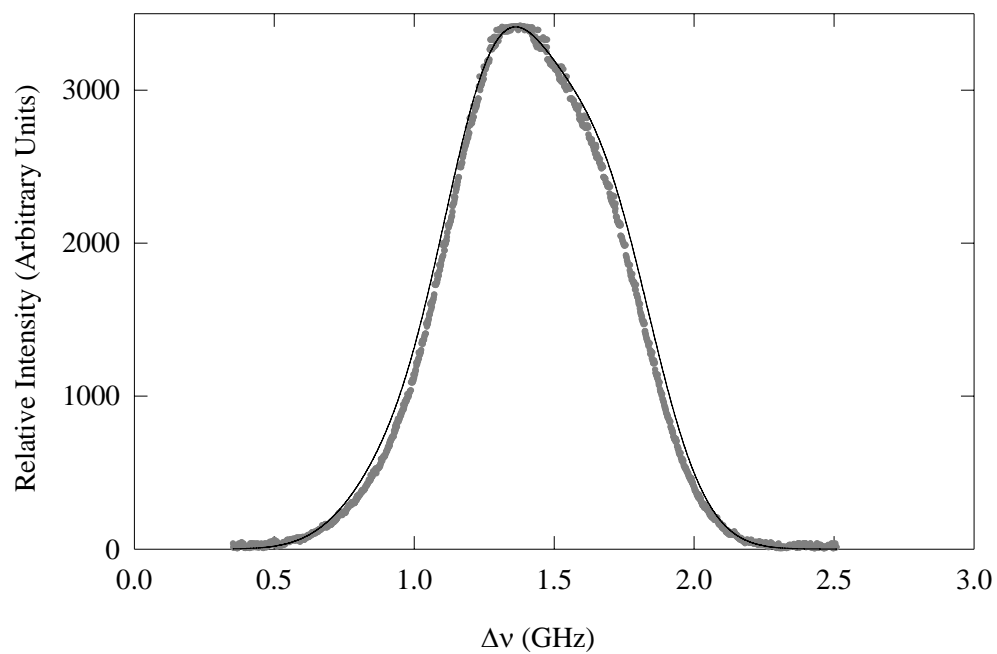


**Figure 38. CBSAS profile of I<sub>2</sub> P(46) 17-1 in static cell. The experimental data points are gray. The theoretical fit to the data is represented by the black line. The measurement was taken at room temperature.**

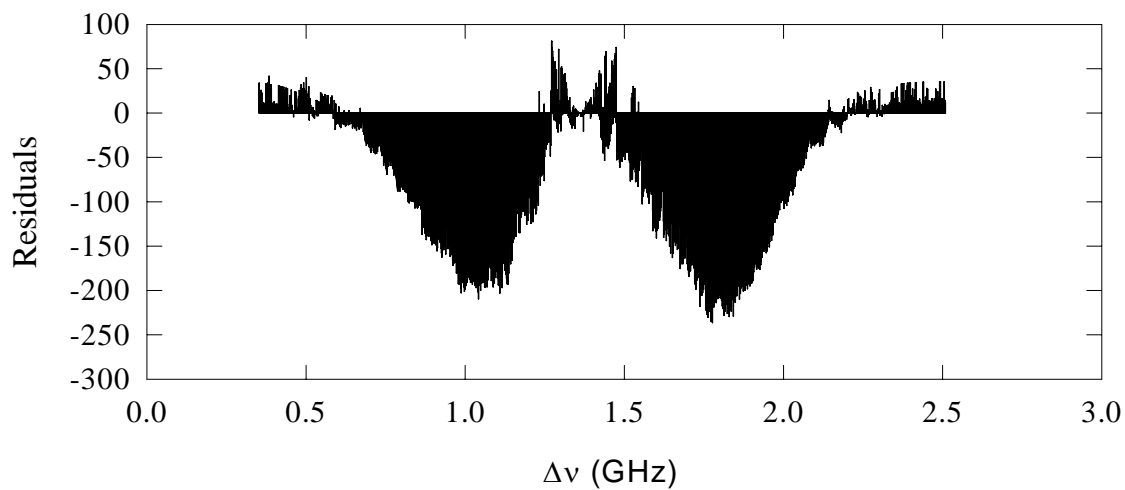


**Figure 39. Residual trend for CBSAS profile of I<sub>2</sub> P(46) 17-1 in static cell.**

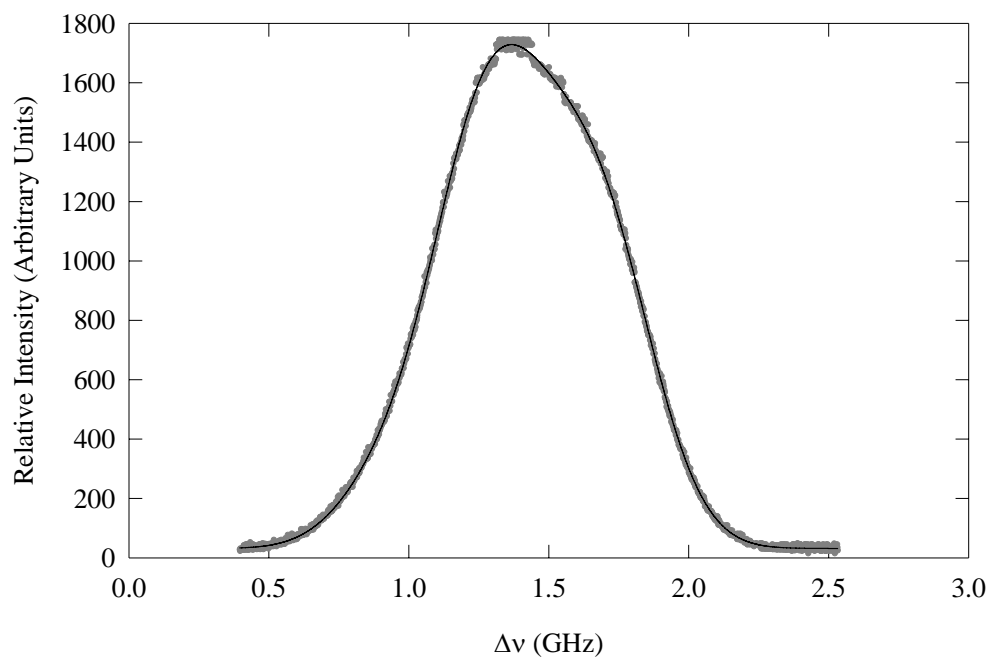


**Figure 40. MPSF profile of I<sub>2</sub> P(46) 17-1 in static cell. The experimental data points are gray. The theoretical fit to the data is represented by the black line. The measurement was taken at room temperature.**

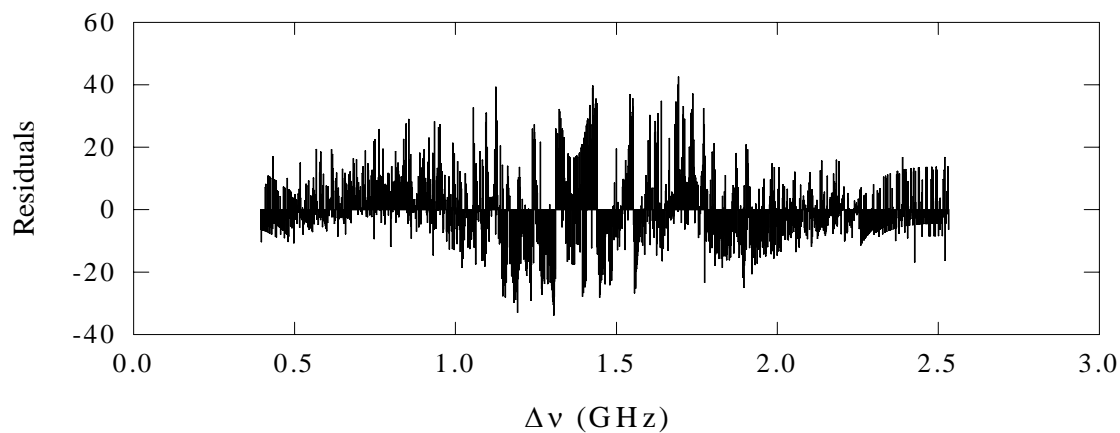


**Figure 41. Residual trend for MPSF profile of I<sub>2</sub> P(46) 17-1 in static cell.**

### *Beam Modulation Frequency and Temperature Extraction.*

The effects of  $f$  on  $T_{ex}$  were obtained for a fixed position in a static cell maintained at 297.3 K as measured by thermocouple. A plot is displayed in Figure 42 of the extracted temperature statistical error,  $\delta T_{ex}$ , for each laser technique as a function of chopping frequency,  $f$ , for a ro-vibrational line with a 15 line HFS, P(70) 17-1, and one with a 21 line HFS, P(53) 19-2. Above 500 Hz,  $\delta T_{ex}$  was less than 1.8 K for all three techniques. Of the three techniques, the CBSAS gave the largest  $\delta T_{ex}$  at all chopping frequencies for both ro-vibrational lines.

Each plot in Figure 43 shows the extracted temperature,  $T_{ex}$ , as a function of  $f$  for a specific laser technique and a particular ro-vibrational line. Measurements were made

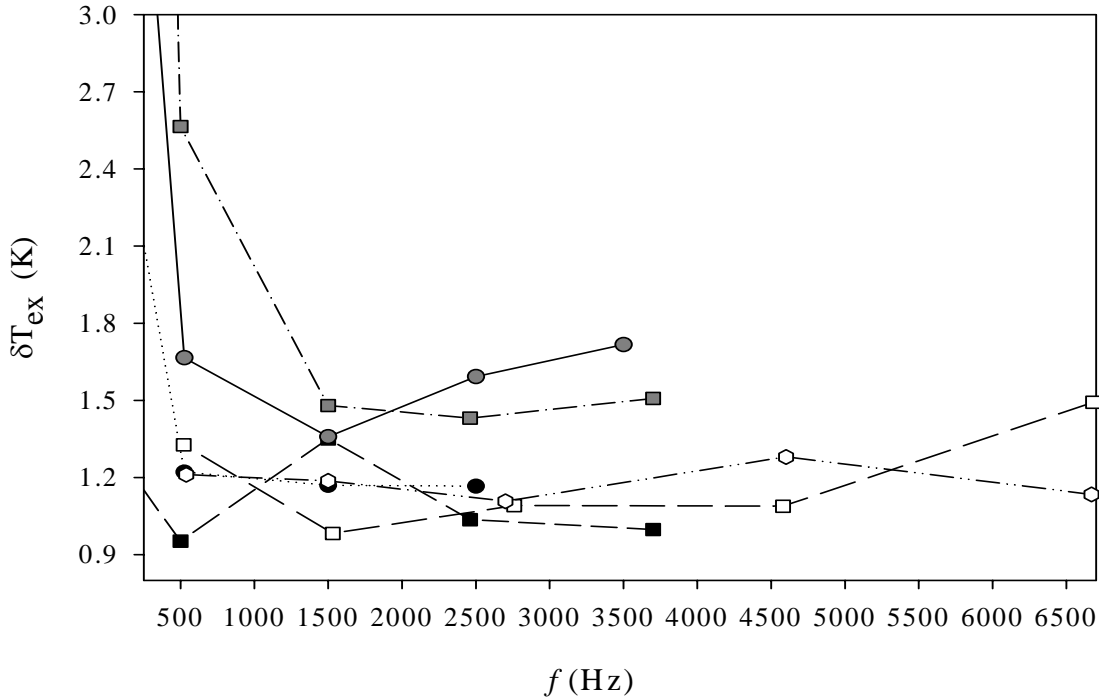


**Figure 42. Extracted-temperature error for various chopping frequencies. Static cell measurements at fixed temperature of 297 K. P(70) 17-1 CBSAS (gray circle), P(70) 17-1 CBIMF (white circle), P(70) 17-1 MPSF (black circle), P(53) 19-2 CBSAS (gray square), P(53) 19-2 CBIMF (white square), P(53) 19-2 MPSF (black square).**

on the P(70) 17-1 line and the P(53) 19-2 line. In a given plot, there is some variation about a nominal temperature value as a function of  $f$ . This variation is smaller in the CBIMF and MPSF results than in the CBSAS results. The MPSF P(53) 19-2 results show the best agreement with the thermocouple temperature,  $T_c = 297.3$  K, for chopping frequencies  $f > 500$  Hz. The closest agreement in  $T_{ex}$  among all the three techniques and with  $T_c$  occurs at 500 Hz. At any given  $f$ , there is substantial difference between each technique's  $T_{ex}$  value and  $T_c$ . The P(53) 19-2 MPSF and CBIMF  $T_{ex}$  data were closest in agreement with  $T_c$  over the range of  $f$ . The P(70) 17-1 MPSF and CBIMF extracted temperatures had closer agreement with one another than with  $T_c$  or P(53) 19-2  $T_{ex}$ .

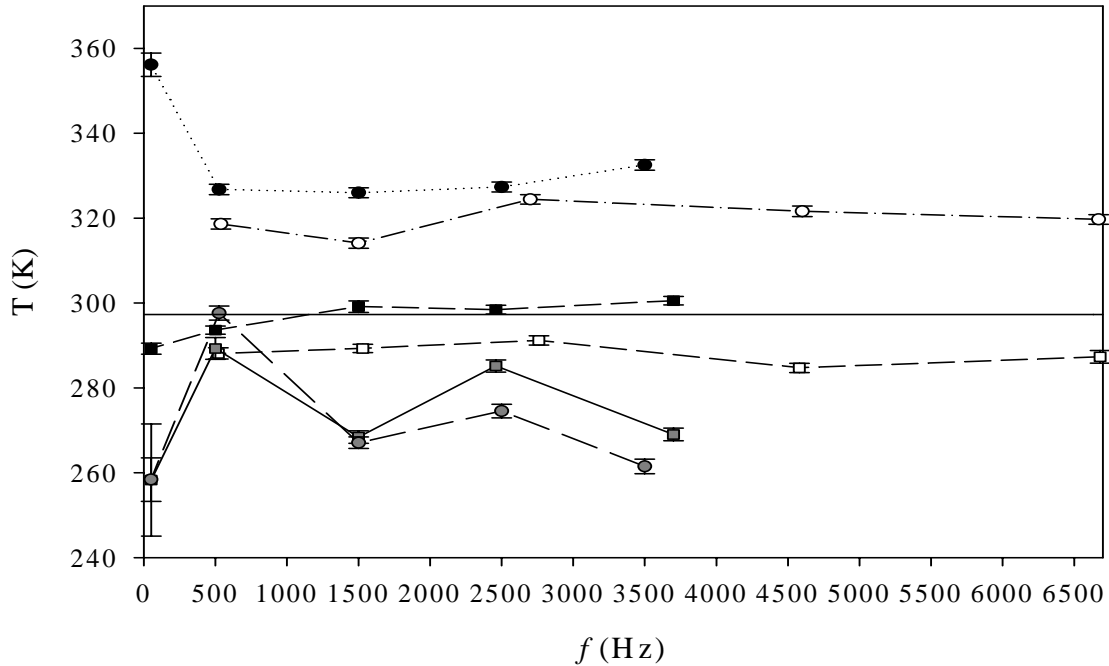


**Figure 43. Extracted temperature for various chopping frequencies. Static cell measurements at fixed temperature of 297 K. P(70) 17-1 CBSAS (gray circle), P(70) 17-1 CBIMF (white circle), P(70) 17-1 MPSF (black circle), P(53) 19-2 CBSAS (gray square), P(53) 19-2 CBIMF (white square), P(53) 19-2 MPSF (black square), thermocouple temperature (solid black line).**

The absorption parameter,  $k$ , proved to be the most difficult parameter of the theoretical signal to fit. Often, the standard error  $\delta k$  exceeded  $k$  in magnitude. A plot of  $k$  versus  $f$  is shown in Figure 44. It was only for the P(70) 17-1 MPSF, and some of the P(70) 17-1 CBIMF  $k$  values that  $\delta k$  was one order or less in magnitude than  $k$  itself. Also, these two data sets were the only ones that showed a noticeable variation in  $k$  with  $f$ .

#### *Iodine Pressure and Temperature Extraction.*

The effects of  $P_{I_2}$  on  $T_{ex}$  were obtained for a fixed position in a static cell held at a fixed temperature of 295 K as measured by thermocouple. As displayed in Figure 45 and Figure 46, the CBIMF technique proved to have the smallest  $\delta T_{ex}$  of all three

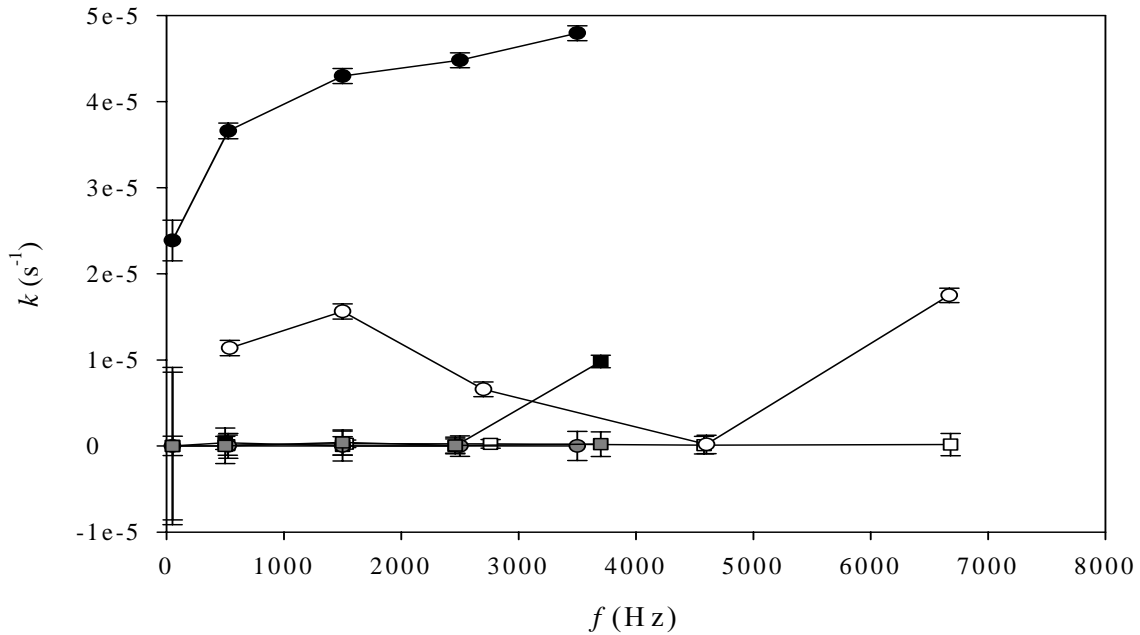


**Figure 44. Absorption parameter at various chopping frequencies. Static cell measurements at fixed temperature of 297 K. P(70) 17-1 CBSAS (gray circle), P(70) 17-1 CBIMF (white circle), P(70) 17-1 MPSF (black circle), P(53) 19-2 CBSAS (gray square), P(53) 19-2 CBIMF (white square), P(53) 19-2 MPSF (black square).**

techniques for  $P_{I_2} > 50$  mTorr. The lowest  $I_2$  pressure at  $\approx 20$  mTorr present after 30 minutes or more of time taken to pump the cell down between each ro-vibrational line measurement showing that a substantial amount of residual  $I_2$  remained in the cell. There was typically enough residual  $I_2$  vapor in the cell to obtain a discernable signal for CBIMF and MPSF measurements. Sufficient SNR was not achieved for CBSAS in these residual  $I_2$  vapor measurements. The strongest SNR at the lowest pressure and all other pressures was obtained with MPSF. However, CBIMF extracted temperatures proved to be the most consistent with the thermocouple measurements followed by MPSF as shown in Figure 47 and Figure 48. The temperatures from CBSAS measurements were consistently below  $T_c = 295$  K. Agreement between  $T_c$  and  $T_{ex}$  improved with increasing  $P_{I_2}$  for all three techniques.

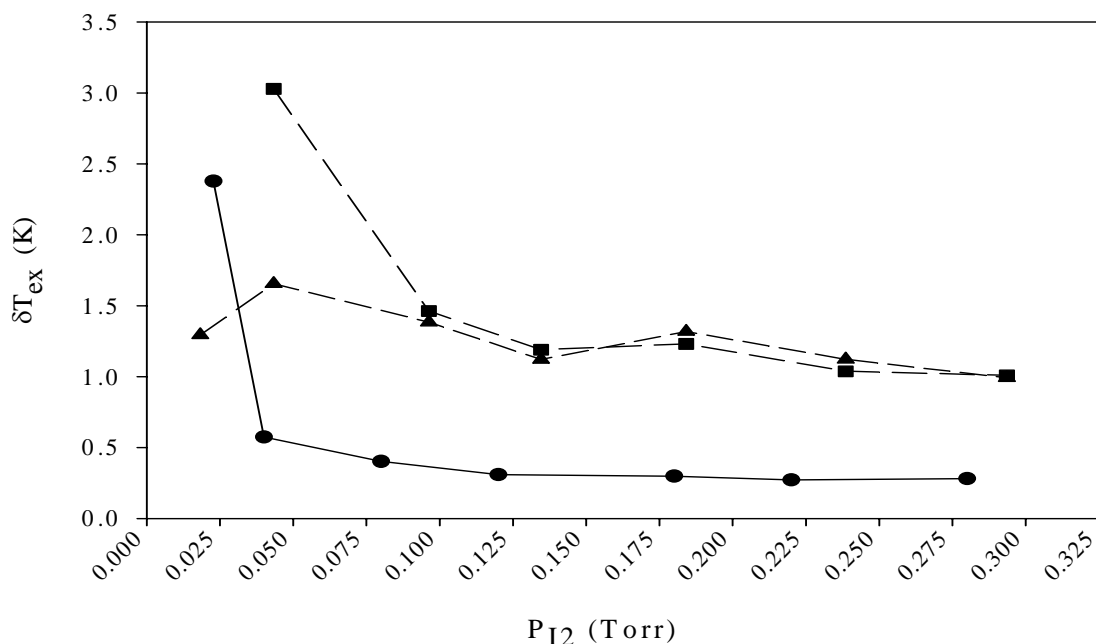


**Figure 45. Extracted-temperature error as a function of  $I_2$  pressure for P(46) 17-1. Static cell measurements at fixed temperature of 295 K. CBSAS (square), CBIMF (circle), MPSF (triangle).**



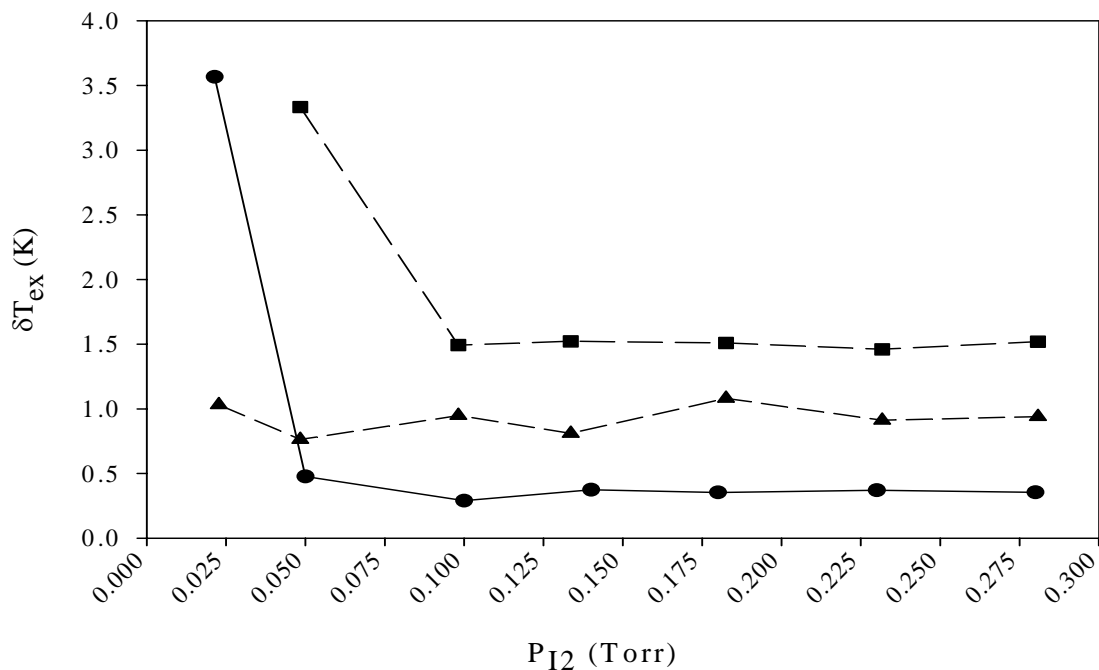


**Figure 46.** Extracted temperature error as a function of  $I_2$  pressure for R(30) 15-0. Static cell measurements at fixed temperature of 295 K. CBSAS (square), CBIMF (circle), MPSF (triangle).

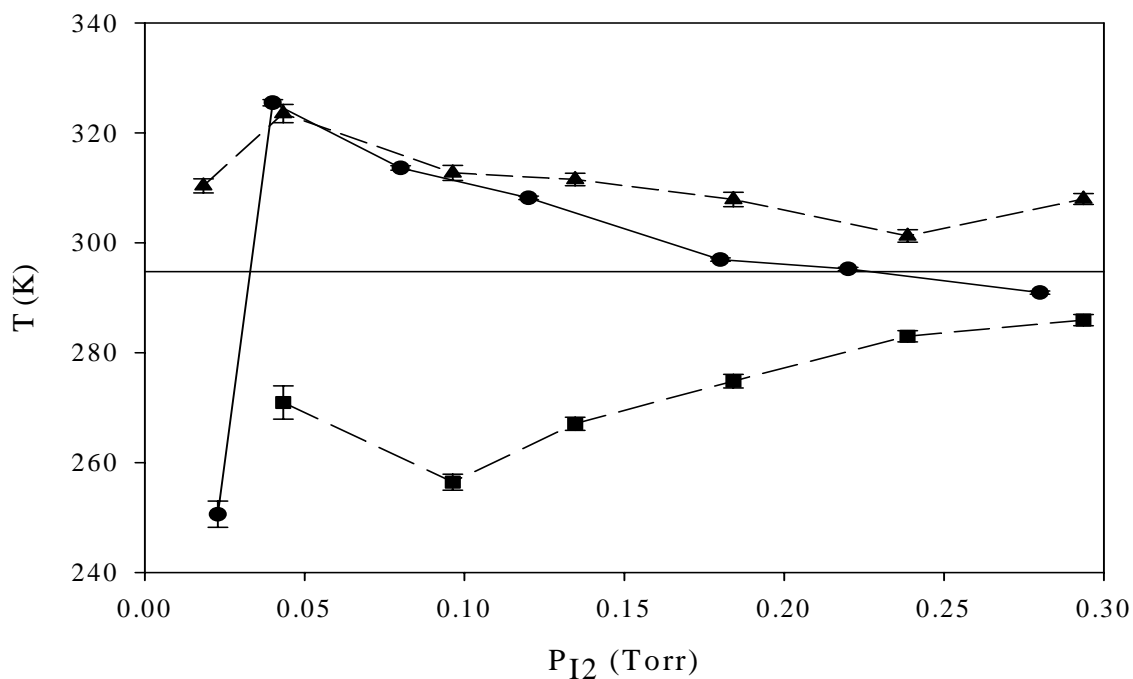


**Figure 47.** Extracted temperature as a function of  $I_2$  pressure for P(46) 17-1. Static cell measurements at fixed temperature of 295 K. CBSAS (square), CBIMF (circle), MPSF (triangle), thermocouple temperature (solid line).

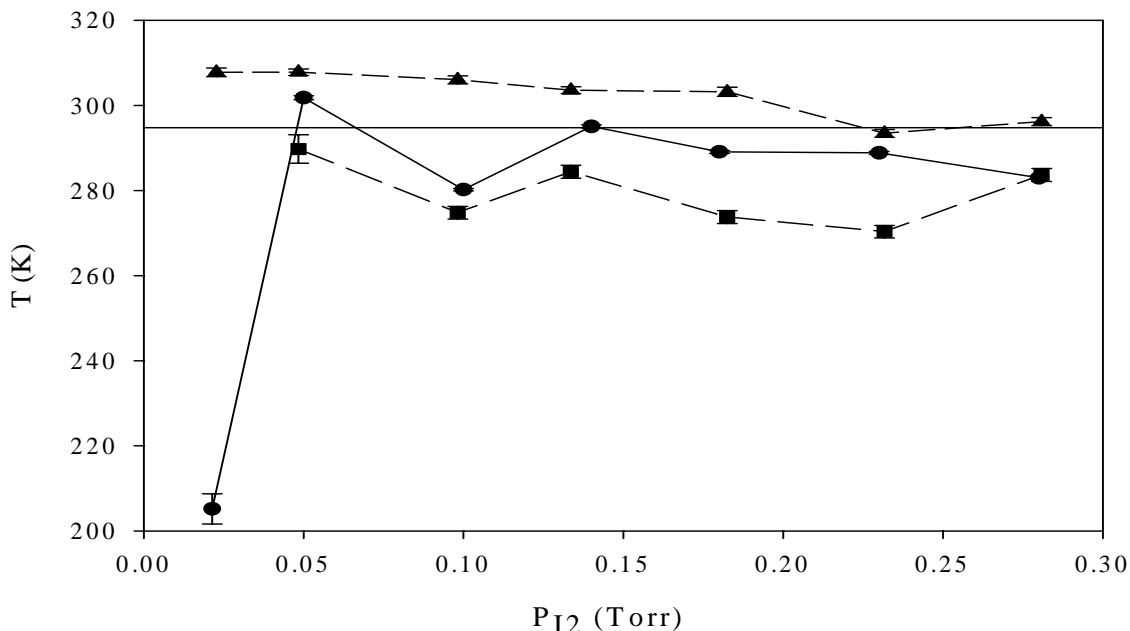


**Figure 48. Extracted temperature as a function of  $I_2$  pressure for R(30) 15-0. Static cell measurements at fixed temperature of 295 K. CBSAS (square), CBIMF (circle), MPSF (triangle), thermocouple temperature (solid line).**

### *Spatially-Resolved Temperatures in a Static Cell.*

The extracted temperatures from each technique are plotted along with the thermocouple temperatures as a function of position,  $X$ , (as defined in Figure 32) for a specific ro-vibrational line as shown in Figure 49 and Figure 50. An estimate of the variation in temperature along the 1.3 cm beam-overlap length centered at the  $X=1$  position in the cell is shown in each graph as errors bars in the upper right corner. All three techniques were capable of resolving temperatures according to spatial location within a thermal gradient. The  $\delta T_{ex}$  results shown in Table 13 were typically  $< 4$  K with the errors being greater for the high temperature measurements. The numerical estimates of temperature variation along the 1.3 cm beam-overlap length at each of the positions in the cell are shown in Table 14. The estimates were based on a best-curve fit to  $T_c$ , as a

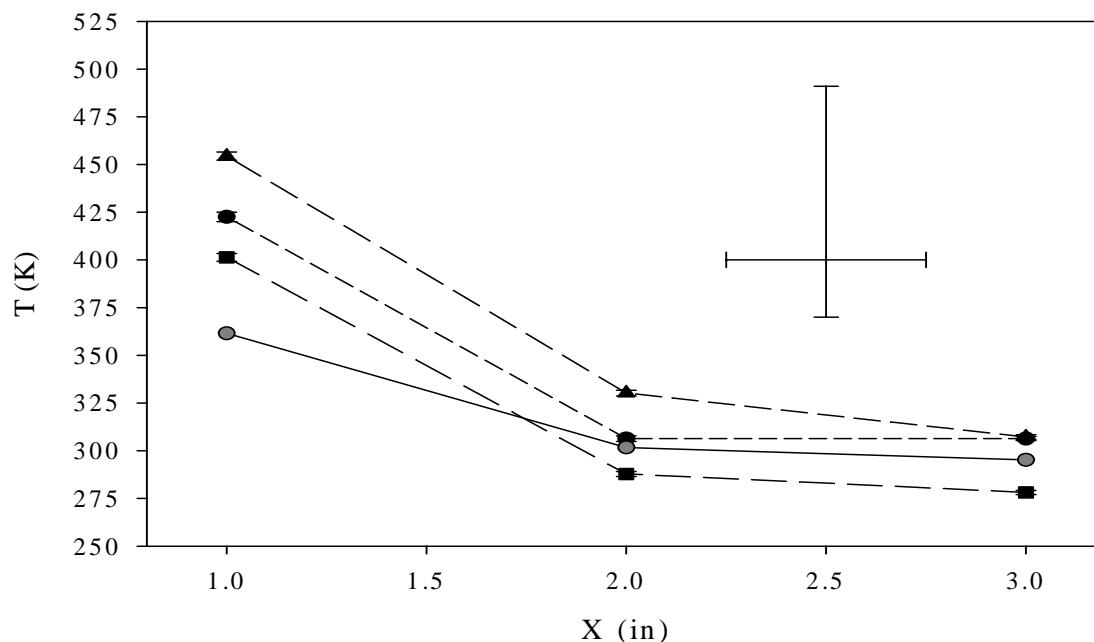


**Figure 49.** Spatially resolved  $T_{ex}$  measurements from  $I_2$  P(114) 18-1 in a static cell with thermal gradient. CBSAS (square), CBIMF (black circle), MPSF (triangle), thermocouple temperature (gray circle). Errors bars indicate  $\Delta T$  along overlap length centered at  $X=1$  as estimated from  $T_c$  measurements.

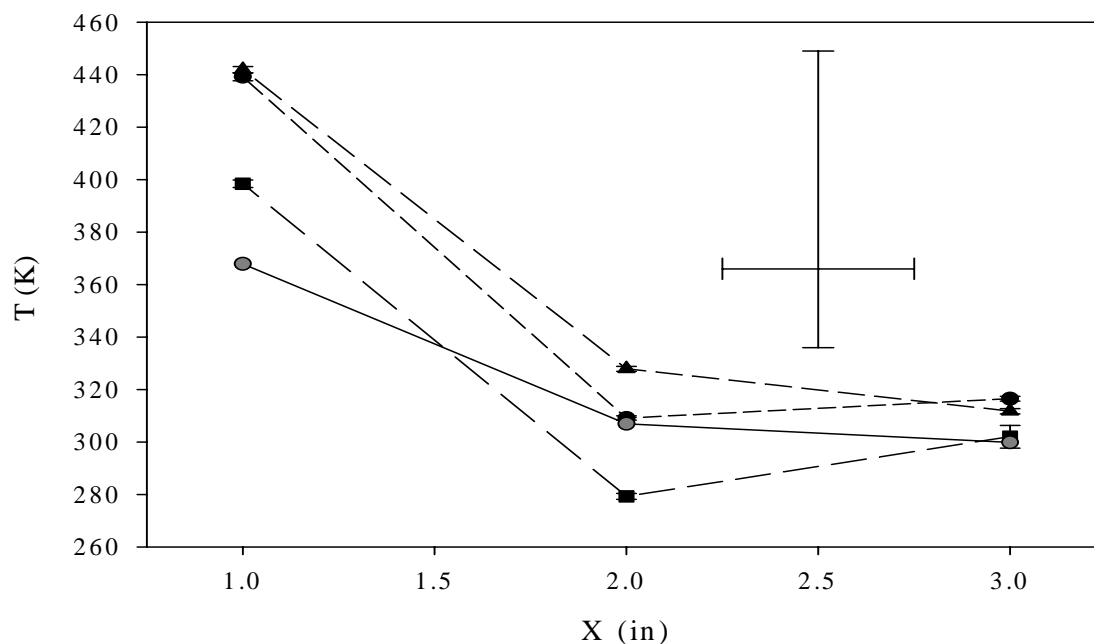


**Figure 50.** Spatially resolved temperature measurements from  $I_2$  P(46) 17-1 in a static cell with thermal gradient. CBSAS (square), CBIMF (black circle), MPSF (triangle), thermocouple temperature (gray circle). Errors bars indicate  $\Delta T$  along overlap length centered at  $X=1$  as estimated from  $T_c$  measurements.

**Table 13. P(46) 17-1 and P(114) 18-1 extracted temperatures from CBIMF, CBSAS, and MPSF in a static cell with a temperature gradient.**

$X$ (in)	$T_{ex}$ (K)	$k$ ( $\times 10^{-5}$ ) (s <sup>-1</sup> )	I <sub>2</sub> Spectral Assignment	Technique
3	316.47 ± 0.91	2.09 ± 0.07	P(46) 17-1	CBIMF
2	309.13 ± 0.84	2.72 ± 0.04	“	“
1	439.21 ± 1.52	3.16 ± 0.08	“	“
3	302.01 ± 4.31	3.08 ± 0.6	P(46) 17-1	CBSAS
2	279.31 ± 1.14	0.0003 ± 0.2	“	“
1	398.43 ± 1.45	0.29 ± 0.08	“	“
3	311.73 ± 1.00	8.36 ± 0.09	P(46) 17-1	MPSF
2	327.89 ± 0.96	3.29 ± 0.06	“	“
1	441.89 ± 1.25	2.25 ± 0.04	“	“
3	306.41 ± 1.10	1.65 ± 0.06	P(114) 17-1	CBIMF
2	306.34 ± 1.44	1.65 ± 0.06	“	“
1	422.56 ± 2.48	3.54 ± 0.1	“	“
3	278.16 ± 1.11	0.003 ± 0.1	P(114) 17-1	CBSAS
2	287.80 ± 1.33	0.009 ± 0.1	“	“
1	401.35 ± 2.04	0.001 ± 0.09	“	“
3	307.22 ± 1.18	4.11 ± 0.09	P(114) 17-1	MPSF
2	330.23 ± 1.51	2.14 ± 0.1	“	“
1	454.41 ± 2.13	1.92 ± 0.08	“	“

**Table 14. Thermocouple measurements and the estimated temperature gradient along the overlap length in static cell for P(46) 17-1 and P(114) 18-1 cross-beam experiments.**

$X$ (in)	$T_c$ (K)	$\Delta T_{ol}^{high}$ (K)	$\Delta T_{ol}^{low}$ (K)	I <sub>2</sub> Spectral Assignment
3	299.75	+1	-1	P(46) 17-1
2	307.15	+5	-3	“
1	366.15	+89	-30	“
3	295.25	+1	-1	P(114) 17-1
2	301.75	+5	+3	“
1	361.55	+91	-30	“

function of position,  $X$ . The difference between  $T_c$  at the center-point of the overlap and the temperature at 0.25" towards the hot end of the cell is designed by  $\Delta T_{ol}^{high}$ . Likewise, the difference between  $T_c$  at the center-point of the overlap and the temperature at 0.25" towards the cold end of the cell is designed by  $\Delta T_{ol}^{low}$ . This shows that the temperature could have varied as much as 50 K along the overlap length of 0.5 inches (1.3 cm) when the beams were positioned at the high temperature measurement position ( $X = 1$ ). Also, as noted in the Figure 32 schematic, there was a small spatial gap between the thermocouple tip and the beam crossing volume at each measurement location.

The MPSF extracted temperatures tended to be the highest of the three techniques at each position regardless of ro-vibrational line and showed the least agreement with  $T_c$  at a given position. The CBIMF extracted temperatures were also typically higher than the corresponding  $T_c$  measurements, and showed better agreement with the MPSF temperatures in some cases. The CBSAS temperatures tended to be higher than  $T_c$  at hot end of the cell, and lower than  $T_c$  at the two other positions in the cell. As shown in Table 13, there was some difficulty with fitting  $k$  in CBSAS where  $\delta k$  exceeded  $k$  by an order of magnitude in all but one case. However, for the CBIMF and MPSF techniques,  $\delta k$  was one to two orders-of-magnitude smaller than  $k$  itself.

The P(46) 17-1 spectral profiles at the various positions in the temperature gradient for each of the laser techniques are shown in Figure 51-Figure 53. For each graph, the maximum amplitude was determined for each profile and scaled relative to the high temperature profile. The relative frequencies for each profile were scaled so the

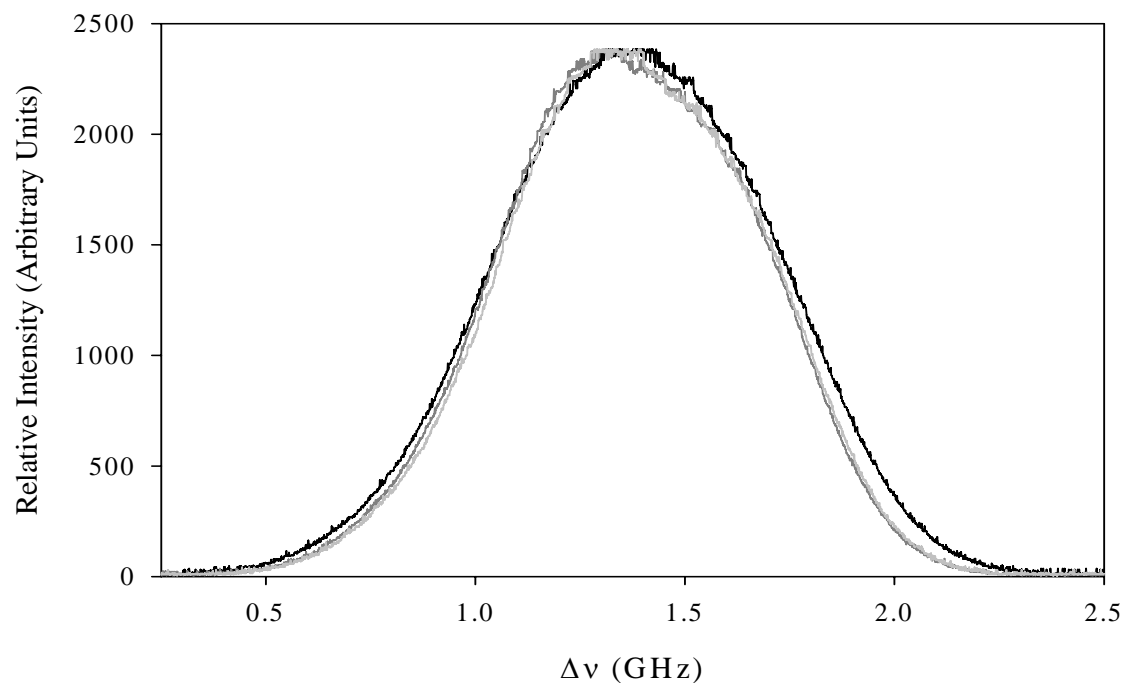


**Figure 51. CBIMF P(46) 17-1 spectral profile at three positions/temperature. Position 1/high temp (black), Position 2 (dark gray), Position 3/low temperature (light gray).**

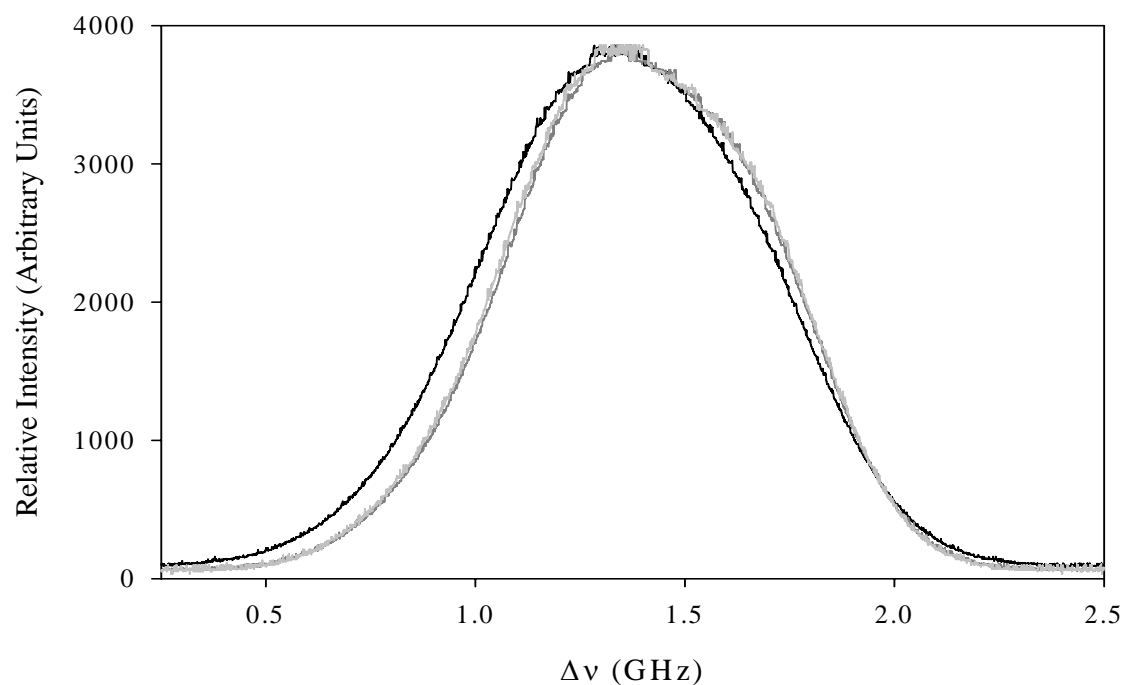


**Figure 52. CBSAS P(46) 17-1 spectral profile at three positions/temperatures. Position 1/high temp (black), Position 2 (dark gray), Position 3/low temperature (light gray).**

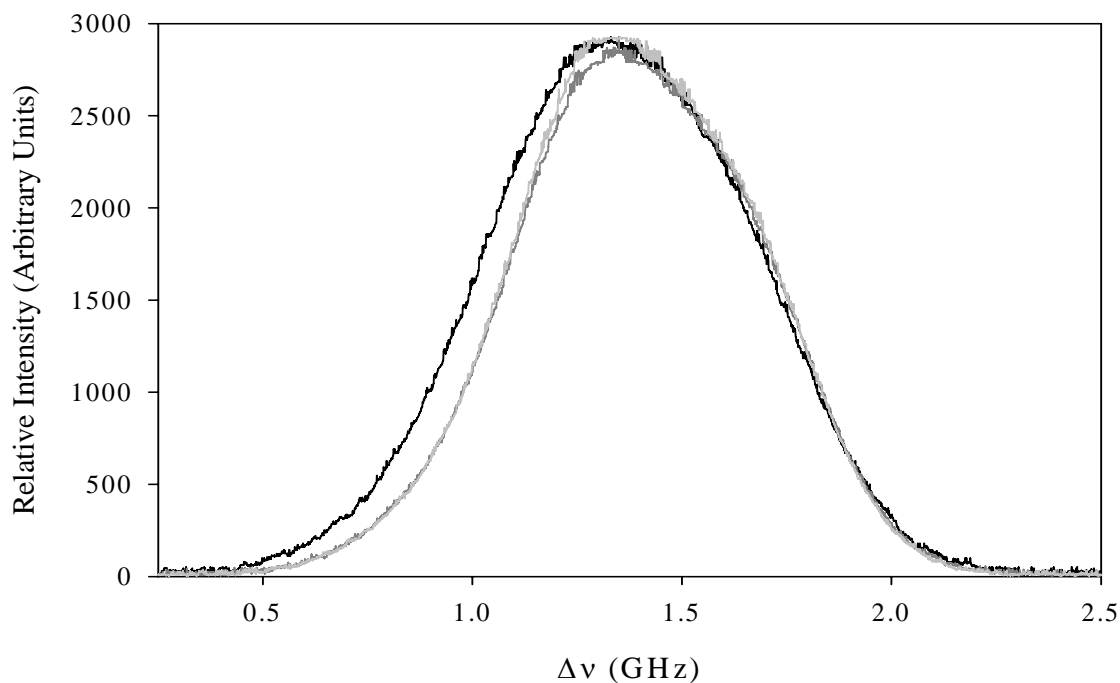


**Figure 53. MPSF P(46) 17-1 spectral profile at three positions/temperatures. Position 1/high temp (black), Position 2 (dark gray), Position 3/low temperature (light gray).**

relative maximum amplitudes coincided. For a given technique, there is only a small difference between the linewidth of the high temperature profile as compared to the lowest temperature profile, and there is a barely discernable difference between the profiles collected at the two lowest temperatures.

Finally, temperatures were extracted from the P(51) 18-2 & P(66) 16-1 blended line using all three techniques in the static cell with a temperature gradient. The results along with the thermocouple temperatures at each position are shown in Figure 54. The same trend occurs here as in the isolated line results. The  $T_{ex}$  is much higher than  $T_c$  at the hot end of the cell where  $X = 1$ . Agreement between  $T_{ex}$  and  $T_c$  is better at the other two positions in the cell. The  $T_{ex}$  results for the blended line are shown in Table 15 along

with the fits to  $k$ . Estimates of the variation in  $T_c$  along the 0.5" beam-overlap length at each of the positions in the cell are shown in Table 16.

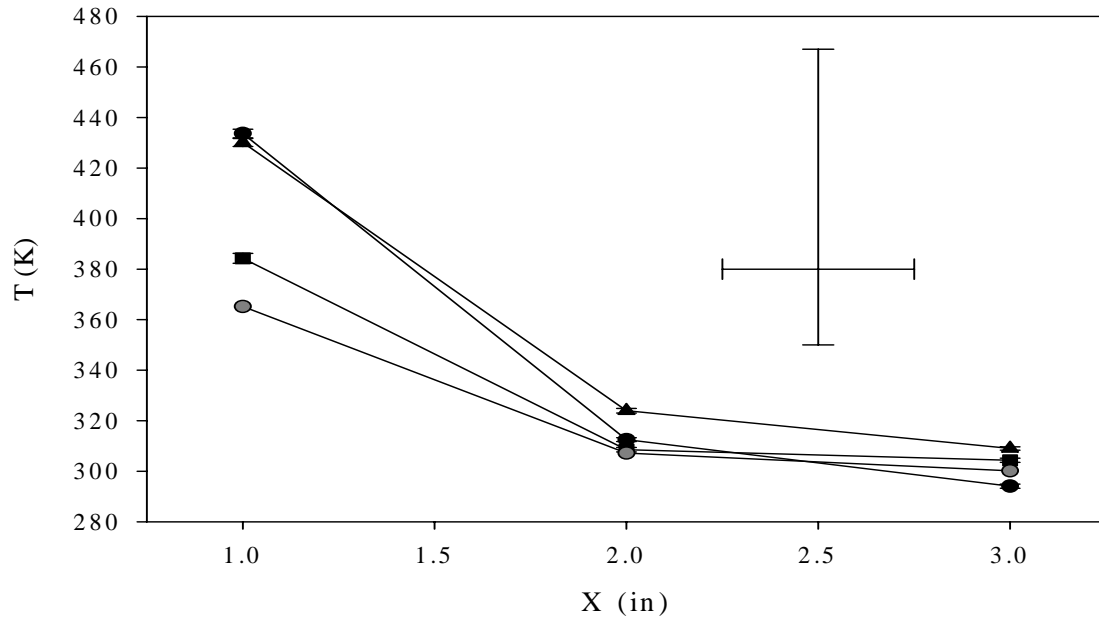


**Figure 54. I<sub>2</sub> P(51) 18-2 & P(66) 16-1 blended line in a static cell with thermal gradient. CBSAS (black square), CBIMF (black circle), MPSF (black triangle), thermocouple (gray circle). Errors bars indicate  $\Delta T$  along overlap length centered at X=1 as estimated from  $T_c$  measurements.**

**Table 15. P(51) 18-2 & P(66) 16-1 extracted temperatures from CBIMF, CBSAS, and MPSF in a static cell with a temperature gradient.**

$X$ (in)	$T_{ex}$ (K)	$k$ ( $\times 10^{-5}$ ) (s <sup>-1</sup> )	Technique
3	$294.09 \pm 0.79$	$3.54 \pm 0.08$	CBIMF
2	$312.50 \pm 0.77$	$2.38 \pm 0.06$	“
1	$433.60 \pm 1.72$	$2.86 \pm 0.11$	“
3	$304.33 \pm 0.82$	$-5.82 \pm 0.1$	CBSAS
2	$308.53 \pm 0.89$	$-1.82 \pm 0.09$	“
1	$384.26 \pm 1.94$	$-3.85 \pm 0.15$	“
3	$309.00 \pm 0.71$	$3.4 \pm 0.04$	MPSF
2	$323.95 \pm 0.95$	$3.6 \pm 0.09$	“
1	$430.07 \pm 1.6$	$1.8 \pm 0.08$	“



**Table 16. Thermocouple measurements and the estimated temperature gradient along the overlap length in static cell for P(51) 18-2 & P(66) 16-1 blended line cross-beam experiments.**

$X$ (in)	$T_c$ (K)	$\Delta T_{ol}^{high}$ (K)	$\Delta T_{ol}^{low}$ (K)
3	300	+1	-1
2	307	+5	-3
1	365	+87	-30

As mentioned in the theory section, the fits to the blended line had to be performed with Mathematica code. Unlike the Peakfit or Tablecurve programs, the nonlinear statistics package in Mathematica did not provide a simple means of constraining the fit parameters. Therefore,  $k$  could not be constrained to positive values as expected for absorption conditions. As it turned out, the Mathematica fits to the CBSAS signals consistently produced negative values for  $k$ .

In the blended line fits shown above, a different fit parameter was assigned to each ro-vibrational line's amplitude to account for the difference in statistical populations between the two lines as was shown in Equation (135). An alternative approach to the blended line fits involved utilizing the temperature dependence present in the amplitude parameter via the Boltzmann factor in addition to the temperature dependence contained in the Doppler linewidth. In this alternative approach, attempts were made to simultaneously constrain each of the two overlapped ro-vibrational lines to the same temperature contained in each ro-vibrational line's amplitude parameter and the Doppler linewidth. Unfortunately, the outcome was very poor fits to the data with a large discrepancy between the  $T_{ex}$  and  $T_c$  at each position in the static cell gradient. A fit result is shown in Appendix A.

### Discussion.

The beam modulation experiments reveal that  $f$  for a temperature diagnostic should be higher than 500 Hz to keep  $\delta T_{ex}$  below 2 K for room temperature measurements. The results for  $T_{ex}$  versus  $f$  shown in Figure 43 were anticipated to be plots coincident with the horizontal line corresponding to the thermocouple measurement. On the contrary, only one plot, MPSF for P(53) 19-2, met this expectation with the other plots showing a small variation about a temperature significantly higher or lower than that of  $T_c$ .

For a given plot, the change in  $T_{ex}$  with  $f$  is small for  $f > 500$  Hz. The variation in  $T_{ex}$  for a given ro-vibrational line and technique is most likely due to systematic errors or noise rather than a change in  $f$  at frequencies above 500 Hz. Regardless of technique, the signal is very smooth and featureless at room temperature.

From the iodine pressure experiments, a temperature diagnostic based on any of the techniques would have greater success for  $P_{I_2}$  approaching 0.3 Torr. The CBIMF technique would be the preferred technique based on temperature accuracy and statistical error as compared to the CBSAS and MPSF techniques. However, there is an advantage of the absorption-based technique over the fluorescence-based techniques. The intended application of a temperature diagnostic is for the COIL. The laser cavity has only two transparent windows parallel to each other and positioned on opposite sides of the cavity. A measurement of fluorescence from a direction perpendicular to the interrogating beam direction would not be possible. This could be overcome by positioning a detector at one of the windows so that it is off-axis from the interrogating beams. CBSAS avoids this difficulty through measurement of transmitted probe-beam intensity.

From the temperature measurements in the static cell with a thermal gradient,  $T_{ex}$  from each technique showed the best agreement with the other techniques and  $T_c$  at the lowest temperature ( $\approx 300$  K). In Figure 49 and Figure 50, for the most part, the extracted temperatures deviate from one another and  $T_c$  in the higher temperatures. At position  $X = 1$ , the beams overlap along an axial length that covers a large span in temperature as a result of the steep temperature gradient. The overlap volume spans a smaller temperature gradient as the cold end of the cell is approached. The variation in temperature along the overlap length is the most likely cause for disagreement between  $T_{ex}$  and  $T_c$  at positions 1 and 2. A smaller overlap volume was not achievable due the limitation of the 1 inch diameter of the glass tube.

The  $T_{ex}$  results at each position in Figure 49 and Figure 50 follow a systematic trend with MPSF typically producing the highest  $T_{ex}$  and CBSAS producing the lowest. In the case of the MPSF signal, the spatial region over which the MPSF signal was collected was determined only by the field-of-view of the PMT lens which differed from that of the beam-overlap volume for CBSAS and CBIMF. The beam intensities could also have also played a role in the results. In the CBSAS set-up, the pump beam intensity was  $I_{pump} = 127 \text{ mW/mm}^2$  and the probe beam intensity was  $I_{probe} \leq 13 \text{ mW/mm}^2$ . Since the laser excitation from the modulated pump beam in the CBSAS configuration is the MPSF signal, it is possible that the beam intensity approaches, or exceeds the saturation intensity and that this affects the lineshape in ways not accounted for in the theoretical signal resulting in an  $T_{ex}$  that is higher than expected. For comparison, each of the two the CBIMF beam intensities was  $64 \text{ mW/mm}^2$ . It is difficult to ascertain if the

beam intensities in all the spatially-resolved measurements were optimal based on saturation intensities in the literature since there is such discrepancy between these reported values as shown in Table 11. The  $I_2$  saturation intensity is difficult to determine due to its dependence on pressure and the relaxation kinetics at a specific temperature. It is also generally expected to be different for each absorption line. Simply using extremely low beam intensities to ensure  $S_o \ll 1$  would not be practical since the SNR in the recorded lineshape would most likely be degraded. This, in turn, would affect the temperature extraction, producing unacceptably large standard errors. For the static cell at fixed pressure with a temperature gradient, the number of molecules participating in the signal decreases at the higher temperatures. This is accompanied by a corresponding change in relaxation kinetics with temperature. These effects could have increased  $S_o$  and dramatically affected  $T_{ex}$  obtained from the hotter positions in the static cell.

To obtain a quantitative estimate of the influence of systematic errors on  $T_{ex}$ , a nonlinear term was introduced into the theoretical signal. The spectral profiles from the P(46) 17-1 measurements in the static cell with a temperature gradient (Figure 51, Figure 52, Figure 53) were fit with the modified theoretical signal of

$$S'_{cb}(\nu) = A' \cdot \left[ \sum_{i=1}^{15 \text{ or } 21} G(\nu; f_i, \nu_{oi}, \Delta \nu_D) \right] \cdot \exp \left( -k \cdot A' \cdot \left[ \sum_{i=1}^{15 \text{ or } 21} G(\nu; f_i, \nu_{oi}, \Delta \nu_D) \right] \right) + a\nu + b \quad (138)$$

where a frequency-dependent nonlinear term is included into the amplitude parameter so that

$$A' = A \nu^{-1/2} \quad (139)$$

where  $A$  is the original amplitude parameter from Equation (133) and the expression

$\nu^{-1/2}$  is a hypothetical choice meant only to illustrate the point of the argument.

Equation (139) can be re-expressed as

$$A' = (A \nu_o) \left( \frac{\nu}{\nu_o} \right)^{-\frac{1}{2}} = A'' \left( 1 + \frac{\Delta \nu}{\nu_o} \right)^{-\frac{1}{2}} \cong A'' \left( 1 - \frac{\Delta \nu}{2 \nu_o} \right) \quad (140)$$

where the last expression is the result of a Taylor series expansion. The modified

lineshape can be expressed in term of the original lineshape and a small correction term

$\varepsilon$  so that

$$S'_{cb}(\nu) = (1 - \varepsilon) S_{cb}(\nu) \quad (141)$$

where the original amplitude,  $A$ , is reinterpreted and

$$\varepsilon = \frac{\Delta \nu}{2 \nu_o} \approx \frac{1.4 \text{ GHz}}{2 (17339 \text{ cm}^{-1}) c} \approx 10^{-6}. \quad (142)$$

in which 1.4 GHz is a typical linewidth for a ro-vibrational line which takes into account

Doppler width and hyperfine structure, and  $17339 \text{ cm}^{-1}$  is a typical wavenumber for an  $\text{I}_2$

ro-vibrational line investigated in this work.

The  $T'_{ex}$  values from the  $S'_{cb}(\nu)$  fits are shown in Table 17 along with the  $T_{ex}$  values from Table 13 and the  $T_c$  values from Table 14 for comparison. The  $S'_{cb}(\nu)$  fits produced  $T'_{ex}$  values that gave closer agreement with  $T_c$  than the  $T_{ex}$  results from the  $S_{cb}(\nu)$  fits. The differences between  $T'_{ex}$  and  $T_{ex}$  ranged from 27 K to less than 1 K.

The quality of the  $S'_{cb}(\nu)$  fits was consistently worse than the quality of the  $S_{cb}(\nu)$  fits. As an example, a graph of the P(46) 17-1 CBIMF profile at  $X=1$  fitted with

$S_{cb}(\nu)$  is shown in Figure 55 and the corresponding residuals are shown in Figure 56.

This is compared to the graph of the P(46) 17-1 CBIMF profile at  $X=1$  fitted with  $S'_{cb}(\nu)$  shown in Figure 57. Its residuals are shown in Figure 58.

The  $S'_{cb}(\nu)$  fits reveal that a very small nonlinearity in y-axis ( $10^{-4}$  %) can yield temperatures differing by 10-20 K for room temperature profiles. Although it's not suggested that  $S'_{cb}(\nu)$  should replace  $S_{cb}(\nu)$  as the correct model, it does indicate that systematic errors in the static cell experiments occurring as small nonlinearities in the spectral profile can have a significant impact on the extracted temperatures.

**Table 17. Extracted temperatures from three positions in the static cell with a temperature gradient for P(46) 17-1 using the CBIMF, CBSAS, MPSF techniques.  $T'_{ex}$  values are the results from fits with  $S'_{cb}(\nu)$ .  $T_{ex}$  values are the results from fits with  $S_{cb}(\nu)$ .**

$X$ (in)	$T_{ex}$ from $S_{cb}(\nu)$ (K)	$T'_{ex}$ from $S'_{cb}(\nu)$ (K)	$T_{ex} - T'_{ex}$ (K)	$T_c$ (K)	Technique
3	$316.47 \pm 0.91$	$294.01 \pm 1.49$	22.46	299.75	CBIMF
2	$309.13 \pm 0.84$	$309.38 \pm 1.85$	-0.25	307.15	“
1	$439.21 \pm 1.52$	$417.19 \pm 2.23$	22.02	366.15	“
3	$302.01 \pm 4.31$	$289.06 \pm 2.33$	12.95		CBSAS
2	$279.31 \pm 1.14$	$308.34 \pm 2.56$	-29.03		“
1	$398.43 \pm 1.45$	$381.61 \pm 2.06$	16.82		“
3	$311.73 \pm 1.00$	$295.40 \pm 1.51$	16.33		MPSF
2	$327.89 \pm 0.96$	$314.81 \pm 1.85$	13.08		“
1	$441.89 \pm 1.25$	$414.97 \pm 1.86$	26.92		“

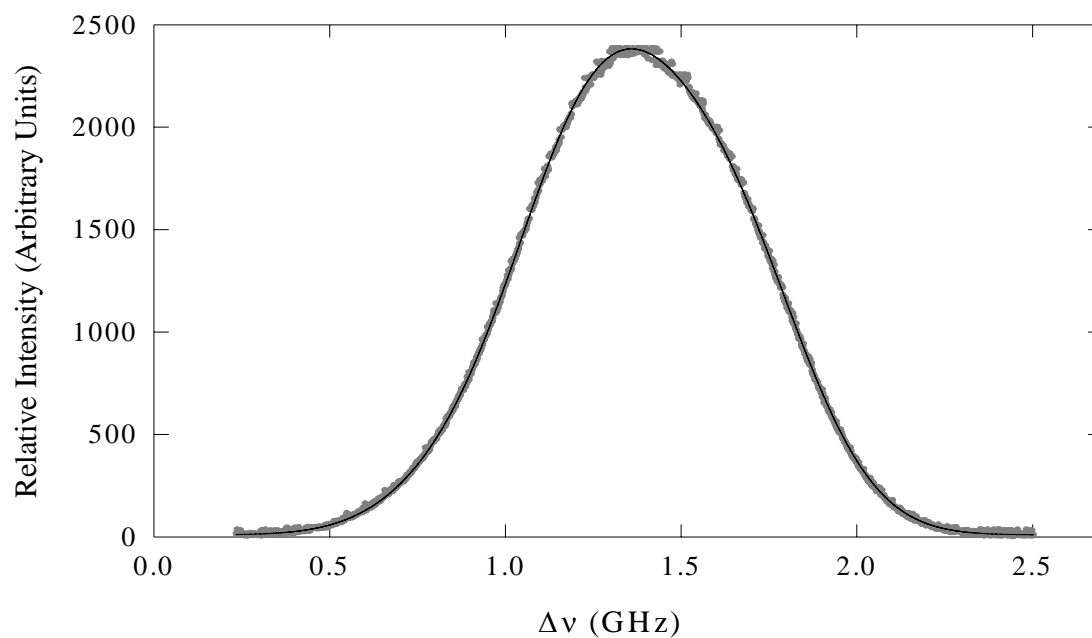


**Figure 55. P(46) 17-1 CBIMF profile at  $X=1$  in static cell with temperature gradient. Experimental data (gray) is fit with  $S_{cb}(\nu)$  (black line).**

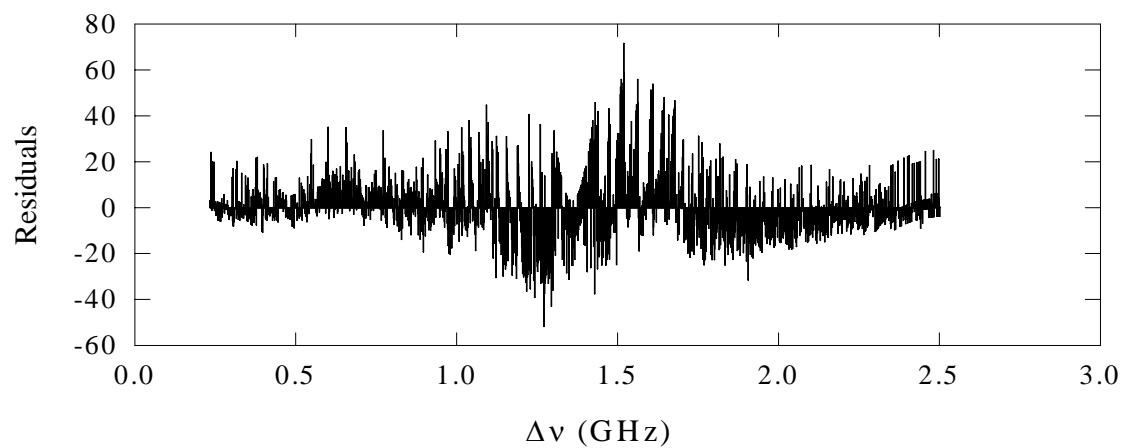


**Figure 56. Residual trend from  $S_{cb}(\nu)$  fit to P(46) 17-1 CBIMF profile at  $X=1$  in static cell with temperature gradient.**

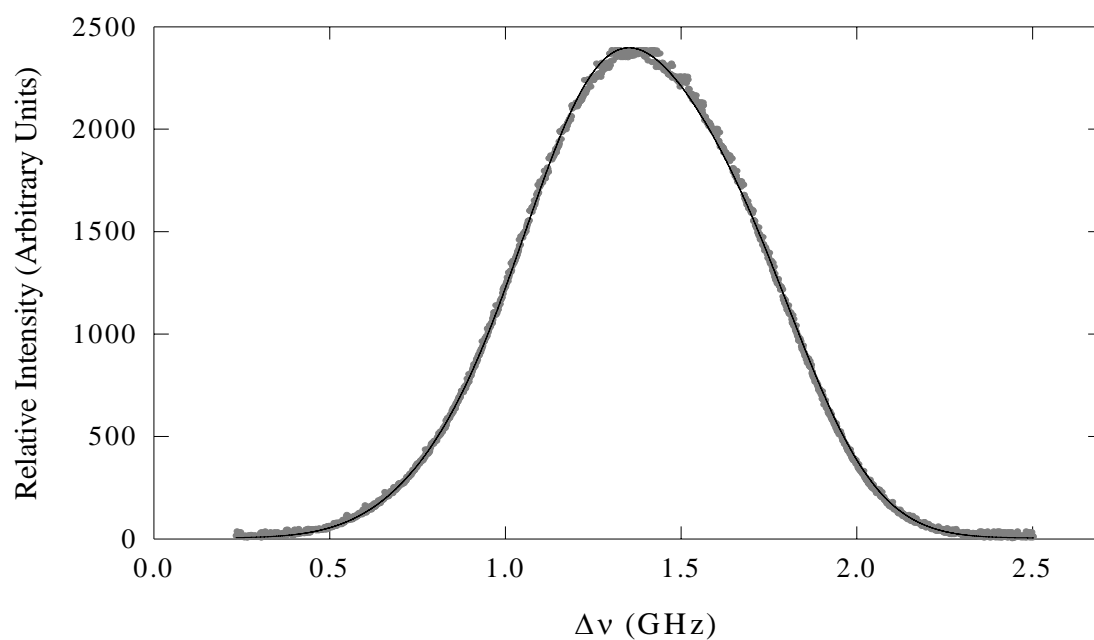


**Figure 57. P(46) 17-1 CBIMF profile at  $X=1$  in static cell with temperature gradient. Experimental data (gray) is fit with  $S'_{cb}(\nu)$  (black line).**

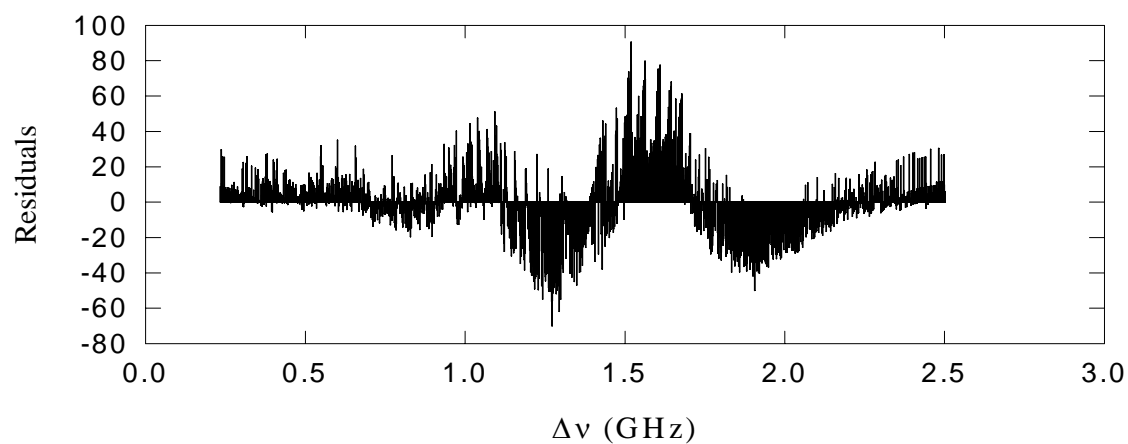


**Figure 58. Residual trend from  $S'_{cb}(\nu)$  fit to P(46) 17-1 CBIMF profile at  $X=1$  in static cell with temperature gradient.**



### C. Spatially-Resolved Temperatures in a Supersonic Nozzle.

#### Experiment.

To assess the applicability of the spatially-resolved temperature diagnostic to COIL, cross-beam measurements were carried out in a small, de Laval nozzle. The nozzle schematic is displayed in Figure 59. The gas/vapor mixture enters the inlet from the left, passes through a diffuser plate, and is accelerated by the converging walls to achieve a Mach number of  $M = 1$  at the throat. The nozzle was designed to achieve a Mach number of  $M = 2$  at the exit plane.<sup>77, 78</sup> Temperature measurements were made by directing the laser beam(s) through the rectangular quartz-glass plates to intersect in the gas flow at the point where the nozzle has a cross-sectional area of  $A=0.7 \text{ cm} \times 1.0 \text{ cm}$ . The small hole in the stainless-steel nozzle-frame is equipped with a quartz glass plug, allowing for optical signal detection perpendicular to the beam direction. The other quartz plug was removed and replaced by a  $\frac{1}{4}$ " OD polyethylene tube with its end positioned flush with the inner wall of the nozzle for pressure measurement. The nozzle itself was housed in a sealed vacuum chamber as shown in Figure 60 and Figure 61. The chamber components were obtained from MDC Vacuum Products Corporation. The nozzle was placed in a stainless steel, six-way cross with minimum clearance between nozzle frame and the cross's inner-walls. The cross was mounted directly to the inlet port of an Alcatel 2063 CP+ vacuum pump (with Alcatel A300 oil) via a short conical reducer. All connections to the cross arms were made with Viton<sup>®</sup> O-ring assemblies and hinge clamps. Two glass view ports were used to transmit the laser beam(s) into and out of the cross. A third glass port was used for viewing laser excitation perpendicular to the beam direction (i.e. fluorescence passing through the quartz glass plug on the nozzle). To connect the  $\frac{1}{2}$ "

glass tubing, external to the cross, to the 1/4" nozzle inlet tube, a 1/2" to 1/4" Cajon<sup>®</sup> fitting was welded in the center of a metal blank, which was fit to the top-most cross-arm. This orients the nozzle vertically with its exhaust directed downward into the pump inlet port. In Figure 61, the tube for pressure measurements inside the nozzle is shown where it extends out of a cross side-arm.

The gas/vapor source consisted of a horizontally positioned 1/2" diameter glass tube in which 5-10 gm of I<sub>2</sub> crystals were laid out along a 4" to 6" length within the tube as shown in Figure 62. The Ar buffer gas passed from its storage tank through 1/4" polyethylene tubing to connect to the upstream end of the glass tube containing the I<sub>2</sub> crystals. The Ar passed over the crystals carrying I<sub>2</sub> vapor into the nozzle. A Baratron pressure transducer was placed at a point just external to the cross for a pressure measurement upstream of the nozzle.

The two nearly co-propagating laser beams were crossed at an angle of  $\theta = 17^\circ$ . The power for each beam (1 mm diameter) was 25 mW as measured at the entrance window on the six-way cross. The overlapping volume of the beams was 2.4 mm<sup>3</sup> and fully contained within the interior of the nozzle. At the face of each rectangular quartz window on the nozzle, a 2 mm spacing between the beams was visually observed. Since the six-way cross was mounted directly on the vacuum pump, the two laser beams had to be directed off the optical table on which the laser rested. A PMT, preceded by a long-pass optical filter, was positioned at the edge of the optical table to view the laser excitation signal that was transmitted through the nozzle quartz plug, then through the glass view port on one of the horizontal cross arms. The distance from the PMT to the face of the cross-arm was 13".

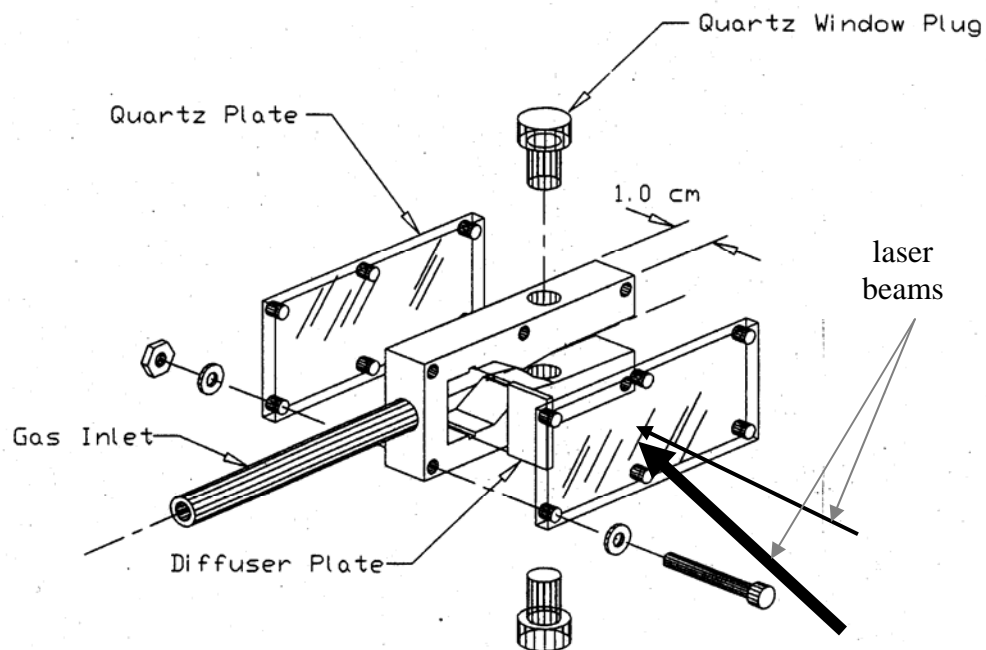
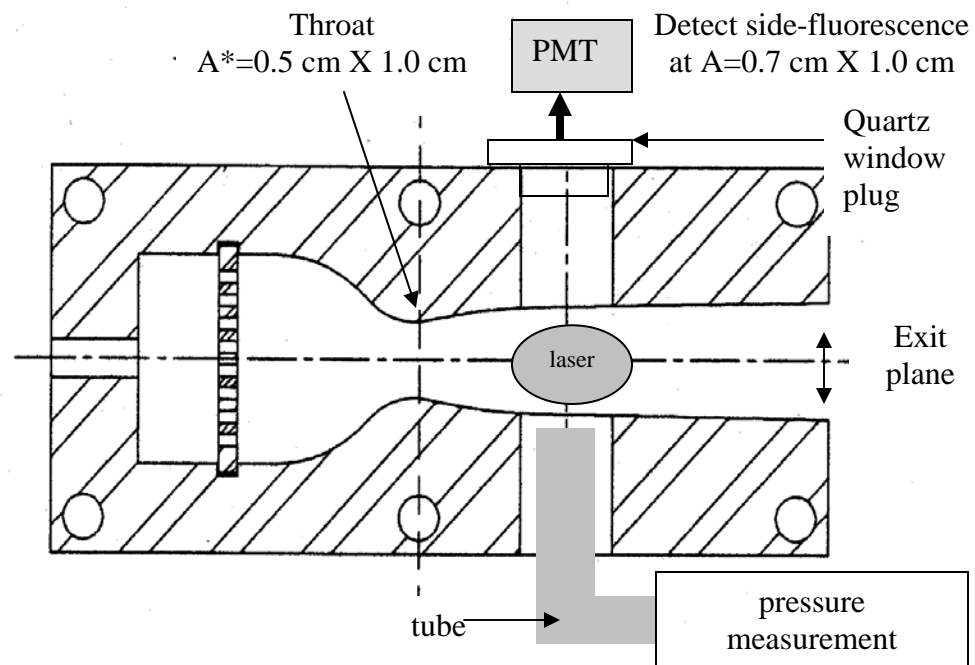


**Figure 59. Nozzle side-view (upper schematic) and nozzle assembly (lower schematic).**

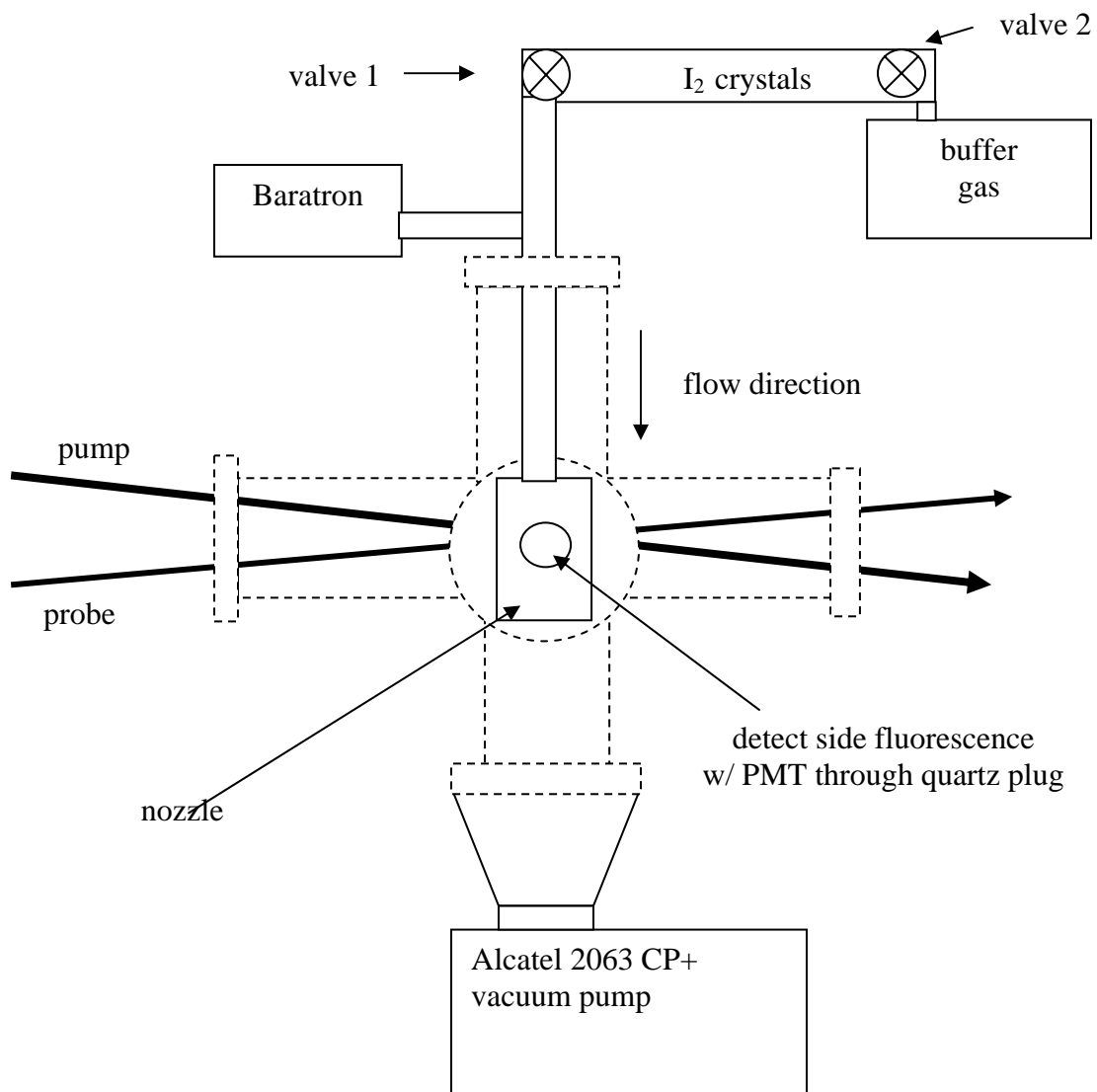


**Figure 60. Supersonic Flow Apparatus (side view).**

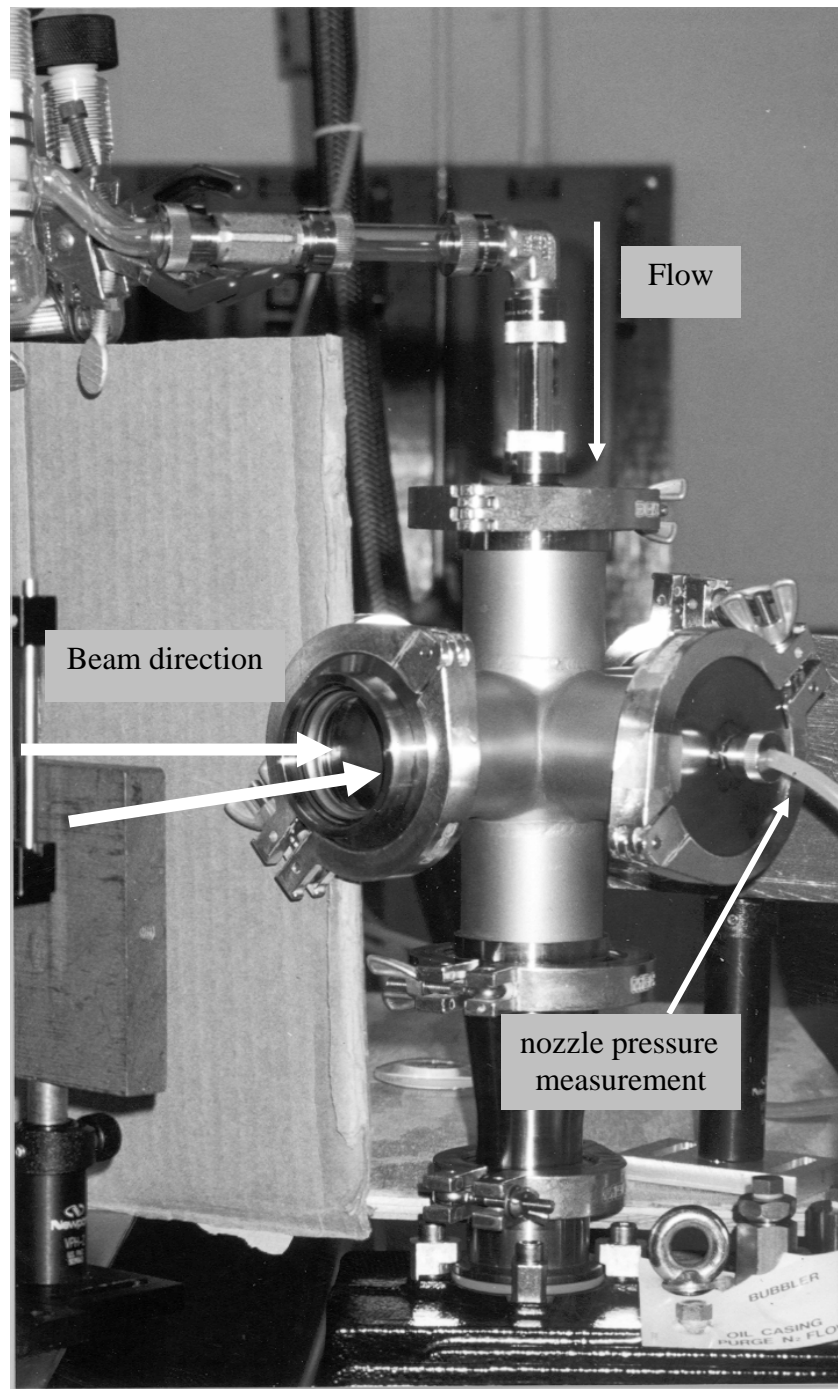


**Figure 61. Six-way cross mounted on pump.**

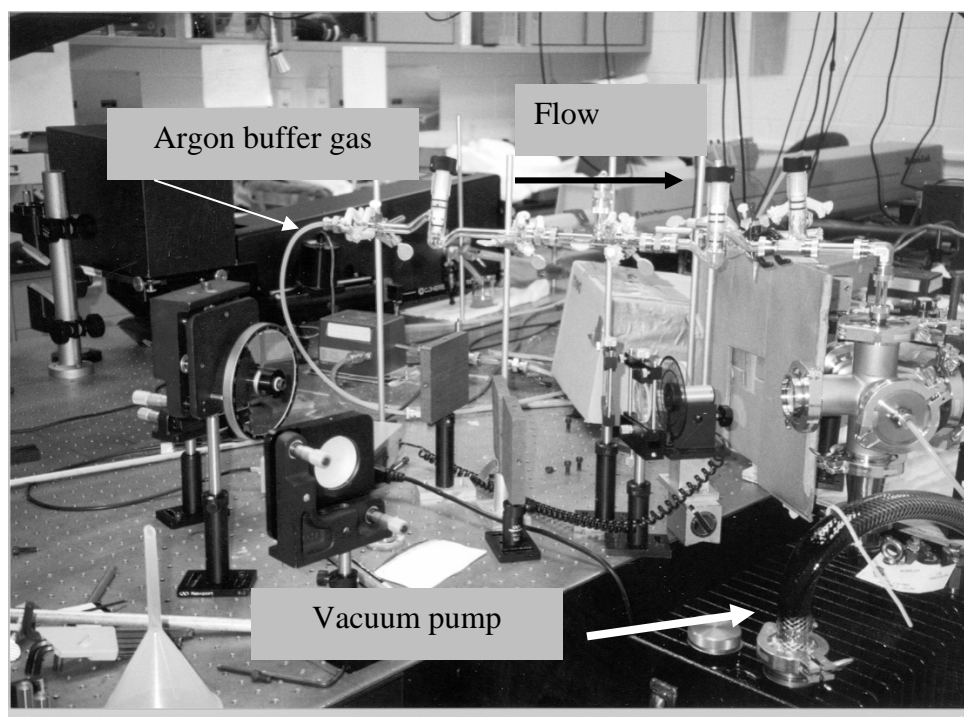
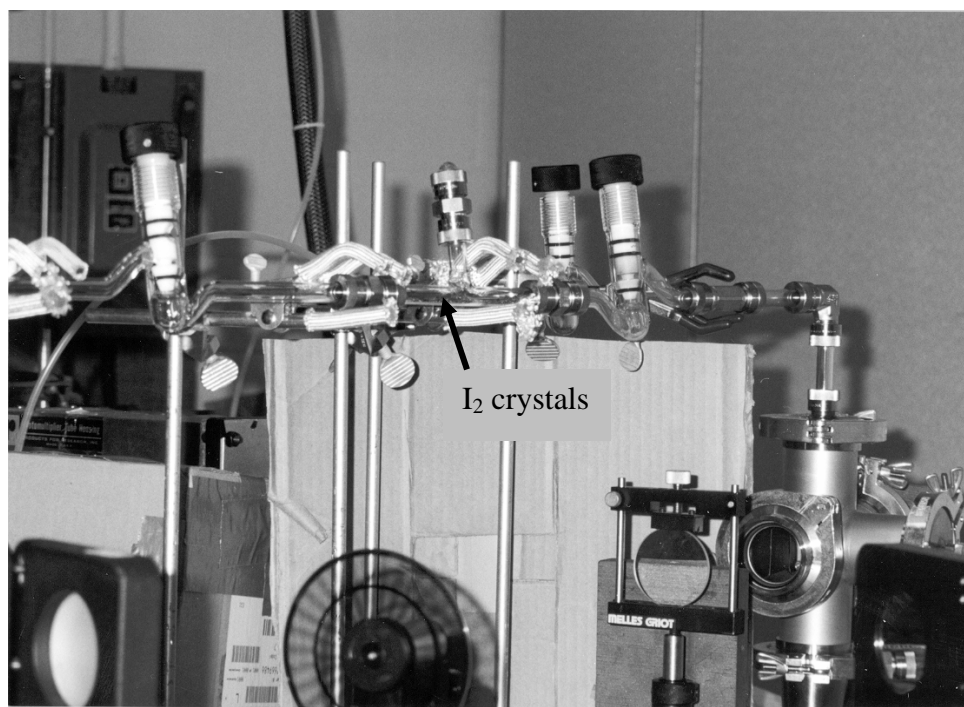


**Figure 62. Gas/vapor inlet plumbing (top photo). Supersonic flow experiment (bottom photo).**

## Results.

To compare against  $T_{ex}$ , a predicted nozzle temperature,  $T_{test}$ , was calculated using Equations (113) and (114) for the test point where the overlapped laser beams interacted with the gas flow. Ar was the choice for the carrier gas. The pertinent data used for the calculations along with the results are displayed in Table 18.

Additional calculations were performed with Equations (115) and (116) to ensure the available vacuum pump could drive the nozzle supersonically. The pertinent data for these calculations and the results are also shown in Table 18. The vacuum pump had a maximum speed of  $S_{max} = 43$  cfm. The maximum volume rate in the nozzle is found from

$$VR_{max} = \frac{w_{max}}{\rho_{throat}} . \quad (143)$$

**Table 18. Nozzle data and calculations.**

Nozzle Design Values	Selected Values	Constants	Calculated Values
$A^* = 0.5 \text{ cm}^2$	$\gamma^{Ar} = 1.669$	$P_{standard} = 101325 \text{ Pa}$	$T_{throat} = 223.61 \text{ K}$
$A_{test} = 0.7 \text{ cm}^2$	$T_o = 298.15 \text{ K}$	$T_{standard} = 273.15 \text{ K}$	$P_{throat} = 14.61 \text{ Torr}$
$M^* = 1$	$P_o = 30 \text{ Torr}$	$\rho_{stp}^{Ar} = 1.7841 \text{ gm/L}^{74}$	$\rho_{throat} = 0.0419 \text{ gm/L}$
$M_{exit} = 2$	$S_{max} = 43 \text{ cfm}$	$R_o = 8.314510 \text{ J/(mole K)}$	$w_{max} = 0.58 \text{ gm/s}$
	$S \cong 38 \text{ cfm}$ @ 3.6 Torr	$\mathcal{M}_{Ar} = 39.948 \text{ gm/mole}$	$M_{test} = 1.858$ @ $A_{test}$
		$R_{Ar} = 208.133 \text{ m}^2/(\text{s}^2 \text{ K})$	$VR_{max} = 29.5 \text{ cfm}$
			$P_{exit} = 3.6 \text{ Torr}$
			$T_{test} = 138.37 \text{ K}$

The mass density of the gas at the throat can be determined from

$$\rho_{throat} = \rho_{stp}^{Ar} \frac{P_{throat}}{P_{standard}} \frac{T_{standard}}{T_{throat}}, \quad (144)$$

where  $\rho_{stp}^{Ar}$  is the Ar gas density at standard temperature and pressure. Using these two equations,  $VR_{max} = 29.5$  cfm. The pump speed,  $S$ , must exceed  $VR_{max}$ . The pump inlet pressure was assumed to be  $P_{exit}$ . From the pump manufacturer's data,  $S \cong 38$  cfm @ 3.6 Torr.<sup>79</sup> This indicated the pump was marginally capable of exceeding the  $VR_{max}$  necessary to drive the nozzle at supersonic speeds.

A spatially-resolved temperature diagnostic was demonstrated in a supersonic flow of Ar seeded with I<sub>2</sub> using CBIMF. A spectral profile obtained from this technique is shown in Figure 63 where the data (in grey) is fit with the Gaussian-based theoretical signal of Equation (134) (in black). The profile shows the highly asymmetric shape as expected from the theoretical predictions at low temperatures shown in Figure 13. The temperature extracted from the fit in Figure 63 is  $T_{ex} = 146.9 \text{ K} \pm 0.4 \text{ K}$ . The residual trend for the fit is shown in Figure 64. The data in Table 19 contains repeated measurements for I<sub>2</sub> P(46)17-1 taken under fixed pressure conditions and at the same location within the nozzle. The first five data files in Table 19 were taken at longer scan times and longer lock-in time constants than were files 6 through 10. The coefficient of determination,  $r^2$ , for the fit improved for a longer scan time and longer time constant. As with the static cell measurements, there was difficulty in the fit to  $k$  as shown in trials 4, 7, 9 and 10.



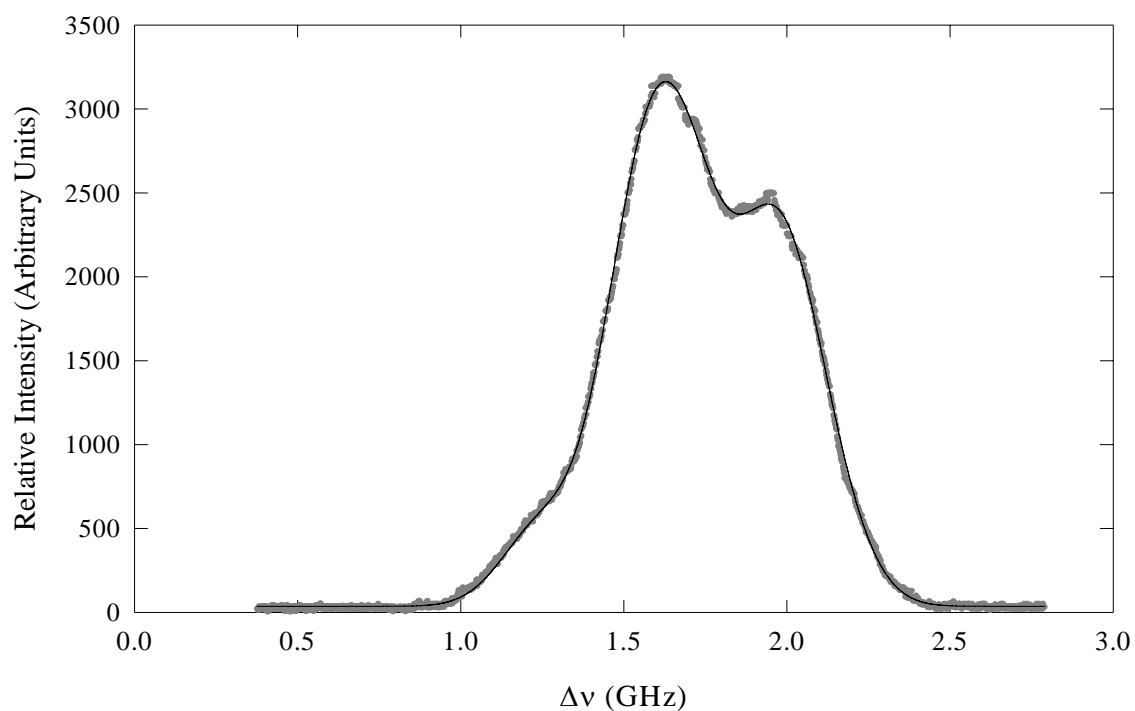


**Figure 63. CBIMF in supersonic nozzle for I<sub>2</sub> P(46) 17-1. The experimental data points are gray. The theoretical fit to the data is represented by the black line.**

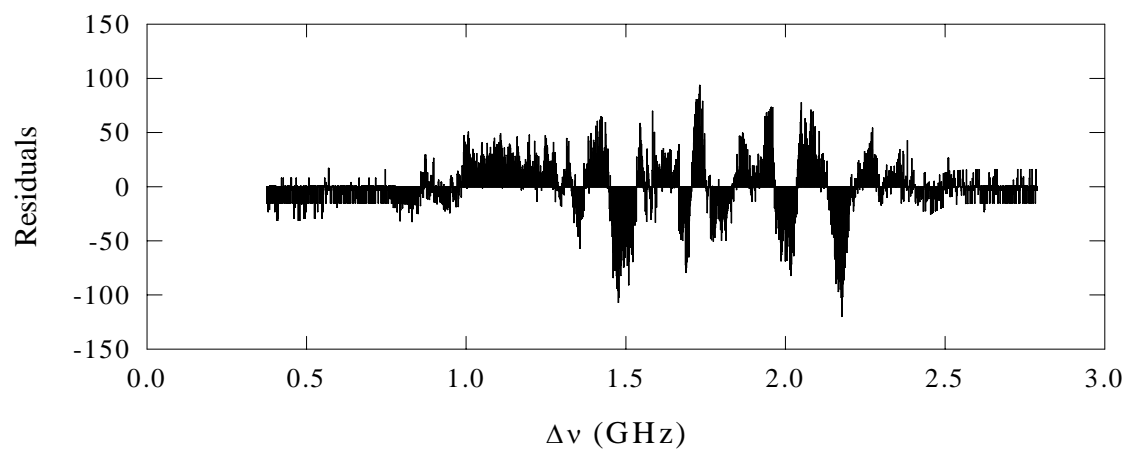


**Figure 64. Residual trend for CBIMF profile of I<sub>2</sub> P(46) 17-1 in supersonic nozzle.**

**Table 19. CBIMF for I<sub>2</sub> P(46) 17-1 in supersonic nozzle with Ar/I<sub>2</sub>. Consecutive measurements for same pressure and location.**

<b>Trial</b>	<b><math>T_{ex}</math> (K)</b>	<b><math>P_{inlet}</math> (Torr)</b>	<b><math>P_{nozzle}</math> (Torr)</b>	<b><math>k</math> (X <math>10^{-5}</math>) (s<sup>-1</sup>)</b>
1	146.89 ± 0.43	14.75	1.2	1.52 ± 0.09
2	150.52 ± 0.62	14.73	1.1	4.19 ± 0.15
3	141.23 ± 0.51	14.70	1.1	4.14 ± 0.15
4	149.24 ± 0.54	14.76	1.1	0.007 ± 0.15
5	162.95 ± 0.64	14.74	1.1	0.3 ± 0.17
6	139.86 ± 0.81	14.91	1.1	2.62 ± 0.26
7	147.17 ± 1.16	15.06	1.2	0.003 ± 0.4
8	136.42 ± 0.81	14.97	1.2	4.81 ± 0.24
9	153.96 ± 1.11	15.06	1.2	0.03 ± 0.4
10	151.61 ± 1.06	14.99	1.2	0.03 ± 0.4
<b>Average</b>	<b>147.98 ± 0.77</b>			

The same type experiment was performed for I<sub>2</sub> P(31) 17-1 ro-vibrational line which has a twenty-one line hyperfine spectrum. The SNR was, in general, lower compared to the P(46) 17-1 data as shown in Figure 65. The residual trend for the fit is shown in Figure 66. Again, as can be seen in Table 20, the absorption parameter proved difficult to fit. However, the average temperature of 147 K obtained from consecutive measurements agrees well with the P(46) 17-1 average  $T_{ex}$  value.

For comparison to the CBIMF technique, laser excitation measurements using Single Beam Side-Fluorescence (SBSF) were performed under the same conditions as stated above for both the P(46) 17-1 and P(31) 17-1 ro-vibrational lines. Without changing the two-beam configuration for the CBIMF experiment, one of the incident beams was simply blocked from entering the six-way cross. The single beam that did enter the six-way cross was oriented at an 8.5° angle relative to a line perpendicular to window on the cross-arm and to the rectangular nozzle window.

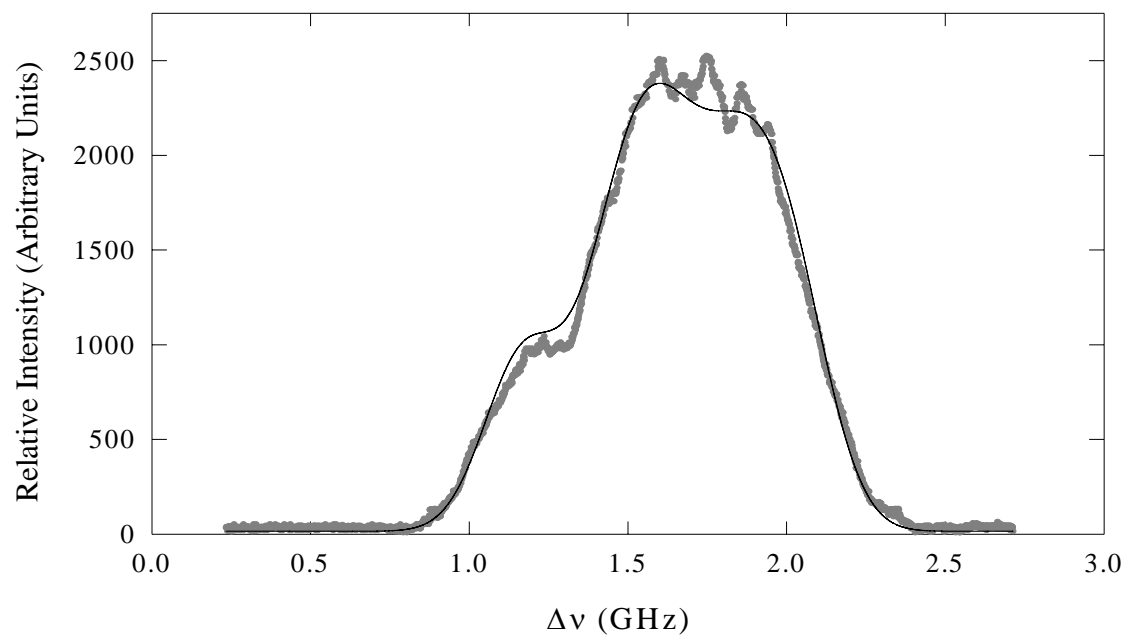


**Figure 65. CBIMF in supersonic nozzle for  $I_2$  P(31) 17-1. The experimental data points are gray. The theoretical fit to the data is represented by the black line.**

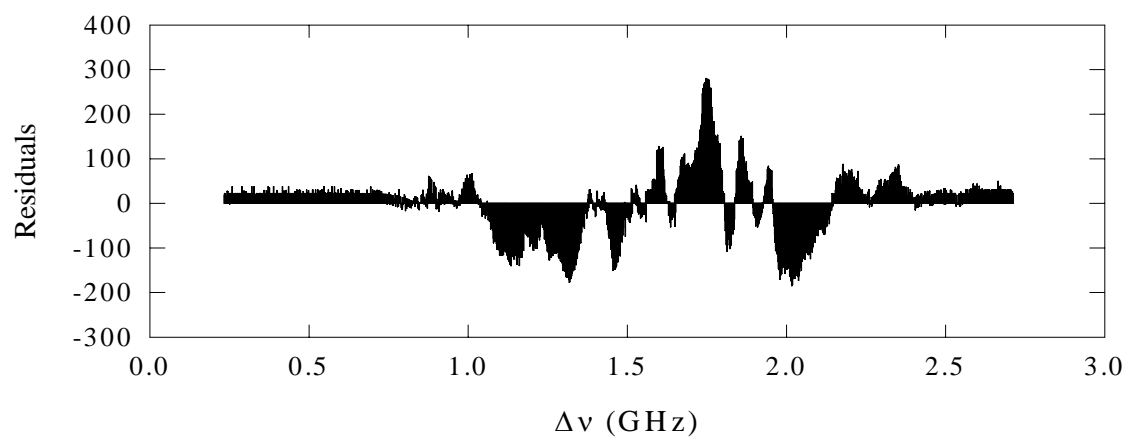


**Figure 66. Residual trend for CBIMF profile of  $I_2$  P(31) 17-1 in supersonic nozzle.**

**Table 20. CBIMF for I<sub>2</sub> P(31) 17-1 in supersonic nozzle with Ar/I<sub>2</sub>. Consecutive measurements for same pressure and location.**

<b>Trial</b>	<b><math>T_{ex}</math> (K)</b>	<b><math>P_{inlet}</math> (Torr)</b>	<b><math>P_{nozzle}</math> (Torr)</b>	<b><math>k</math> (X 10<sup>-5</sup>) (s<sup>-1</sup>)</b>
1	139.50 ± 1.36	14.79	1.1	0.0003 ± 0.3
2	147.29 ± 1.43	14.85	1.1	0.0001 ± 0.3
3	145.98 ± 1.54	14.87	1.1	0.00003 ± 0.3
4	142.30 ± 1.38	15.14	1.1	0.003 ± 0.3
5	157.55 ± 1.79	15.05	1.1	0.0002 ± 0.4
<b>Average</b>	<b>146.52 ± 1.50</b>			

A fit to the SBSF signal for the P(46) 17-1 ro-vibrational line is shown in Figure 67. The residual trend for the P(46) 17-1 SBSF fit is shown in Figure 70. A fit to the SBSF signal for the P(31) 17-1 ro-vibrational line is shown in Figure 69. The residual trend for the P(31) 17-1 SBSF fit is shown in Figure 70. Again, repeated measurements were performed under similar conditions for each ro-vibrational line and the extracted temperatures, pressure conditions, and absorption parameters are listed in Table 21 for P(46) 17-1 and in Table 22 for P(31) 17-1. The signal for the single beam side-fluorescence measurements is two orders of magnitude stronger than for the CBIMF measurement. The fits to the SBSF signals are better than for the CBIMF signals according the residual trends. In general, the standard errors in  $T_{ex}$  and  $k$  were smaller for SBSF than for CBIMF. The average SBSF temperature for both ro-vibrational lines was 47-48 K higher than for the corresponding CBIMF data, which was expected since the single beam was not oriented perpendicular to the gas flow. The SBSF beam interacted with the flow simultaneously at upstream positions and downstream positions which were at different temperatures. Fluorescence from all positions contributed to the SBSF signal.

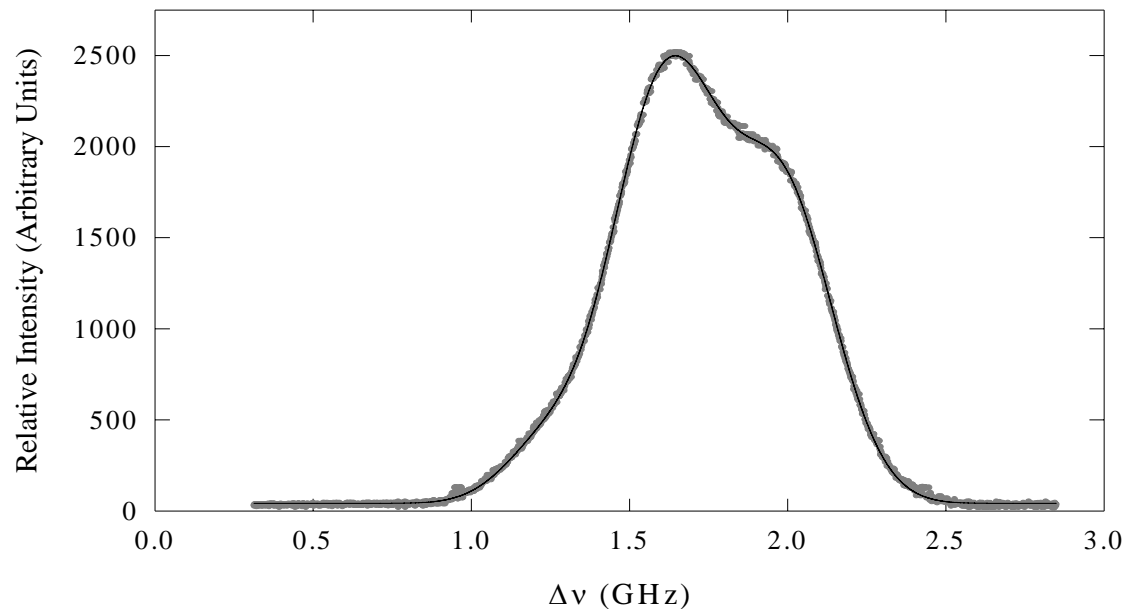


**Figure 67. Single Beam Side Fluorescence in supersonic nozzle for P (46) 17-1. The experimental data points are gray. The theoretical fit to the data is represented by the black line.**

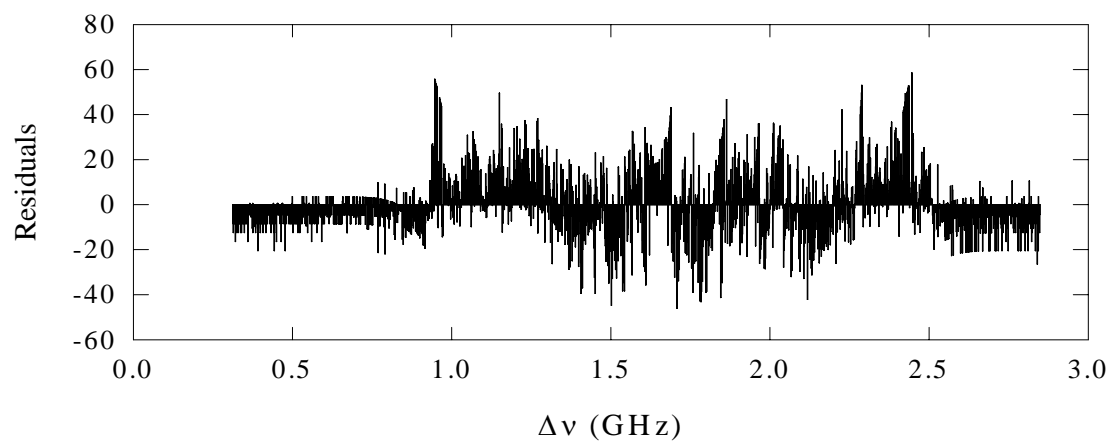


**Figure 68. Residual trend for SBSF profile of I<sub>2</sub> P(46) 17-1 in supersonic nozzle.**

**Table 21. Single Beam Side Fluorescence for I<sub>2</sub> P(46) 17-1 in supersonic nozzle with Ar/I<sub>2</sub>. Consecutive measurements for same pressure and location.**

<b>Trial</b>	<b><math>T_{ex}</math> (K)</b>	<b><math>P_{inlet}</math> (Torr)</b>	<b><math>P_{nozzle}</math> (Torr)</b>	<b><math>k</math> (X <math>10^{-5}</math>) (s<sup>-1</sup>)</b>
1	195.65 ± 0.45	15.09	1.2	3.68 ± 0.06
2	198.36 ± 0.47	15.06	1.2	3.21 ± 0.07
3	196.54 ± 0.40	14.92	1.2	2.90 ± 0.06
4	196.40 ± 0.43	15.11	1.2	2.29 ± 0.07
5	197.86 ± 0.42	15.06	1.2	2.48 ± 0.07
<b>Average</b>	<b>196.96 ± 0.43</b>			

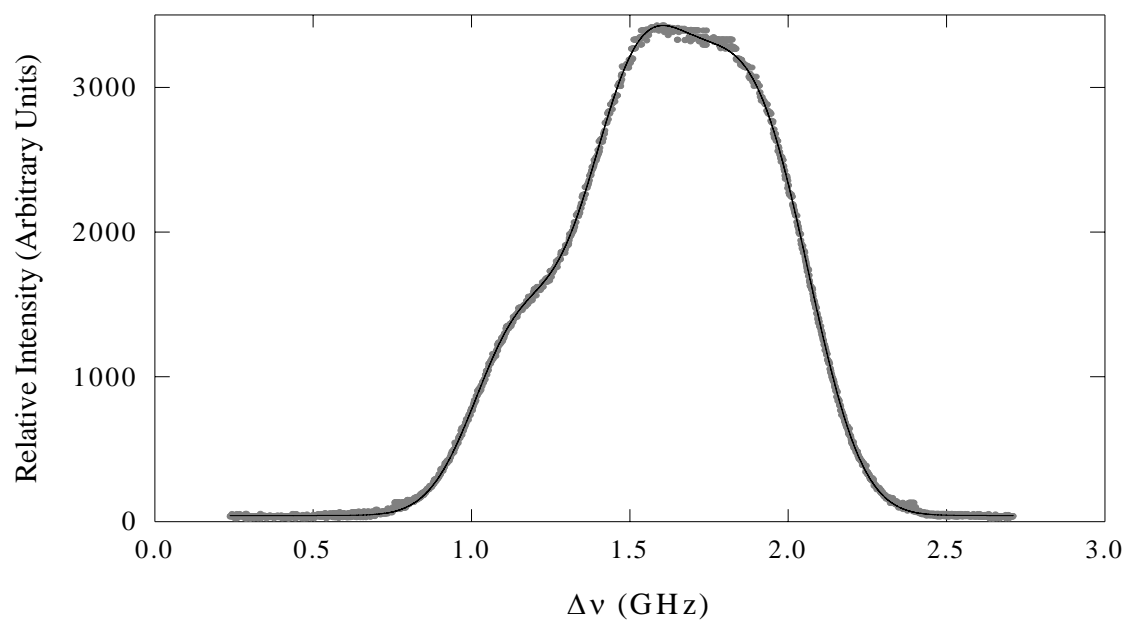


**Figure 69. Single Beam Side Fluorescence in supersonic nozzle for P(31) 17-1. The experimental data points are gray. The theoretical fit to the data is represented by the black line.**

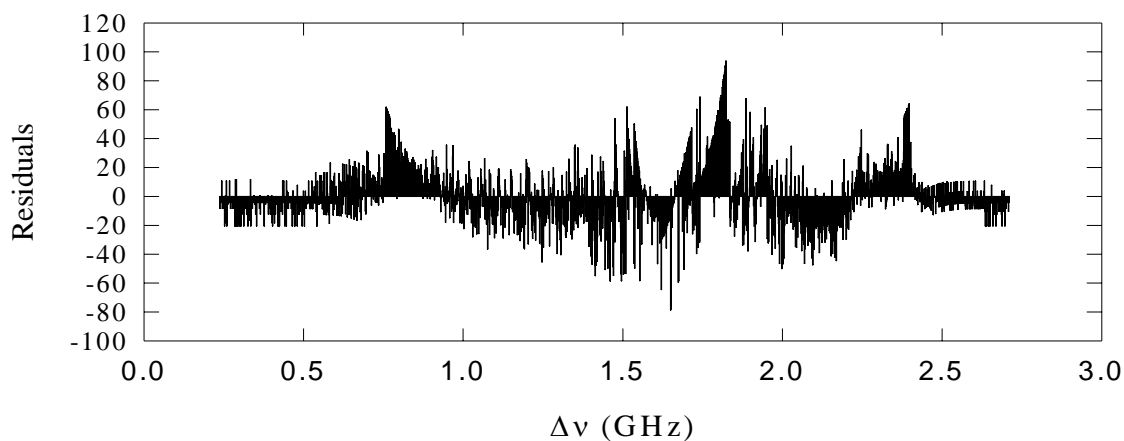


**Figure 70. Residual trend for SBSF profile of I<sub>2</sub> P(31) 17-1 in supersonic nozzle.**

**Table 22. Single Beam Side Fluorescence for I<sub>2</sub> P(31) 17-1 in supersonic nozzle with Ar/I<sub>2</sub>. Consecutive measurements for same pressure and location.**

<b>Trial</b>	<b><math>T_{ex}</math> (K)</b>	<b><math>P_{inlet}</math> (Torr)</b>	<b><math>P_{nozzle}</math> (Torr)</b>	<b><math>k</math> (X <math>10^{-5}</math>) (s<sup>-1</sup>)</b>	<b>nozzle condition</b>
1	$289.77 \pm 1.78$	0.1763	0.1674	$0.02 \pm 0.1$	no flow
2	$194.71 \pm 0.42$	15.13	1.2	$0.004 \pm 0.04$	flow
3	$195.07 \pm 0.42$	15.08	1.2	$0.009 \pm 0.04$	“
4	$195.70 \pm 0.46$	15.02	1.2	$0.0005 \pm 0.05$	“
5	$193.83 \pm 0.42$	15.15	1.2	$0.02 \pm 0.04$	“
6	$193.78 \pm 0.48$	15.12	1.2	$0.6 \pm 0.05$	“
<b>Average #2-#6</b>	<b><math>194.62 \pm 0.44</math></b>				

Spectral profile data was also collected for the P(10) 19-2 & R(104) 18-1 blended line using both the SBSF at non-perpendicular angle to the gas flow and CBIMF, as shown in Figure 71 and Figure 72, respectively. The SBSF and CBIMF measurements listed in Table 23 were taken at several different pressures. The annotation “no flow/

residual” means the vacuum pump was running, but the valves in Figure 60 were closed preventing gas flow from entering the nozzle. In some cases, even after pumping down the six-way cross overnight, there was typically enough residual  $I_2$  remaining in the test region to produce an easily detectable SBSF signal, and occasionally a weak and noisy CBIMF signal. The “no flow” SBSF linewidth extracted temperature of  $293\text{ K} \pm 1.4\text{ K}$  has reasonable agreement with a room temperature measurement by thermocouple external to the cross of  $296\text{ K}$ .

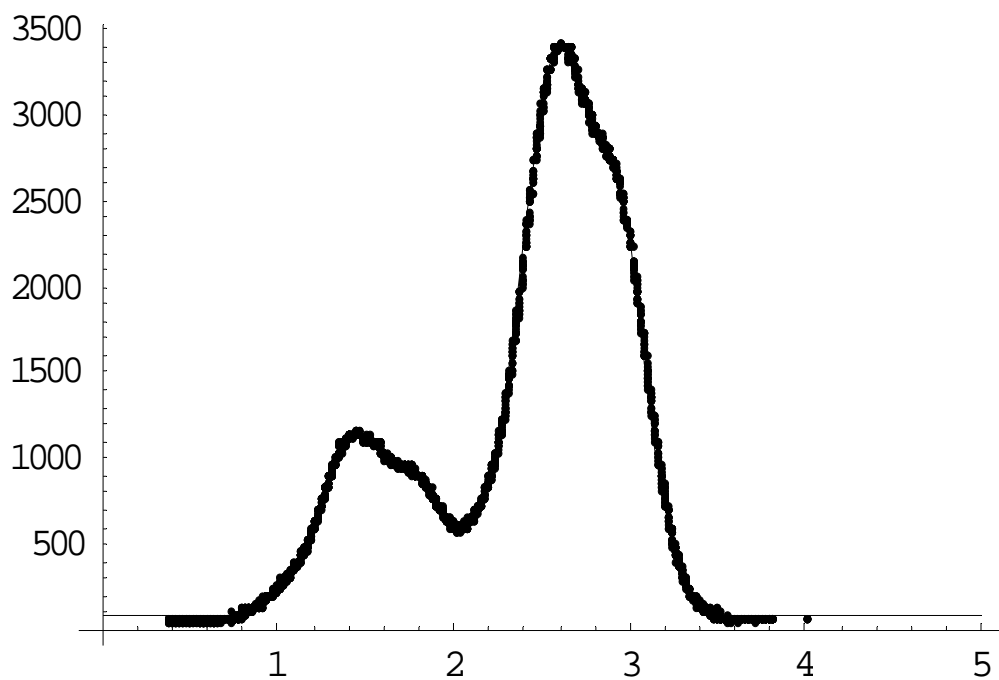


**Figure 71. SBSF in supersonic nozzle for P(10) 19-2 & R(104) 18-1. The y-axis is Relative Intensity (Arbitrary Units). The x-axis is  $\Delta\nu$  (GHz).**



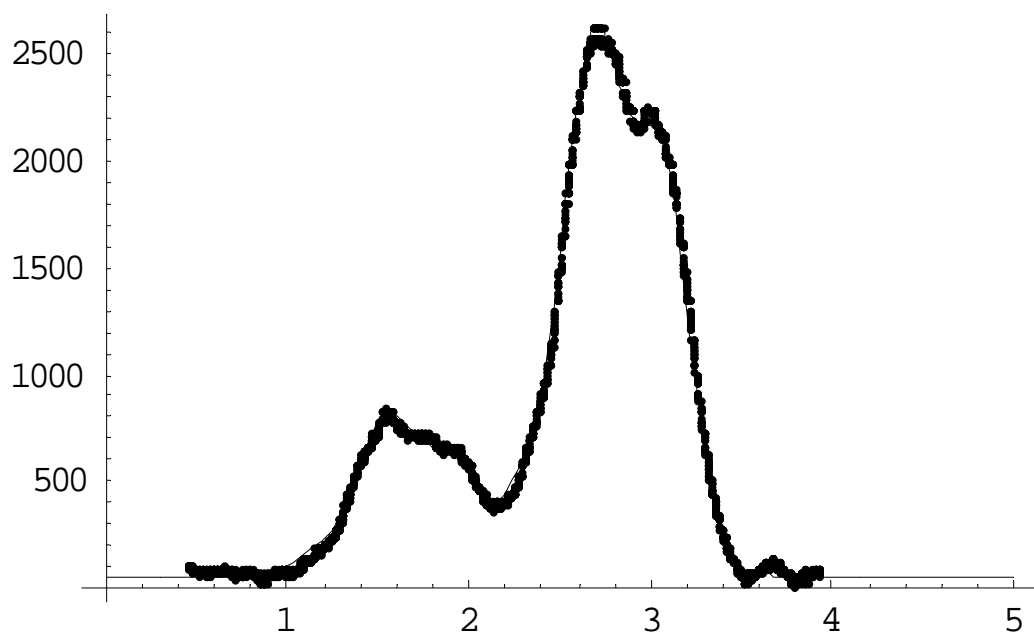


**Figure 72. CBIMF in supersonic nozzle for P(10) 19-2 & R(104) 18-1. The y-axis is Relative Intensity (Arbitrary Units). The x-axis is  $\Delta\nu$  (GHz).**

**Table 23. SBSF and CBIMF measurements for P(10) 19-2 & R(104) 18-1 in supersonic nozzle.**

<b>Trial</b>	<b><math>T_{ex}</math> (K)</b>	<b><math>P_{inlet}</math> (Torr)</b>	<b><math>P_{nozzle}</math> (Torr)</b>	<b>Gas Flow</b>	<b>Technique</b>
1	$292.51 \pm 1.39$	0.17	0.16	no flow	SBSF
2	$317.87 \pm 1.17$	0.21	0.15	I <sub>2</sub> only	SBSF
3	$229.08 \pm 0.48$	13.93	1.07	I <sub>2</sub> + Ar	SBSF
4	$229.40 \pm 0.50$	29.94	2.10	“	SBSF
5	$165.88 \pm 0.65$	13.56	1.05	“	CBIMF
6	$174.28 \pm 1.15$	15.05	1.10	“	CBIMF

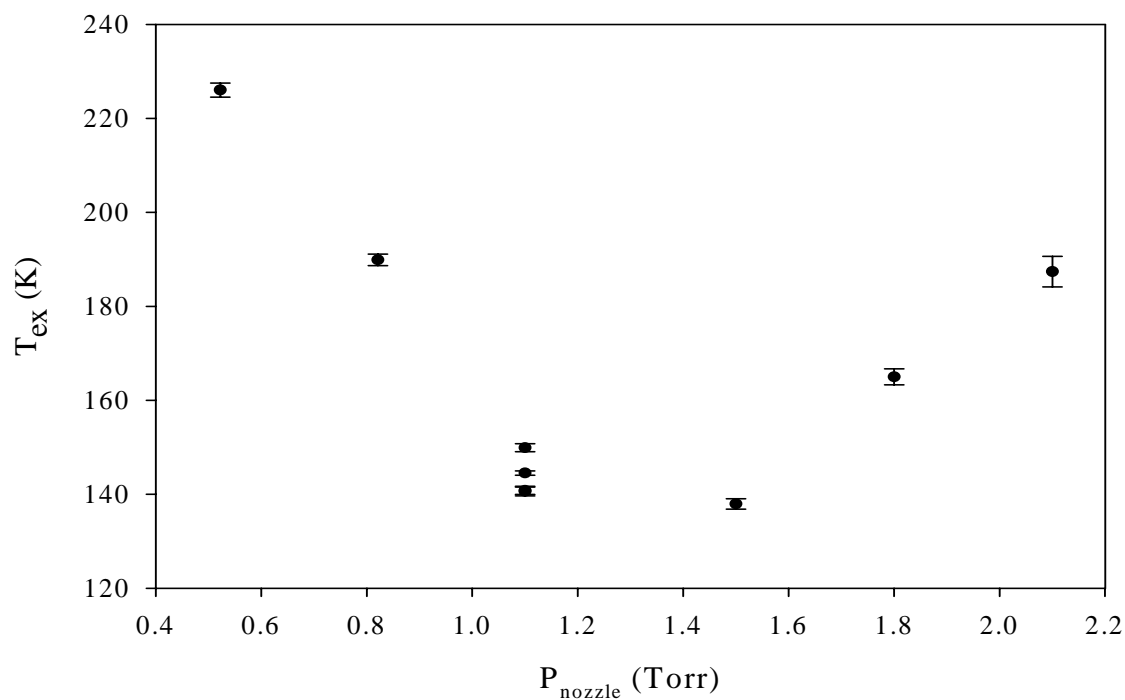


**Figure 73.** CBIMF for P(46) 17-1 in nozzle for various  $I_2/\text{Ar}$  pressures.

**Table 24.** CBIMF for P(46) 17-1 in nozzle for various  $I_2/\text{Ar}$  pressures.

Trial	$T_{\text{ex}}$ (K)	$P_{\text{inlet}}$ (Torr)	$P_{\text{nozzle}}$ (Torr)	$k$ (X $10^{-5}$ ) ( $\text{s}^{-1}$ )
1	$140.61 \pm 0.93$	13.94	1.1	$2.31 \pm 0.3$
2	$149.92 \pm 0.84$	14.42	1.1	$2.31 \pm 0.1$
3	$144.52 \pm 0.45$	14.55	1.1	$3.45 \pm 0.07$
4	$140.84 \pm 0.88$	14.54	1.1	$2.53 \pm 0.2$
5	$226.02 \pm 1.48$	5.4	0.52	$0.0003 \pm 0.2$
6	$189.89 \pm 1.25$	10.26	0.82	$1.19 \pm 0.3$
7	$137.95 \pm 1.11$	20.91	1.5	$0.0005 \pm 0.3$
8	$165.00 \pm 1.72$	25.28	1.8	$0.002 \pm 0.5$
9	$187.40 \pm 3.25$	30.19	2.1	$0.002 \pm 0.95$

It was observed that the nozzle produced supersonic flow and a minimum temperature when the inlet pressure was  $\approx 15$  Torr corresponding to nozzle pressure  $\approx 1.1$  Torr measured at the beam crossing point. The CBIMF extracted temperature obtained using Gaussian fits increased with increasing nozzle pressure as shown in Figure 73 and Table 24. The same was observed for SBSF measurements made at the oblique angle to the nozzle as displayed in Figure 74 and Table 25. For CBIMF, the SNR deteriorated rapidly above a 30 Torr inlet pressure. Higher-pressure measurements were obtained for the SBSF due to stronger SNR. The increase in  $T_{ex}$  with increasing pressure above 15 Torr inlet pressure was not entirely due to pressure broadening. Attempts to fit the data with Voigt profiles constrained to have a fixed Lorentzian width still resulted in higher temperatures at the higher pressures. As the pressure in the nozzle is increased by increasing the inlet pressure, it is plausible that it begins to exceed the pressure (the “back pressure”) in the six-way cross external to the nozzle as maintained by the vacuum pump. If so, a shock wave could form inside the nozzle at a position dependent on the extent to which  $P_{nozzle}$  exceeds the back pressure. As  $P_{nozzle}$  increases above the back pressure, the shock wave will appear further upstream and approach the throat. This disturbance in the gas flow could influence the temperature measurement at the test point.

#### Discussion.

The temperature of a gas in a supersonic nozzle was obtained from CBIMF and SBSF measurements. The experimental signals agree with the theoretical predictions shown in Figure 13 and Figure 14. Given the differences between the simple calculation of temperature in an ideal nozzle and the flow dynamics

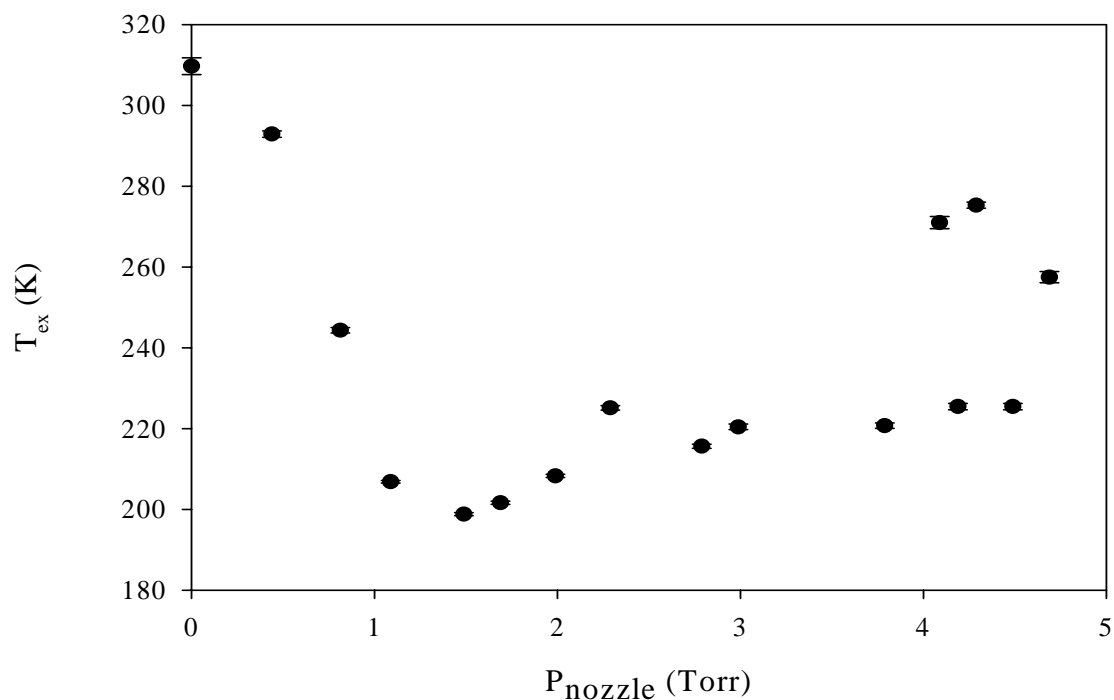


**Figure 74.** SBSF for P(46) 17-1 in nozzle for various I<sub>2</sub>/Ar pressures.

**Table 25.** SBSF for P(46) 17-1 in nozzle for various I<sub>2</sub>/Ar pressures.

Trial	$T_{\text{ex}}$ (K)	$P_{\text{inlet}}$ (Torr)	$P_{\text{nozzle}}$ (Torr)	$k$ (X 10 <sup>-5</sup> ) (s <sup>-1</sup> )
1	309.43 ± 1.89	0.1	0.1	5.24 ± 0.12
2	287.58 ± 0.71	5.8	0.4	2.29 ± 0.07
3	241.72 ± 0.62	11.8	0.8	4.33 ± .01
4	206.08 ± 0.33	15.4	1.1	2.4 ± 0.03
5	195.34 ± 0.35	21.4	1.5	1.34 ± 0.05
6	199.91 ± 0.38	25.6	1.7	1.99 ± 0.06
7	204.85 ± 0.38	30.2	2.0	3.16 ± 0.06
8	218.26 ± 0.50	35.0	2.3	2.15 ± 0.04
9	213.56 ± 0.48	40.0	2.8	2.60 ± 0.05
10	218.48 ± 0.63	43.0	3.0	0.05 ± 0.09
11	211.50 ± 0.58	51.3	3.8	2.58 ± 0.08
12	214.73 ± 0.70	51.3	3.8	2.58 ± 0.08
13	222.20 ± 0.66	60.4	4.5	2.51 ± 0.06
14	243.00 ± 0.75	65.8	4.7	1.99 ± 0.07
15	270.51 ± 0.73	70.6	4.3	1.93 ± 0.06
16	265.12 ± 1.33	80.5	4.1	2.58 ± 0.1

in a real nozzle, the  $T_{ex}$  values are reasonable. The CBIMF results for the blended line P(10) 19-2 & R(104) 18-1 were higher in temperature than those for the isolated lines by at least 17 K. The profile for this blended line in Figure 72 shows features due to noise which likely contributed to the inaccuracy of the extracted temperature. Using isolated lines, the experiments in which extracted temperature varied with gas/vapor pressure further establish the temperature diagnostic as an indicator of the nozzle performance.

In addition to the CBIMF and SBSF measurements, efforts were made to employ CBSAS in the nozzle. There was not sufficient SNR in the CBSAS signal for reliable temperature extraction. This was most likely due to the small overlap volume and the difficulty in detecting a small change in a large signal. To operate within the constraints of the experimental configuration, it was necessary to use a minimum  $17^\circ$  beam-crossing angle to ensure the overlap volume was contained within the nozzle. Therefore, it was not possible to explore any the advantage that a smaller crossing angle (and correspondingly larger overlap volume) could provide for the CBSAS technique.

To estimate the influence of systematic errors on the extracted temperatures in the nozzle, the CBIMF results for P(46) 17-1 were fit with  $S'_{CB}(\nu)$  from Equation (138). The extracted temperatures from these fits are shown in Table 26 where the results from Table 19 are repeated for comparison. The effect of the nonlinearity term in  $S'_{CB}(\nu)$  typically lowers the temperatures by less than 8 K. The statistical errors, with one exception, are larger. The fits of  $S'_{CB}(\nu)$  to the data are worse in all cases than the  $S_{CB}(\nu)$  fits. As an example, a  $S'_{CB}(\nu)$  fit is shown in Figure 75. The spectral data is the same as the data in Figure 63. The residuals for the  $S'_{CB}(\nu)$  fit are shown in Figure 76.

In general, the differences  $T_{ex} - T'_{ex}$  were smaller for the  $S'_{CB}(\nu)$  fits to the nozzle signals than for the static cell signals listed in Table 17. At the nozzle temperatures, the spectral profile reveals more features of the hyperfine structure than at temperatures  $> 293$  K where the spectral profiles are broad and featureless. A small variation in the spectral signal due to a nonlinearity in the y-axis appears to have less of an impact on the extracted temperature for temperatures much less than 293 K.

*Applicability of Temperature Diagnostic to COIL.*

To ascertain if the temperature diagnostic would be practical for use in the COIL, it is necessary to present some background on the device with emphasis on the operating temperature in addition to an estimate of the  $I_2$  pressure in the gain region. The physical configuration of the COIL must also be considered as it pertains to accessing the gain region with the diagnostic.

**Table 26. CBIMF for  $I_2$  P(46) 17-1 in supersonic nozzle with Ar/ $I_2$ . Consecutive measurements for same pressure and location.  $T'_{ex}$  values are the results from fits with  $S'_{CB}(\nu)$ .  $T_{ex}$  values are the results from fits with  $S_{CB}(\nu)$ .**

<b>Trial</b>	<b><math>T_{ex}</math> from <math>S_{CB}(\nu)</math> (K)</b>	<b><math>T'_{ex}</math> from <math>S'_{CB}(\nu)</math> (K)</b>	<b><math>T_{ex} - T'_{ex}</math> (K)</b>
1	$146.89 \pm 0.43$	$140.47 \pm 0.73$	6.43
2	$150.52 \pm 0.62$	$144.35 \pm 0.56$	6.17
3	$141.23 \pm 0.51$	$136.04 \pm 0.78$	5.19
4	$149.24 \pm 0.54$	$154.59 \pm 0.82$	-5.35
5	$162.95 \pm 0.64$	$155.73 \pm 0.76$	7.22
6	$139.86 \pm 0.81$	$134.61 \pm 1.08$	5.25
7	$147.17 \pm 1.16$	$144.20 \pm 1.24$	2.97
8	$136.42 \pm 0.81$	$129.63 \pm 0.96$	6.78
9	$153.96 \pm 1.11$	$145.87 \pm 1.10$	8.09
10	$151.61 \pm 1.06$	$150.48 \pm 1.41$	1.14
<b>Average</b>	<b><math>147.98 \pm 0.77</math></b>	<b><math>143.60 \pm 0.94</math></b>	<b>4.39</b>

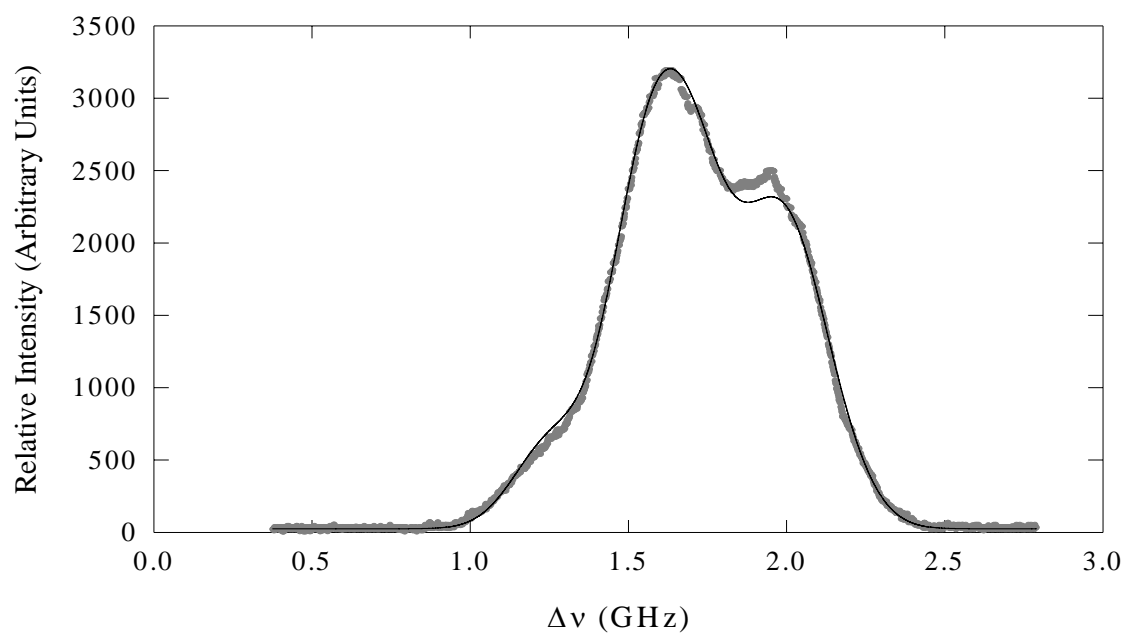


**Figure 75.** CBIMF in supersonic nozzle for  $I_2$  P(46) 17-1. Experimental data (gray) is fit with  $S'_{CB}(\nu)$  (black line).

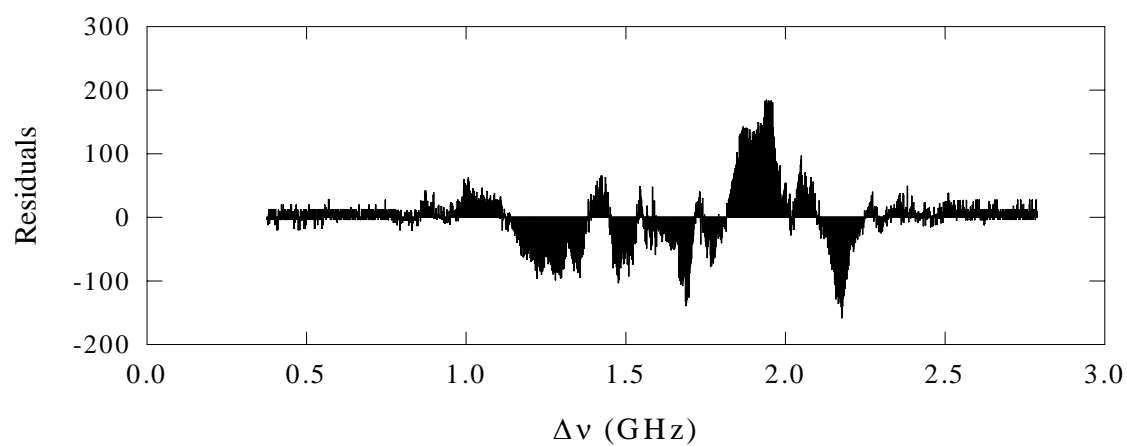


**Figure 76.** Residual trend from  $S'_{CB}(\nu)$  fit to CBIMF in supersonic nozzle for  $I_2$  P(46) 17-1.

The COIL relies on an exothermal chemical reaction to create a population inversion. Initially, oxygen is prepared in a metastable excited state,  $O_2(a^1\Delta)$  with a radiative lifetime of 64 minutes. The energy from this metastable reservoir is transferred by collision to atomic iodine in the  $^2P_{1/2}$  state. A population inversion is established between  $I(^2P_{1/2})$  and  $I(^2P_{3/2})$ . Lasing occurs at the wavelength  $\lambda = 1.315\mu m$ . The relationship between the energy levels of the two species is illustrated in Figure 77. Details concerning laser generation can be found in numerous references.<sup>7, 80</sup>

The threshold for lasing is dependent on the concentration ratio of  $O_2(a^1\Delta)$  to total oxygen. At a temperature of 295 K, this ratio is approximately 15%. Exploiting the dependence of the equilibrium constant on temperature can reduce this threshold. By employing a supersonic nozzle to mix the oxygen and iodine, a temperature of 160 K is attainable at which the threshold yield (the ratio  $O_2(a^1\Delta)/O_2$ ) is reduced to 5%.<sup>10</sup> A schematic of a supersonic COIL is shown in Figure 78.

In a typical COIL gain region, the static pressure of the supersonic flow is 5 Torr. The gas flow is comprised mostly of He and  $O_2$  in a ratio of 4:1 plus any secondary He flow which is typically added to improve nozzle performance. The  $I_2$  molar flow rate is typically 1.5 % of the  $O_2$  molar flow rate. In a device which has a  $Cl_2$  molar flow rate of 0.5 moles/s, the  $O_2$  molar flow rate will be approximately 0.5 moles/s. The corresponding molar flow rates for He and  $I_2$  are 2 moles/s and 0.0075 moles/s, respectively. If a secondary He flow rate of 1 mole/s is assumed, then the total molar flow rate is 3.5075 moles/s with  $I_2$  comprising 0.21% of the flow rate. The partial pressure of  $I_2$  is then 11 mTorr.



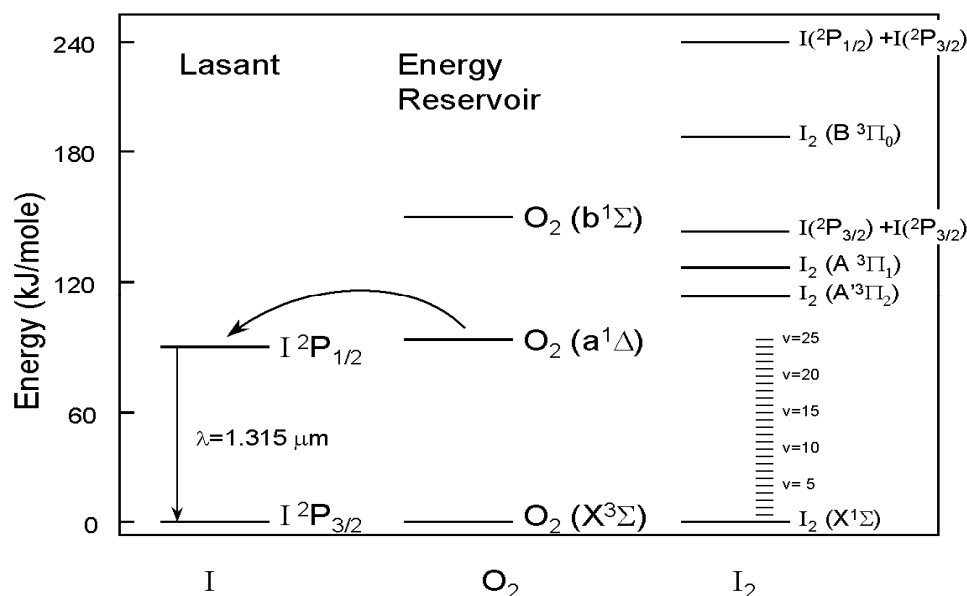


Figure 77. “Energy-level diagram for the Chemical Oxygen-Iodine Laser illustrating the resonant energy transfer from the metastable reservoir  $O_2(a^1\Delta)$  to the upper laser level of atomic Iodine,  $I(^2P_{1/2})$ . The energy-levels for several key states involved in the dissociation of molecular Iodine are also provided”.<sup>10</sup>

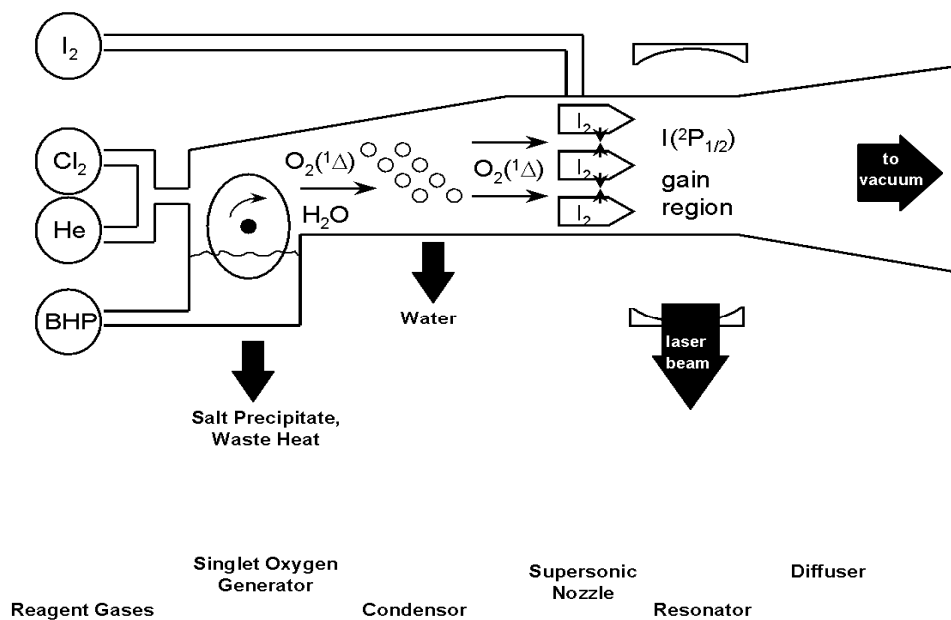


Figure 78. Schematic diagram of a typical supersonic Chemical Oxygen-Iodine Laser (COIL).<sup>10</sup>

A  $\delta T_{ex} < 1$  K is the goal for the temperature diagnostic in COIL. From the measurements made in the static cell at room temperature (see Figure 45 and Figure 46), this goal was achieved for  $P_{I_2} > 50$  mTorr using CBIMF. The CBSAS technique and the MPSF gave  $\delta T_{ex} > 2$  K for pressures  $> 50$  mTorr. For  $P_{I_2} = 11$  mTorr in a static cell held at room temperature or higher, a  $\delta T_{ex} < 1$  K or less could prove difficult for the same overlap volume.

There is an advantage to recording lineshapes at temperatures well below 293 K. Fits to the uniquely contoured profiles at temperatures  $\ll 298$  K had smaller standard errors in the fit parameters as compared to the fits to the broad featureless profiles at room temperature and higher. Since COIL operates at around 160 K, the advantage in fitting the lineshape may offer some reduction in  $\delta T_{ex}$  to counter the low SNR expected at  $P_{I_2} = 11$  mTorr. In terms of experimental apparatus, incorporation of a photon-counting detection technique into the diagnostic may further improve the SNR.<sup>61</sup>

The Air Force uses the Advanced COIL Test Stand for laser research and development in support of the Airborne Laser Program. The gain length is 10 cm, the length of the nozzle bank. Each nozzle is approximately 0.5 cm in width. Power is extracted transverse to the gas flow coming out of the nozzle bank using 2 mirrors separated by 1 m. The circular gain mirrors are 2" in diameter. The rest of the cavity is opaque. From a standpoint of geometry, the CBSAS technique would be the best choice. However, for the reasons discussed above, obtaining a signal with sufficiently high SNR may not be possible. While the CBIMF technique would most likely provide improved SNR, it is not possible to observe the fluorescence from a direction perpendicular to

diagnostic laser beams. When the COIL is operated without extracting power, the 2” circular mirrors can be replaced with 3.5” X 11” rectangular windows which are used for other diagnostic purposes. In this configuration, it would be possible to use the CBIMF technique with the detector positioned at one of the windows and off-axis from the diagnostic beams. If SNR is still insufficient, SBSF can be used, but the spatial resolution would have to be achieved by employing optics in front of the detector. With the rectangular windows, there are more options to increase the beam diameters and decrease crossing angles with the CBSAS or CBIMF techniques to optimize the SNR. The consequence would be, of course, a loss of spatial resolution.

A second difficulty with either CBIMF or SBSF involves repositioning the detector system for measurements in a different location. This would be most difficult with SBSF, less so with CBIMF. With CBSAS, repositioning the overlap volume transverse to the flow only requires changing the position where the pump beam crosses the probe beam; whereas changing the position of the overlap volume upstream or downstream of the flow would require moving the detector.

The Air Force also conducts a research program for an Advanced Tactical Laser (ATL), a small scale COIL device to be used in lower altitude missions that operates at lower powers than the ABL. The COIL test stand for this program has a 20 cm gain length. For general diagnostic purposes, a mirror “box” is positioned on either side of the nozzle bank allowing optical access to the gain region beyond the exit plane of the nozzle bank. The “mirror box” is an evacuated chamber containing optical components to facilitate observation of the gain region. In addition, a rectangular window is incorporated into the top side of the gain cavity. So, the CBIMF technique could be employed in its

usual configuration by directing the diagnostic beams through the mirror boxes and collecting the fluorescence through the top-side window. Both the CBSAS and SBSF could be utilized in the ATL, but the CBIMF would be the first choice.

## IV. Conclusion

The primary result from this research is the successful demonstration of the CBIMF technique as a non-intrusive method for measuring the translational temperature of an  $I_2$  seeded, Ar gas flow in a small supersonic nozzle. This cross-beam laser saturation technique is a new development. It offers a significant advantage over previous single beam LIF methods by providing three-dimensional spatial resolution limited only by the volume defined by the overlapping beams. Temperatures extracted from a  $2.4 \text{ mm}^3$  overlap volume with  $\approx 1 \text{ K}$  statistical errors are of sufficient accuracy for characterizing the temperature of the gas flow in the COIL. In addition, these results indicate that the cross-beam technique could be applied to the research areas of flow-field characterization and nozzle design where the primary gas is seeded with  $I_2$  to facilitate laser-induced fluorescence.<sup>81, 82</sup>

Another new development is the CBSAS technique which also offers three-dimensional spatial resolution. It has an advantage over CBIMF with its simpler experimental arrangement. However, CBSAS, as implemented in this work, was not successful in the nozzle experiments and therefore not likely to succeed as a diagnostic for COIL where the  $I_2$  partial pressure is approximately 11 mTorr. Otherwise, the CBSAS technique would have greater success for application in a flow field test environment where the  $I_2$  concentration can be controlled.

The Doppler-limited theoretical signal developed for this work is a critical part of the diagnostic. It is the first time such a theoretical model constructed from the hyperfine components has been used successfully for temperature extraction. The concept of

modeling the hyperfine structure has been attempted previously in connection with a single beam experiment, but the temperature extraction was not successful.<sup>83</sup> Unique to this work, however, is the demonstrated need for a self-absorption term in the theoretical signal to account for the attenuation of the interrogating laser beam(s). Although it is applied to cross-beam spectral data, the theoretical signal is not restricted to these techniques. In situations where a single beam LIF experiment is appropriate, the theoretical signal is applicable. This was shown in the fits to the SBSF nozzle measurements.

Additional measurements for multiple ro-vibrational lines were made with the cross-beam techniques in a static cell with a steep thermal gradient at temperatures  $> 293$  K. The extracted temperatures differed from thermocouple measurements by more than 10 K in several cases. The statistical errors in extracted temperatures were a few degrees and typically increased with increasing temperature in cell. This work demonstrated that the cross-beam signal at temperatures greater than 293 K is sensitive to the presence of a small nonlinearity in the amplitude. If a systematic error in a cross-beam technique manifested itself as a nonlinearity in the measured cross-beam signal, it is arguable that the nonlinearity could produce large discrepancies (10-20 K) between extracted and thermocouple-measured temperatures (as was observed in the static cell experiments) if the nonlinearity was not modeled in the theoretical cross-beam signal. This does not exclude the possibility that other modifications of the theoretical cross-beam signal may be necessary to achieve accuracy in a static environment at temperatures above 293 K. In contrast to the static cell measurements, the theoretical cross-beam signal does appear sufficient for use in a supersonic nozzle environment. The CBIMF signal at

approximately 145 K was demonstrated to be less susceptible to the introduction of a nonlinearity in the amplitude of the theoretical cross-beam signal.

The Doppler-free experiments performed to support the diagnostic development produced some valuable results also. The first known Ar pressure broadening rates were determined for I<sub>2</sub> hyperfine lines using SAS. The sub-Doppler technique was also an important practical method for selecting isolated ro-vibrational lines as candidates for the diagnostic by examining the hyperfine spectrum for overlapping components from adjacent ro-vibrational lines.

Recommendations for future research include exploring ways to optimize the temperature diagnostic. Logical follow-on efforts would be to utilize the CBIMF and CBSAS techniques to measure the temperature in the gain region of the Air Force's Advanced Tactical Laser test stand and the Advanced COIL test stand as well as in nozzle test environments or wind tunnels. In conjunction with these efforts, efforts could be made improve the signal to noise ratio of both the CBIMF and CBSAS techniques. One direction to explore is advantage frequency modulation may provide in SNR over amplitude modulation. There is also the possibly of exploring the advantages of adapting other Doppler-free techniques, such polarization spectroscopy, to a cross-beam configuration.

Other areas of investigation could focus on basic spectroscopic phenomena. Efforts could be made to resolve the discrepancies between I<sub>2</sub> lifetimes measured with fluorescence decay methods and I<sub>2</sub> linewidths obtained from Doppler-free techniques. Contributions could also be made in determining pressure broadening rates of I<sub>2</sub> hyperfine components due to buffer gases. Finally, further investigations of velocity

changing collisions and their effects on the  $I_2$  hyperfine spectrum could lead to insight into rotational and vibrational energy transfer mechanisms.



## Appendix A. Blended Lines

A Mathematica<sup>®</sup> program was used to simultaneously constrain the blended line fits to the temperature information contained in the lineshape amplitudes and the common Doppler linewidth. From Equation (123), the amplitude from a CBSAS profile is given by

$$A_{cbsas} = C \alpha' L' I_{probe}^o I_{pump}^o = C' \alpha' = C' \alpha_o \frac{\sigma_o}{R^* h \nu} = C' \frac{(\sigma_o)^2}{R^* h \nu} \Delta N^o \quad (145)$$

where the unsaturated population difference, for degenerate energy levels, is

$$\Delta N^o = \frac{g_2}{g_1} N_1^o - N_2^o = \left( \frac{g_2}{g_1} f_1 - f_2 \right) N_{I_2} = \Delta f N_{I_2} \quad (146)$$

where  $g_1 = (2J'' + 1)$ , and  $g_2 = (2J' + 1)$  are the rotational energy-level degeneracies,

and  $f_i = N_{evJ}^i / N_{I_2}$  is the fractional population density for a particular level, and  $N_{I_2}$  is

the total population density of iodine molecules. The population density  $N_{evJ}^i$  is given by

Equation (15). Substituting Equation (146) and the expression for the absorption cross-section  $\sigma_o$ , Equation (81), into Equation (145) yields

$$A_{cbsas} = C' \frac{1}{h \nu R^*} \left( A_{21} \frac{\lambda^2}{4 \pi^2 \Delta \nu_h} \right)^2 \Delta f N_{I_2} . \quad (147)$$

for the CBSAS signal amplitude. The Einstein coefficient for spontaneous emission,  $A_{21}$ , given by Equation (10) can be substituted into Equation (147) to yield for the amplitudes of lines A and B:

$$A_{cbsas}^A = \frac{C'}{R_A^* h \nu_A} \left( \frac{16 \pi^2}{3 h (\Delta \nu_h)_A} \frac{c}{\lambda_A} \left( \frac{S_{J',J''}^A}{2 J'_A + 1} \right) \left| \mu_e^A(\bar{R}) \right|^2 \left| \langle \Psi_{\nu'}^A | \Psi_{\nu''}^A \rangle \right|^2 \right)^2 \Delta f^A N_{I_2}, \quad (148)$$

and

$$A_{cbsas}^B = \frac{C'}{R_B^* h \nu_B} \left( \frac{16 \pi^2}{3 h (\Delta \nu_h)_B} \frac{c}{\lambda_B} \left( \frac{S_{J',J''}^B}{2 J'_B + 1} \right) \left| \mu_e^B(\bar{R}) \right|^2 \left| \langle \Psi_{\nu'}^B | \Psi_{\nu''}^B \rangle \right|^2 \right)^2 \Delta f^B N_{I_2}. \quad (149)$$

In  $I_2$   $B$ - $X$  transitions,  $S_{J',J''}/(2J'+1) \cong 1/2$  for large  $J'$ .<sup>23, 37</sup> In addition, the

$\left| \mu_e^i(\bar{R}) \right|^2$  values are  $\approx 1$ .<sup>84</sup> Using these approximations,

$$A_{cbsas}^A \cong \frac{C' 64 \pi^4 \nu_A}{9 h^3 R_A^* (\Delta \nu_h)_A^2} \left( \left| \langle \Psi_{\nu'}^A | \Psi_{\nu''}^A \rangle \right|^2 \right)^2 \Delta f^A N_{I_2} \quad (150)$$

$$A_{cbsas}^B \cong \frac{C' 64 \pi^4 \nu_B}{9 h^3 R_B^* (\Delta \nu_h)_B^2} \left( \left| \langle \Psi_{\nu'}^B | \Psi_{\nu''}^B \rangle \right|^2 \right)^2 \Delta f^B N_{I_2} \quad (151)$$

Recognizing that the upper state fractional population densities,  $f_2^i$ , are effectively zero,

Equations (150) and (151) can be approximated further to yield

$$A_{cbsas}^A \approx C_A'' \left( \left| \langle \Psi_{\nu'}^A | \Psi_{\nu''}^A \rangle \right|^2 \right)^2 g_2^A g_n^A \exp\left(-\frac{E_A''}{k_B T}\right) \quad (152)$$

and

$$A_{cbsas}^B \approx C_B'' \left( \left| \langle \Psi_{\nu'}^B | \Psi_{\nu''}^B \rangle \right|^2 \right)^2 g_2^B g_n^B \exp\left(-\frac{E_B''}{k_B T}\right) \quad (153)$$

where, in general,

$$C'' = \frac{C' 64 \pi^4 \nu}{9 h^3 R^* (\Delta \nu_h)^2} N_{I_2}. \quad (154)$$

For the purposes of the model, the constant  $C''$  is approximated to be the same for line A and line B;  $C''_A \cong C''_B$ . Doing so allows  $C''$  to be used as a common fit parameter in the computer calculation. The close proximity of the resonant frequencies,  $\nu_A \approx \nu_B$ , supports the approximation. The homogeneous linewidth of the two adjacent lines should be very nearly the same. The real concern is whether or not  $R_A^*$  and  $R_B^*$  can be considered nearly equal. With these assumptions, however, the amplitudes of the two overlapping lines depend primarily on their respective energy-level degeneracies, FCFs, and the fractional population densities for the lower energy levels.

A fit to the CBSAS blended line signal of P(51) 18-2 & P(66) 16-1 is shown in Figure 79. The data is from the CBSAS static cell experiment. The fit is clearly very poor in the vicinity of the P(51) 18-2 line. The extracted temperature is 293 K +/- 0.4 K compared to the thermocouple-measured temperature of 300 K +/- 1 K. The difficulty in using this approach to fit profiles lies in correctly estimating  $R_A^*$  and  $R_B^*$ . Given the complexity of the kinetics involved, it would seem that this approach isn't practical for extracting temperatures in a gas at 300 K or higher temperatures.

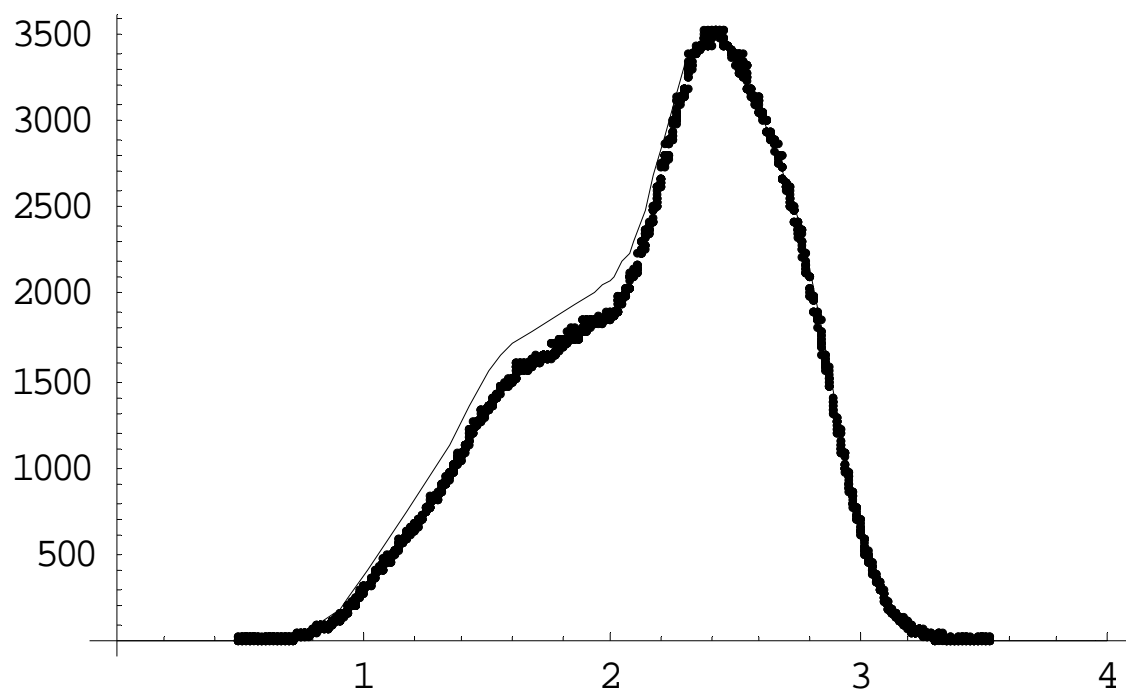


**Figure 79. A fit to CBSAS signal of the P(51) 18-2 & P(66) 16-1 blended line recorded in a static cell experiment. The amplitudes of each ro-vibrational line and the common Doppler linewidth are constrained to temperature. The y-axis is Relative Intensity (Arbitrary Units). The x-axis is Relative Frequency (GHz).**

## Bibliography

1. The Boeing Company. "Airborne Laser." website.  
<http://www.boeing.com/defense-space/military/abl/flash.html>. 8 Mar 2005.
2. Duffner, Robert W. *Airborne Laser: Bullets of Light*. New York: Plenum Trade, 1997.
3. Hecht, Jeff. "Airborne Laser Achieves "First Light" Milestone," *Laser Focus World*, 41: 15-17 (2005).
4. McDermott, W. E., N. R. Pchelkin, D. J. Benard, and R. R. Bousek. "An Electronic Transition Chemical Laser," *Applied Physics Letters*, 32: 469-70 (1978).
5. Air Force Research Laboratory, Office of Public Affairs. "Chemical Oxygen-Iodine Laser (COIL)." Article. <http://www.de.afrl.af.mil/factsheets/coil.html>. 3 May 2004.
6. Bloembergen, N., and C.K.N. Patel, et al. "Report to the American-Physical Society of the Study-Group on Science and Technology of Directed Energy Weapons," *Reviews of Modern Physics*, 59: S1 (1987).
7. Truesdell, K. A., C. A. Helms, and G. D. Hager. "A History of COIL Development in the USA," *Proceedings of the SPIE - The International Society for Optical Engineering*, 2502: 217-37 (1995).
8. Truesdell, K. A., S. E. Lamberson, and G. D. Hager. *AIAA*, 92: 3003 (1992).
9. Keating, P. B., C. A. Helms, B. T. Anderson, T. L. Rittenhouse, K. A. Truesdell, and G. D. Hager, "Two-Dimensional Gain and Cavity Temperature Maps of a Small-Scale Supersonic COIL," in *Proceedings of the International Conference on Lasers '96*, 194-201, V. J. Corcoran and T. A. Goldman, STS Press, McLean, VA (1997).
10. Perram, Glen P., "Chemical Lasers," in *Wiley Encyclopedia of Electrical and Electronics Engineering*, Vol. 3. Ed. J. G. Webster. New York: John Wiley & Sons, 1999.
11. Mulliken, Robert S. "Iodine Revisited," *The Journal of Chemical Physics*, 55: 288-309 (1 July 1971).

12. Gerstenkorn, S., and P. Luc. *Atlas du Spectre d'Absorption de la Molecule de l'Iode Entre 14800-20000 cm<sup>-1</sup>*. Paris: Presses du CNRS, 1985.
13. Velchev, I., R. Van Dierendonck, W. Hogervorst, and W. Ubachs. "A Dense Grid of Reference Iodine Lines for Optical Frequency Calibration in the Range 571-596 nm," *Journal of Molecular Spectroscopy*, 187: 21-7 (1998).
14. Privalov, Vadim E., and Sergey K. Savelyev. "Atlas of Molecular Iodine Absorption Lines," *Proceedings of SPIE The International Society for Optical Engineering*, 3687: 2-5 (1999).
15. Xu, S. C., R. van Dierendonck, W. Hogervorst, and W. Ubachs. "A Dense Grid of Reference Iodine Lines for Optical Frequency Calibration in the Range 595-696 nm," *Journal of Molecular Spectroscopy*, 201: 256-266 (2000).
16. Glessner, John W. *Amplified Spontaneous Emission of the Iodine B<sup>3</sup>Π(O<sup>+</sup><sub>u</sub>)-X<sup>1</sup>Σ(O<sup>+</sup><sub>g</sub>) System*. Air Force Institute of Technology (AU), Wright-Patterson AFB, OH, May 1987 (AD-A182590).
17. Capelle, G. A., and H. P. Broida. "Lifetimes and Quenching Cross Sections of I<sub>2</sub>(B<sup>3</sup>Π<sub>0u</sub><sup>+</sup>)\*," *Journal of Chemical Physics*, 58: 4212-22 (1973).
18. Broyer, M., J. Vigue, and J. C. Lehmann. "Direct Evidence of the Natural Predissociation of the I<sub>2</sub> B State through Systematic Measurements of Lifetimes," *Journal of Chemical Physics*, 63: 5428-31 (1975).
19. Bernath, Peter F. *Spectra of Atoms and Molecules*. New York: Oxford University Press, 1995.
20. Townes, C. H., and A. L. Schawlow. *Microwave Spectroscopy*. New York: Dover Publications, Inc., 1975.
21. Herzberg, Gerhard. *Molecular Spectra and Molecular Structure, Vol. I: Spectra of Diatomic Molecules*. New York: Van Nostrand, 1950.
22. Luc, P. "Molecular Constants and Dunham Expansion Parameters Describing the B-X System of the Iodine Molecule," *Journal of Molecular Spectroscopy*, 80: 41-55 (1980).
23. Tellinghuisen, J. "Intensity Factors for the I<sub>2</sub> B-X Band System," *Journal of Quantitative Spectroscopy and Radiative Transfer*, 19: 149-61 (1978).
24. Kroll, M., and K. K. Innes. "Molecular Electronic Spectroscopy by Fabry-Perot Interferometry. Effect of Nuclear Quadrupole Interactions on the Line Widths of

- the  $B^3\Pi_{o+}-X^1\Sigma_{g+}$  Transition of the  $I_2$  Molecule," *Journal of Molecular Spectroscopy*, 36: 295-309 (1970).
25. Hansch, T. W., M. D. Levenson, and A. L. Schawlow. "Complete Hyperfine Structure of a Molecular Iodine Line," *Physical Review Letters*, 26: 946-9 (1971).
  26. Levenson, M. D., and A. L. Schawlow. "Hyperfine Interactions in Molecular Iodine," *Physical Review A (General Physics)*, 6: 10-20 (1972).
  27. Razet, A., and S. Picard. "A Test of New Empirical Formulas for the Prediction of Hyperfine Component Frequencies in  $^{127}I_2$ ," *Metrologia*, 34: 181-6 (1997).
  28. Robinson, G. Wilse, and C. D. Cornwell. "The Interaction with Molecular Rotation of the Nuclear Electric Quadrupole Moments of Two Nuclei Having Spins  $3/2$ ," *Journal of Chemical Physics*, 21: 1436-1442 (1953).
  29. Kroll, M. "Hyperfine Structure in the Visible Molecular-Iodine Absorption Spectrum," *Physical Review Letters*, 23: 631-3 (1969).
  30. Heaven, Michael C. Professor, Physical Chemistry, Chemistry Building, Department of Chemistry, Emory University, Atlanta, GA 30322. Original FORTRAN program provided through personal correspondence. August 2002.
  31. Hirota, E., "High Resolution Spectroscopy of Transient Molecules," in *Springer Series in Chemical Physics, Vol. 40*. Ed. E. Hirota. Berlin: Springer-Verlag, 1985.
  32. Hanes, G. R., J. Lapierre, P. R. Bunker, and K. C. Shotton. "Nuclear Hyperfine Structure in the Electronic Spectrum of  $^{127}I_2$  by Saturated Absorption Spectroscopy, and Comparison with Theory," *Journal of Molecular Spectroscopy*, 39: 506-15 (1971).
  33. Yokozeki, Akimichi, and J. S. Muentner. "Laser Fluorescence State Selected and Detected Molecular Beam Magnetic Resonance in  $I_2$ ," *Journal of Chemical Physics*, 72: 3796-3804 (1980).
  34. National Bureau of Standards. *The Calculation of Rotational Energy Levels and Rotational Line Intensities in Diatomic Molecules*. NBS Monograph-115, Washington, DC, 1970.
  35. Shotton, K. C., and G. D. Chapman. "Lifetimes of  $^{127}I_2$  Molecules Excited by the 632.8 nm He/Ne Laser," *Journal of Chemical Physics*, 56: 1012-13 (1972).
  36. Klein, U. K. A., J. Mastromarino, and A. Suwaiyan. "Rotational Level Lifetimes and Self-Quenching of  $^{127}I_2$  by Fluorescence Demodulation Spectroscopy," *Chemical Physics Letters*, 217: 86-90 (1994).

37. Tellinghuisen, J. "The Electronic Transition Moment Function for the  $\text{B}0^+_u(^3\Pi)-\text{X}^1\Sigma^+_g$ ," *Journal of Chemical Physics*, 106: 1305-8 (1997).
38. Sorem, M. S., and A. L. Schawlow. "Saturation Spectroscopy in Molecular Iodine by Intermodulated Fluorescence," *Optics Communications*, 5: 148-51 (1972).
39. Bennett, S. J., and P. Cerez. "Hyperfine Structure in Iodine at the 612 nm and 640-nm Helium-Neon," *Optics Communications*, 25: 343-7 (1978).
40. Duffey, T. P., D. Kammen, A. L. Schawlow, S. Svanberg, H.-R. Xia, G.-G. Xiao, and G.-Y. Yan. "Laser Spectroscopy Using Beam-Overlap Modulation," *Optics Letters*, 10: 597-599 (December 1985).
41. Cheng, Wang-Yau, and Jow-Tsong Shy. "Wavelength Standard in 543 nm and the Corresponding  $^{127}\text{I}_2$  Hyperfine Transitions," *CPEM Digest*, 471-472 (2000).
42. Mironov, A. V. "Broadening and Saturation of Iodine-127 R(127) 11-5 Line (0.63299  $\mu\text{m}$ ) in a Helium-Neon Laser," *Optics and Spectroscopy*, 65: 471-3 (1988).
43. Brillet, A., and P. Cerez. "Quantitative Description of the Saturated Absorption Signal in Iodine Stabilized He-Ne lasers," *Metrologia*, 13: 137-9 (1977).
44. Smith, P. W., and T. Hansch. "Cross-Relaxation Effects in the Saturation of the 6328 Å Neon-Laser Line," *Physical Review Letters*, 26: 740-743 (29 March 1971).
45. Corney, Alan. *Atomic and Laser Spectroscopy*. Oxford: Clarendon Press, 1977.
46. Hindmarsh, W. R., and Judith M. Farr. "Collision Broadening of Spectral Lines by Neutral Atoms," *Progress in Quantum Electronics*, 2: 141-214 (1973).
47. Eickhoff, Mark L., and J. L. Hall. "Optical Frequency Standard at 532 nm," *IEEE Transactions on Instrumentation and Measurement*, 44: 155-158 (2 April 1995).
48. Astill, A. G., A. J. McCaffery, M. J. Proctor, E. A. Seddon, and B. J. Whitaker. "Pressure Broadening of the Nuclear Hyperfine Spectrum of  $^{127}\text{I}_2$  by He and Xe," *Journal of Physics B (Atomic and Molecular Physics)*, 18: 3745-57 (1985).
49. Kireev, S. V., S. L. Shnyrev, and Yu. P. Zaspa. "Effect of Buffer Gases on Broadening of the Iodine-127 Resonance Absorption Line at a 633-nm He-Ne Laser Wavelength," *Optics and Spectroscopy*, 78: 550-552 (1995).



50. Berjot, M., L. Bernard, and T. Theophanides. "Variation du Facteur de Depolarisation de la Bande Fondamentale de l'iode au Cours du Passage Continu de la Fluorescence de Resonance a l'effet Raman de Resonance," *Canadian Journal of Spectroscopy*, 18: 128-130 (September/October 1973).
51. Fletcher, D. G., and J. C. McDaniel. "Collisional Shift and Broadening of Iodine Spectral Lines in Air Near 543 nm," *Journal of Quantitative Spectroscopy and Radiative Transfer*, 54: 837-850 (1995).
52. Wallard, A. J., J. M. Chartier, and J. Hamon. "Wavelength Measurements of the Iodine Stabilized Helium-Neon Laser," *Metrologia*, 11: 89-95 (1975).
53. Cerez, P., A. Brillet, and F. Hartmann. "Metrological Properties of the R(127) Line of Iodine Studied by Laser Saturated Absorption," *IEEE Transactions on Instrumentation and Measurement*, IM-23: 526-8 (1974).
54. Titov, A., I. Malinovsky, and M. Erin. "Determination of Saturation Parameter in Iodine and Precise Molecular Linewidth Measurements in He-Ne/I<sub>2</sub> Standard at 633 nm," *Optics Communications*, 136: 327-334 (15 March 1997).
55. Glaser, M. "An Improved He-Ne Laser at  $\lambda=612$  nm, Stabilized by Means of an External Absorption Cell," *Metrologia*, 23: 45-53 (1986).
56. Sakurai, T., S. Iwasaki, T. Oshida, and K. Tanaka. "Pressure and Power Broadenings of the Saturated Absorption Lines of Iodine at 633 nm," *Japanese Journal of Applied Physics*, 18: 1199-200 (1979).
57. Taylor, John R. *An Introduction to Error Analysis*. Mill Valley CA: University Science Books, 1982.
58. TableCurve 2D. Version 5.01.01, IBM, 22.6 MB, CD-ROM. Computer software. SYSTAT Software Inc., 501 Canal Blvd, Suite C, Point Richmond CA 94804-2028, USA, 2002.
59. Letokhov, V. S., and V. P. Chebotayev. *Nonlinear Laser Spectroscopy*. Berlin: Springer Verlag, 1977.
60. Letokhov, V. S., "Saturation Spectroscopy," in *High-Resolution Laser Spectroscopy, Topics in Applied Physics, Vol. 13*. Ed. K. Shimoda. Berlin, West Germany: Springer-Verlag, 1976.
61. Demtroder, Wolfgang. *Laser Spectroscopy*. Berlin: Springer, 1998.
62. Cerez, P., and S. J. Bennett. "Helium-Neon Laser Stabilized by Saturated Absorption in Iodine at 612 nm," *Applied Optics*, 18: 1079-83 (1979).

63. Couillaud, B., A. Ducasse, and A. Dienes. "Experimental Method for the Measurement of Hyperfine Transition Saturation Intensities in a Gaseous Medium," *Applied Physics*, 21: 135-40 (1980).
64. Shimoda, K., ed. *Topics in Applied Physics, Volume 13: High Resolution Laser Spectroscopy*. Berlin: Springer-Verlag, 1976.
65. Bennet, W. R. "Hole-Burning Effects in a He-Ne-Optical MASER," *Physical Review*, 126: 580 (1962).
66. Lamb, W. E. "Theory of an Optical MASER," *Physical Review A*, 134: 1429 (1964).
67. Hanes, G. R., and C. E. Dahlstrom. "Iodine Hyperfine Structure Observed in Saturated Absorption at 633 nm," *Applied Physics Letters*, 14: 362-4 (1969).
68. Knox, J. D., and Yoh-Han Pao. "Absorption Profiles and Inverted Lamb Dips of I<sub>2</sub> Vapor at 633 nm as Studied with a He-Ne Laser," *Applied Physics Letters*, 16: 129-131 (1970).
69. Shapiro, Asher H. *The Dynamics and Thermodynamics of Compressible Fluid Flow, Vol. 1*. New York: John Wiley & Sons, 1953.
70. Goldsmith, J. E. M. "Spatially Resolved Saturated Absorption Spectroscopy in Flames," *Optics Letters*, 6: 525-7 (1981).
71. Kychakoff, George, Robert D. Howe, and Ronald K. Hanson. "Spatially Resolved Combustion Measurements Using Cross-Beam Saturated Absorption Spectroscopy," *Applied Optics*, 23: 1303-1305 (1 May 1984).
72. Zizak, G., F. Cignoli, and S. Benecchi. "Spatially Resolved Saturation Absorption Measurements of OH in Methane-Air Flames," *Applied Optics*, 26: 4293-7 (1987).
73. Baklanov, E. V., and V .P. Chebotaev. "Resonance Interaction of Unidirectional Waves in Gases," *Soviet Physics JETP*, 34: 490-493 (March 1972).
74. *Alfa Aesar*. Research Chemicals, Metals, and Materials Catalog. publishing place unknown: Johnson Matthey Catalog Company, Inc., 1999-2000.
75. Sansonetti, C. J. "Precise Measurements of Hyperfine Components in the Spectrum of Molecular Iodine," *Journal of the Optical Society of America B (Optical Physics)*, 14: 1913-20 (1997).

76. Morinaga, A. "Cross-Relaxation Effects on the Saturation of Visible Absorption Lines of the Iodine Molecule," *Journal of the Optical Society of America B (Optical Physics)*, 4: 906-9 (1987).
77. Van Marter, Todd, Michael C. Heaven, and David Plummer. "Measurement of the Rate Constant for the Quenching of  $I(^2P_{1/2})$  by  $O_2(X)$  at 150 K," *Chemical Physics Letters*, 260: 201-207 (20 September 1996).
78. Atkinson, Dean B., and Mark A. Smith. "Design and Characterization of Pulsed Uniform Supersonic Expansions for Chemical Applications," *Review of Scientific Instruments*, 66: 4434-4446 (September 1995).
79. Alcatel. Pumping and Leak Detection Systems Selection Guide. publishing place unknown: Alcatel CIT High Vacuum Technology, April 1997.
80. Bernard, D. J., W. E. McDermott, N. R. Pchelkin, and R. R. Bousek. "Efficient Operation of a 100-W Transverse-Flow Oxygen-Iodine Chemical Laser," *Applied Physics Letters*, 34: 40-1 (1979).
81. Hiller, B., and R. K. Hanson. "Properties of the Iodine Molecule Relevant to Laser-Induced Fluorescence Experiments in Gas Flows," *Experiments in Fluids*, 10: 1-10 (1990).
82. Fletcher, D. G., and J. C. McDaniel. "Temperature Measurement in a Compressible Flow Field using Laser-Induced Iodine Fluorescence," *Optics Letters*, 12: 16-18 (1987).
83. Hirai, Etsuro, Koji Teshima, Koichi Kurita, and Shigeru Takahara. "Velocity Measurements of Free Jets Using Nuclear Hyperfine Structure of  $I_2^*$ ," *Japanese Society of Mechanical Engineers International Journal Series B*, 40: 501-508 (1997).
84. Bhale, G. L., S. F. Ahmad, and S. P. Reddy. "A Study of Variation of Electronic Transition Moment of the B-X System of  $I_2$  from its Laser-Excited Fluorescence Spectrum," *Journal of Physics B (Atomic and Molecular Physics)*, 18: 645-55 (1985).

## **Vita**

Major Grady T. Phillips graduated from Wofford College in Spartanburg, SC with a BS in Physics and a BA in Mathematics. He entered graduate studies at Clemson University where he pursued research in high temperature superconductivity and graduated with a MS in Physics. He was commission through the Air Force Officer Training School at Maxwell AFB, Alabama.

His first assignment was Air Force Global Weather Central, Offutt AFB, NE where he served as a Communications-Computer Systems Officer performing software acquisitions program management. Next, he went to the Air Force Technical Applications Center, Patrick AFB, FL as an acquisitions officer where he was a Radio Frequency Systems Program Manager. He was then selected to attend the Graduate School of Engineering and Management at the Air Force Institute of Technology, Wright-Patterson AFB, OH. He is currently assigned to the Space Vehicles Directorate of the Air Force Research Laboratory, Kirtland AFB, NM where he serves as the Deputy Chief for the Space Based Infrared Technology Center of Excellence.

REPORT DOCUMENTATION PAGE				Form Approved OMB No. 074-0188	
<p>The public reporting burden for this collection of information is estimated to average 1 hour per response, including the time for reviewing instructions, searching existing data sources, gathering and maintaining the data needed, and completing and reviewing the collection of information. Send comments regarding this burden estimate or any other aspect of the collection of information, including suggestions for reducing this burden to Department of Defense, Washington Headquarters Services, Directorate for Information Operations and Reports (0704-0188), 1215 Jefferson Davis Highway, Suite 1204, Arlington, VA 22202-4302. Respondents should be aware that notwithstanding any other provision of law, no person shall be subject to a penalty for failing to comply with a collection of information if it does not display a currently valid OMB control number.</p> <p><b>PLEASE DO NOT RETURN YOUR FORM TO THE ABOVE ADDRESS.</b></p>					
1. REPORT DATE (DD-MM-YYYY) 23-03-2006		2. REPORT TYPE Doctoral Dissertation		3. DATES COVERED (From – To) Aug 1999 – Mar 2006	
4. TITLE AND SUBTITLE  Spatially-Resolved Temperature Diagnostic For Supersonic Flow Using Cross-Beam Doppler-Limited Laser Saturation Spectroscopy				5a. CONTRACT NUMBER	
				5b. GRANT NUMBER	
				5c. PROGRAM ELEMENT NUMBER	
6. AUTHOR(S)  Phillips, Grady, T., Major, USAF				5d. PROJECT NUMBER 01-145	
				5e. TASK NUMBER	
				5f. WORK UNIT NUMBER	
7. PERFORMING ORGANIZATION NAMES(S) AND ADDRESS(S) Air Force Institute of Technology Graduate School of Engineering and Management (AFIT/EN) 2950 Hobson Way WPAFB OH 45433-7765				8. PERFORMING ORGANIZATION REPORT NUMBER  AFIT/DS/ENP/06-03	
9. SPONSORING/MONITORING AGENCY NAME(S) AND ADDRESS(ES)  N/A				10. SPONSOR/MONITOR'S ACRONYM(S)	
				11. SPONSOR/MONITOR'S REPORT NUMBER(S)	
12. DISTRIBUTION/AVAILABILITY STATEMENT APPROVED FOR PUBLIC RELEASE; DISTRIBUTION UNLIMITED					
13. SUPPLEMENTARY NOTES					
14. ABSTRACT <p>Optical techniques for measuring the temperature in three-dimensional supersonic reactive flows have typically depended on lineshape measurements using single-beam laser absorption spectroscopy. However, absorption over extended path lengths in flows with symmetric, turbulent eddies can lead to systematically high extracted temperatures due to Doppler shifts resulting from flow along the absorption path. To eliminate these problems, Cross-Beam Saturation Absorption Spectroscopy (CBSAS) and Cross-Beam Inter-Modulated Fluorescence (CBIMF) have been developed which utilize two crossed and nearly copropagating laser beams to record the spectral signal of an I<sub>2</sub> ro-vibrational line in a small three-dimensional volume using a tunable CW dye laser. Temperature is extracted by fitting the recorded signal with a theoretical signal constructed from the Doppler-broadened hyperfine components of the ro-vibrational line. The CBIMF technique proved successful for extracting the temperature of an I<sub>2</sub>-seeded, Ar gas flow within a small, Mach 2, Laval nozzle where the overlap volume of the two 1 mm diameter laser beams was 2.4 mm<sup>3</sup>. At a test point downstream of the nozzle throat, the average temperature of 146 K +/- 1.5 K extracted from measurements of the I<sub>2</sub> P(46) 17-1 spectral line compared favorably with the 138 K temperature calculated from isentropic, one-dimensional flow theory.</p>					
15. SUBJECT TERMS saturation spectroscopy, iodine, linewidth, hyperfine spectrum, temperature diagnostic					
16. SECURITY CLASSIFICATION OF:			17. LIMITATION OF ABSTRACT  UU	18. NUMBER OF PAGES 185	19a. NAME OF RESPONSIBLE PERSON Glen P. Perram, AFIT/ENP
REPORT U	ABSTRACT U	c. THIS PAGE U			19b. TELEPHONE NUMBER (Include area code) (937) 255-3636, ext 4504; e-mail: Glen.Perram@afit.edu